Spring 2019

Evaluating Corrosion Altering Properties of Thiophene Based Copolymers

Robert Peterson
University of Southern Mississippi

EVALUATING CORROSION ALTERING PROPERTIES OF THIOPHENE BASED COPOLYMERS

by

Robert Peterson

A Dissertation
Submitted to the Graduate School,
the College of Arts and Sciences
and the School of Polymer Science and Engineering
at The University of Southern Mississippi
in Partial Fulfillment of the Requirements
for the Degree of Doctor of Philosophy

Approved by:

Dr. James W. Rawlins, Committee Chair
Dr. Sarah E. Morgan
Dr. Sergei I. Nazarenko
Dr. William L. Jarrett
Dr. Robson F. Storey

Dr. James W. Rawlins Committee Chair	Dr. Jeffrey S. Wiggins Director of School	Dr. Karen S. Coats Dean of the Graduate School

May 2019

Published by the Graduate School

ABSTRACT

There is an important and ongoing debate on how or whether conductive polymers (CP**)** alter corrosion performance with some researchers reporting that CP**s** ultimately accelerate corrosion and others saying CPs, if understood could possibly replace the world's best standard for corrosion prevention, i.e., chromium based inhibitors. The primary project goal was to improve our understanding of how CP**s** alter corrosion chemistry by 1) controlling the polymer structure and 2) in-turn the properties and then 3) targeting the best protocol for fast corrosion kinetic evaluation.

We detail the copolymer synthesis results and shift in corrosion protection properties for a series of polythiophene copolymers with variation in solubility and measured onset oxidation potential. Controlled polymerization can be achieved, the properties were predictable based upon the resulting comonomer composition, and we explain how these properties affect corrosion kinetics. We confirm that the lower onset oxidation potential decreases corrosion rates over steel substrates, however performance peaks at an onset oxidation potential of 0.24 V vs Fc/Fc^{+}. Further, we confirmed our hypothesis that CP**s** like polythiophenes affect corrosion primarily by a combination of differences in ion barrier properties and shifted anodic polarization of the substrate. Additionally, another hypothesis is further supported in that there is/was an optimal 3,4-ethylenedioxythiophene content for the polymer to achieve the best performance for steel.

The data presented here helps improve our understanding on how CP affect corrosion, the characteristic properties that are tunable for better CP design towards anti-corrosive primers, and how to adequately evaluate the material combinations performance.

ACKNOWLEDGMENTS

I cannot thank my advisor Dr. James Rawlins enough for helping me to become a better scientist, and for helping me grow professionally. I thank my committee for their time taken evaluating my work. Special thanks to Dr. Robson Storey. Had he not recruited me as an undergrad, I would have never found Southern Miss. Also, thank you to everyone in TRRG for being such an encouraging and productive research group.

I would like to acknowledge the work of several undergraduate researchers. Alexandra Jarriel (trained by Dr Brandon Achord on GRIM polymerization) helped test P3HT and 2,5-dibromo-3,4-ethylenedioxythiophene synthesis along with ReactIR data collection. Prashant Karki helped collect water uptake data and synthesized many copolymer batches after I optimized the procedure. Robert Bennet helped collect water uptake data and prepared Go9v10 samples for EIS. Logan McCary helped collect OCP and Tafel data. Finally, Dane Wedgeworth helped collect NMR spectra for several samples. Their help effectively allowed twice the experiments in similar timeframes. Thank you!

This project was possible thanks to funding from the DoD through the technical corrosion collaboration (TCC). The annual meetings and review sessions for TCC gave me many opportunities to learn from others, discuss ideas, and provide presentations to review my data and progress. Critiques from members of the TCC helped to strengthen my scientific arguments.

Finally, thank you to Dr. Jeremy Moskowitz and Dr. Phillip Pickett for being the best roommates I could ask for, and to Melissa Graham for being a supportive and loving partner.

DEDICATION

To my friends and family for their constant words of encouragement, especially Mom, Dad, and Melissa.

TABLE OF CONTENTS

LIST OF TABLES

LIST OF FIGURES

LIST OF SCHEMES

LIST OF ABBREVIATIONS

3HT	3-hexylthiophene
BK	Brasher-Kingsbury
CP	conductive polymer
CP#	Poly(3-hexylthiophene-co-3,4-ethylenedioxythiophene) from feed ratio #:1 DB3HT:DBEDOT
CPE	constant phase element
CV	cyclic voltammetry
DB3HT	2,5-dibromo-3-hexylthiophene
DBEDOT	2,5-dibromo-3,4-ethylenedioxythiophene
DGEBA	diglycidyl ether of bisphenol A
DI	deionized
DMA	dynamic mechanical analysis
DMF	dimethylformamide
DoD	Department of Defense
DVS	dynamic vapor sorption
EDOT	3,4-ethylenedioxythiophene
EFM	electrochemical frequency modulation
EIS	electrochemical impedance spectroscopy
FET	field effect transistor
FTIR	Fourier transform infrared
GCMS	gas chromatography mass spectroscopy

Go9v10	epoxy-amine films described in section 5.2.1
GPC	gel permeation chromatography
GRIM	Grignard metathesis
HOMO	highest occupied molecular orbital
HSP	Hanson solubility parameter
LUMO	lowest unoccupied molecular orbital
MeOH	methanol
MPCAP	measured primary current amplitude peak
NACE	National Association of Corrosion Engineers
NBS	n-bromosuccinimide
$Ni(dppp)Cl_2$	[1,3-Bis(diphenylphosphino)propane] dichloronickel(II)
NIR	near infrared
NMR	nuclear magnetic resonance
OCP	open circuit potential
OPV	organic photovoltaic
P(3HT-co-EDOT)F#:1	Poly(3-hexylthiophene-co-3,4-ethylenedioxythiophene) from feed ratio #:1 DB3HT:DBEDOT
P3HT	poly(3-hexylthiophene)
PCBM	[6,6]-phenyl-C61-butyric acid methyl ester
PDI	polydispersity index
PEDOT	poly(3,4-ethylenedioxythiophene

PLED	polymer light emitting diode
RH-DMA	relative humidity chamber dynamic mechanical analysis
RPVC	relative pigment volume concentration
SDMPCAP	squared difference in measured primary current amplitude peaks
SKP	scanning Kelvin probe
TCC	Technical Corrosion Collaboration
THF	tetrahydrofuran
TRRG	Thames Rawlins Research Group
UV-Vis	ultraviolet and visible

LIST OF EQUATION SYMBOLS

[X]	Concentration of X. Examples include [benzyl] for benzyl groups, [ox] for oxidant, [red] for reductant, and [water] for water.
$(i_{\omega 1}^{*})_B$	Measured amplitude current from the intermodulation spectrum using the second base angular frequency at angular frequency 1
$(i_{\omega 2}^{*})_B$	Measured amplitude current from the intermodulation spectrum using the second base angular frequency at angular frequency 2
A	Either area, arbitrary coefficient, or first quadratic coefficient
$A_{i\omega 1}$	First quadratic coefficient when solving the angular frequency 1 relationship
$A_{i\omega 2}$	First quadratic coefficient when solving the angular frequency 2 relationship
A_r	NIR peak area ratio
A_{4620}	Area of NIR peak at 4620 cm^{-1}
A_{5200}	Area of NIR peak at 5200 cm^{-1}
α	CPE idealness constant

α_a	Butler-Volmer anodic charge transfer coefficient
α_c	Butler-Volmer cathodic charge transfer coefficient
B	Second quadratic coefficient
$B_{i\omega 1}$	Second quadratic coefficient when solving the angular frequency 1 relationship
$B_{i\omega 2}$	Second quadratic coefficient when solving the angular frequency 2 relationship
β_a	Anodic Tafel slope
β_c	Cathodic Tafel slope
C	Capacitance
C2	EFM causality factor 2
C3	EFM causality factor 3
C_α	Simplified capacitance pulled from CPE Q values
$C_{\alpha\omega 1}$	Simplified capacitance pulled from CPE Q values related to base angular frequency 1
$C_{\alpha\omega 2}$	Simplified capacitance pulled from CPE Q values related to base angular frequency 2
C_{eff}	Effective capacitance
C_{ideal}	Capacitance for an ideal capacitor
C_p	Polymer capacitance

C_{po}	Initial polymer capacitance
C(x)	Capacitance at time x
D	Diffusion coefficient
d(x)	Film thickness at time x
E	Electrode potential
e	electron charge
E_{eq}	Equilibrium electrode potential
efm	Electromotive force
E_o	Initial electrode potential, or electrode potential amplitude
E^o	Electrode potential under standard conditions
E_t	Electrode potential at time t
EW_{benzyl}	Equivalent weight of benzyl units
ε	Dielectric constant
ε_w	Dielectric constant of water
F	Faraday constant
f	frequency
$\mathfrak{F}$	Fourier transform
i	Current
i_o	Initial current, or current amplitude
i_t	Current at time t
i_{corr}	Corrosion current

i_{Ct}	Capacitive charging current
i_{fr}	Faraday rectification current
i_o	Initial current, or current amplitude
i_t	Current at time t
i_{ω_1}	Current amplitude from the intermodulation spectrum at angular frequency 1
i_{ω_2}	Current amplitude from the intermodulation spectrum at angular frequency 2
$i_{\omega_1}{}^*$	Measured amplitude of the intermodulation spectrum at angular frequency 1
$i_{\omega_2}{}^*$	Measured amplitude of the intermodulation spectrum at angular frequency 2
i_{ω_1,ω_2}	Current amplitude from the intermodulation spectrum at angular frequency 1 or 2 (theoretically are equal)
$i_{\omega_2 \pm \omega_1}$	Current amplitude from the intermodulation spectrum at angular frequency 2 plus or minus angular frequency 1
$i_{2\omega_2 \pm \omega_1}$	Current amplitude from the intermodulation spectrum at angular frequency 2 times 2 plus or minus angular frequency 1

$i_{2\omega_1}$	Current amplitude from the intermodulation spectrum at angular frequency 1 times 2
$i_{2\omega_2}$	Current amplitude from the intermodulation spectrum at angular frequency 2 times 2
$i_{3\omega_1}$	Current amplitude from the intermodulation spectrum at angular frequency 1 times 3
$i_{3\omega_2}$	Current amplitude from the intermodulation spectrum at angular frequency 2 times 3
$i_{2\omega_1 \pm \omega_2}$	Current amplitude from the intermodulation spectrum at angular frequency 1 times 2 plus or minus angular frequency 2
j	$\sqrt{-1}$
K	Linear coefficeint
k	Boltzmann constant
L	Coating thickness
l(x)	Length as a function of x time
λcopoly	Wavelength of UV-Vis absorption maximum for a copolymer
λ_{P3HT}	Wavelength of UV-Vis absorption maximum for P3HT
λ_{PEDOT}	Wavelength of UV-Vis absorption maximum for PEDOT

M or m	Mass
m_{epon}	Mass of EPON 825
M_∞	Mass at saturation time
m_{BA}	Mass of benzyl amine
M_c	Molecular weight between crosslinks
M_o	Initial mass
M_t	Mass at time t
MW	Molecular weight
MW_{BA}	Molecular weight of benzyl amine
MW_{water}	Molecular weight of water
m_{water}	Mass of water
m_{film}	Mass of film
m_{matrix}	Mass of matrix
n	Arbitrary integer
n_ω	Angular frequency multiplier
$\rho_{polymer}$	Polymer density
ϕ	Phase angle, or water volume fraction
ϕ_{EIS}	Water volume fraction calculated using EIS
ϕ_{grav}	Water volume fraction calculated using gravimetric techniques
Q	CPE primary constant (analogous to capacitance or resistance)
Q_o	CPE primary constant amplitude

R	Universal gas constant, resistance, or fast EFM R value
r	Capacitance, CPE Q value relation function
R_e	Electrolyte resistance
RE	Real portion
T	Temperature
t	Time
τ	Reduced time
T_g	Glass transition temperature
U_o	Applied voltage amplitude
V	Voltage
χ_{EDOT}	Molar fraction of EDOT
χ_{wt}	Weight fraction
χ_{3HT}	Molar fraction of 3HT
χ_{PEDOT}	Molar fraction of PEDOT
χ_r	molar fraction ratio
Y_{CPE}	Constant phase element admittance
Z	Impedance
z	Number of electrons involved
Z_c	Impedance for a capacitor
Z_{CPE}	Constant phase element impedance
Z_i	Imaginary impedance
Z_o	Impedance amplitude

Z_r	Real impedance
ω	Angular frequency ($2\pi f$)
ω_1	Applied angular frequency 1
ω_2	Applied angular frequency 2
ω_b	Base angular frequency
ω_{bB}	Second base angular frequency

CHAPTER I – Hypotheses and General Background

1.1 Project Purpose

A 2002 National Association of Corrosion Engineers (NACE) report[1] estimated that the annual direct cost of corrosion to the United States economy was $276 billion and, according to Dr. Jackson at G2MT Laboratories,[2] has risen to over $1 trillion in 2013. Currently, the best technologies available for corrosion protection are sacrificial and inhibitor-based coatings utilizing chromium. Many years have been devoted towards optimizing chromium based coatings, but hexavalent chromium is ecologically unfavorable due to its high toxicity[3] As alternatives to chromium, sol gel coatings, plasma deposition coatings, and conductive polymers (CP) have exhibited promising preliminary results, thereby promoting research for alternatives to legacy corrosion control technologies[4] Although there is a plethora of literature on CPs for applications in organic photovoltaics (OPV),[5] polymer light emitting diodes (PLED),[6] field effect transistors (FET),[7] and electron/hole transporting materials[8], this knowledge has not been used in understanding their corrosion control properties.

Despite focusing on restricting the use of chromium for corrosion control, there are only a limited few transformative material solutions for asset protection. Therefore, our research goal is to understand the effect of electronic structure on anticorrosive properties of CP**s** by developing fundamental characterization methods and validating their potential as corrosion control materials.

1.2 Driving Hypotheses

The original hypotheses driving this work were:

Hypothesis 1: The statistical copolymer synthesis from thiophene derivatives will allow facile tuning of electronic structure, thereby enabling the testing of CP anti-corrosion efficacy in the absences of backbone structure differences.

Hypothesis 2: The electrode kinetics of CPs with equivalent backbone structure are primarily dictated by electronic structure.

Hypothesis 3: There exists an optimal electronic structure for anticorrosive performance for a given substrate, each having electrode kinetics sufficient for effective corrosion control.

As experimental data were collected the primary hypotheses shifted/changed as summarized below. Hypothesis 1 remained unaltered. Hypothesis 2 was modified to reflect the limited number of samples that can be tested in a reasonable period of time:

New Hypothesis 2: Traditional electrochemical techniques are sufficient for evaluating the anti-corrosion properties of polythiophene films.

Hypothesis 3 was also modified to focus mainly on steel:

New Hypothesis 3: For steel substrates there exists an optimal onset oxidation potential for anticorrosive performance which does not accelerate corrosion and yet is not too low to prevent passivation.

Although other hypotheses were examined throughout the project, these are the primary hypotheses pursued in this study.

1.3 Rationale

1.3.1 Hypothesis 1 Rationale

Statistical copolymerization od CPs has previously been accomplished using step polymerizations, yielding materials with controlled HOMO and LUMO energy levels.[9-11] similar progress have been reported for polythiophenes using GRIM polymerization.[12-14] It seemed reasonable that copolymerizations using GRIM would provide control over the properties needed for improved corrosion performance. When this project began there were limited examples of methods that controlled CP electronic structure and molecular weight,[11,15,16] although currently they have become more prevalent. GRIM polymerization is primarily used for synthesizing block copolymers; therefore there was/is a need to further validate the applicability statistical copolymerization holds for controlling polymer properties.[17]

1.3.2 Hypothesis 2 Rationale

Traditional electrochemical techniques have been used to study uncoated[18] and coated substrates for a number of years,[19] However, we believe assumptions used for interpreting the data were not adequate and thus should be investigated further (particularly electrochemical impedance spectroscopy, (EIS) with coated substrates). Also, because polythiophenes are semi-conductive and tend to have low water and

oxygen barrier properties compared to thick epoxy amine films we hypothesized that these techniques would have less complications. As will be discussed, this was proven not to be the case.

1.3.3 Hypothesis 3 Rationale

The mechanism(s) of corrosion protection by polymer-based coatings with conductive polymers is still debated, with some researchers believing that they primarily accelerate corrosion when continuous morphologies are present.[20] Nevertheless, it is generally agreed that conductive polymers polarize the substrate,[21] whereby the materials and process inducing passive states under the right conditions. We hypothesized that if the onset oxidation potential of the polymer is too high, then the polarization induces corrosion because any previously established passive layers would be destroyed, similar to applying too high a voltage for anodic protection.[22] If the potential is too low, passive behavior will not occur, accelerating corrosion by anodic polarization of the polymer.

1.4 General Background

1.4.1 Electrode Kinetics

Electron transfer reactions are unique because a general relationship exists between thermodynamic driving force and kinetic rate constants.[23-27] The thermodynamic driving forces of electrochemical reactions are described using electrode potentials (defined as Galvani potential differences).[28] Galvani potential is the energy required to remove an electron without the influence of chemical interactions;[28] therefore, the electrode potential can be viewed as the electronic nature of the dominant electrochemical species. A lower electrode potential describes an electron rich species, whereas a higher electrode potential describes an electron poor species. A metal corrodes because it is electron rich compared to the corrosive environment, and will lose electrons via oxidation. The kinetics of electrochemical reactions are most often measured by quantifying the current through electrochemical cells, which is directly proportional to reaction rates, especially for uncoated substrates.[28]

An electrode is an interface where electrochemical reactions take place, and electrode processes are electrochemical reactions occurring at the electrode.[29] A metal/electrolyte interface is an example of an electrode, with reversible reductive deposition and oxidative dissolution serving as an electrode process. If an external voltage is applied to two or more electrodes in a circuit (i.e. an electrochemical cell) the electrode process equilibria are offset, and a net current is observed and measured. When observing a single reversible reaction with respect to a reference, the exchange current, or, the current from either oxidation or reduction at equilibrium, can be determined for that system. According to mixed potential theory,[30-32] when two species react, as in a

corrosion cell, the steady state current or rate of corrosion can be determined under these conditions. Observing current at given applied voltages is termed linear polarization, and the analysis of linear polarization data at large over-voltages designed to obtain steady state or exchange currents is termed Tafel analysis.[18,28,33,34] An important point in this dissertation is that each measurement requires timeframes that rival some corrosion processes and mechanisms under consideration for the relative importance in early corrosion processes.

Besides Tafel analysis, other important techniques for studying electrochemical systems include: 1) Cyclic voltammetry[26,35] (CV) - the cycling of applied voltages and measuring the current response; 2) potentiostatic[36] - applying a constant voltage and measuring current; 3) galvanostatic[37] - applying a constant current and measuring the resulting voltage; and 4) electrochemical impedance spectroscopy[37] (EIS) - applying an oscillating current or voltage and measuring the dynamic voltage or current at different frequencies.

1.4.1.1 Butler Volmer Theory

Julius Tafel was the first to observe an empirical relationship between overpotential and current for electrochemical processes in the early 1900's.[38,39] The Tafel equation for determining electrode kinetics is given by:

$$E - E_{eq} = A * ln\left(\frac{i}{i_o}\right) \quad (1.1)$$

eventually, theoretical underpinnings of the empirical equation were described by John Butler and Max Volmer in the 1930's.[39] The Butler-Volmer equation useful in describing conventional electrode kinetics is shown below:

$$i = i_o \left\{ exp\left[\frac{\alpha_a zF}{RT}\left(E - E_{eq}\right)\right] - exp\left[\frac{-\alpha_c zF}{RT}\left(E - E_{eq}\right)\right]\right\} \quad (1.2)$$

The Butler-Volmer equation reduces to the Tafel equation at high overpotentials and exhibits linear behavior at lower overpotentials, behavior observed for electrochemical reactions (i.e. linear polarization techniques).

1.4.1.2 General Electrochemical Impedance Spectroscopy Theory

Electrochemical impedance spectroscopy (EIS) is an AC technique for evaluating electrochemical cells, commonly employed as a complimentary method to Tafel Analysis for studying corrosion.[40] Although less destructive, EIS-based resistance cannot provide complete electrode kinetic data Tafel slopes.[18,41] EIS is also commonly used for corrosion cells with high impedance, substrates coated with a polymer film.[19,42,43] This is because the technique does not require high current flow for accurate results.

In EIS an AC voltage is applied to the substrate at voltages low enough to ensure a linear current response. This linearity will permit the application of Ohm's law, with the phase shift between the applied voltage and the measured current dependent on the capacitive behavior of the cell:

$$Z = \frac{E_t}{i_t} = \frac{E_o \sin(\omega t)}{i_o \sin(\omega t + \phi)} \quad (1.3)$$

This allows the calculation of impedance, which can be described as a complex number with real and imaginary components.

$$Z(\omega) = Z_o(cos\phi + j * \sin\phi) \quad (1.4)$$

As i is already used to represent current, the letter j is used for $\sqrt{-1}$. Note that the real portion of the impedance describes resistance whereas the imaginary component describes capacitance. Inductive behavior will not be covered, although they are another

element type that can be described using impedance. In this context, the technique can be thought of as an electrochemical analogue to dynamic mechanical analysis. A high imaginary impedance at a given frequency means current does not flow through the cell in that time scale, but instead charges buildup at the interfaces. A high real impedance at a given frequency means current does flow through the cell within that time frame, with current flow is decreasing at higher resistances. In addition, cell responses can be described in terms of relaxation times. Longer relaxation times suggest that the cell has a higher barrier to ion transport, thereby requiring lower frequencies to allow current to flow in the time frame of the experiment. This is similar to DMA behavior, whereby a longer relaxation time means a lower frequency is needed to allow viscous flow of the material within the time frame of the experiment.

1.4.2 Semiconductor Theory Applied to Conductive Polymers

The electronic structure of solid phase materials are generally described using energy bands as opposed to distinct energy levels. The two main bands are the valance band and the conductive band. The conductive band describes ground state energies, whereas the valance band describes excited states(i.e. lowest unoccupied molecular orbital (LUMO) energy levels and highest occupied molecular orbital (HOMO) and of organic or molecular systems, respectively). Because conductive and valence bands overlap for conductive materials, thermal energy excites a significant number of electrons into the conducting band, leading to high conductivity; however for semiconducting materials a relatively small (0.7 to 1.1 eV) band gap exists between the valence and conductive bands, resulting in lower conductivity.[18]

Fermi-Dirac statistics are applied to determine the occupation of bands at a given temperature. Solution of the Fermi-Dirac distribution function shows that the Fermi level is the average of the two band energies, with this energy level matching the electrochemical potential needed for electron transfer between phases.[44-46] For CPs, the electronic structure can be altered via substituents and copolymer composition, and the HOMO and LUMO energy band positions can be conveniently estimated via CV.[33,34]

Fermi levels and electronic structures are key aspects of the theoretical works of H. Gerischer[46,47] H. Reiss,[48] and S. Trasatti,[49,50] who focused on defining absolute electrode potentials using work functions. The work function of a material is the energy required to remove an electron, similar to Galvani potential. However, it also includes chemical interactions and can be quantified using scanning Kelvin probe (SKP) methods.[51] This energy is equal to the difference between Fermi level and vacuum level; therefore, a higher Fermi level, a lower work function, a lower electrode potential, or higher HOMO/LUMO energy levels all describe an electronic rich nature.

1.4.3 Proposed Protection Mechanisms

The most prevalent mechanisms for corrosion protection using CPs deal with passivation.[35] Passivation is the formation of an intimately bound layer that blocks ion diffusion needed for corrosion to occur.[52] Passive layers form either by inhibition[52] or anodic polarization. Inhibition uses small molecules (inhibitors) that either directly bind to the metal or incorporate into the oxide layer, thereby stabilizing it.[53] Anodic polarization is the positive shift in electrode potential that forms a passive oxide layer.[52] Corrosion control via passivation requires stabilization of the passive layer. Corrosive environments often do not polarize a substrate sufficiently for passivation. Anodic

protection functions by pulling electrons from the metal, thereby polarizing the substrate sufficiently for passivation.[52] Because the electrode potentials of common CPs (determined by the reduction potential of the oxidation process for the polymer) are higher than the electrode potentials of the metal dissolution process, anodic polarization is expected.[54-58] L. Zhong et al. have shown evidence from galvanic coupling experiments of impressed current towards passivation.[55] CPs predicted to passivate substrates by anodic protection include polypyrroles,[59] polyanilines,[37] and polythiophenes.[60] There continue to be disagreements in this field, due to differing perspectives on whether protection is afforded via mechanisms like oxygen diffusion,[61] cathode spreading,[62] adhesion improvement,[63] and inhibitor release.[62] Galvanic coupling experiments do not always suggest the attainment of sufficient polarization.[64] For example, some substrates such as steel cannot self-passivate under neutral and acidic environments,[61] and there is evidence using SKP techniques that support the prevalence and importance of in situ dopant release based mechanisms.[62]

Anodic protection requires very little current; this promotes longevity but limits the method to only substrates that form stable or semi-stable oxides, with diminished or insufficient current accelerating corrosion rates.[18,28] An alternative protection method is cathodic protection, which supplies electrons to the substrate and thereby causes a negative shift in electrode potential.[65] The cathodic protection process shifts the metal dissolution equilibrium towards deposition, thus preventing corrosion of the metal. In addition, the cathodic reduction of oxygen and water is driven by electrons from the source as opposed to the oxidation of the metal substrate.

Literature on this mechanism is scarce; we attributed this to the arduous task of designing and developing (synthesis limited) cathodic CPs.[66] Additionally, cathodic N-doped CPs are generally less stable against atmospheric corrosion, making long term cathodic protection difficult or impractical.[66,67]

Fortunately, this approach is already employed in metal-rich coatings,[36] and the incorporation of CPs into these metal-rich primers have, in a few examples, increased corrosion control efficiency.[67] These examples of used P-doped CPs to improve such primers,[68] no example of N-doped CPs has been found in the open literature. The closest example by M. C. Yan et al.[67] showed N-doped CPs without sacrificial pigments was successful at cathodic protection during the laboratory testing, ultimately limited mainly by short longevity.

It is apparent that protection mechanisms are not universal or well understood, with each substrate and CP material response dependent upon the corrosive environment,[54] the substrate type or form,[56,57] coating type, formulation, processing, cure/annealing, material characteristic,[69] and nature of doping and dopant.[67] In some cases, CP failure occurs via accelerated delamination, leading to significant controversy on the efficacy of CPs for corrosion protection. Some research groups predict the ultimate failure of all CP primers by catastrophic delamination,[62] whereas others believe they can serve as a possible chromate replacement based on limited laboratory characterization.[37]

Studies concerning the efficacy of CPs for corrosion protection have focused on dopant types,[70] substrate pretreatments,[54] and corrosion conditions.[54] However, little emphasis has been placed on CP electronic structure. We hypothesize that CPs act as

sources for anodic or cathodic protection, with dopant release acting synergistically with these primary modes of protection. We believe an electron-rich CP can be designed using electron donating substituents, thereby allowing easier P-doping or more difficult N-doping, thereby increasing or decreasing the source of electrons which in turn reduces or increases the thermodynamic driving force. Alternatively, an electron-poor CP can be designed using electron withdrawing substituents to provide the opposite effect. Therefore, we hypothesize there exists an optimal electronic structure that maximizes the needed source size for longevity while maintaining the required thermodynamic driving force needed for sufficient electron transfer.

1.5 Project Plan

The primary project plan was to 1) Synthesize a series of polythiophenes having controlled molecular weight and controlled onset oxidation potentials (electrode potentials); 2) evaluate traditional electrochemical techniques using bare and non-conductive coated substrates, and then apply the results to study polythiophene films to better understand how onset oxidation potential alters corrosion performance.

CHAPTER II – Synthesis of Copolymers

This chapter describes the synthesis of the monomers used to produce a series of polythiophene copolymers used to determine structure property relationships for conductive polymers and their anticorrosive properties as well as demonstrate the ability to control composition of polythiophene copolymers via Grignard Metathesis (GRIM) polymerization.

2.1 Introduction

Copolymerization was used to control polythiophene properties, with monomer selection based on both affordability and potential to alter solubility and onset oxidation potentials of the resulting polythiophenes. The two primary monomers selected for this work were 2,5-dibromo-3-hexylthiophene (DB3HT) and 2,5-dibromo-3,4-ethylendioxythiopene (DBEDOT). Synthesis of these monomers was facile:

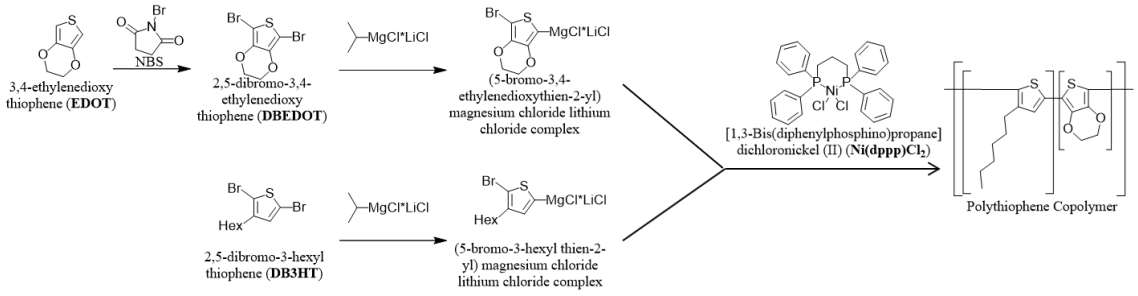

Scheme 2.1 Overall synthetic route for polythiophenes using GRIM polymerization.

We hypothesized that the hexyl substituent promotes solubility as compared to the ethylenedioxy substituent, with the stronger electron donating ethylenedioxy substituent lowering the onset oxidation potential of the resulting polythiophenes. This was based on

previously established homopolymer properties found in the literature.[71-73] Polythiophene solubilities are low compared to conventional polymers due to their backbone rigidity and strong π-π interactions, both afforded by aromatic thiophene repeat units. Both homopolymers, poly-3-hexylthiophene (P3HT) and poly-3,4-ethylenedioxythiophene (PEDOT), have been synthesized previously in literature.[12,74] The P3HT homopolymer is soluble in several conventional organic solvents including THF and chloroform; however, PEDOT homopolymer is not soluble. Generally, PEDOT is prepared as an aqueous dispersion by doping with polystyrene sulfonate.[75] Additionally, the onset oxidation potential of PEDOT is lower than P3HT.[71,72] There is little literature concerning the copolymerization of these monomers.[15,76,77] The primary purpose of this chapter is to show that quasi-living conditions can be maintained when copolymerizing these monomers, and that feed ratios primarily control composition and properties of the resulting polythiophene copolymers.

Quasi-living conditions are achieved when the Grignard metathesis step prior to polymerization is facile. Previous work by the Rawlins research group and others on the homopolymerization of P3HT have shown that the metathesis step is vital for achieving controlled polymerizations via the GRIM method. If the metathesis step is not completed, the growing chains can be terminated by the unreacted molecules. McCullough and coworkers[13] used several Grignard reagents, including t-butyl MgCl, for the metathesis step. Although this reagent is still commonly used in the literature, it has been replaced with i-proMgCl*LiCl. The trend in Grignard reagent nucleophilicity is aryl < methyl < isopropyl < t-butyl reflecting the stability of the partial negative charge on the carbon. The aromatic carbon magnesium bond on the thiophene ring is more

stable than the t-butyl carbon magnesium bond, thereby promoting metathesis to occur. Heat is commonly used to drive the metathesis reaction, with the reaction vessel cooled to 0 °C or room temperature prior to addition of the nickel catalyst to initiate the polymerization.[12,78] The metathesis step is often not driven to completion when using t-butyl MgCl; thus a different Grignard reagent having greater nucleophilicity was proposed by S. Wu et al. in order to facilitate metathesis with the thiophene.[79] Due to LiCl breaking the Grignard dimer, i-proMgCl*LiCl is a stronger Grignard reagent for metathesis. Although this Grignard reagent is stronger and ensures metathesis completion, it also increases the nucleophilicity of the monomers during polymerization, thereby increasing the propensity for growing chains to couple. Verswyvel et al.[80] observed that using i-proMgCl*LiCl promotes GRIM polymerization of monomers that normally do not polymerize. For this reason, we chose to use i-proMgCl*LiCl for the Grignard reagent. It should be noted that the use of i-proMgCl*LiCl became more prevalent in the literature during the time span of this project.

Using the conditions presented in this document, the metathesis step is fast and quantitative, with controlled GRIM polymerizations achieved. Additionally, the feed ratio controls the composition of the copolymers; however due to solubility limits a minimum of two 3-hexylthiophene repeat units are needed per 3,4-ethylenedioxythiophene unit before losing control over composition and living properties. The synthesis of the monomers and the polymers are described herein.

2.2 Materials and Methods

2.2.1 Synthesis of 2,5-dibromo-3-hexylthiophene

For most of the experiments 2,5-dibromo-3-hexylthiophene was purchased from Acros chemicals, Waterstone Technologies, or synthesized in house; the results were identical regardless of monomer source used. For the in house synthesis of 2,5-dibromo-3-hexylthiophene, n-bromosuccinimide (NBS) and 3-hexylthiophene where purchased from Acros and used without further purification. Chloroform and glacial acetic acid were obtained from Fischer Scientific.

A slightly modified literature procedure was used for the synthesis of 2,5-dibromo-3-hexylthiophene.[81] 3-hexylthiophene (1.68, 10 mmol) was added to 20 mL of a 1:1 (by volume) chloroform: acetic acid solution in a 100 mL round bottom flask. An addition funnel was charged with NBS (3.74 g, 21 mmol) dissolved in 20 mL of 1:1 (by volume) chloroform:acetic acid. The entire apparatus was purged with nitrogen, and the NBS solution slowly added to the 3-hexylthiophene solution at 0°C and reacted overnight. The reaction solution was then washed with cold DI water, 3 times with saturated sodium bicarbonate solution, once again with DI water, and finally with a saturated NaCl solution. The organic layer was dried with sodium sulfate, and the crude product was purified via column chromatography using a 1:9 ethylacetate:hexane carrier. After rotary evaporation a clear oil was obtained (93-97% yield).

2.2.2 Synthesis of 2,5-dibromo-3,4-ethylenedioxythiophene

The reagent 3,4-ethylenedioxythiophene was purchased from Acros and TCI. NBS was purchased from Acros, and THF, DMF, and acetic acid were obtained from Fischer Scientific. The 3,4-ethylenedioxythiophene was normally used without

purification; occasionally it was filtered through a plug of silica with hexane as the eluent to remove yellow impurities present.

Several slightly different procedures were used to synthesize 2,5-dibromo-3,4-ethylenedioxythiophene. We originally started using the literature procedure from Yongbao Zhu et al.[82] 3,4-ethylenedioxythiophene was dissolved in either THF, 1:1 THF:acetic acid, or DMF, with NBS either added as a solid or dissolved in solvent and added slowly to the reaction vessel. Usually the reaction was conducted at 0°C, though room temperature work was also attempted. Sometimes the NBS was dissolved in the solvent and a solution of 3,4-ethylenedioxythiophene was added dropwise to the reaction vessel. Reactions were performed with and without nitrogen purge; we observed that this had little effect on the yield.

The best procedure was as follows: In a 100 mL round bottom flask 3,4-ethylenedioxythiophene (1.42 g, 10 mmol) was dissolved into 20 mL of DMF. An addition funnel was charged with NBS (3.74 g, 21 mmol) dissolved into 20 mL of DMF. The reaction was purged with nitrogen, and the NBS solution slowly added to the thiophene solution and allowed to react at 0°C for 4 hours. The reaction solution was then slowly poured into cold DI water to precipitate the crude product. The white needle-like crystals were then rinsed with cold DI water and then recrystallized from a mixture of DI water and ethanol to yield the final product (75%-97% yield).

2.2.3 In-Situ FTIR

In-situ FTIR analysis was conducted under nitrogen atmosphere inside a glovebox. The FTIR scans were acquired using a Mettler Toledo ReactIR equiped with a

9.5 mm Agx Si Comp fiber optic probe and a Teflon seal. Scans were collected every 5 secs (the fastest rate available)

In order to monitor the metathesis reaction, a library was created using different reagents dissolved in THF to aid in peak identification. A background of THF was obtained prior to reaction for background subtraction. The thiophene was then added in steps in order to test monitoring its concentration; the Grignard reagent used for metathesis was added in similar fashion. Additional Grignard reagent was not added until the reaction reached completion; however, for these experiments that was nearly instantaneous. Finally, the reaction vessel was quenched with acetone.

For the co-metathesis experiments, instead of quenching the reaction with acetone, the competing thiophene was added to allow co-metathesis between the monomers. This was done to see which monomer would form a more stable Grignard reagent.

2.2.4 Gas Chromatography and Mass Spectroscopy

Quantification of monomer concentration for kinetic studies was performed on a Hewlett Packard HP6890 Series with Mass Selective Detector using 1 μL injection size @ 250°C in splitless mode, a He carrier gas pressure of 1.8 psi, and a flow rate of 1.2 mL/min. The temperature ramp used was as follows: initial temperature of 90°C, followed by a 100 °C/min to 160 °C, hold 1 min, a ramping temperature of 5 °C/min to 170 °C, hold 1 min, increasing temperature of 10 °C/min to 245 °C, hold for 10 min. Toluene was used as an internal standard for all measurements.

2.2.5 Polythiophene Synthesis

Polymerization was conducted via a modified literature procedure.[15] Several different reaction conditions were used; the main method is described below. In an oven-dried 20 mL vial was dissolved 1.36 mmol of monomer into THF. For P(3HT-co-EDOT) two separate flasks containing 5 mL each were used for the metathesis step. One vial having 10 mL of THF was used for P3HT. An oven-dried 150 mL round bottom flask was charged with 30 mL of THF and [1,3-Bis(diphenylphosphino)propane]dichloronickel(II) (Ni(dppp)Cl_2) (~2 mol% of monomer) and stirred between 0-6.0°C. A final concentration of 2.5 mg/mL was obtained for each monomer vial, and each were spiked with anhydrous toluene for use as an internal standard. The metathesis step was conducted over a 30 min period with stirring in the 20 mL vials using either 1.05 or 0.95 eq. of i-proMgCl*LiCl at room temperature. For copolymerizations the vials were added together and stirred between 0-6.0°C for 15 min; at this juncture an aliquot was removed and quenched with methanol or 5 M HCl to act as T0. Polymerization was initiated by injecting the metathesis reaction solution into the Ni(dppp)Cl_2 suspension. Volumetric aliquots were periodically taken and quenched in methanol or 5 M HCl for GCMS and GPC analysis. The organics were extracted using t-butyl methyl ether and filtered to separate unreacted monomer and polymer. The unreacted monomer layer was diluted using acetone and analyzed using GCMS to determine conversion, whereas the solid portion was dried under vacuum, dissolved into THF, and analyzed via GPC for molecular weight analysis. After 2 hours the entire reaction vessel was quenched by the drop-wise addition of 5 M HCl or with 1M allyl MgCl, and the polymer precipitated using 10 mL of methanol. If kinetic trials were not

being conducted, the reaction vessel was quenched after 50 min to avoid coupling reactions, which can occur after long reaction times. All polythiophenes were purified via Soxhlet extraction in MeOH, followed by chloroform and rotary evaporation. Polythiophenes were dried under vacuum to remove as much trapped solvent as possible and stored in a dark place to avoid photodegradation. Soxhlet extraction in hexanes after MeOH is commonly reported in the literature. However, we found this artificially narrows the PDI of the polymer, so this step was avoided unless samples were collected for NMR analysis (to make sure all monomer was removed).

The best composition and molecular weight control was obtained when the monomer was injected into the vessel with the catalyst. However, reasonable composition and molecular weight control was obtained when injecting a catalyst suspension into the reaction vessel containing the monomer. This method is more convenient, because the monomer vessel can be prepared in a glovebox and the reaction initiated in a fume hood. However, initiation is slower, creating a longer lower molecular weight tail and resulting in a higher PDI. The effect on final PDI is small (generally between 0.03 and 0.07), but the compositions were similar.

2.3 Results and Discussion

2.3.1 Synthesis of DB3HT and DBEDOT

3-hexylthiophene needed to synthesize 2,5-dibromo-3-hexylthiophene was purchased from Aldrich and used without purification. 2,5-dibromo-3-hexylthiophene was also purchased from Acros and Waterstone Technologies; no difference in the results were obtained. Scheme 2.1 outlines the synthesis of 2,5-dibromo-3-hexylthiophene. A straight forward bromination was conducted using NBS, with ^{1}H NMR spectroscopy

confirming the structure. Figure 2.1 shows the proton spectra of 3-hexylthiophene as received and of 2,5-dibromo-3-hexylthiophene after purification. As slightly modified literature procedures were used, no complications were expected. Therefore, we hypothesized that the NMR results would match feed ratios used in the polymerization. Here the peaks of interest are the aromatic peaks at 6.94 ppm and 6.77 ppm. The aromatic peak at 7.22 ppm is observed by the chloroform peak at 7.26 ppm. Additional shifts are observed in the alkyl region, especially those for the alpha and beta positions relative to the thiophene ring. The observed peaks are consistent with literature values.[83]

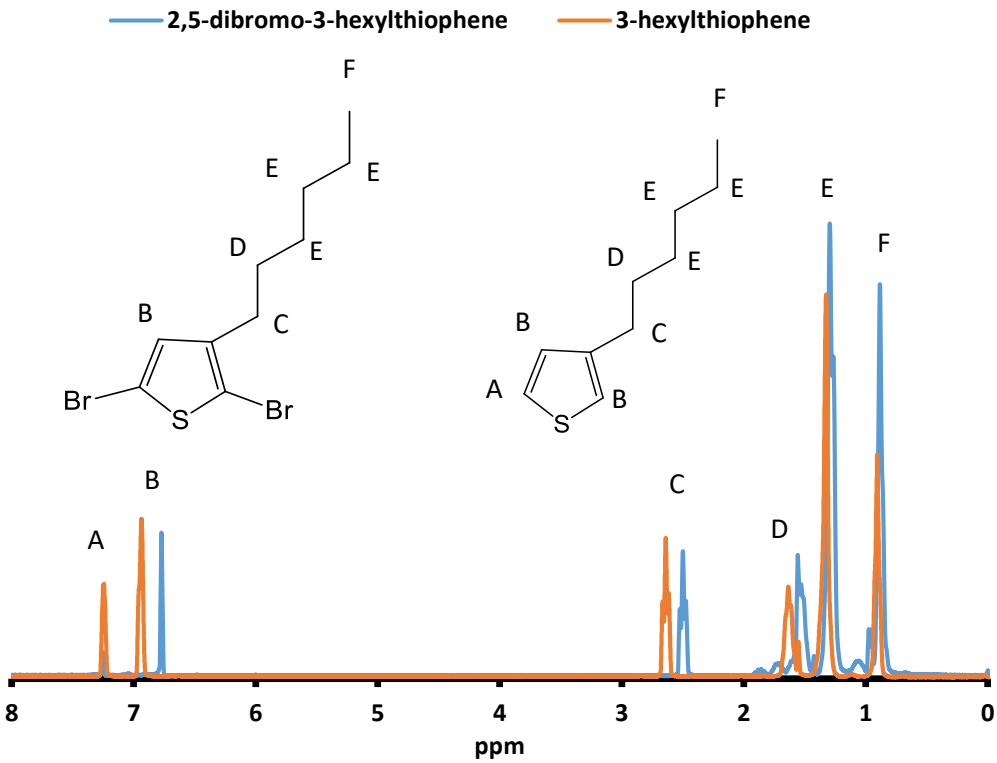

Figure 2.1 Proton NMR spectra of 3-hexylthiophene and 2,5-dibromo-3hexylthiophene.

Note: Both NMR were taken as received dissolved in $CDCl_3$. The NMR for the synthesized 2,5-dibromo-3-hexylthiophene matched the purchased samples.

Synthesis of 2,5-dibromo-3,4-ethylenedioxythiophene followed a similar procedure, with 2 equivalents of NBS used to brominate the monomer. The as received (from Aldrich) 3,4-ethylenedioxythiophene ^{1}H NMR spectrum is displayed in Figure 2.2. No purification was required prior to the synthesis of 2,5-dibromo-3,4-ethylendioxythiophene. The purified 2,5-dibromo-3,4-ethylenedioxythiophene ^{1}H NMR spectrum is also shown in Figure 2.2. The symmetric nature of these molecules is evident in the spectra. Complications in the monomer synthesis were not expected based on the literature procedure. However, the monomer can homopolymerize during the reaction. Literature reports that both 2,5-dibromo-3,4-ethylenedioxythiophene[84,85] and 2-bromo-3,4-ethylenedioxythiophene[86] can undergo solvent free homopolymerization. The proposed synthetic routes are shown below:

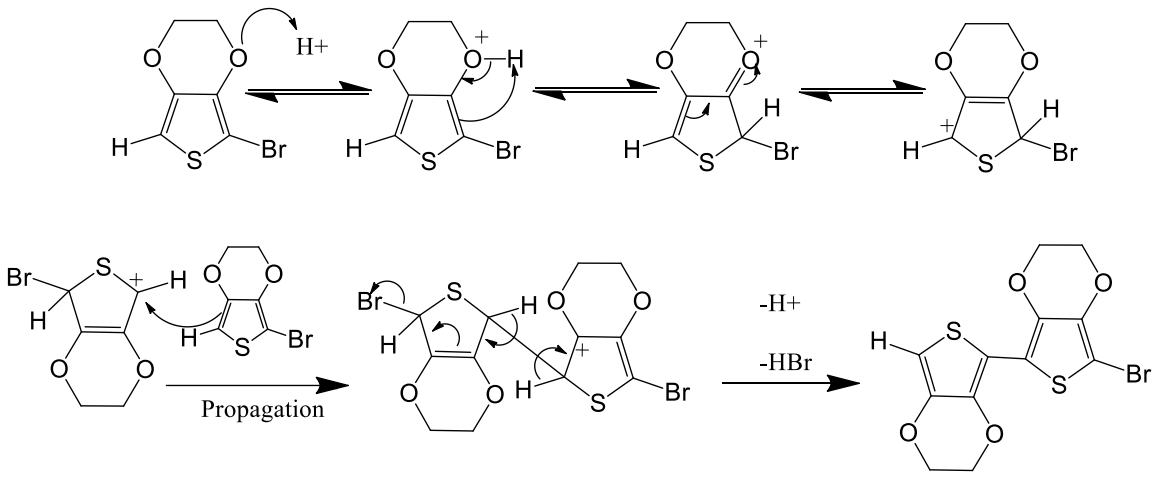

Scheme 2.2 Homopolymerization route for PEDOT proposed by Yin et al.[86]

Note: This route is the acid catalyzed route for homopolymerization of 2-bomo-3,4-ethylenedioxythiophene.

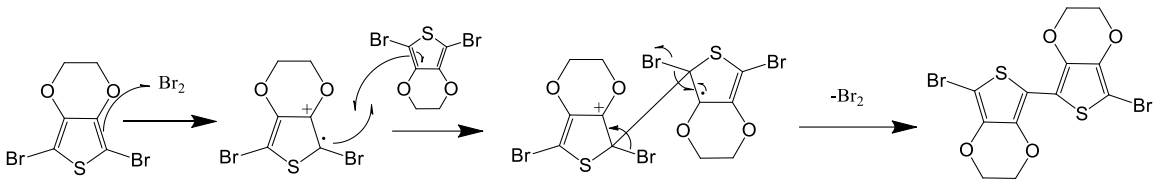

Scheme 2.3 Homopolymerization route for PEDOT proposed by Meng et al.[85]

Note: This route is for the solid state homopolymerization of 2,5-dibromo-3,4-ethylenedioxythiophene.

The bromination of thiophenes using NBS forms small amounts of HBr, which increases homopolymerization of the mono and dibromo 3,4-ethylenedioxyhtiophenes. Visual evidence of this phenomena is a blue tinge in the reaction vessel, along with a dramatically decreased yield. In extreme cases the synthesis created batches of purple sludge with little to no yield. Additionally, after the precipitation step it is vital to dry the crystals quickly and without heat to avoid homopolymerization. Recrystallization must also be performed quickly and with care to avoid homopolymerization. We recommend using a two-solvent recrystallization protocol using water and ethanol for purification. Homopolymerization is faster in the solid state, quickly dissolving the monomer in ethanol and adding water to reach saturation reduces the time of heating.

Different reaction conditions were tried to alleviate the problem; however, the exact cause of some batches homopolymerizing was not definitively identified. Originally a THF acetic acid mixture was used, as prescribed by Yongbao Zhu et al.[82] The first batches gave excellent yields (>90%) with high purity, but later batches quickly turned to purple sludge. Homopolymerization was acid catalyzed, so acetic acid was removed from the solvent even though acetic acid generally improves bromination for thiophenes. Using pure THF rarely gave good yields, whether the NBS was added as a

solid or dropwise as a THF solution using an addition funnel. High yields were obtained when using DMF as a solvent, and the final procedure of using an ice bath and dropwise addition of an NBS solution gave the most consistent results. The purity of the thiophene appeared to also play a large role in promoting homopolymerizations. Samples of 3,4-ethylendioxythiophene that were filtered using a silica "plug" generally did not yield homopolymerized products. Yields using DMF did not fall below 50%, even if homopolymerization occurred. Therefore, we utilized this procedure as described in the materials and methods section of this chapter. Most yields were >90%; in cases where homopolymerization occurred, yields were between 50-75% yield.

Successful polymerization was evident by the disappearance of the aromatic proton peak at 6.33 ppm, which is substituted with bromines. In addition, there is a slight shift in the alkoxy proton peak at 4.20 ppm to 4.27 ppm. All peaks shifts were consistent with literature values.[87,88]

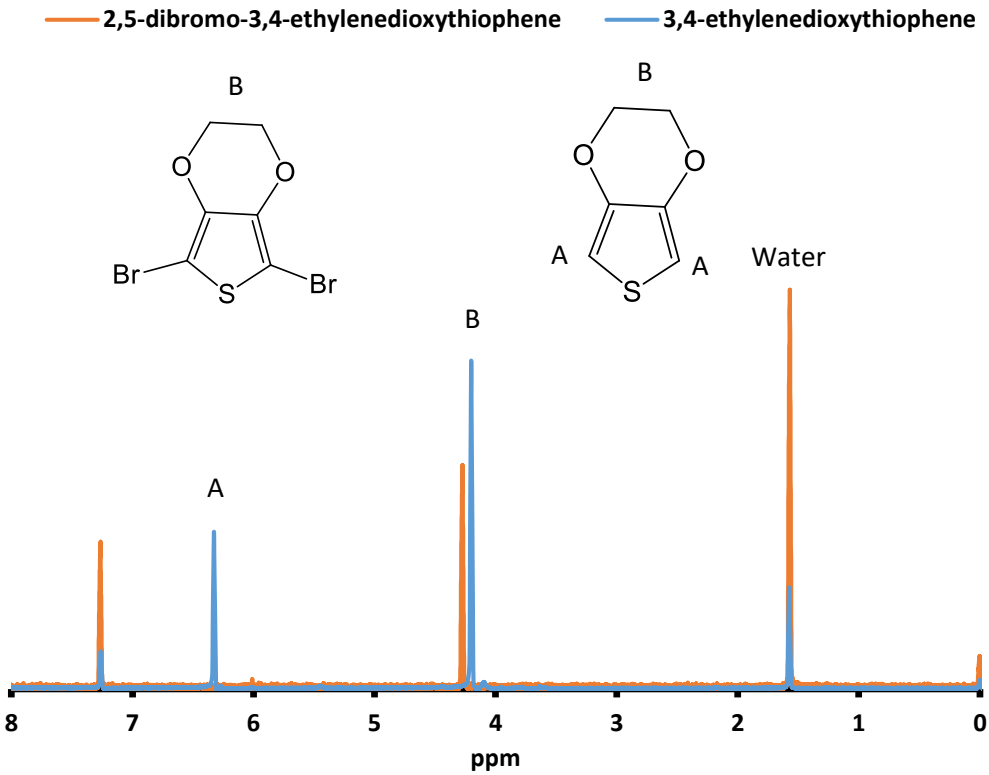

Figure 2.2 Proton NMR spectra of 3,4-ethylenedioxythiophene and 2,5-dibromo-3,4-ethylenedioxythiophene.

Note: Both were dissolved in $CdCl_3$ the 3,4-ethylenedioxythiophene was as received, and the 2,5-dibromo-3,4-ethylenedioxythiophene was after recrystallization.

Based on the NMR results, the synthesis of both 2,5-dibromo-3-hexylthiophene and 2,5-dibromo-3,4-ethylenedioxythiophene were successful. These monomers were therefore used for Grignard metathesis experiments and polymerizations.

2.3.2 Grignard Metathesis Step

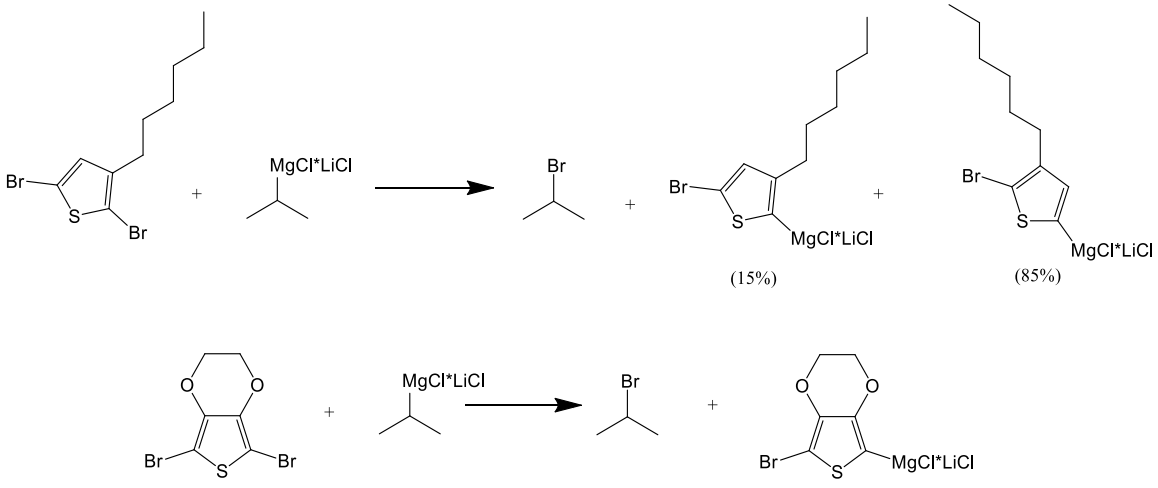

Scheme 2.2 shows the Grignard metathesis step for both thiophenes used in this project.

The Grignard metathesis step is important for obtaining controlled polymerizations, as shown in previous work.[89] The use of t-butyl MgCl for the Grignard metathesis step is common due to the strong nucleophilicity created by the steric hinderance of the t-butyl group. This yields a faster and more complete metathesis step. Between 2008 and 2011, papers were published demonstrating that i-pro MgCl*LiCl also provided good results.[79,80,90]

We monitored the metathesis step using in-situ FTIR methods to demonstrate how quickly metathesis occurs using i-proMgCl*LiCl. In a co-metathesis experiment, we also show that the 3,4-ethylenedioxthiophene based Grignard reagent is more stable compared with its 3-hexylthiophene counterpart.

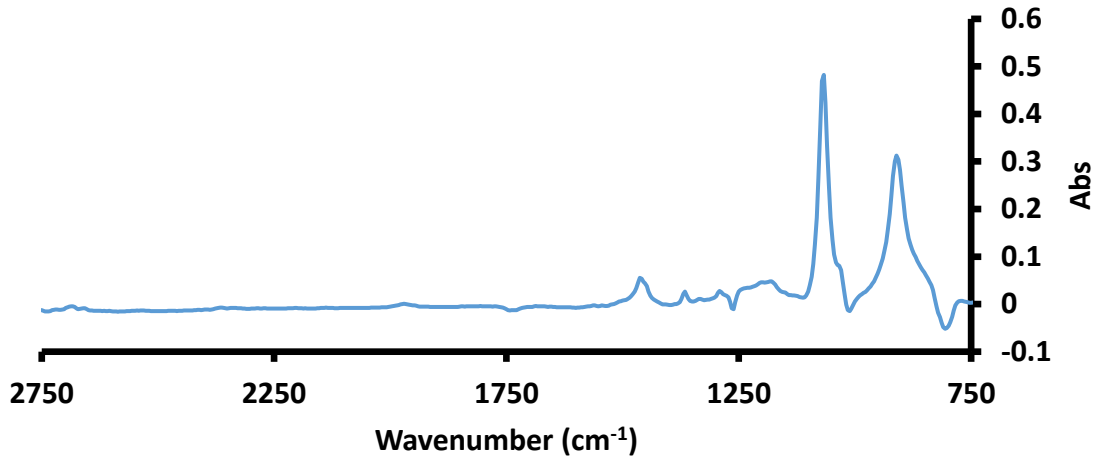

Figure 2.3 In-Situ FTIR spectrum of THF.

When monitoring the reaction, a THF FTIR spectrum was initially acquired using the in-situ ReactIR setup (Figure 2.3). Reagents were then introduced into the vessel, and the THF background subtracted to obtain FTIR spectra for the metathesis reagents.

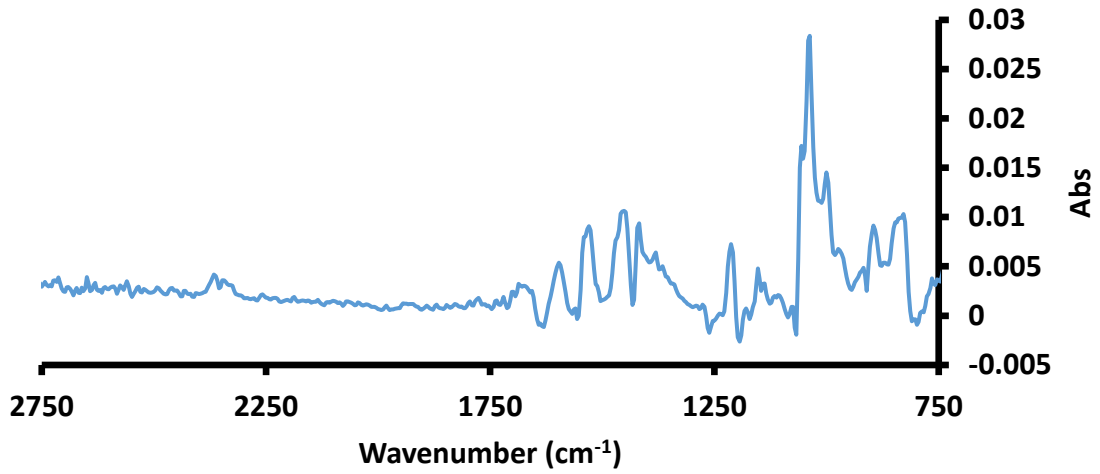

Figure 2.4 In-Situ FTIR spectrum of 2,5-dibromo-3-hexylthiophene with THF background subtracted.

Figure 2.4 shows the resulting FTIR spectrum (after THF background subtraction) for 2,5-dibromo-3-hexylthiophene. The peaks of interest for tracking metathesis are the aromatic C=C stretches. These will shift upon replacement of the bromine by the Mg.

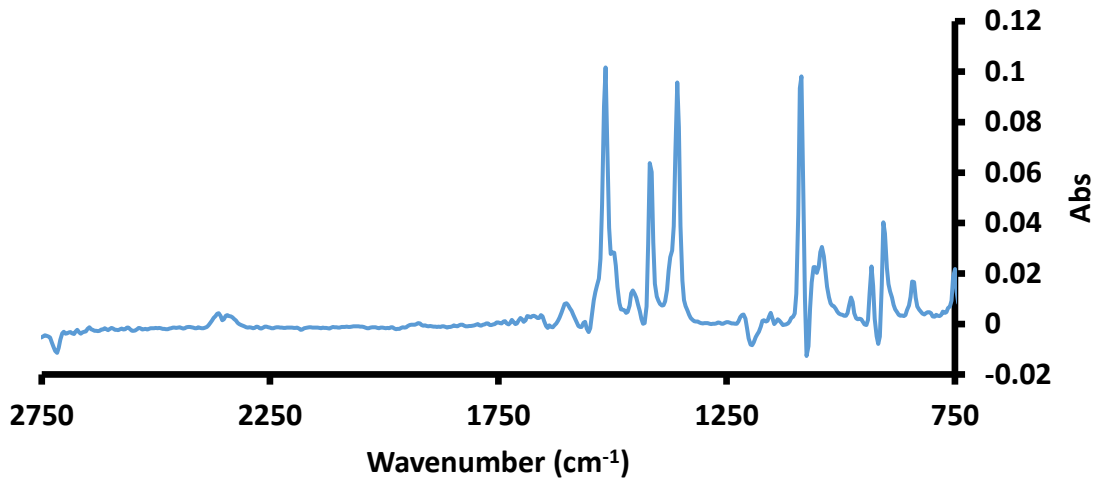

Figure 2.5 In-Situ FTIR spectrum of 2,5-dibromo-3,4-ethylenedioxythiophene with THF background subtracted.

Figure 2.5 displays the FTIR spectrum (after THF background subtraction) for 2,5-dibromo-3,4-ethylenedioxythiophene. Similar to 2,5-dibromo-3-hexylthiophene, the peaks of interest are the aromatic C=C stretches.

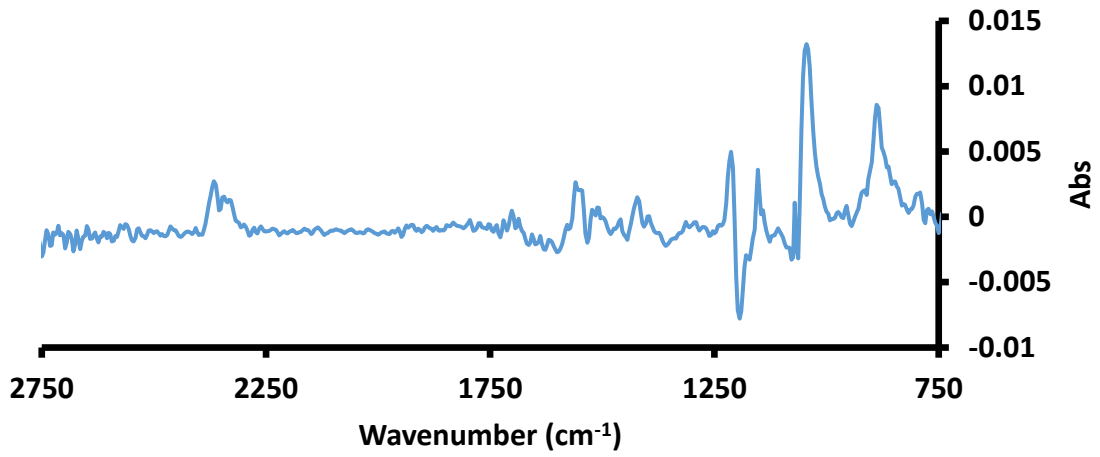

Figure 2.6 In-Situ FTIR spectrum of i-proMgCl*LiCl with THF background subtracted.

Figure 2.6 shows the FTIR spectrum (after THF background subtraction) for i-pro MgCl*LiCl. The vibrational modes for the i-pro substituent are very weak and fall outside the range of the instrument. However, a shift in the THF vibrational modes are observed upon chelation with the Grignard reagent, with the THF ether stretches at 1071 and 907 cm^{-1} shifting to 1049 and 884 cm^{-1}, respectively. The effect has been reported in the literature.[91,92] Thus, the peak shifts can be used to monitor the Grignard concentration. These peaks do not shift or disappear after metathesis; therefore, they can only be used to monitor total Grignard concentration, which should hold constant during metathesis.

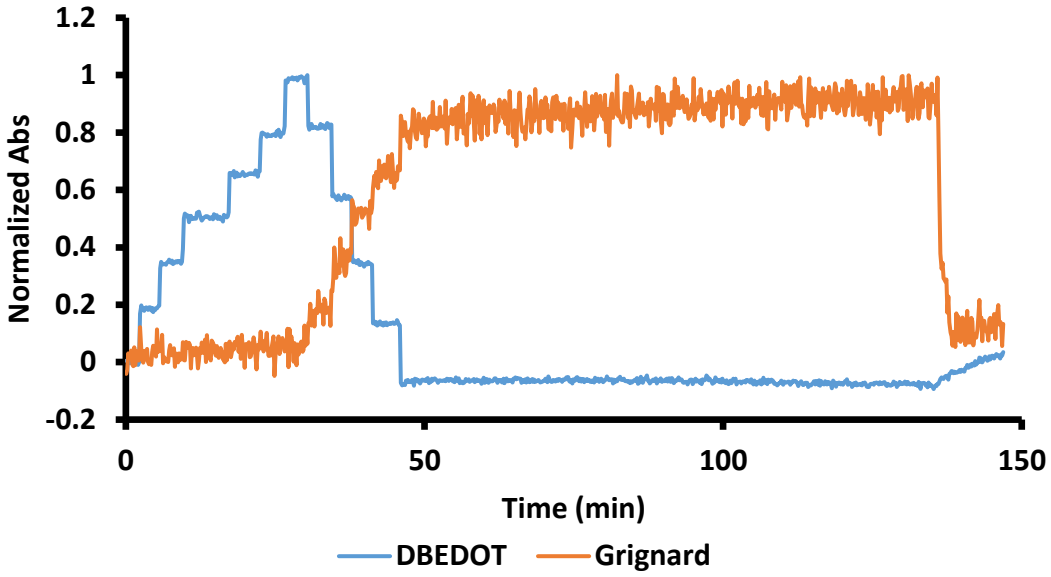

Figure 2.7 In situ ReactIR plots for Grignard metathesis of 2,5-dibromo-3,4-ethylenedioxythiophene.

Note: The Grignard reagent was i-proMgCl*LiCl. The Grignard peak accounts of total Grignard including the thiophene after metathesis. At 135 min the reaction was quenched with acetone.

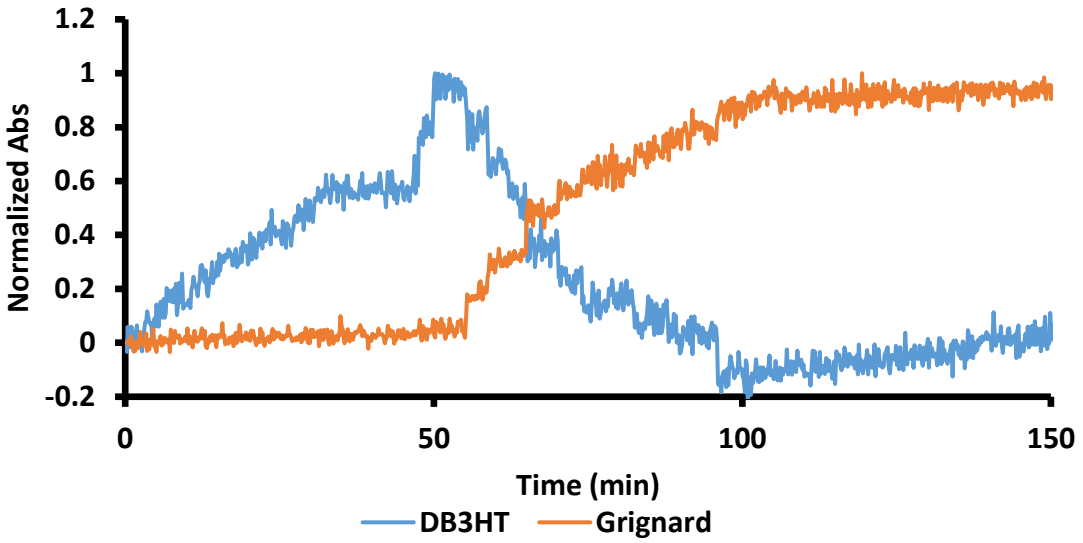

Figure 2.8 In situ ReactIR plots for Grignard metathesis of 2,5-dibromo-3-hexylthiophene.

Note: The Grignard reagent was i-proMgCl*LiCl. The Grignard peak accounts of total Grignard including the thiophene after metathesis. This reaction was not quenched with acetone while being monitored.

Figures 2.7 and 2.8 show the ReactIR data for the metathesis step of 2,5-dibromo-3,4-ethylenedioxythiophene and 2,5-dibromo-3-hexylthiophene, respectively. The Grignard peak correlates with the total Grignard concentration in the reaction, so metathesis is primarily monitored by the disappearance of the dibromothiophene species. The peaks for 2,3-dibromo-ethylenedioxythiophene are much stronger and easier to observe compared with the peaks for 2,5-dibromo-3-hexylthiopehene, making analysis easier. The metathesis reaction with 2,5-dibromo-3,4-ethylenedioxythiophene was quenched with acetone to show that the Grignard peak does indeed reflect the active Grignard species concentration. Both figures show that the metathesis step is incredibly fast when using i-proMgCl*LiCl as the Grignard reagent. The time resolution for IR scans was 5 secs; thus it appears that the reaction completed within this time frame. This

is in stark contrast to using i-butyl MgCl, which requires hours to complete and usually needs heating to drive the reaction towards completion.

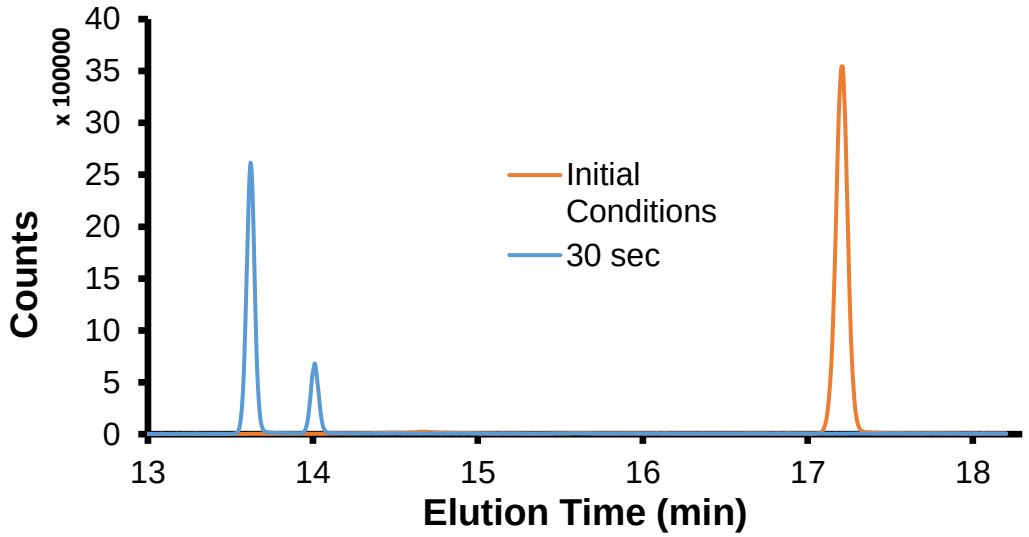

Figure 2.9 GC-MS chromatogram for the Grignard metathesis of 2,5-dibromo-3-hexylthiophene.

Note: The initial conditions were before addition of i-pro MgCl*LiCl and the 30 sec was the time after addition of i-pro MgCl*LiCl. The reaction was in THF at room temperature inside a glovebox with nitrogen atmosphere.

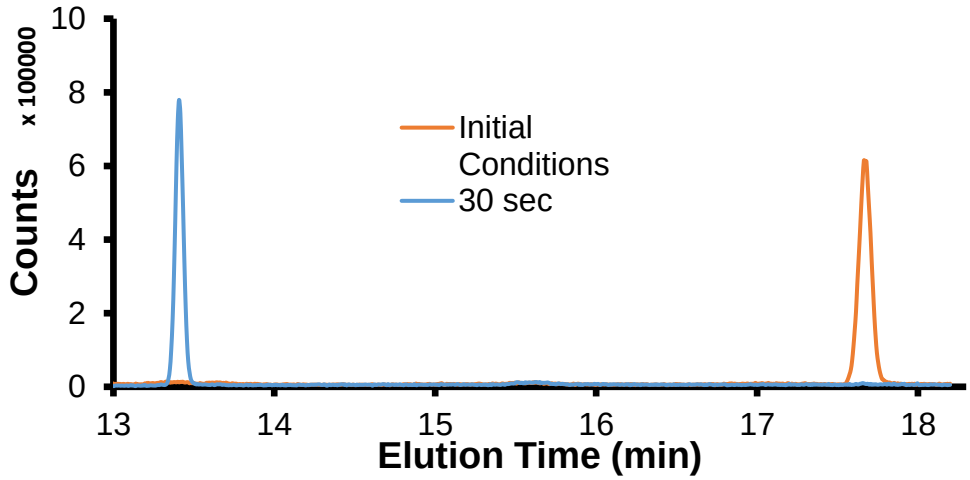

Figure 2.10 GC-MS chromatogram for the Grignard metathesis of 2,5-dibromo-3,4-ethylenedioxythiophene.

Note: The initial conditions were before addition of i-pro MgCl*LiCl and the 30 sec was the time after addition of i-pro MgCl*LiCl. The reaction was in THF at room temperature inside a glovebox with nitrogen atmosphere.

To further confirm the success of the metathesis step, the reaction was quenched and GCMS analysis conducted to quantify the resulting products before and 30 seconds after addition of i-proMgCl*LiCl. Figures 2.9 and 2.10 show the chromatographs for the 2,5-dibromo-3,4-ethylenedioxythiophene and 2,5-dibromo-3-hexylthiophene metathesis results, respectively. Metathesis for both reagents are fast and quantitative, confirming why i-proMgCl*LiCl helps control the resulting polymerizations.

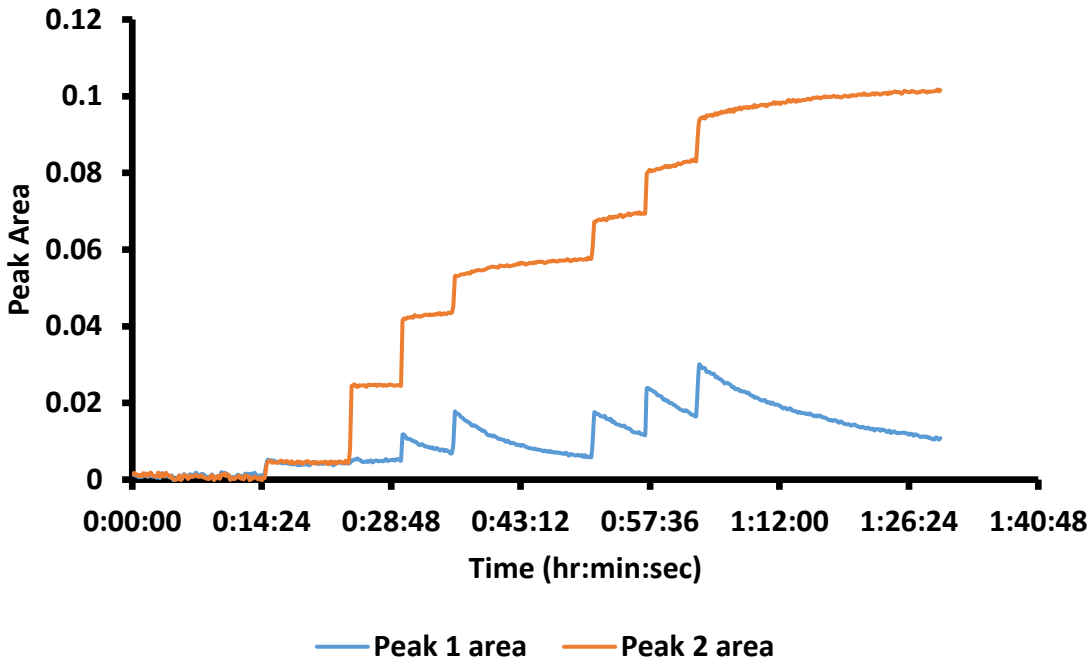

Figure 2.11 ReactIR data for monitoring Grignard metathesis between thiophenes.

Note: (5-bromo-4-hexylthiophen-2-yl)magnesium chloride and 2,5-dibromo-3,4-ethyelendioxythiophene in THF at room temperature. Peak 1 corresponds with 2,5-dibromo-3,4-ethylenedioxythiophene. Peak area 2 corresponds with the total thiophene, which would include both (5-bromo-4-hexylthiophen-2-yl)magnesium chloride and 2,5-dibromo-3,4-ethyelendioxythiophene.

To test which thiophene gives the more stable Grignard reagent, we did a metathesis reaction between (5-bromo-4-hexylthiophen-2-yl)magnesium chloride and

2,5-dibromo-3,4-ethylenedioxythiophene. Peak area 1 in Figure 2.11 shows how much 3,4-ethylenedioxythiophene like reagent is present in the reaction vessel, whether that is 2,5-dibromo-ethylendioxythiophene or (7-bromo-3,4-ethyelenedioxythiophen-2-yl)magnesium chloride. Peak are 1 shows how much 2,5-dibromo-3,4-ethylenedioxythiophene is present. This shows that (5-bromo-4-hexylthiophen-2-yl)magnesium chloride*LiCl can metathesize 2,5-dibromo-3,4-ethylenedioxythiophene, therefore, the 3,4-ethylendioxythiophene species gives a more stable Grignard reagent. This was unexpected because the 3,4-ethylenedioxy substituent is more electron donating and Grignard reagents create partial negative charges, which would be less stable with electron donating substituents. We hypothesize that the adjacent oxygen can help chelate the Grignard reagent and stabilize the reagent, despite being more electron donating.

2.3.3 Polymerization Kinetics

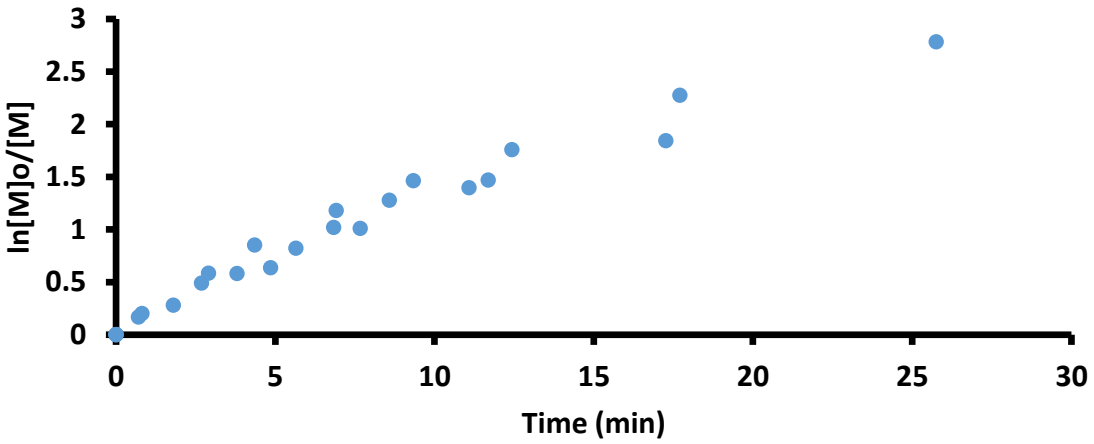

Figure 2.12 Pseudo-first order monomer consumption for P3HT polymerization.

Note: Aliquots were quenched with MeOH. The plot uses data from three separate reactions.

Monomer consumption kinetics were monitored using GCMS methods. The pseudo-first order kinetic plot is displayed in Figure 2.12. The plot approximates linearity, indicating the concentration of growing chains remains constant during the polymerization. Deviation from linearity became significant at conversions above 85%, with the decrease in slope at these higher conversions suggesting a decrease in the number of growing chains and thus loss of control. It is unclear if chain death is the result of solubility limits, or if the system has inherently poor control compared with other living polymerizations. Another possibility is the number of chain ends are not decreasing but instead that the effective number of growing chains decreases due to chain walking away from the chain end.[93]

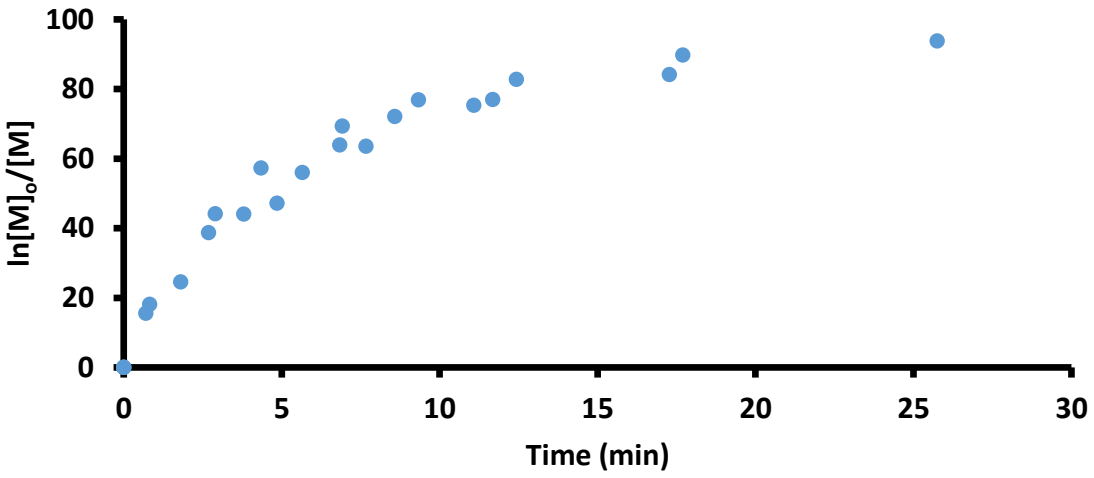

Figure 2.13 Conversion vs Time plot for P3HT polymerization.

Note: Aliquots were quenched with MeOH. The plot uses data from three separate reactions.

Figure 2.13 shows an example plot of the conversion versus time for the polymerization of P3HT. Almost 100% conversion is achieved, but to maintain optimal control it is recommended not to exceed 85% conversion under these polymerization conditions.

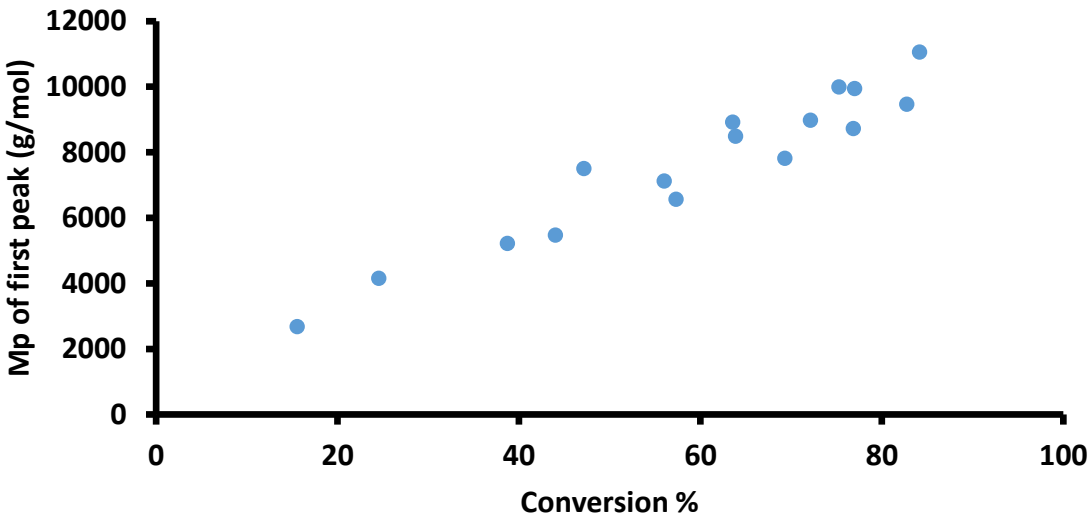

Figure 2.14 Molecular weight vs conversion for P3HT.

Note: All molecular weights were determined via GPC with THF was the mobile phase using polystyrene standards. The aliquots were quenched with MeOH, which causes coupling and a bimodal molecular weight distribution, so the reported molecular weights are the peak values of the low molecular weight peak. The data were from three separate reactions.

The molecular weight growth versus conversion plot for P3HT is displayed in Figure 2.14. The linear nature of the plot indicates that uniform growth is occurring on initiated chains, with little chain transfer. The zero intercept for the plot suggests a high level of control for the polymerization. Under different conditions a non-zero y-intercept is observed, probably caused by poor initiation. If initially only a small number of chains start growing, then those will grow rapidly with conversion. After initiation has finished, the polymerization can continue in a quasi-living manner, exhibiting linear growth with

conversion. Typically the pseudo-first order kinetic plot would show a lower slope reflecting the slow initiation period, but here the polymerization and initiation are extremely fast. The earliest aliquot, removed after ~42 sec after initiation, has already reached 15% conversion.

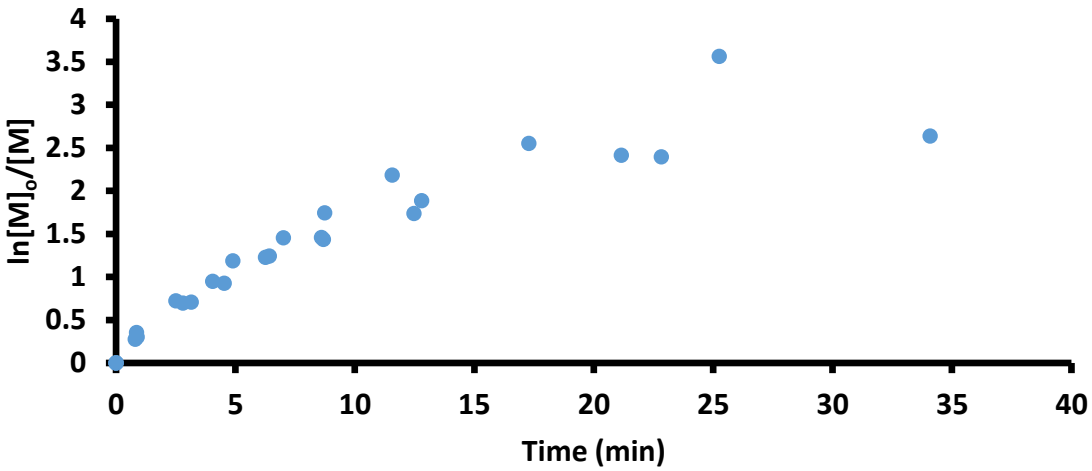

Figure 2.15 Pseudo-first order kinetic plot for consumption of the EDOT based monomer for copolymerization of 3:1 3HT:EDOT.

Note: Aliquots were quenched with MeOH. The plot uses data from three separate reactions.

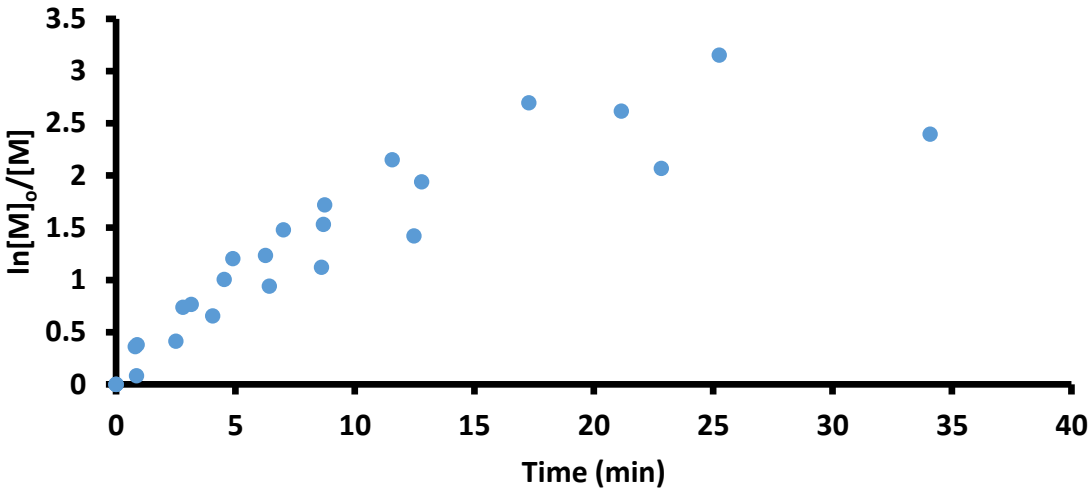

Figure 2.16 Pseudo-first order kinetic plot for consumption of the 3HT based monomer for copolymerization of 3:1 3HT:EDOT.

Note: Aliquots were quenched with MeOH. The plot uses data from three separate reactions.

Pseudo-first order kinetic plots are shown in Figures 2.15 and 2.16 for copolymerizations using 3:1 feed ratio of 3HT:EDOT based monomers. Near linear behavior is observed, indicating a constant concentration of growing chain ends during the polymerization which decreases at higher conversions. The slope for both monomers are about the same, suggesting that the reactivity ratios for the monomers is approximately 1. This is unexpected, based on the difference in Grignard stability for the two monomers. This suggests the polymerization approaches diffusion control during the reaction.

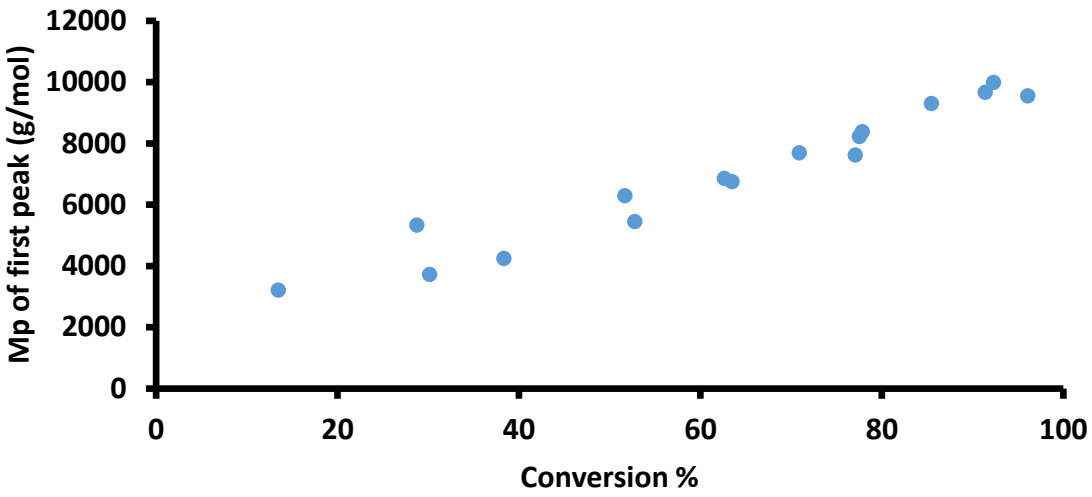

Figure 2.17 Molecular weight vs conversion plot for P(3HT-co-EDOT)F3:1.

Note: All molecular weights were determined via GPC with THF was the mobile phase using polystyrene standards. The aliquots were quenched with MeOH, which causes coupling and a bimodal molecular weight distribution, so the reported molecular weights are the peak values of the low molecular weight peak. The data were from three separate reactions.

The molecular weight growth plot for the copolymerization are also linear, with the y-intercept almost zero. This suggests the copolymerization has a higher level of control.

2.3.4 Polythiophene Composition and Molecular Weight

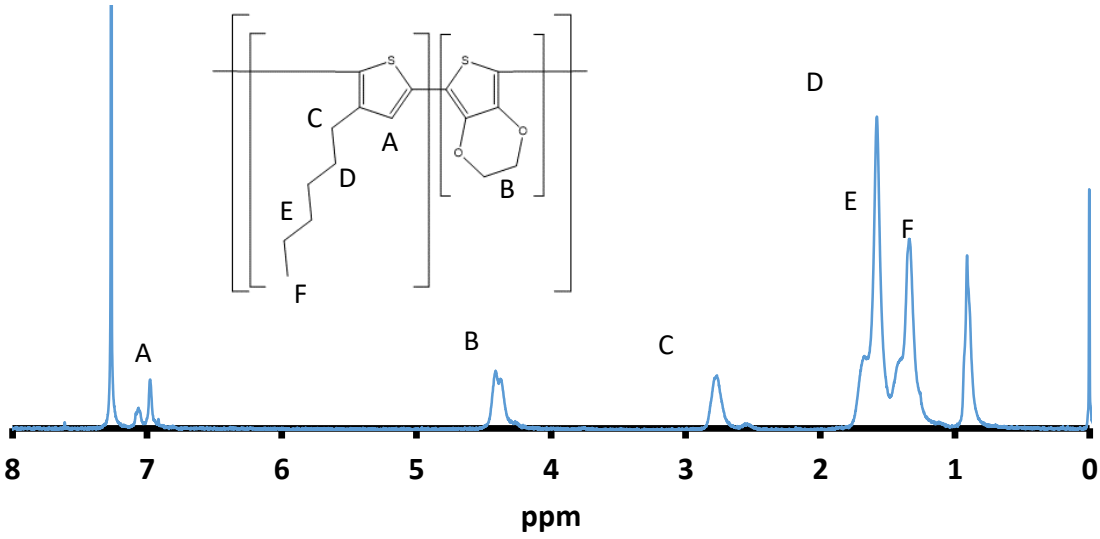

Figure 2.18 Proton NMR of P(3HT-co-EDOT)F2:1.

Note: The solvent was $CDCl_3$, and the polymer was first purified via Soxhlet extraction to remove any residual monomer and other side products from the polymerization process.

Figure 2.18 is the H^1NMR spectrum for the copolymer. The observed peaks support the successful synthesis of this copolymer, with the observed peak shifts consistent with literature values.[15] Polymer composition was determined by integrating peaks B and C.

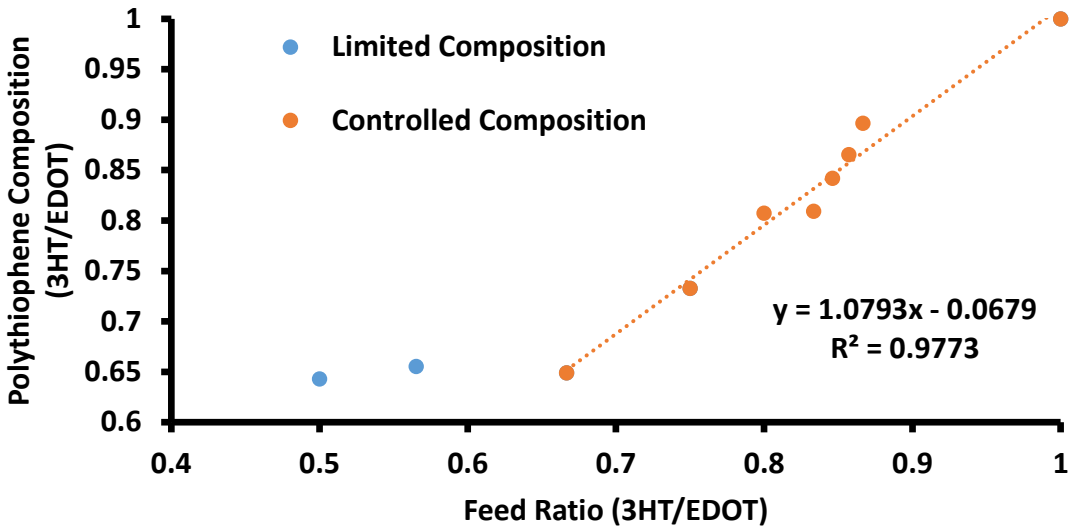

Figure 2.19 Polythiophene feed and composition relationship.

Figure 2.19 shows the plot of copolymer composition versus feed ratio. The copolymerization solubility limited composition, with the number of EDOT repeat units lowering the polymer solubility. Polymerizations using feed ratios less than 0.66 had lower soluble polymer yields (i.e. insoluble product). Soluble copolymers are not possible using compositions lower than 0.66, suggesting the composition is limited by the introduction of EDOT repeat units. Most of the kinetic data were collected using methanol to quench the aliquots. This method causes coupling of the chains; the presented molecular weights were the lower molecular weight peaks from a bimodal molecular weight distribution. This phenomena has been previously observed in literature, and the evidence of coupling supports that the polymerizations are controlled. The use of HCl is reported to alleviate the coupling problem for P3HT,[94] but quenching the copolymerization yields a completely insoluble product. We hypothesize this coupling is caused by a stepwise polymerization route. For example, coupling is

observed for PEDOT under similar acid catalyzed conditions. Unimodal molecular weight distributions are obtained by quenching with allyl-MgCl. However, this approach does not work well for quenching aliquots. Therefore, in order to maintain the same conditions between homopolymer and copolymer, aliquots were quenched with MeOH.

To show polymerization conditions provided good molecular weight control along with reasonable PDI values, a homopolymerization reaction was conducted using HCl quenching. The molecular weight growth plot is shown in Figure 2.20. Here a small y-intercept is observed. A higher molecular weight was also achieved, eventually reaching a plateau in the molecular weight growth. This is caused by limited solubility, which leads to a loss of control. This behavior has been previously reported in the literature.[16] The PDI values (somewhat inaccurate due to the rod like nature of the polymers) remain low throughout the polymerization.

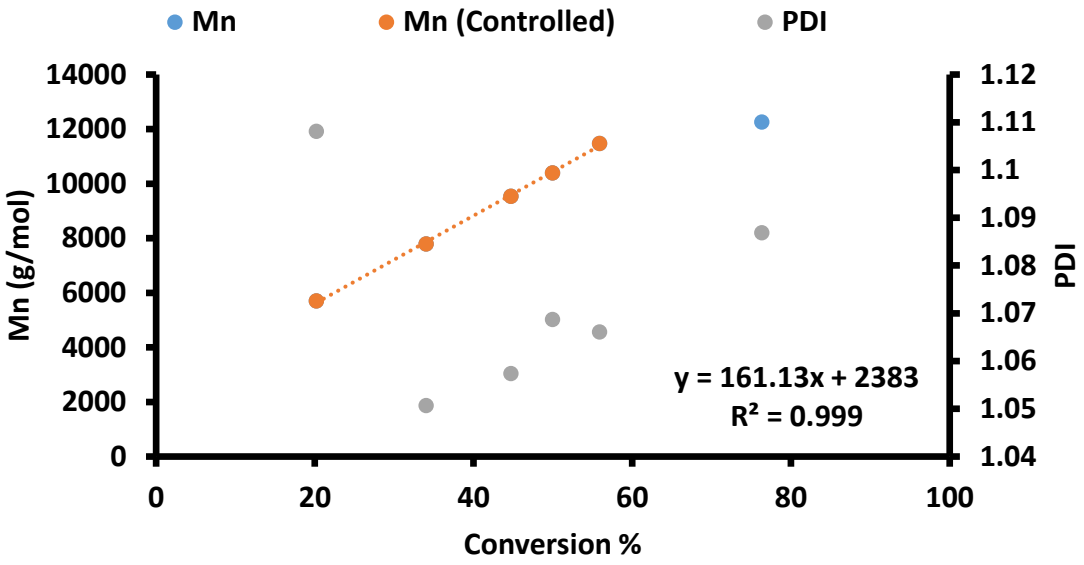

Figure 2.20 Molecular weight vs conversion plot for HCl quenched.

Note: All molecular weights were determined via GPC with THF as the mobile phase using polystyrene standards. The aliquots were quenched with HCl, which avoids coupling. Number average molecular weights are reported along with PDI. At higher conversion control is lost (blue data point).

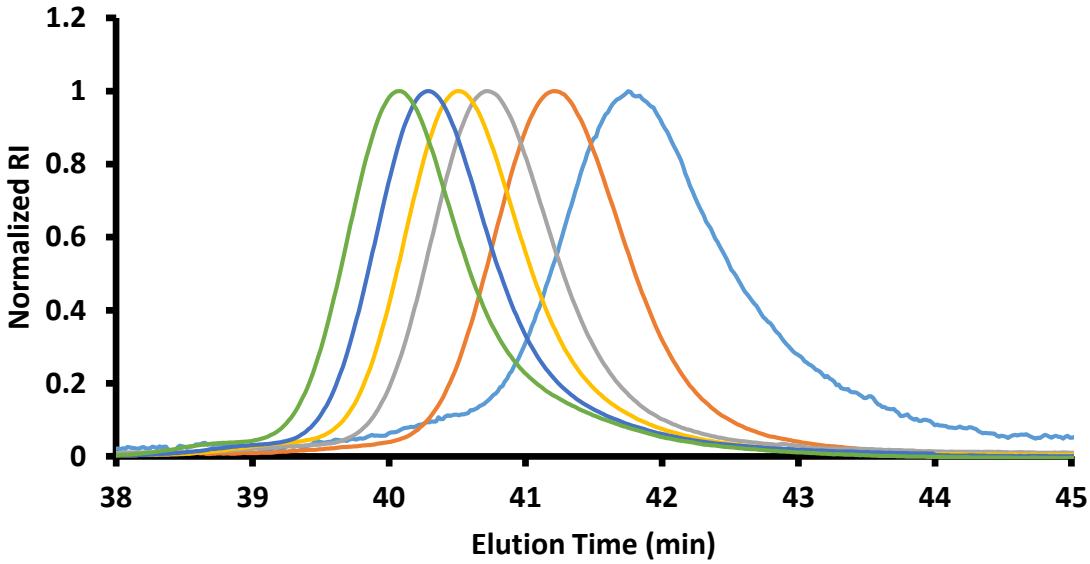

Figure 2.21 GPC trances for the different aliquots from P3HT polymerization.

Note: The RI traces were normalized to make shape comparison easier. These aliquots were quenched with HCl to avoid coupling.

Figure 2.21 shows the GPC traces for the polymerization aliquots with normalized intensities to facilitate comparisons. They are narrow and are unimodal, expected when quenching with HCl. There is tailing in the lower molecular weights, which we hypothesize is the result of poor initiation. Nevertheless, we concluded the polymerizations were successful for both the homopolymer and the copolymers. Unimodal products for both polymer types are obtained by quenching with allyl MgCl, with composition controlled by changing the feed ratios. Using the described conditions quasi-living polymerizations are possible, with the molecular weight reliably controlled.

2.4 Conclusions

We originally hypothesized that quasi-living conditions for GRIM polymerization of 2,5-dibromo-3-hexylthiophene and 2,5-dibromo-3,4-ethylenedioxythiophene could be achieved, and the feed ratio would ultimately control composition of the resulting polythiophenes. Quasi-living conditions were indeed obtained; however, there was a solubility limit for control over composition. We established the composition ratio needed to maintain solubility, namely no fewer than two 3-hexylthiophene repeat units for each 3,4-ethylenedioxthiophene unit. Although 3,4-ethylenedioxythiophene has higher donating properties, the resulting Grignard reagent is more stable, which we attribute to chelation of the adjacent oxygen with the metal center. The reactivity ratios of the comonomers are approximately 1, and composition control via feed ratio was observed. Acid catalyzed homopolymerization of 3,4-ethylenedioxythiophene based units caused complications for copolymerizations. Cooling the reaction to ~0°C, adding excess thiophene to NBS, and using DMF as a solvent helps prevent homopolymerization during the synthesis of 2,5-dibromo-3,4-ethylenedioxythiophene. Quenching copolymers

with HCl causes side reactions, leading to insoluble products. Quenching with MeOH results in coupling that creates bimodal molecular weight distributions. This can be alleviated using allyl magnesium chloride as the quenching reagent. Overall molecular weight and composition control were achieved for copolymerizations. In the following chapter we will discuss the resulting properties of these copolymers.

CHAPTER III – Polythiophene Properties

The purpose of this chapter is to document the properties of the polythiophene copolymers and demonstrate the level of control over these properties that we hypothesized would have a correlation with anti-corrosive performance.

3.1 Introduction

Based on the homopolymer properties found in the literature, we expect that the solubility of the copolymers will decrease with increasing 3,4-ethylenedioxythiophene content and that the reduction potential of the oxidation process will decrease as well. Becuase the homopolymer PEDOT has a lower optical bandgap, we expect the optical bandgap to decrease with increasing 3,4-ethylendioxythiophene content, and the rigid rod nature of PEDOT leads us to hypothesize that T_g will increase as well.

When it comes to corrosion protection there are really two categories of coating properties that need to be addressed: the electrochemical properties and the barrier properties. For most anti-corrosion films the electrochemical properties are bestowed by loading inhibitors or metallic pigments into the coating. Polythiophenes are semi-conductive polymers and have their own electrochemical properties, so it was thought to better understand how polythiophenes alter corrosion kinetics we first need to understand the electrochemical properties of the polythiophenes in question.

3.2 Methods

3.2.1 UV-Vis Spectroscopy

A BioTek was used to obtain absorption spectra scanning from 350 nm to 750 nm at 2 nm steps. Spectra were taken from 150 uL volumes of the solutions described in the

appendix (solutions 1 and 2 were used for preparation of calibration curves). See the appendix for an index of the solutions and solvent mixtures used for this experiment.

3.2.2 Cyclic Voltammetry

Cyclic voltammetry was acquired on a Princeton Applied Research VersaSTAT 4 using a 3 electrode cell with Pt counter electrode, P3HT or P(3HT-co-EDOT) coated Pt working electrode, and silver quasi-reference electrode calibrated using a ferrocenium/ferrocene couple (cell solution was 0.03M tetrabutyl ammonium hexafluorophosphate in acetonitrile) was conducted to quantify oxidation potential. A 100 mV/sec rate was applied from -0.2 to 1.2 volts vs REF.

3.2.3 Hanson Solubility Determination

The P3HT was purchased from Sigma Aldrich at 54,000-75,000 Mn. P3HT was also synthesized in house. The P3HT was dissolved in bromobenzene with the aid of heat (50°C) at a concentration of 1.25 mg/mL. A series of solutions (see appendix) were prepared using this stock solution. Good and poor solvents were determined from the onset of absorbance near 610 nm, whereas HSP were calculated using a minimum sphere calculation.

3.3 Results and Discussion

3.3.1 UV-Vis and fluorescence Analysis

Bandgap energies of CP solutions and films were estimated using UV-Vis spectroscopy. Results can support electrochemically determined HOMO and LUMO energy levels. Polythiophene composition predictably alters the UV-Vis absorption spectra in solution. However, shifts are insignificant between polythiophene films. The UV-vis spectra of polythiophene solutions are displayed in Figure 3.1.

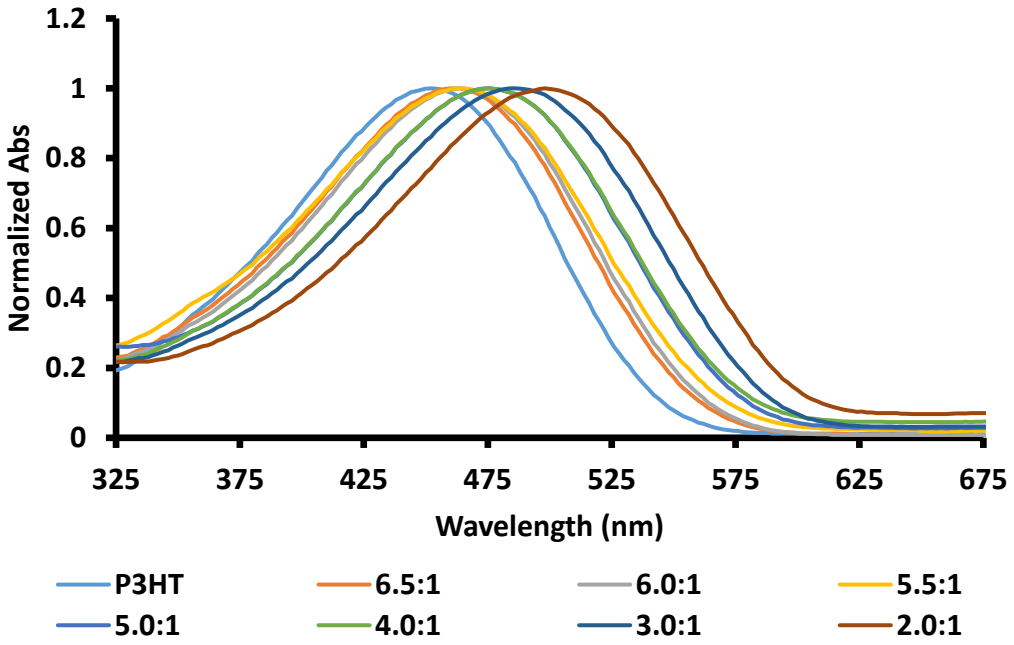

Figure 3.1 UV-Vis absorption spectra for polythiophenes in solution.

Note: All polythiophenes were dissolved in bromobenzene at 0.01 mg/g and bromobenzene blanks were subtracted prior to normalization. The UV-Vis spectra shown for each polythiophene were an average created from 3 samples. The ratios in the legend are for 3HT:EDOT from the feed during synthesis.

The absorption max for the polythiophenes can be predicted using an equation analogous to the Fox equation:

$$\frac{1}{\lambda_{copoly}} = \frac{\chi_{EDOT}}{\lambda_{PEDEOT}} + \frac{\chi_{3HT}}{\lambda_{P3HT}} \qquad (3.1)$$

Here $\boldsymbol{\chi}$ denotes mole fraction and λ denotes the max absorbance in nm. λ_{P3HT} is 452 nm whereas the value of PEDOT is unknown due to insolubility. The following equation allows λ_{copoly} prediction:

$$\frac{1}{\lambda_{copoly}} = \frac{\chi_{EDOT}}{\lambda_{PEDEOT}} + \frac{(1-\chi_{EDOT})}{\lambda_{P3HT}} = \left(\frac{1}{\lambda_{PEDOT}} - \frac{1}{\lambda_{P3HT}}\right)\chi_{EDOT} + \frac{1}{\lambda_{P3HT}} \qquad (3.2)$$

A linear relationship is expected when plotting $\frac{1}{\lambda_{copoly}}$ vs χ_{EDOT}.

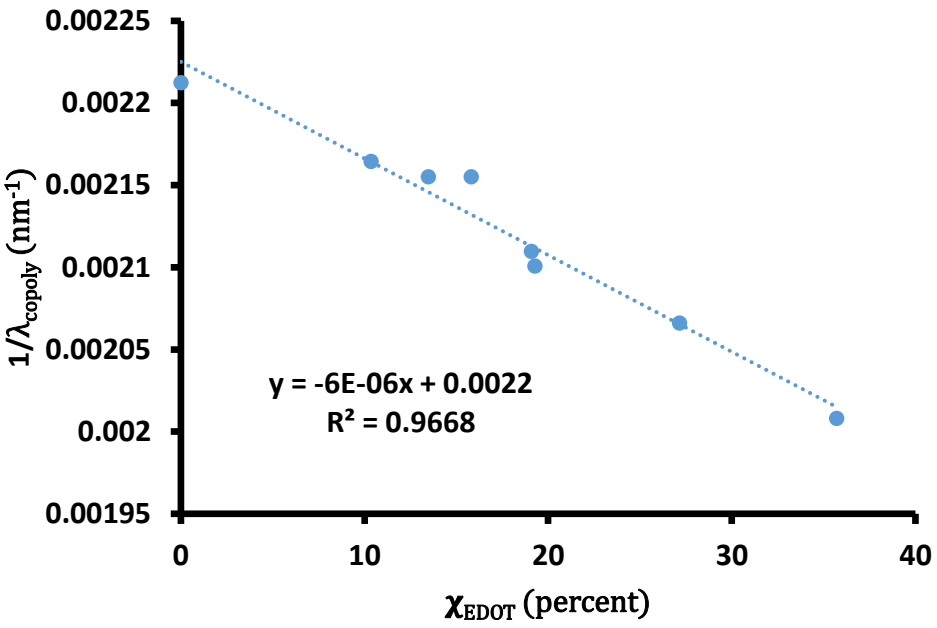

Figure 3.2 Plot of $\frac{1}{\lambda_{copoly}}$ vs χ_{EDOT} for polythiophenes.

Note: The R^2 demonstrates how well the Fox-like equation can predict the $\lambda_{copolyer}$ for a given polythiophene based on the composition.

The calculated λ_{P3HT} was 454 nm, similar to the observed value of 452 nm. The calculated λ_{PEDOT} was 625 nm. The λ_{PEDOT} of dedoped PEDOT films from Meng et al.,[85] is between 610 and 630 nm. Our calculated λ_{PEDOT} in solution is similar.

Onset absorption allows bandgap energy estimation.[95] The HOMO and optical bandgaps for three polythiophenes are shown in Table 3.1.

Table 3.1 Polythiophene HOMO and calculated optical bandgaps.

Polythiophene name	Comonomer ratio (3HT:EDOT)	Onset of Oxidation (V vs FC/FC+)	HOMO (eV)	Bandgap energy (eV)
P3HT	homo	0.41	-5.51	1.93
P(3HT-co-EDOT)F3:1	3:1	0.21	-5.31	1.88
P(3HT-co-EDOT)F2:1	2:1	0.01	-5.11	1.90

Bandgap energies of CPs are related to the effective conjugation length.[96] CPs in solution have sufficient mobility to allow torsion, decreasing effective conjugation lengths. However, packed and crystalline polythiophene film morphologies increase effective conjugation length, leading to red shifts in UV-Vis spectra (Figure 3.3).

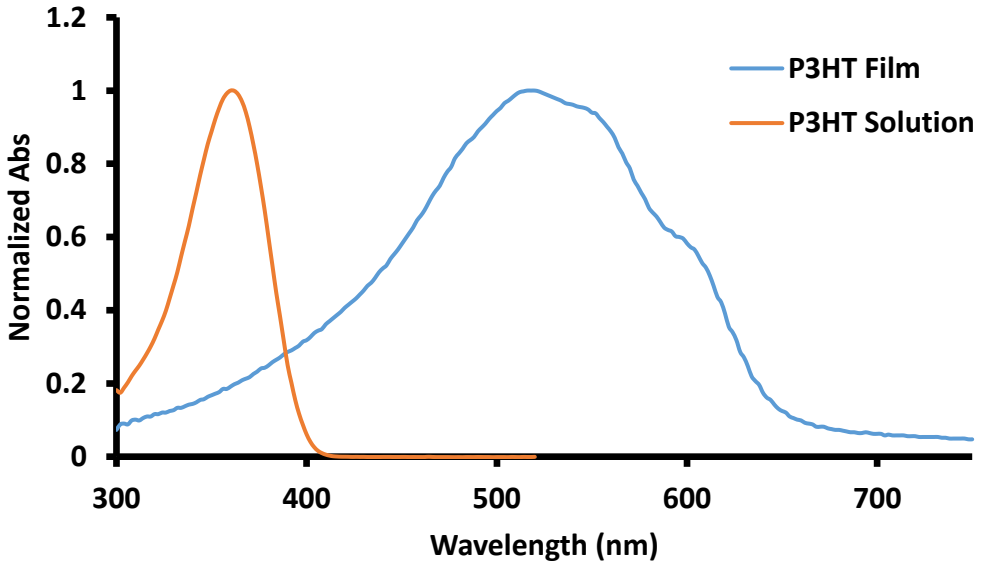

Figure 3.3 UV-Vis spectrum for P3HT.

Note: The P3HT was dissolved in chlorobenzene and a chlorobenzene blank was subtracted prior to normalizing the abs for the P3HT in solution UV-Vis spectrum. The P3HT film was drop cast from chloroform onto the bottom of the glass vial used for UV-Vis collections to obtain the film spectrum.

The more red shifted a CP's UV-Vis spectrum, the more packed and ordered the film morphology is.

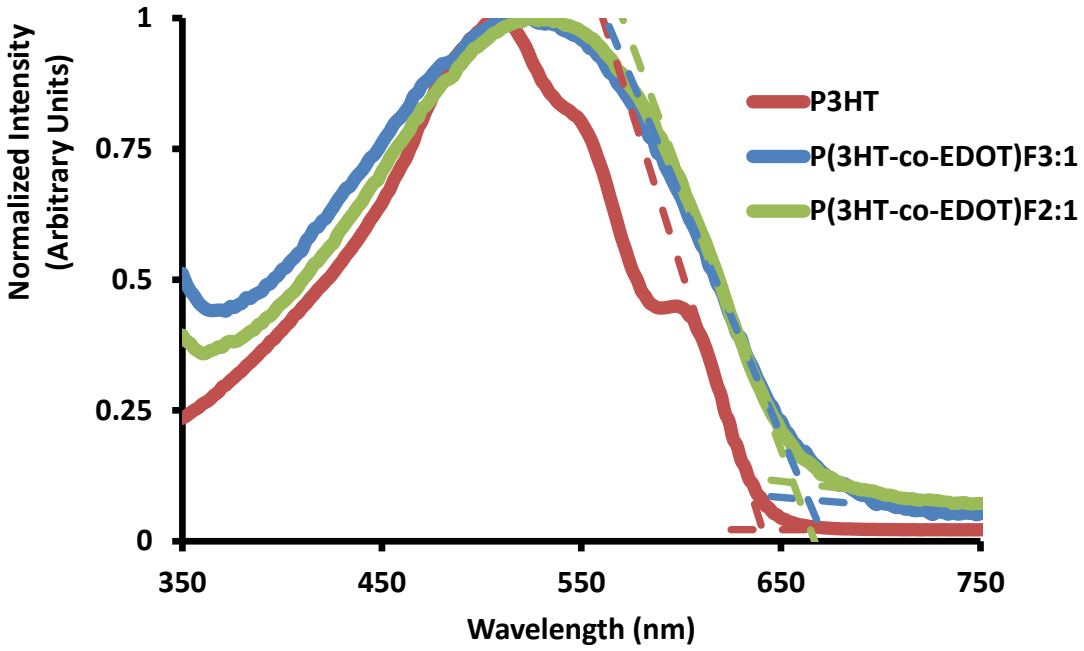

Figure 3.4 UV-Vis spectra for three polythiophene films.

Note: The polythiophene films were drop cast from chloroform unto the glass vials used for UV-Vis collection. The dotted lines are for showing the onset for calculating the optical bandgaps. Notice that the two copolymers overlap to the point that the calculated bandgaps would be equivalent.

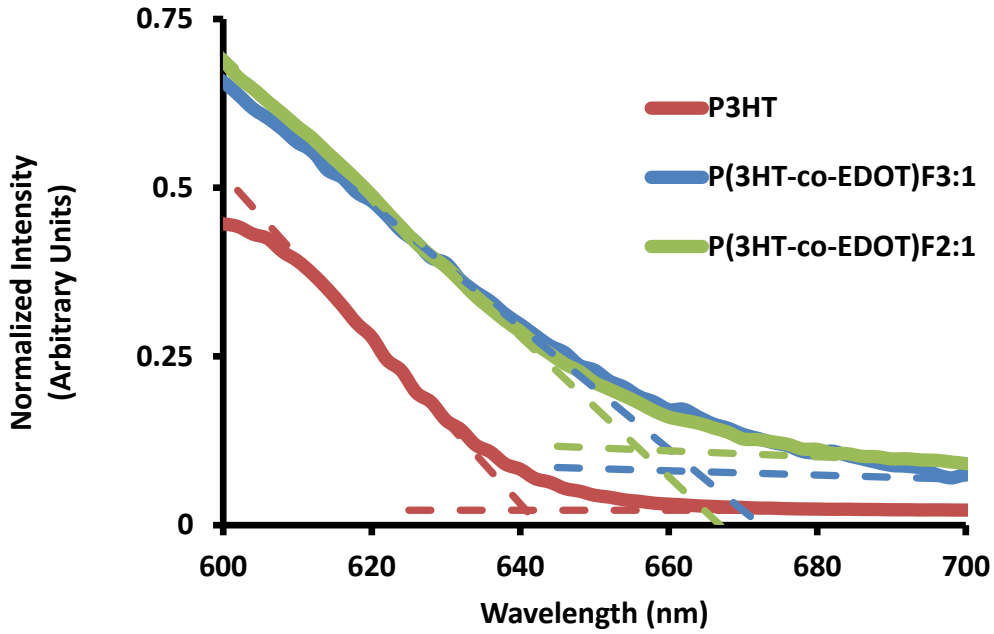

Figure 3.5 Zoomed in UV-Vis spectra for three polythiophene films.

Note:The polythiophene films were drop cast from chloroform unto the glass vials used for UV-Vis collection. The dotted lines are for showing the onset for calculating the optical bandgaps. By zooming in, it is easier to see how close the bandgaps are.

Similar optical bandgap energies were observed for polythiophene films. We originally hypothesized a lower optical bandgap for the copolymers due to PEDOT having a lower optical bandgap. However, the effect was insignificant. P3HT optical bandgaps were 1.93 eV (642 nm onset) compared with the copolymer bandgap of 1.89 eV (655 nm onset). No statistical differences between the 3:1 and 2:1 feed copolymers were observed.

It is possible that introducing 3,4-ethylenedioxythiophene decreases packing efficiency and crystallization, thus reducing effective conjugation length. This could lessen the effect of intrinsic bandgap energies, leading to similar optical bandgaps despite expectations.

3.3.2 Cyclic Voltammetry

The HOMO energy level of the polythiophene, related to the reduction potential of oxidation process of the repeat units (many times called the oxidation potential or onset oxidation potential in the literature), can be quantified by the onset potential of the oxidation peak from cyclic voltammetry of the polythiophene films.[97] The HOMO energy level is then determined using the following equation:

$$-5.1 - Potential\ of\ onset\ oxidation = HOMO\ in\ eV \qquad (3.3)$$

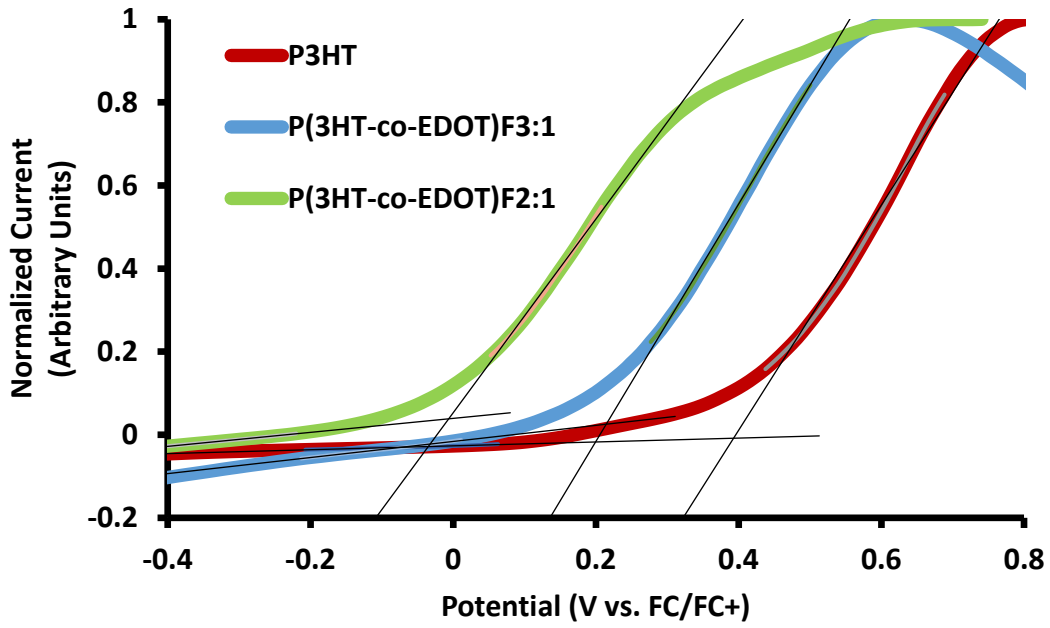

Figure 3.6 Current normalized cyclic voltammetry results for three polythiophenes.

Note: The black lines are used to show the onset of oxidation for calculating the onset oxidation potential of the polythiophene as well as the HOMO energy levels for the polythiophenes.

Zoomed in CV of the oxidation process for a series of polythiophenes with different composition are shown in Figure 3.6. By plotting the onset of oxidation, we can get a

relationship between the HOMO of the polymer and the composition of the polythiophene.

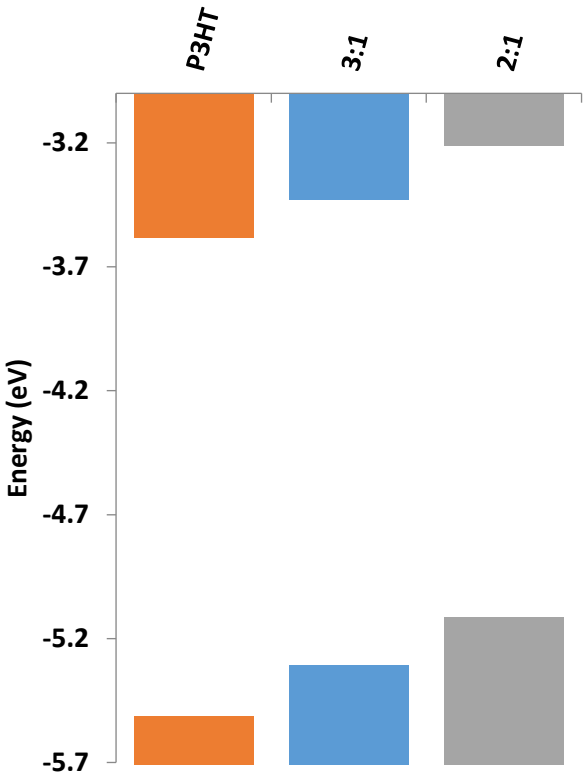

Figure 3.7 Bar diagram for the energy levels of the polythiophenes.

Note: The bottom bar represents the HOMO levels and the top bars represent the LUMO levels calculated using the optical bandgaps for the polythiophenes.

3.3.3 Hanson Solubility Parameters

Quantifying the Hansen solubility parameters (HSP) of polymers can be tedious, and usually requires using a large series of solvents. In 2012 Machui et al.[98] developed a binary solvent method for quantifying the HSP of P3HT and [6,6]-phenyl-C61-butyric acid methyl ester (PCBM). The strong absorption properties of P3HT and PCBM make it

easier to quantify saturation concentrations using UV-Vis spectroscopy. The technique requires preparation of saturated samples, which is both tedious and uses a large quantity of material (which can be expensive when dealing with these materials). Due to the strong relationship between π orbital overlap and polymer chain conformation of conjugated polymers like P3HT, the UV-vis absorption properties of these polymers change considerably when they crash out of solution. The transition from soluble to insoluble, therefore, can be easily quantified and less material is required to determine HSP of the polythiophenes in question.

3.3.3.1 Calibration Curves

Serial dilution of P3HT dissolved in bromobenzene and dispersed in MeOH were used for creating calibration curves for absorption of solubilized P3HT (450 nm) and dispersed P3HT (560 nm), respectively (Figure 3.8 and 3.9). The y-intercept in the calibration curve for the dispersed P3HT is likely caused by scattering difference with the effective blank used when subtracting (the blank had significantly less scattering). The dispersed P3HT samples are much more sensitive to inaccuracy from scattering, which also explains the lower R2 value for the fit.

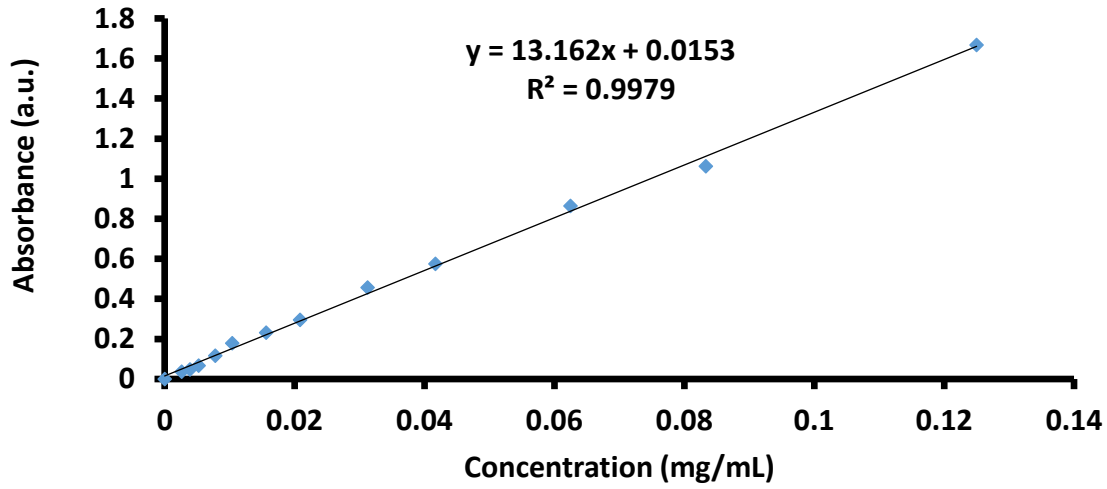

Figure 3.8 Absorption calibration curve for P3HT in solution.

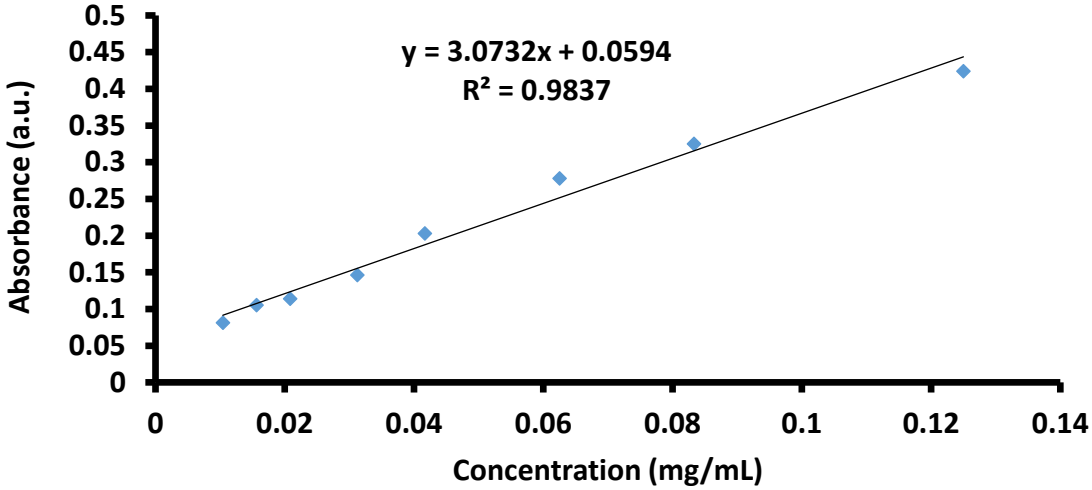

Figure 3.9 UV-Vis absorption calibration curve using dispersed P3HT.

When a series of solvent blends was used to prepare solutions of P3HT the solubility limit could be seen by color shifts. As the solvent composition shifts towards the poor solvent, the P3HT begins to crash out and the absorption spectrum changes for the solution/dispersion. The absorption spectra for the dispersed P3HT are not consistent.

This is expected because the morphology of the particles will be different depending on the solvent mixture used. The changes in peaks found at 560 and 610 nm are commonly used to study P3HT nanowires.[99] Additionally the absorption for the dispersion decreases when the aggregation of P3HT is too high because the aggregates do not necessarily find themselves in the path probed by the instrument(prominently seen in the case of bromobenzene:acetone mixtures in Figure 3.11). Even though this makes quantifying the amount of P3HT that has crashed out difficult, there is still a clear transition from good to poor solvent by the sudden change in absorption found at 610 nm.

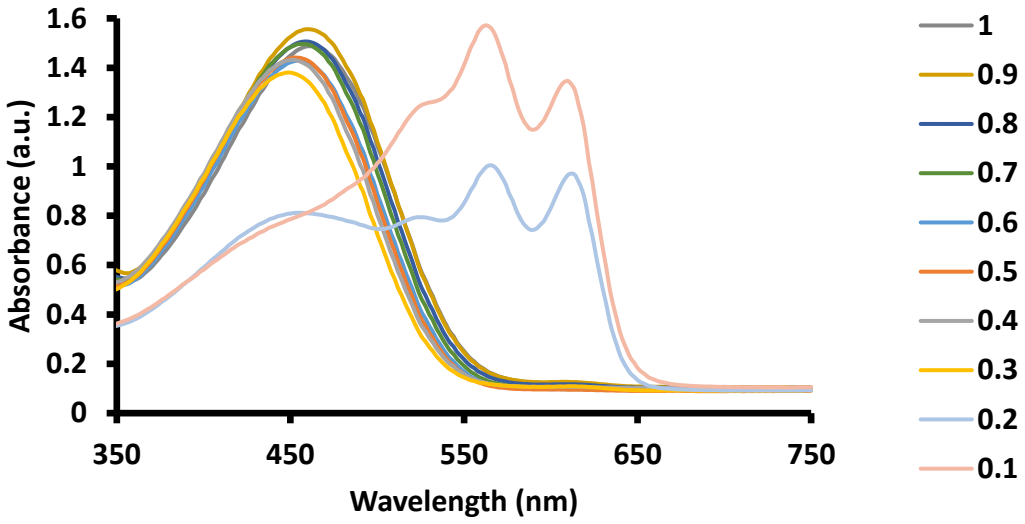

Figure 3.10 UV-Vis absorption spectra for P3HT solutions/dispersion in bromobenzene:cyclohexane mixtures. The volume fraction of bromobenzene are seen in the legend.

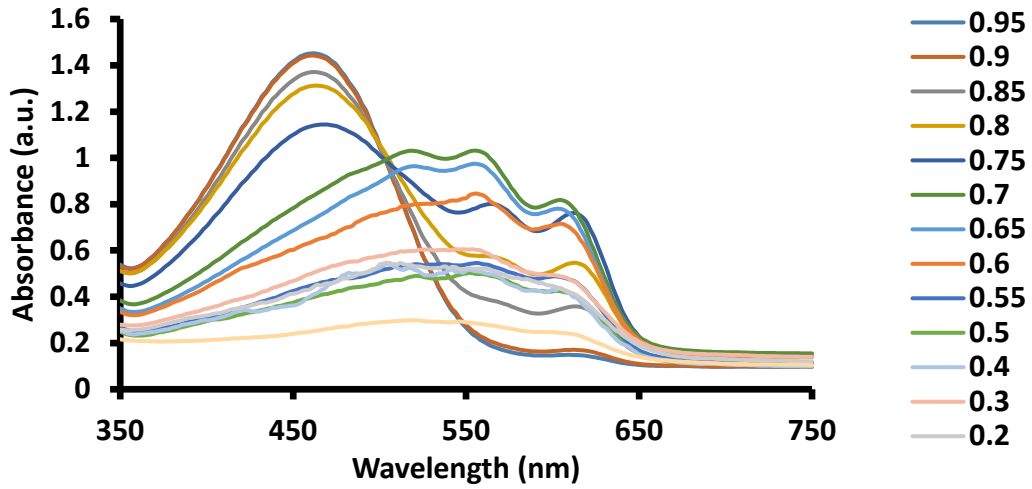

Figure 3.11 UV-Vis absorption spectra for P3HT solutions/dispersion in bromobenzene:acetone mixtures. The volume fraction of bromobenzene are seen in the legend.

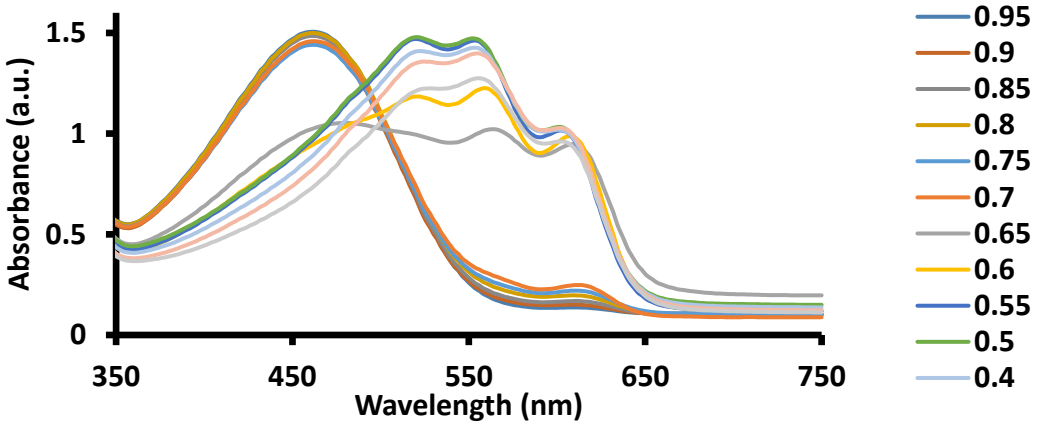

Figure 3.12 UV-Vis absorption spectra for P3HT solutions/dispersion in bromobenzene:oleic acid mixtures. The volume fraction of bromobenzene are seen in the legend.

The identification of "good" and "poor" can be used with the HSP of the solvent blends to quantify HSP of P3HT. By plotting the absorbance at 610 nm it is easier to see the solubility transition for P3HT.

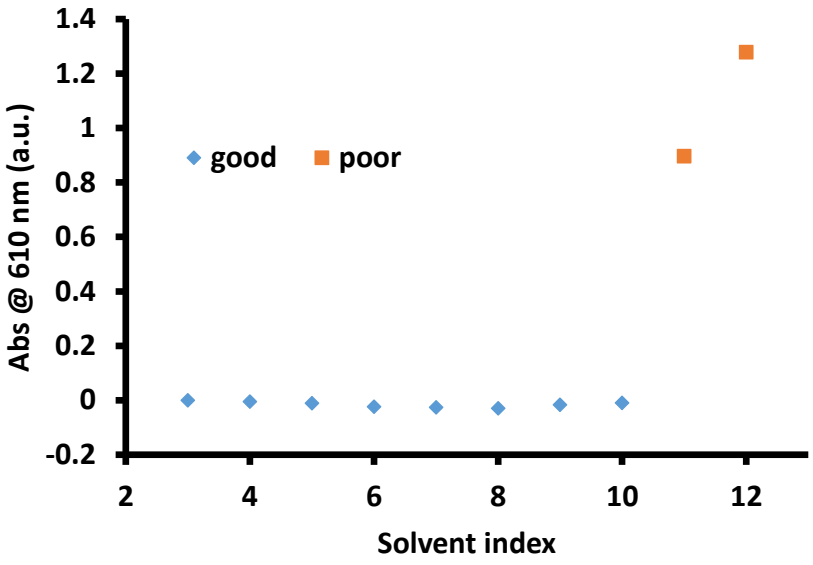

Figure 3.13 Absorbance at 610 nm for the different P3HT solutions/dispersion. The solvent index can be found in the appendix. These blends are for bromobenzene:cyclohexane mixtures.

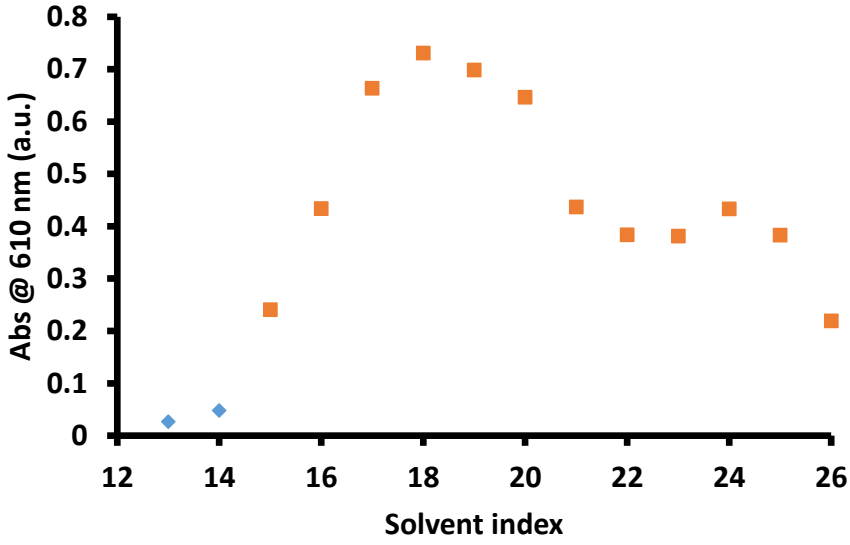

Figure 3.14 Absorbance at 610 nm for the different P3HT solutions/dispersion. The solvent index can be found in the appendix. These blends are for bromobenzene:acetone mixtures.

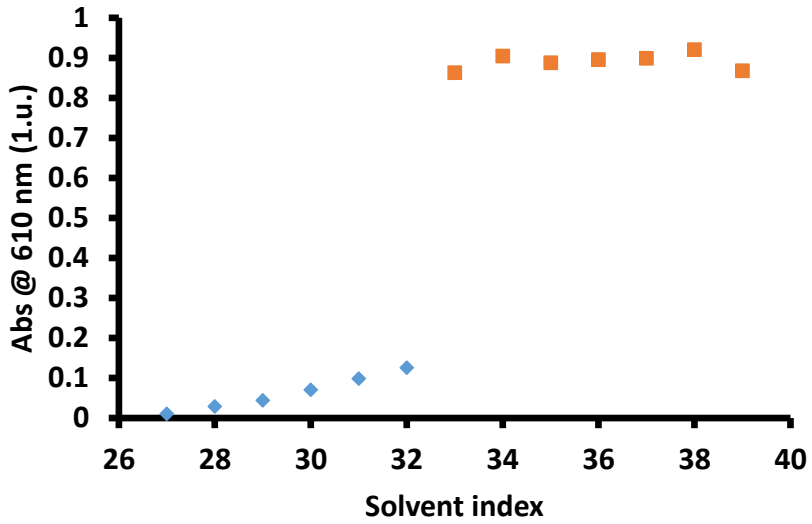

Figure 3.15 Absorbance at 610 nm for the different P3HT solutions/dispersion. The solvent index can be found in the appendix. These blends are for bromobenzene:oleic acid mixtures.

A sphere of minimum radius that encompasses the good solvents was analytically calculated to find the HSP of P3HT. More accurate results would be obtained with 4 solvent blends because the position of a sphere can be analytically determined with 4 points. Table 1 shows the comparison of HSP values from Machui et al.[98]

Table 3.2 HSP values for P3HT from literature and from our UV-Vis technique.

	D (MPa1/2)	P (MPa1/2)	H (MPa1/2)
Classical HSP Technique[98]	18.4	3.7	6.3
Binary solvent Technique[98]	17.9	3.2	0.9
UV-Vis shift technique	18.7	4.5	1.7

Fluorescence can similarly be used to quantify the solubility transition for the polymers. The HSP for the copolymers was also quantified using this technique.

3.4 Conclusions

We originally hypothesized that each the solubility, the onset oxidation potential , and the optical bandgap would decrease with increasing 3,4-ethylenedioxythiophene content in the polythiophene copolymers synthesized in chapter 2. This was because of the general properties singularly of the homopolymers P3HT and PEDOT found in the literature. Indeed, the onset oxidation potential and solubility decreased as expected, but the optical bandgaps appeared to not change significantly.

The higher electron donating aspect of the ethylenedioxy substituent helps to stabilize positive charges that would form in the backbone due to oxidation of the polymer, which decreases the onset oxidation potential of the resulting polymer. We did not expect there to be such small changes in the optical bandgap for the copolymers. This is likely caused by difference in effective conjugation length of the polymers. The switching between 3-hexylthiophene and 3,4-ethylenedioxythiophene would disrupt chain packing and crystallization, and the effective chain length of the copolymer would be lower than the homopolymers PEDOT and P3HT are singularly. The result is that even though the intrinsic optical bandgap of the copolymers would be lower than P3HT, the lower effective chain length of the copolymer results in little to no change in the optical bandgap of the solid-state films. In the next chapter we will discuss the applicability of different electrochemical techniques for evaluating corrosion and describe what techniques should be used under different circumstances.

CHAPTER IV – Corrosion Evaluation Techniques

The purpose of this chapter is to introduce and evaluate how effective the different techniques for studying corrosion performance are, and to describe the recommended approach for evaluating polymer films via electrochemical techniques.

4.1 Introduction

An electrode is any electrically conductive material where electrochemical reactions can take place. An electrode placed into a solution develops a potential difference between its surface and the immersion solution, usually leading to dissolution of the electrode. Unlike general chemical process like dissolution of NaCl into water, electrochemical dissolution is controlled by chemical potential as well as electrical potential differences. The electrode primarily dissolves as ions with a single type of charge; for metals this is usually positively charged ions, leaving the electrode with a net negative charge and the solution with a net positive charge. Equilibrium is reached when the chemical potential for dissolution is equal to the electric potential resulting from this net charge difference. As the electrical potentials due to net charge differences are quite large, the equilibrium concentration for electrochemical dissolution is extremely small, making it impractical to measure the ion concentration directly; instead the electrical potential is measured. Because the chemical potential for dissolution varies between electrodes, an electrical potential difference will exist between two different electrodes at equilibrium. The open circuit potential is the measured electrical potential between two electrodes not in electrical contact.

The open circuit potential is proportional to the thermodynamic drive for an electrochemical cell. They are measured using a working electrode and a reference

electrode. Reference electrodes are chosen based on their highly reproducible and stable thermodynamic properties, and are designed to be at thermodynamic equilibrium with a constant environment and reagent concentration to ensure that equilibrium does not shift or drift during experiments. A working electrode is any electrode used to study an electrochemical reaction.

Electrochemical reactions are basically oxidation and reduction reactions driven by the net charge difference at an electrode surface. An electrochemical cell is the environment whereby electrochemical reactions occur. These are generally described using a combination of half-cell reactions, each describing the reduction and oxidation processes present in the cell. For a correctly designed electrochemical cell, the OCP is used to indirectly measure the thermodynamic properties of these half-cell reactions via the Nernst equation.[100]

$$emf = E = E^o - \frac{kT}{ne} ln\left(\frac{[Red]}{[Ox]}\right) \quad (4.1)$$

The Nernst equation describes the relationship between the electromotive force and the concentration of reagents. Here the electromotive force is the electrical potential between the two electrodes and is synonymous with OCP. Half-cell reactions are usually studied using electrochemical cells designed to control the electrochemical reactions that take place, usually by placing two separate electrodes into containers with controlled reagent concentrations. One electrode will act as an anode (oxidation process taking place), the other as the cathode (reduction reactions taking place). The electrodes are connected with an ionically conductive bridge, and the OCP is measured between the electrodes with a voltmeter.

Corrosion is a combination of electrochemical reactions at a metal electrode that degrade its performance properties. A generalized version of common corrosion reactions is given below:

$$Anode\ (oxidation)\ \ M \rightarrow M^{ne+} + ne^{-}$$

$$Cathode\ (reduction)\ H_2O + \frac{1}{2}O_2 + 2e^{-} \rightarrow 2OH^{-}$$

$$H_2O + \frac{1}{2}O_2 + 2e^{-} + M \rightarrow M^{ne+} + ne^{-} + 2OH^{-}$$

The oxidation process is the electrochemical dissolution of the metal, involving the reduction of oxygen facilitated by the net negative charge that develops on the metal electrode surface. Unlike an explicitly designed electrochemical cell used to measure half-cell reactions, there is only one electrode present in corrosion, the metal. Here the anodes are locations on the metal whereby dissolution primarily occurs, with locations on the same metal whereby oxygen reduction is occurring serving as cathodes. There are no separate electrodes for the traditional measurement of potential differences. However, the net potential difference between the corroding metal substrate and a reference electrode can be determined. In addition, unlike traditional cells used to study half-cell reactions, the metal is not at a state close to equilibrium. Instead the OCP of the metal normally shifts continually. However, under some conditions the corrosion process will reach a steady state and the OCP will stabilize.

Electrochemical kinetics are highly dependent on the electrodes where reduction and oxidation reactions are occurring. Thus, the electrochemical kinetics for a specific electrode are generally studied in contrast to the kinetics for chemical process in general.

Although the term electrode kinetics is commonly used, and it should be understood, that these terms are interchangeable and yet do not net the same outcome.

The most widely used electrode kinetic theory is the Butler-Volmer theory:

$$i = i_o \left\{ exp\left[\frac{\alpha_a zF}{RT}\left(E - E_{eq}\right)\right] - exp\left[\frac{-\alpha_c zF}{RT}\left(E - E_{eq}\right)\right]\right\} \quad (4.2)$$

This equation describes the relationship between the electrode kinetics and an applied voltage. Maintaining a potential difference away from equilibrium requires a constant flow of electrons because electrochemical reactions allow current to flow through the cell. Based on the stoichiometric relationship between electrons and the other chemical species, the electrical current is a direct measurement of the electrochemical rates at that applied potential.

Two regions of interest for the Butler-Volmer equation are the low and high overpotential regimes. Overpotential is the difference in the equilibrium or steady state electrode potential and the applied electrode potential. At low overpotentials electrode kinetics follow a linear relationship and thus can be described using Ohms law.[100]

$$i = i_o \frac{zF}{RT}\left(E - E_{eq}\right) \quad (4.3)$$

The linear polarization resistance technique for measuring corrosion kinetics is applicable in this regime, with the resistance used to calculate the exchange current density. This exchange current density is the rate of the oxidation and reduction reactions at equilibrium, which also reflects the rate of corrosion.

$$i = i_o exp\left[\frac{\alpha_a zF}{RT}\left(E - E_{eq}\right)\right] \; when \left(E - E_{eq}\right) \gg \frac{zF}{RT} \quad (4.4)$$

$$i = i_o exp\left[\frac{-\alpha_c zF}{RT}\left(E - E_{eq}\right)\right] \; when \left(E - E_{eq}\right) \ll \frac{-zF}{RT} \quad (4.5)$$

The high overpotential regime follows an exponential form. This regime describes the Tafel relationship empirically derived in the 1900s,[38,39] and allows the calculation of kinetic rates using Tafel slopes, which are the slopes of the plots of overpotential versus the log of current. The exchange current density is calculated from the x-intercept via extrapolation. Tafel analysis is very common in corrosion literature but is potentially misused in some polymer coated substrate examples.

4.2 Materials and Methods

4.2.1 Open Circuit Potential

Open circuit potential measurements were performed on either a Princeton Applied Research VersaSTAT 4 or a Gamry Interface E1000 instrument. A 3 electrode cell was employed, using either a Pt or graphite counter electrode, mirror polished steel working electrodes (400 grit, 600 grit, then 1μm diamond paste), and Ag/AgCl reference electrodes. The electrolyte was 5% w/v NaCl, and the open circuit potential measurement interval was set to every sec.

4.2.2 Tafel Analysis

With the same cell setup for OCP, Tafel analyses were conducted using varied scan rates; most experiments were conducted at 1 mV/sec.

4.2.3 Electrochemical Impedance Spectroscopy

EIS measurements were performed on a Princeton Applied Research VersaSTAT 4 or a Gamry Interface E1000 instrument equipped with a 3 electrode cell. Either Pt or graphite counter electrodes were used. The working electrodes were QD steel coated with PKHH. A Ag/AgCl reference electrode was employed. The electrolyte was 5% w/v NaCl. Impedance data was collected from 100 kHz to 100 Hz. After longer immersion

times the frequency range was increased from100 kHz to 100 mHz to obtain low frequency impedance data for coating resistance evaluation.

4.2.4 Electrochemical Frequency Modulation

4.2.4.1 Variable Base Frequency Experiment

An acetone cleaned QD steel plate was clamped to an 80 mL vertical paint cell and tape used to mask the steel, creating a 6 mm diameter circular region (28.26 mm^2 area). The cell was filled with ca. 40 mL of 5% w/v NaCl solution and allowed to sit for 24 hours to create a uniform layer of loose rust on the steel. A carbon graphite rod and Ag/AgCl in saturated KCl reference electrode was placed in the cell using a rubber stopper with 2 holes. The reference electrode was placed approximately 3 cm from the steel surface and the counter electrode was approximately 5 cm from the surface. An open circuit experiment was conducted to ensure that the steel had reached steady state corrosion so that all EFM spectra reflects data on a surface with equivalent corrosion rates. After confirmation the steel surface had reached steady state corrosion, a Gamry Interface 1000E was used to collect EFM data with frequency multipliers 2 and 5, applied voltage amplitude of 10 mv, 5 cycles of collection, and various base frequencies. The highest base frequency in each sample characterization was tested first, ending with the lowest frequency to minimize the timeframe of applied voltage to the substrate, which is known to alter the corrosion rate.[101] When testing lower frequencies, longer times were allowed between experiments to help facilitate substrate relaxation back to steady state corrosion. Three EFM experiments were conducted at each frequency for reproducibility. Fourier transformation was applied to the current data to produce EFM spectra (i.e. intermodulation peak spectra).

4.2.4.2 Fast Acquisition EFM

Fast acquisition EFM is acquired in a manner similar to normal EFM, except a higher frequency is used and 2 data set are collected. Although 2 spectra are obtained, the higher frequency method decreases the acquisition time by nearly an order of magnitude or more, depending on the frequencies used. For kinetics on the early stages of corrosion, 2 spectra were collected at base frequencies 1 and 2 Hz.

4.2.5 PKHH Film Preparation

The working electrode of QD steel for EIS was coated with PKHH. This was prepared by 8 mil wet drawdowns of 20 wt% solutions in 85:15 bromobenzene:cyclohexanone (mass ratio) and then dried for 6 hours at 75°C. The PKHH solutions were heated to 75°C prior to casting from draw down bars.

4.3 Results and Discussion

4.3.1 Open Circuit Potential

There are several different environmental factors affecting the OCP of a corroding metal substrate; each can be described using the Nernst equation. The concentration of metal ions from the dissolution process, the pH of the electrolyte in contact with the metal, and the concentration of oxidizing species like oxygen will all shift the OCP of the metal. The OCP only stabilizes when all these contributors reach a steady state concentration. The corrosion kinetics, therefore, dictate the OCP of a corroding metal substrate. Monitoring the OCP of a corroding metal over time, along with the OCP at steady state (if possible) can help us to understand the corrosion process occurring. Complimentary experiments, however, are required to fully understand what is occurring.

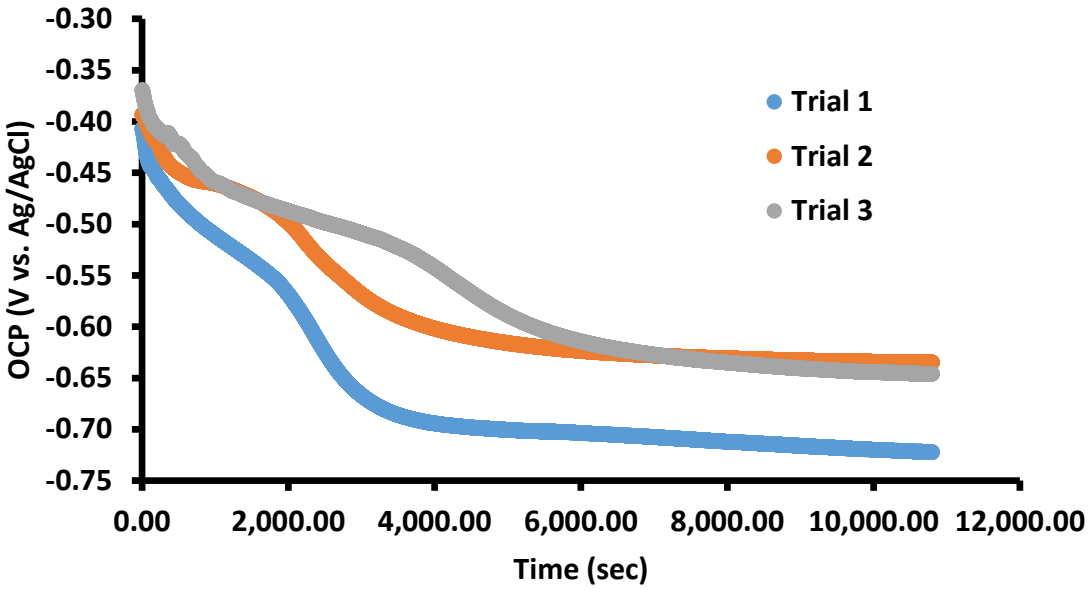

Figure 4.1 Three separate trials of open circuit potential data collection for steel.

Note: Steel was mirror polished and allowed to freely corrode in 5% w/v NaCl. The poor overlap demonstrates the chaotic nature of corrosion.

As seen in Figure 4.1, the OCP for bare steel in 5% w/v/ NaCl generally begins at -390 mV, dropping to between -600 and -750 mV (vs Ag/AgCl). This drop is caused by dissolution of the metal and change in the pH. Introduction of a polymer film is expected to slow the change in OCP, with a slightly higher initial OCP. This is because the metal dissolution process is slowed due to the need for electrolyte to migrate to the metal polymer interface. An additional complication is created when using polymer films. The polymer is primarily non-conductive, creating a capacitor when it is placed between the conductive metal and electrolyte phases. The highly resistive polymer causes a current resistance or IR drop (also termed an Ohmic drop)[102] between the reference and the working electrodes. Ohmic drops result when current flows through a resistive element; thus the measured potential does not correctly represent the electrochemistry of the

substrate. Usually IR drops are calculated based on the resistance and added to the measurement to provide a more accurate potential describing the electrochemistry. Another approach is to redesigned the cell to reduce the resistance and thus reduce the IR drop effects. Many modern potentiostats can correct for IR drops if they are not excessively large. Usually the resistance of the film is used to calculate the IR drop, with the substrate potential recalculated. Simply measuring the potential without considering the effect of coating resistance can result in false conclusions about polarization of the substrate. Allowing for the effects of IR drops are necessary in order to use OCP to indirectly measure ion barrier properties of a film. Additionally, if the polymer has sufficient resistance, any leaking current from the potentiostat measurement can cause charging of the working electrode. This can potentially drive corrosion or artificially protect the substrate from corrosion while simultaneously altering the pH of the interface, leading to film delamination. The highly capacitive behavior of a coated film could also result in continual charging of the surface, causing a constant change in the measured OCP of the system.

Polythiophenes are semi-conductive materials and therefore do not behave like typical polymers. If the metal substrate was charged, polythiophenes would oxidize and reduce accordingly, thereby allowing current to flow through the film.[103] Also, because polythiophenes are redox active materials, some redox reactions should occur at the polymer electrolyte interface as well as the metal polymer interface. Considering the onset oxidation potential of most polythiophenes are higher than steel, we expect the OCP to shift to higher potentials due to polarization. The same results are be expected

for non-conductive films due to concentration shifts;[104] therefore, OCP cannot be the only test used to study the corrosion altering properties of polythiophenes.

4.3.2 Tafel Analysis

Example of Tafel analysis for steel are shown in Figures 4.2 through 4.7. Tafel analysis is highly sensitive. As the corrosion process can change dramatically between environmental conditions, acquiring reproducible Tafel plots for corrosion can be difficult. Tafel analysis requires the corrosion process to be at steady state.[105,106] However, reproducible steady state conditions are almost never obtained except for a freely corroding system. An example of a freely corroding system is the corrosion of steel or iron under acidic conditions. Here the primary reduction reaction is the production of hydrogen by reducing protons.[107] The low pH prevents iron hydroxides from precipitating out of solution, which makes achieving steady state difficult. This simplifies the corrosion process and makes reproducible Tafel analysis possible.

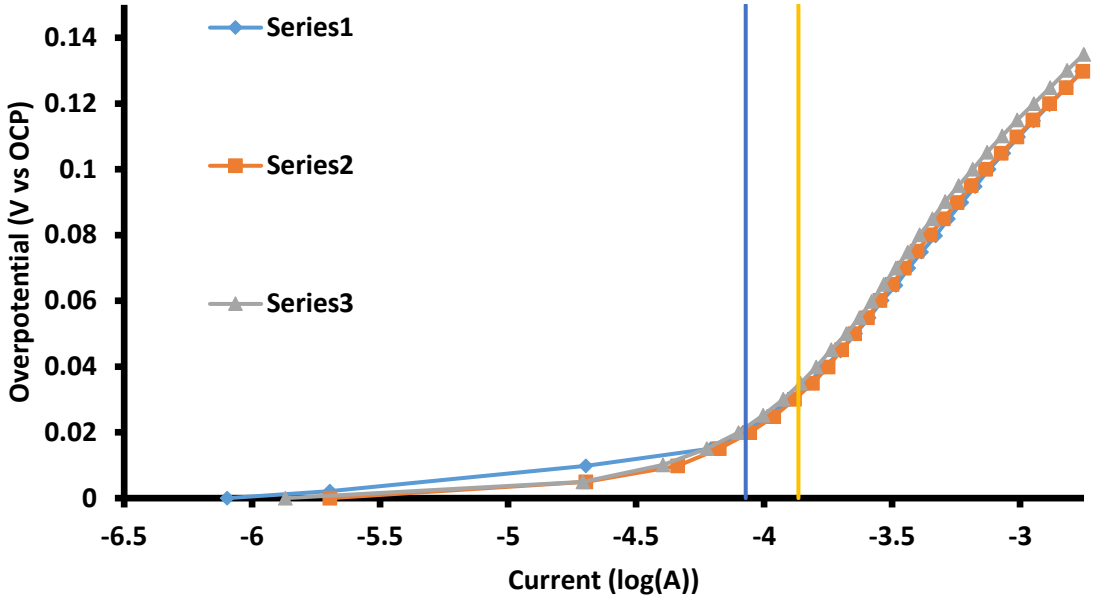

Figure 4.2 Anodic Tafel plot for steel in 1 M HCl.

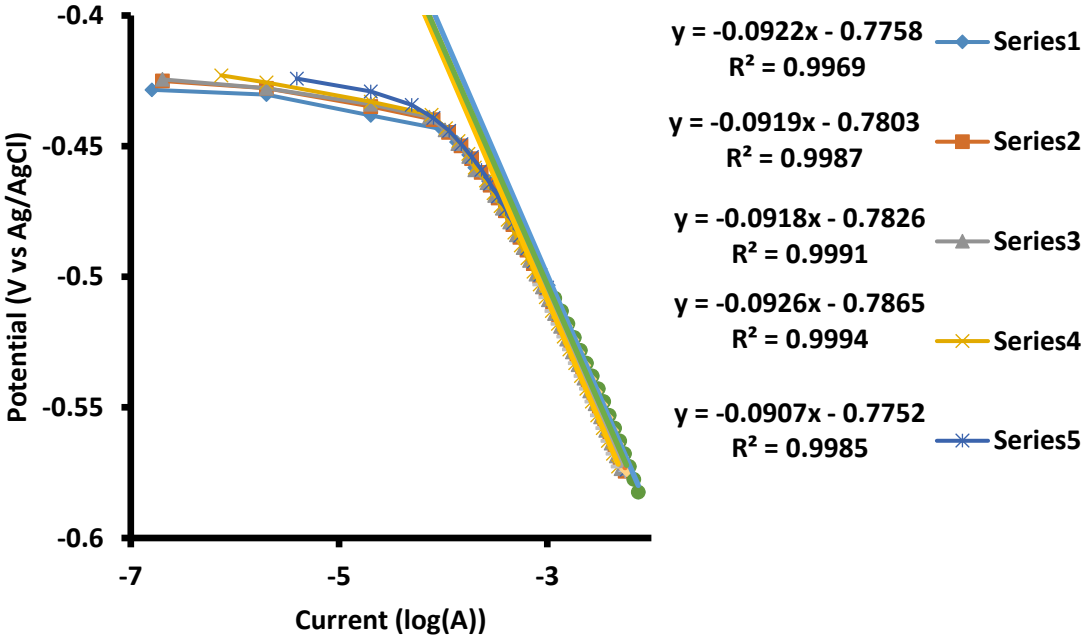

Figure 4.3 Cathodic Tafel plots for steel in 1 M HCl.

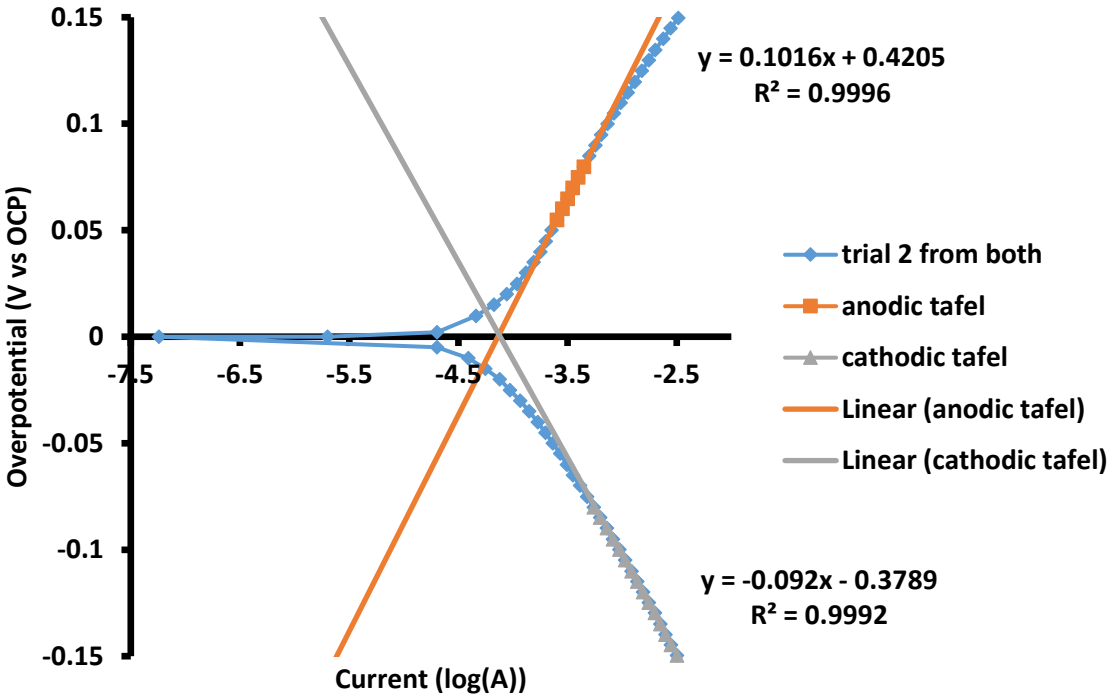

Figure 4.4 Combined anodic and cathodic branches of Tafel plots for steel in 1 M HCl.

Note: This Tafel plot was constructed using two separate sets of data, one for the cathodic branch and one for the anodic branch. Under these conditions the free corrosion of steel gives reproducible and reliable Tafel plots for accurate calculation of corrosion kinetic data.

Figures 4.2 and 4.3 demonstrates the reproducibility of Tafel analysis of steel in 1M HCl. Figure 4.2 shows anodic branches, Figure 4.3 the cathodic branch, with Figure 4.4 displaying the combined branches for comparison. Each branch was collected separately because high overpotentials destroy the substrate and then alter the electrode kinetics, skewing the data.[108]

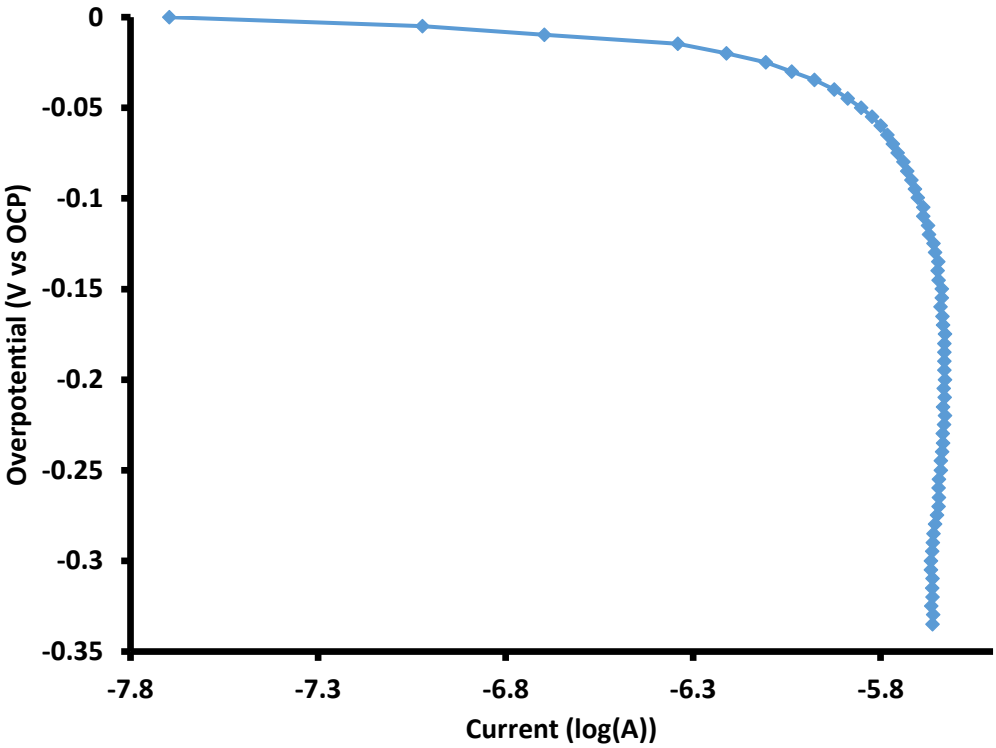

Figure 4.5 Example of a cathodic branch Tafel plot for steel in 5% w/v NaCl

Note: The scan rate was at 1 mv/sec.

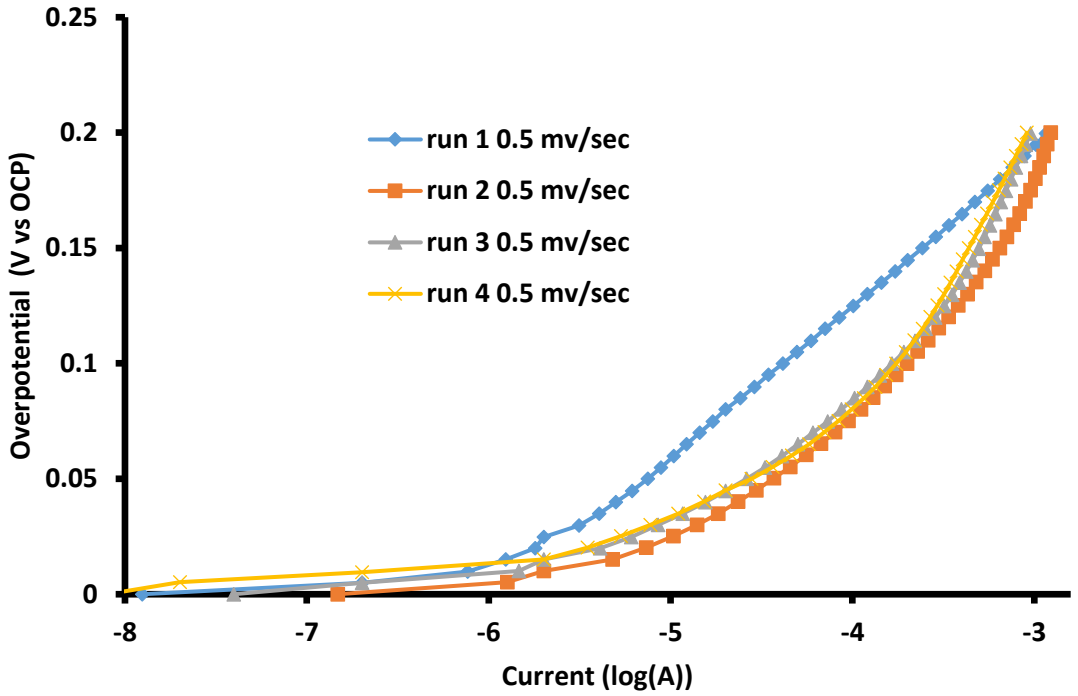

Figure 4.6 Anodic branch Tafel plots for steel in 5% w/v NaCl taken in sequential order.

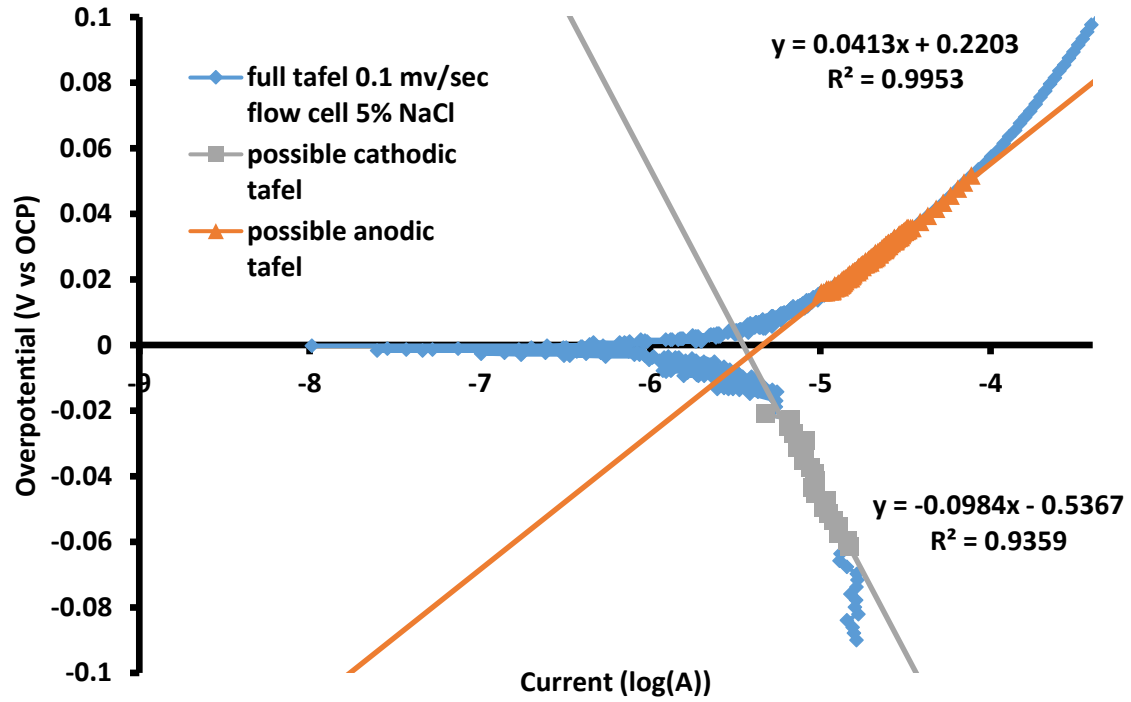

Figure 4.7 Combined Tafel plot for steel in 5% w/v NaCl using a flow cell.

Note: Using a flow cell helps to reduce the effect of diffusion control on the corrosion kinetics.

This work focused on corrosion occurring in salt solutions, as it closely resembles corrosion observed in the field. It should be noted there are significant differences between corrosion in the field and that observed in salt solutions. Nevertheless, this was the standard used in our lab for studying corrosion of coated substrates.

The previous Tafel plots for steel in 5% w/v NaCl exhibit differences between scans for the anodic branches, a behavior not present under acidic (1 M HCl) conditions. This is because forcing the corrosion alters the salt solution properties more than the 1 M HCl system. The excess of protons for the HCl solution makes that pH shifts smaller, whereas the free iron ions precipitate and alter the substrate properties for the NaCl system. The important point is that data collection for full a Tafel analysis will **destroy** the substrate and alter the corrosion properties between scans.

Another difference is observed for cathodic branches. Unlike the 1 M HCl system, the cathodic branch for the 5% w/v NaCl solution exhibits diffusion limits instead of a clear Tafel region.[18] This is because the primary oxidizing agent is oxygen, not protons. Oxygen molecules require time to diffuse to the substrate prior to reduction. The 1 M HCl solution has sufficient proton concentration to circumvent diffusion limitations, thus yielding a clear Tafel region.

For coated substrates diffusion limited Tafel behavior is predicted for both the anodic and cathodic branches. In addition, the highly capacitive behavior of the polymer films would cause capacitive charging, which alters the results. Thus, it is best to scan in both directions when collecting data. Lower scan rates also decrease the effect of capacitive charging. Generally, Tafel analysis is not a good tool for analyzing coated substrates unless the film is thin or has sufficiently low resistance.

For the semi-conductive polythiophene films these problems will not be as significant, thereby making Tafel analysis valid. Also, Tafel slopes of the bare metal are still required in order to perform corrosion rate calculations for coated substrates using AC techniques. The techniques most commonly used to analyze non-conductive coated substrates will be described in the next section.

4.3.3 Electrochemical Impedance Spectroscopy

The biggest disadvantage of Tafel analysis is the destructive nature of the characterization technique. Therefore, linear polarization and electrochemical impedance spectroscopy (EIS) are used to compliment Tafel data. Linear polarization resistance, although less destructive than Tafel analysis, does provide you as much information as EIS; therefore, we focused on the latter technique.

EIS can measure both capacitance and resistance of the corrosion process. The basics of EIS was reviewed in Chapter 1 of this document; here the inherent problems using EIS with coatings is described, especially when studying defect free coatings. Also, the methods for alleviating problems from incorrect assumptions is discussed.

Current literature proposes that electrochemical impedance spectroscopy (EIS) can be used to quantify water uptake, supported by empirical evidence from gravitational and Fourier transform infra-red (FTIR) techniques.[109-111] The method depends on monitoring the capacitance of the coating, which should increase with water uptake due to its higher dielectric constant. However, it is somewhat difficult to obtain coating capacitance from EIS data. Equivalent circuit modeling is sometimes used to determine capacitance from EIS data, but the capacitance varies with the circuit and the fitting parameters or protocol used. Many models use a constant phase element (CPE) for the

capacitor, because the coating does not act as an ideal capacitor. However, obtaining effective capacitance values from CPE parameters is not trivial.[112] Additionally, as coating properties change due to corrosion events, mechanical failure, and varying degrees of hydroplasticization, the effective circuit for the system also changes, further complicating the technique. Although EIS results correlate well with other methods, it is necessary to understand the limitations of using EIS for water uptake analysis.

Based on FTIR data, the following equations relate EIS analysis to coating water uptake.[109]

$$C_p = \frac{1}{2\pi f Z_i} \tag{4.6}$$

$$\phi = \frac{\log\left(\frac{C_p}{C_{po}}\right)}{\log(\varepsilon_w)} \tag{4.7}$$

Here C_p is the coating capacitance, f is the AC frequency, Z_i is the imaginary portion of the impedance measured, ϕ is the volume fraction of water, and ε_w is the dielectric constant for water (78 at standard conditions).[113] Equation 4.7 is the Brasher-Kingbury equation,[114] which we show in Chapter 5 overestimates water content. However, our initial focus will be the limitations of equation 4.6.

Equation 4.6 is simply a different form of the equation for the impedance of an ideal capacitor:

$$Z_C = Z_i = \frac{1}{2\pi f C_{ideal}} \tag{4.8}$$

For an ideal capacitor capacitance only contributes to the imaginary impedance. Examining the imaginary impedance effectively ignores in series resistance. This approach does not account for resistance in parallel. In addition, corrosion cells do not

typically behave as ideal capacitors. This equation is normally used for high frequency data, because in that frequency regime the impedance is dominated by capacitive elements. This is clearly evident in the impedance equations for a simple RC circuit, where the capacitor is parallel with a resistor:

$$Z_r = \frac{\frac{R}{\omega^2 C^2}}{R^2 + \frac{1}{\omega^2 C^2}} \approx R \; when \; \omega \ll RC = \tau \tag{4.9}$$

$$Z_i = \frac{\frac{R^2}{\omega C}}{R^2 + \frac{1}{\omega^2 C^2}} \approx \frac{1}{\omega C} \; when \; \omega \gg RC = \tau \tag{4.10}$$

Here Z_r is the real portion of the impedance, ω is the angular frequency of the applied AC voltage, R is the resistance, and τ is the relaxation time of the curcuit.

These equations are also invalid when the system does not respond in a capacitive manner. The phase angle for an ideal capacitor is -90°; therefore, in order to obtain a good approximation of the capacitance, the frequency should be as large as possible where the phase angle is close to -90°. Figure 4.8 shows EIS data for thermoplastic PKHH films acquired at various frequencies. Note the noise increases with frequency; thus there is a trade-off between using higher frequencies to force the impedance to be dominated by capacitive effects and the S/N of the data.

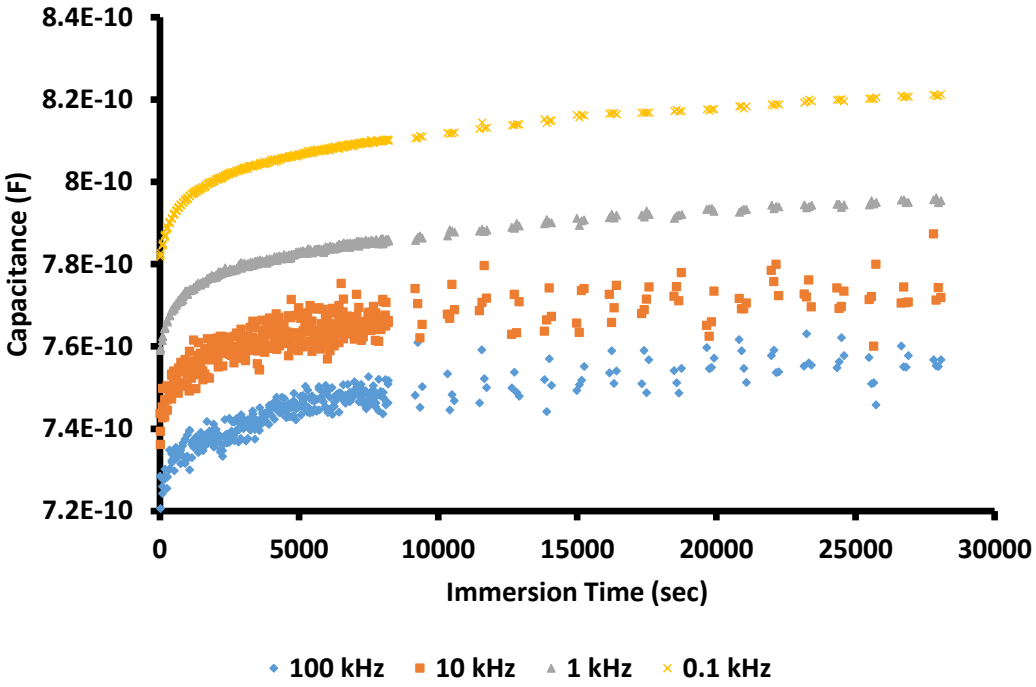

Figure 4.8 Capacitance determined at different frequencies for PKHH on steel.

Note: The capacitance was calculated using equation 4.6. The working electrode was unpolished QD steel with a PKHH film, and the electrolyte was 5% w/v NaCl.

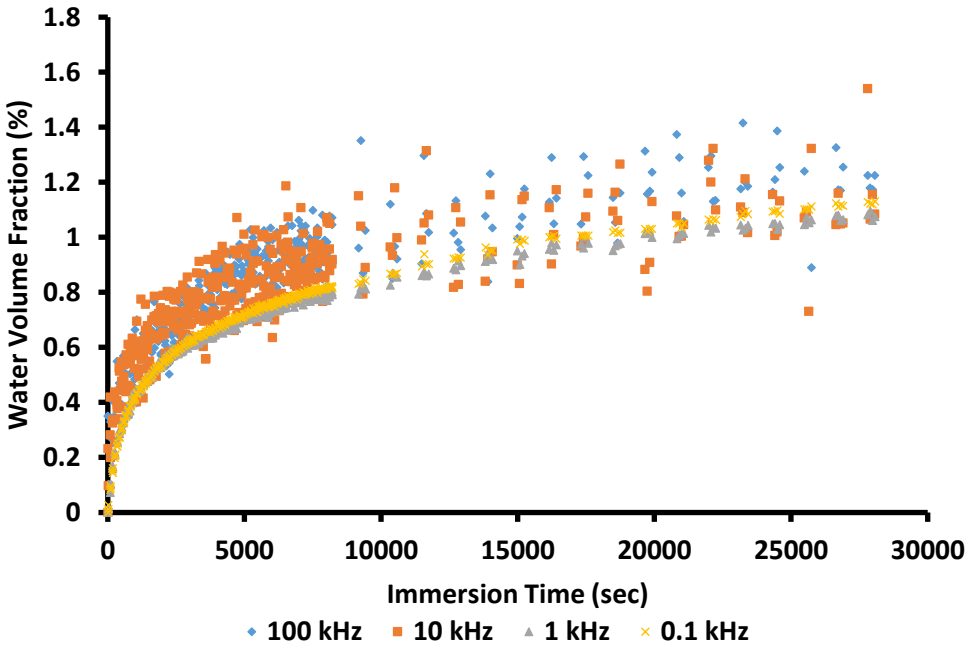

Figure 4.9 The water volume fraction for a substrate bound PKHH using the BK equation (equation 4.7).

Note: The working electrode was immersed in 5% w/v NaCl.

Figure 4.8 shows that measured capacitance varies with frequency. This dependence, however, is minimized by normalization in the Brasher-Kingsbury equation, evident in the plot of water volume fraction versus immersion using capacitance to determine water uptake (Figure 4.9). It was unclear whether this shift in capacitance with frequency is a limitation of the method or the scatter observed at higher frequencies. Additionally, the coating capacitance may be an important parameter to monitor separately; therefore, we investigated methods to correct this trend with frequency.

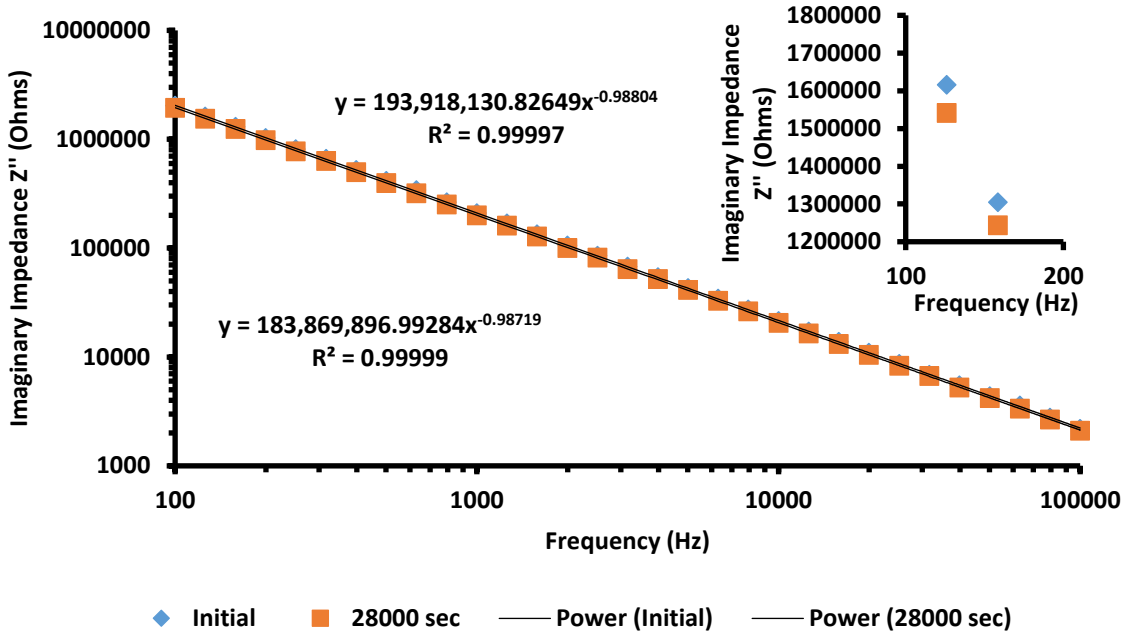

Figure 4.10 Bode plot for the imaginary impedance of a substrate bound PKHH film.

Note: The data was collected directly after immersion and after 28000 sec of immersion in 5% w/v NaCl. A power law fit was used to demonstrate how linear the log log plot is.

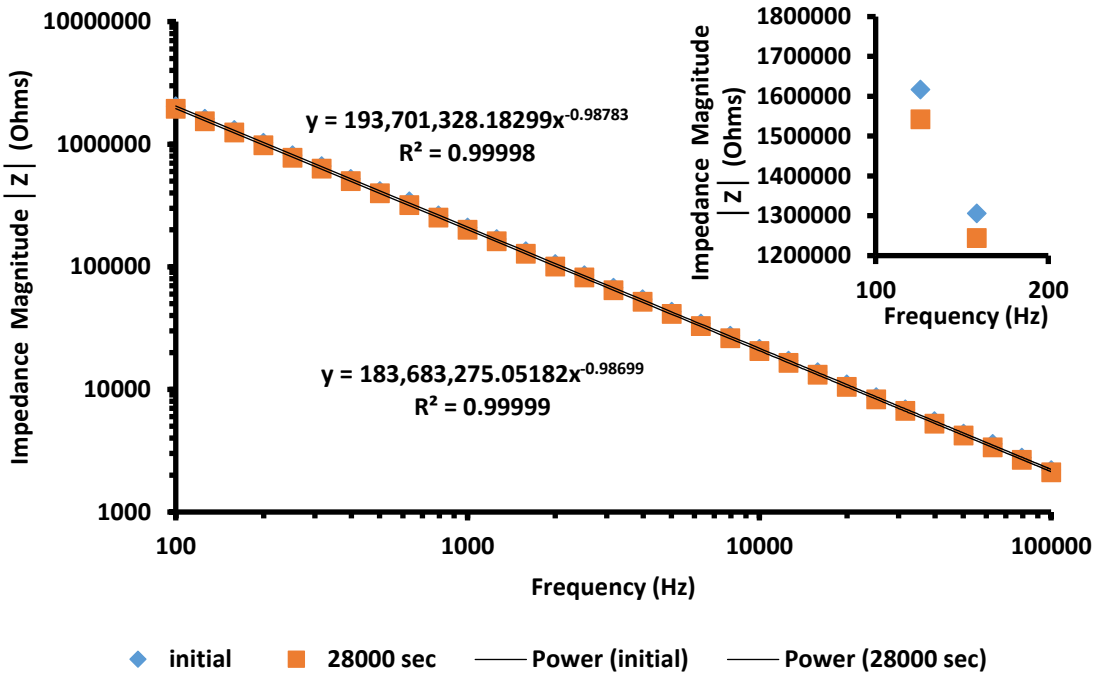

Figure 4.11 Bode plot for the magnitude impedance of a substrate bound PKHH film.

Note: The data was collected directly after immersion and after 28000 sec of immersion in 5% w/v NaCl. A power law fit was used to demonstrate how linear the log log plot is.

Figures 4.10 and 4.11 show Bode plots of the impedance data for a PKHH film immediately after immersion and 28000 sec later using either the imaginary portion of the impedance or the magnitude. If the coating is behaving similarly to a capacitor, Bode plots should exhibit a linear relationship with respect to the log of the frequency with slope of -1. The fits for the Bode plots were excellent, with an empirical relationship with the system impedance at higher frequencies given by:

$$Z = (2\pi f Q)^{-\alpha} \qquad (4.11)$$

Equation 4.11 also is the equation describing a CPE. In this case a plot of CPE capacitance (Q) versus frequency is constant, indicating no frequency dependence (Figure 4.12).

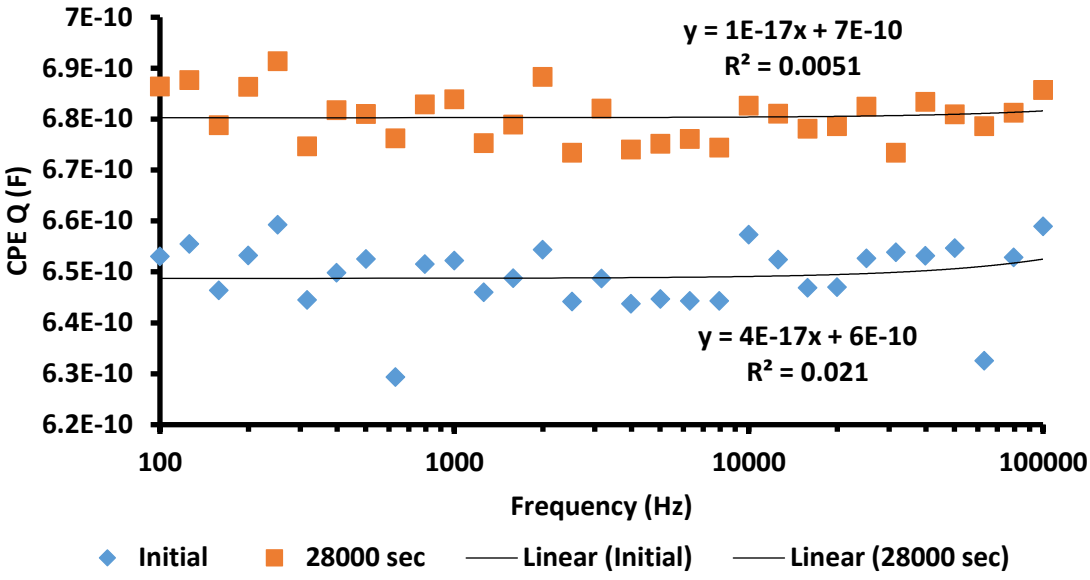

Figure 4.12 The calculated Q value from impedance data of substrate bound PKHH.

Note: The data was collected immediately after immersion (initial) and after 28000 sec of immersion. The slope has no statistically significant difference from zero (p=0.437 and p=0.704 for initial and 28000 sec, respectively). This shows that frequency does not affect the Q value.

It is possible to generate improved water uptake curves using these values. However, Q is fundamentally different from capacitance. Literature concerning the physical interpretations of CPEs suggests they are empirically useful for modeling complex heterogeneous systems.[112] For example, consider the following figure from Hirschorn et al.[112]

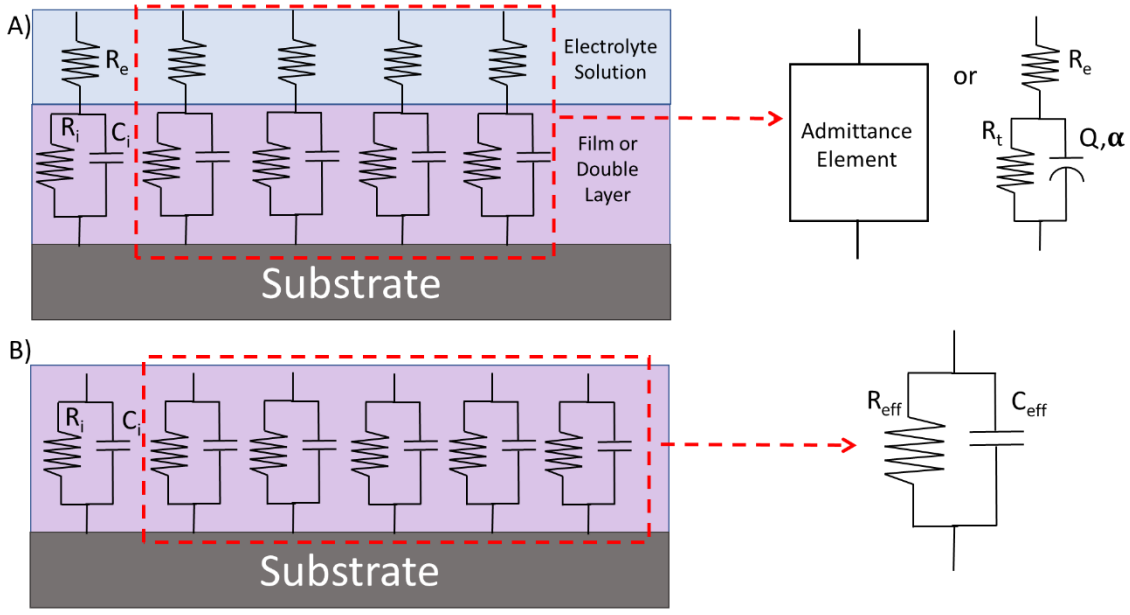

Figure 4.13 Possible circuit diagrams for polymer films based on work from Hirschorn et al.[112]

Note: This figure is a recreation of a figure from Hirschorn et al. with a few additions for clarity. The original caption from Hirschorn et al.[112] is given to avoid misinterpretation "Schematic representation of a surface distribution of time constants: (a) distribution of time constants in the presence of an Ohmic resistance resulting in a distributed time-constant behavior that, for an appropriate time-constant distribution, may be expressed as a CPE; and (b) distribution of time constants in the absence of an Ohmic resistance resulting in an effective RC behavior. The admittance Yi shown in (a) includes the local interfacial and Ohmic contributions."

An electrode surface exhibiting multiple RC circuit behavior can be modeled using a single CPE. To determine the system's effective capacitance requires equations that ultimately depend on this distribution.[112] Fortunately, for a system exhibiting large resistances the effect of this distribution cancels, yielding the following relationship:

$$C_{eff} = Q^{\frac{1}{\alpha}} R_e^{\frac{1-\alpha}{\alpha}} \qquad (4.12)$$

Here R_e is the resistance of the electrolyte above the coating, which can be experimentally measured.[112]

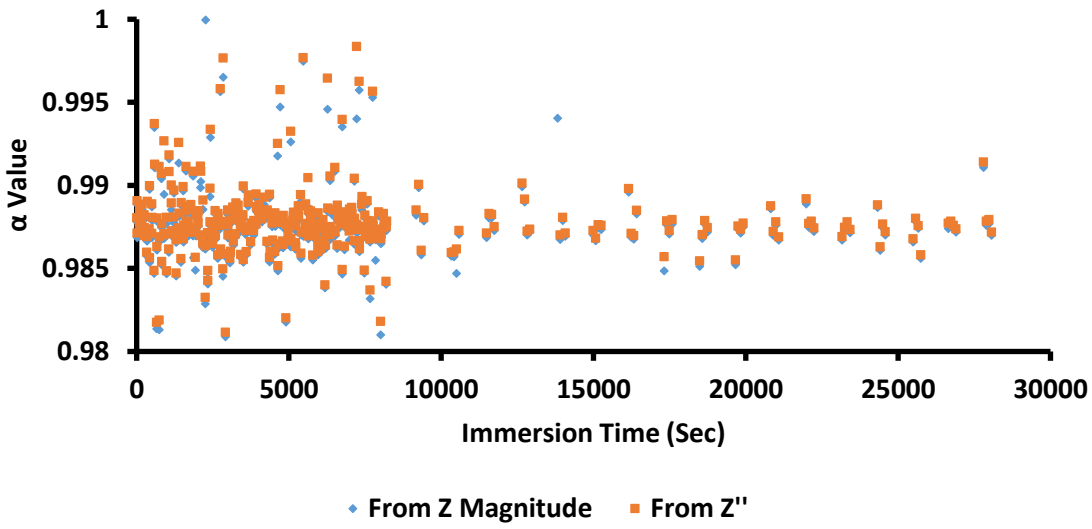

Figure 4.14 Calculated alpha values from impedance data for a substrate bound PKHH film.

Note: There was no statistically significant difference between a linear regression slope and zero (p=0.514 and p=0.944 for calculations from Z mag and Z imaginary, respectively).

The plot of determined alpha values versus immersion time is shown in Figure 4.14. The two series are based on imaginary impedance and magnitude impedance, respectively. This suggests the two Bode plots, when the coating can be considered an ideal capacitor, effectively provide the same results. In addition, it is important to note that the value does not vary with time for the time period used in this work. The physical interpretation of alpha is still not well known, but there seems to be a link between alpha and morphology based on the ability to model different distributions of RC circuits with a CPE. This suggests water uptake for the PKHH films for the time periods used does not change the coating morphology significantly. However, other techniques are required to confirm this.

Equations found in literature approximate the water uptake of coatings, provided they are mostly capacitive. However, they cannot quantify the coating capacitance due to its frequency dependence. The capacitances frequency dependence can be removed by using a CPE, similar to the evaluation of the Bode plots. Until coating morphology is better understood, a coating's effective capacitance can only be approximated using equation 4.12. The alpha values for the PKHH films showed no significant change as a function of immersion time, suggesting the morphology of the coating does not change.

Regarding the use of EIS to evaluate polymer films, we recommend examining alpha values over a defined period of time and then using the equation that estimates capacitance the best. If the film's real capacitance is the object of investigation, equation 4.12 should be used to calculate capacitance from EIS data. Fitting the complete impedance data to a circuit model is not recommended for calculating capacitance for water uptake, as the change in the system is too great for one model to accurately fit the data, although this is normally reported in literature.

4.3.4 Electrochemical Frequency Modulation

Electrochemical frequency modulation is a recent technique that uses applied AC voltages to obtain corrosion kinetic data. The method provides Tafel slopes with significantly less destruction of the substrate. However, the technique has been criticized in the literature for overestimating corrosion rates. In this section we will investigate the primary cause of overestimation along with capacitive charging, and show that it can be compensated to allow more accurate corrosion kinetic data calculations. This will permit the use of EFM for substrates coated with polythiophenes along with faster acquisition times.

The expected current response for electrochemical frequency modulation (EFM) performed at higher frequencies with significant capacitive charging can be modeled using a constant phase element approach. We show the capacitive charging can be calculated using two EFM spectra at high frequencies. EFM fast acquisition times allowed acquisition of corrosion kinetic data during the early stages of steel corrosion in 5% w/v/NaCl solutions before the corrosion cell has stabilized to a relatively constant rate. The method developed could prove useful for studying corrosion cells having poor stability, high capacitance, or particular sensitivity to changes caused by applied voltages.

Electrochemical frequency modulation or potential intermodulation technique[115], is a technique that applies mixed sinusoidal voltages (usually multiples of 2 and 5 Hz) to an electrochemical cell in order to quantify electrode kinetics by modeling the resulting Faradaic distortion, which are current responses that occur at harmonic and intermediated frequencies.[115] The theoretical basis of this method originate from the work of Mèszàros and Dèvay.[116-119] However, their work received little attention Bogaerts and coworkers[115] described an alternative evaluation of the response using Taylor expansions. Most papers published within the last 15 years employing EFM use the approach described in Bogaerts et al. paper published in 2001, which introduced the concept of causality factors as data quality checks.[9]

Capacitance charging is a source of significant error[18,120-122], Bogaerts and coworkers[115] suggested that this could be corrected via subtraction. Many researchers avoid the capacitive charging limitation by using low frequency voltages; however, there are papers reporting the use of higher frequencies.[123] The application of higher frequencies depends on the nature of the system. High capacitance systems like steel in

NaCl solutions require low frequencies to obtain accurate results, although these low frequencies may not possess sufficiently short acquisition times to acquire corrosion kinetic data before the corrosion cell changes due to instability of the cell or it's sensitivity to the applied voltages.

The Thames Rawlins group is currently focused on the early stages of corrosion, especially coated substrates. The lateral diffusion of corrosive species along with the hydration of the polymer suggests the corrosion cell does not stabilize until hours after immersion, at which point it is no longer possible to study the early stages of corrosion. To achieve faster acquisition times the effect of capacitive charging needs to be corrected.[115] In this document we describe how the capacitive charging can be modeled using a constant phase element, with accurate corrosion rates obtained using two EFM spectra collected at higher frequencies. We show that this technique is applicable for corrosion cells that have not stabilized by acquiring corrosion rate data during the early stages of steel corrosion in 5% w/v NaCl. The method described herein will also make determining more accurate corrosion kinetics of polythiophene coated substrates possible.

4.3.4.1 Using a Constant Phase element for Capacitive Charging

The main theoretical work for EFM, and the derivation of most of the important equations for EFM were already described by W. F. Bogaert and coworkers.[115] In their research papers[9,115] they mention that there are some general limitations to the technique that need to be accounted for. One such limitation is the effect of capacitive charging. In the document they mention that when an AC voltage of two mixed frequencies that do not have interference between harmonic and intermodulated frequencies (such as

multiples of 2 and 5) is applied to a corrosion cell, the current should follow a Tafel expression like the following:

$$i = i_{corr}\begin{bmatrix} exp\left(\frac{U_o sin(\omega_1 t) + U_o sin(\omega_2 t)}{\beta_a}\right) \\ -exp\left(\frac{U_o sin(\omega_1 t) + U_o sin(\omega_2 t)}{\beta_c}\right) \end{bmatrix} = i_{corr}\begin{bmatrix} exp\left(\frac{U_o sin(\omega_1 t)}{\beta_a}\right) + exp\left(\frac{U_o sin(\omega_2 t)}{\beta_a}\right) \\ -exp\left(\frac{U_o sin(\omega_1 t)}{\beta_c}\right) - exp\left(\frac{U_o sin(\omega_2 t)}{\beta_c}\right) \end{bmatrix} \quad (4.13)$$

Using a combination of Taylor series expansion, trigonometric identities, and algebra, which were originally derived by W. F. Bogaert and coworkers[115] the following equations can be derived:

$$\begin{aligned} i = i_{fr} + i_{\omega_1} sin(\omega_1 t) + i_{\omega_2} \sin(\omega_2 t) - i_{2\omega_1} cos(2\omega_1 t) \\ - i_{2\omega_2} cos(2\omega_2 t) - i_{3\omega_1} sin(3\omega_1 t) - i_{3\omega_2} sin(3\omega_2 t) \\ + i_{\omega_2 \pm \omega_1} cos(\omega_2 t - \omega_1 t) - i_{\omega_2 \pm \omega_1} cos(\omega_2 t + \omega_1 t) \\ + i_{2\omega_2 \pm \omega_1} sin(2\omega_2 t - \omega_1 t) - i_{2\omega_2 \pm \omega_1} sin(2\omega_2 t + \omega_1 t) \\ + i_{2\omega_1 \pm \omega_2} sin(2\omega_1 t - \omega_2 t) - i_{\omega_1 \pm \omega_2} sin(2\omega_1 t + \omega_2 t) \end{aligned} \quad (4.14)$$

$$- i_{\omega_1 \pm \omega_2} sin(2\omega_1 t + \omega_2 t) \quad (4.15)$$

$$i_{\omega_1} = i_{\omega_2} = i_{corr}\left(\frac{U_o}{\beta_a} + \frac{U_o}{\beta_c}\right) \quad (4.16)$$

$$i_{2\omega_1} = i_{2\omega_2} = \frac{1}{4} i_{corr}\left[\left(\frac{U_o}{\beta_a}\right)^2 - \left(\frac{U_o}{\beta_c}\right)^2\right] \quad (4.17)$$

$$i_{3\omega_1} = i_{3\omega_2} = \frac{1}{24} i_{corr}\left[\left(\frac{U_o}{\beta_a}\right)^3 - \left(\frac{U_o}{\beta_c}\right)^3\right] \quad (4.18)$$

$$i_{\omega_2 \pm \omega_1} = \frac{1}{2} i_{corr} \left[\left(\frac{U_o}{\beta_a} \right)^2 - \left(\frac{U_o}{\beta_c} \right)^2 \right] \tag{4.19}$$

$$i_{2\omega_2 \pm \omega_1} = i_{2\omega_1 \pm \omega_2} = \frac{1}{8} i_{corr} \left[\left(\frac{U_o}{\beta_a} \right)^3 - \left(\frac{U_o}{\beta_c} \right)^3 \right] \tag{4.20}$$

W. F. Bogaerts and coworkers suggested using the following equations for correcting for capacitive charging from EFM experiments:[115]

$$i_{Ct} = U_o \omega C sin(\omega_1 t) \tag{4.21}$$

$$i_{\omega}{}^* = \mathfrak{F}\{i_{\omega} sin(\omega t) + i_{Ct}\} \tag{4.22}$$

$$i_{\omega_1}{}^* = \sqrt{i_{\omega_1,\omega_2}{}^2 + (U_o \omega C)^2} \tag{4.23}$$

$$i_{\omega_2}{}^* = \sqrt{i_{\omega_1,\omega_2}{}^2 + (U_o \omega_2 C)^2} \tag{4.24}$$

where the star for $i_{\omega}{}^*$, $i_{\omega_1}{}^*$, and $i_{\omega_2}{}^*$ denotes measured current amplitude and the subscripts ω_1 and ω_2 denote the frequency for the mixed applied AC voltage for the experiment. We found that the capacitive charging from the double layer was better modeled with a constant phase element as opposed to a pure capacitor. The impedance of a constant phase element is:

$$Z_{CPE} = \frac{1}{Y_{CPE}} = \frac{1}{Q_o (j\omega)^{\alpha}} \tag{4.25}$$

where Y_{CPE} is the admittance, Q_o is a constant analogous to capacitance, $j = \sqrt{-1}$, and α is a constant between 0 and 1 that describes deviation from a pure capacitor. The resulting current function for a constant phase element becomes:

$$i_{CPE} = Y_{CPE} V = Re\{Q_o (j\omega)^{\alpha} (-j U_o e^{j\omega t})\} = U_o \omega^{\alpha} Q_o sin(\omega_1 t + \phi) \tag{4.26}$$

where ϕ is a phase angle $\frac{\pi}{2}\alpha$. Unfortunately using equation 4.26 instead of equation 4.21 for determining ${i_\omega}^*$ with equation 4.22 results in a transcendental function that has no simple analytic solution for α. The lack of an analytical solution makes using equation 4.26 with only a few EFM spectra result in large error, due to having to fit data to solve for α. Instead the following equation was used for the capacitive charging:

$$i_{Ct} = U_o \omega C_\alpha sin(\omega t + \phi) \tag{4.27}$$

where the value C_α would relate to Q_o using a variable r that is meant to partially account for the effect of α on the amplitude of the capacitive charging current.

$$C_\alpha = Q_o r \tag{4.28}$$

Using equation 4.27 with equation 4.22 gives equations 4.28 and 4.29 for the measured primary current amplitude peaks (MPCAPs) ${i_{\omega_1}}^*$ and ${i_{\omega_2}}^*$, respectively.

$${i_{\omega_1}}^* = \sqrt{{i_{\omega_1,\omega_2}}^2 + (U_o \omega_1 C_\alpha)^2 + 2 i_{\omega_1,\omega_2} U_o \omega_1 C_\alpha \cos(\phi)} \tag{4.29}$$

$${i_{\omega_2}}^* = \sqrt{{i_{\omega_1,\omega_2}}^2 + (U_o \omega_2 C_\alpha)^2 + 2 i_{\omega_1,\omega_2} U_o \omega_2 C_\alpha \cos(\phi)} \tag{4.30}$$

As a result, we expect that the relationship between base frequency and the difference between the squared currents from the 2 applied frequencies to follow a quadratic relationship that approaches zero as frequency approaches zero.

$$\begin{aligned} \left({i_{\omega_2}}^*\right)^2 - \left({i_{\omega_1}}^*\right)^2 &= (U_o \omega_2 C_\alpha)^2 - (U_o \omega_1 C_\alpha)^2 + 2 i_{\omega_1,\omega_2} U_o \omega_2 C_\alpha cos(\phi) \\ &\quad -2 i_{\omega_1,\omega_2} U_o \omega_1 C_\alpha cos(\phi) \\ &= {U_o}^2 {C_\alpha}^2 \left({n_{\omega_2}}^2 - {n_{\omega_1}}^2\right) {\omega_b}^2 + 2 i_{\omega_1,\omega_2} U_o C_\alpha cos(\phi) \left(n_{\omega_2} - n_{\omega_1}\right) \omega_b \\ &= A {\omega_b}^2 + B \omega_b \end{aligned} \tag{4.31}$$

where the base frequency ω_b is related to frequencies ω_b and ω_b by equation 4.32:

$$\omega_1 = n_{\omega_1} \omega_b \; and \; \omega_2 = n_{\omega_2} \omega_b \tag{4.32}$$

Equations 4.29, 4.30, and 4.31 were the basis for correcting for capacitive charging current during fast acquisition EFM when monitoring early stages of corrosion of steel in 5% w/v NaCl solutions.

4.3.4.2 Solving for Faradaic Current Amplitude

For situations where taking many EFM spectra is applicable, such as if the experimenter only wishes to correct for capacitive charging or only wishes to use higher frequencies to reduce perturbation of the substrate, equations 4.29 and 4.30 can be used. They show that the squared MPCAPs have the same y intercept of ${i_{\omega_1,\omega_2}}^2$ when plotted vs frequency (base or otherwise). For fast acquisition EFM, equations 4.29 and 4.30 need further evaluation for accuracy, which was shown by how well equation 4.31 can be used to correct for capacitive charging. Solving for the theoretical Faradaic current amplitude i_{ω_1,ω_2} was accomplished by taking advantage of the relationship between the difference in squared MPCAPs $\left({i_{\omega_2}}^*\right)^2 - \left({i_{\omega_1}}^*\right)^2$ and the applied base frequency. Equation 4.31 shows that the squared difference in MPCAPs (SDMPCAPs) should follow quadratic relationships with base frequency and should have a y intercept of zero. Also, simple algebraic manipulation of equation 4.31 shows that the quadratic coefficients should follow:

$$A = {U_o}^2 {C_\alpha}^2 \left({n_{\omega_2}}^2 - {n_{\omega_1}}^2\right) \tag{4.33}$$

$$\therefore\ C_\alpha = \sqrt{\frac{A}{{U_o}^2\left({n_{\omega_2}}^2 - {n_{\omega_1}}^2\right)}} \tag{4.34}$$

$$B = 2 i_{\omega_1,\omega_2} U_o C_\alpha cos(\phi)\left(n_{\omega_2} - n_{\omega_1}\right) \tag{4.35}$$

$$\therefore 2i_{\omega_1,\omega_2}U_oC_\alpha cos(\phi) = \frac{B}{n_{\omega_2} - n_{\omega_1}} \tag{4.36}$$

$$\therefore {i_{\omega_1}}^* = \sqrt{{i_{\omega_1,\omega_2}}^2 + \left(U_o\omega_1\sqrt{\frac{A}{{U_o}^2\left({n_{\omega_2}}^2 - {n_{\omega_1}}^2\right)}}\right)^2} + \frac{B\omega_1}{n_{\omega_2} - n_{\omega_1}} \tag{4.37}$$

$$\therefore i_{\omega_1,\omega_2} = \sqrt{\left({i_{\omega_1}}^*\right)^2 - {\omega_1}^2\frac{A}{\left({n_{\omega_1}}^2 - {n_{\omega_2}}^2\right)}} - \frac{B\omega_1}{n_{\omega_1} - n_{\omega_2}} \tag{4.38}$$

Equation 4.38 has little practical application but can be used to better evaluate equations 4.29 and 4.30. Using equation 4.38 did not fully account for the capacitive charging from the double layer (see section 4.3.4.3) but was sufficient for removing the frequency dependence on calculated corrosion current. To better account for the capacitive charging the relationship shown in equation 4.28 must be given more attention. The variable r is not technically a constant, therefore, ${C_\alpha}^2$ cannot completely be factored out to give equation 4.33. From equation 4.26 we expect that the variable r is in some way related to frequency, and that C_α will be different for ω_1 and ω_2. We also know that technically the variable r will be different in the term $2i_{\omega_1,\omega_2}U_o\omega_1C_\alpha cos(\phi)$ vs the term $(U_o\omega_1C_\alpha)^2$ because one term has the frequency squared and the other does not. The result is the squared MPCAPs will be close to a quadratic relationship with base frequency, but the quadratic coefficients will not all be completely described using equations 4.29 and 4.30.

$$\begin{aligned}\left({i_{\omega_1}}^*\right)^2 &= {i_{\omega_1,\omega_2}}^2 + (U_o\omega_1C_\alpha)^2 + 2i_{\omega_1,\omega_2}U_o\omega_1C_\alpha cos(\phi)\\ &= A_{i\omega1}{\omega_b}^2 + B_{i\omega1}\omega_b + {i_{\omega_1,\omega_2}}^2\end{aligned} \tag{4.39}$$

$$\begin{aligned}\left({i_{\omega_2}}^*\right)^2 &= {i_{\omega_1,\omega_2}}^2 + (U_o\omega_2C_\alpha)^2 + 2i_{\omega_1,\omega_2}U_o\omega_2C_\alpha cos(\phi)\\ &= A_{i\omega2}{\omega_b}^2 + B_{i\omega2}\omega_b + {i_{\omega_1,\omega_2}}^2\end{aligned} \tag{4.40}$$

$$\left(i_{\omega_1}{}^{*}\right)_B{}^{2} = i_{\omega_1,\omega_2}{}^{2} + (U_o\omega_{1B}C_\alpha)^2 + 2i_{\omega_1,\omega_2}U_o\omega_{1B}C_\alpha cos(\phi)$$
$$= A_{i\omega1}\omega_{bB}{}^{2} + B_{i\omega1}\omega_{bB} + i_{\omega_1,\omega_2}{}^{2} \quad (4.41)$$

$$\left(i_{\omega_2}{}^{*}\right)_B{}^{2} = i_{\omega_1,\omega_2}{}^{2} + (U_o\omega_{2B}C_\alpha)^2 + 2i_{\omega_1,\omega_2}U_o\omega_{2B}C_\alpha cos(\phi)$$
$$= A_{i\omega2}\omega_{bB}{}^{2} + B_{i\omega2}\omega_{bB} + i_{\omega_1,\omega_2}{}^{2} \quad (4.42)$$

where the subscript B denotes results from an EFM spectrum collected at a different base frequency. This gives 4 equations and 5 unknowns. At least one other equation is required to solve for i_{ω_1,ω_2}. Using the same estimation when deriving equation 4.33, where C_α is a constant for all coefficients, the following relationships will be true.

$$\frac{A_{i\omega2}}{A_{i\omega1}} = \frac{n_{\omega_2}{}^{2}}{n_{\omega_1}{}^{2}} = 6.25 \; for \; n_{\omega_2} = 5 \; and \; n_{\omega_2} = 2 \quad (4.43)$$

$$\frac{B_{i\omega2}}{B_{i\omega1}} = \frac{n_{\omega_2}}{n_{\omega_1}} = 2.5 \; for \; n_{\omega_2} = 5 \; and \; n_{\omega_2} = 2 \quad (4.44)$$

Empirically the relationships in equations 4.43 and 4.44 do not match theoretical values (see results and discussion) but calculating i_{ω_1,ω_2} for each relationship and averaging results can give accurate estimations used for calculating corrosion currents so long as C_α does not deviate too much. Solving for i_{ω_1,ω_2} using equation 4.43 as the 5th equation tended to underestimate i_{ω_1,ω_2}, whereas using equation 4.44 tended to overestimate i_{ω_1,ω_2}, and in some situations solving using equation 4.43 can give a negative value for i_{ω_1,ω_2}, which is intuitively not a true value of i_{ω_1,ω_2}. Deviations of C_α will have a larger effect on the error when solving with equation 4.43, which means that there will be situations when even averaging the results with equations 4.43 and 4.44 gives a net negative value for i_{ω_1,ω_2}. To better account for the larger error introduced from variable

r on the coefficients $A_{i\omega1}$ and $A_{i\omega2}$ compared to coefficients $B_{i\omega1}$ and $B_{i\omega2}$ the following relationship was proposed:

$$C_{\alpha\omega1}R = C_{\alpha\omega2} \tag{4.45}$$

It follows from equation 32 that equations 30 and 31 become:

$$\frac{A_{i\omega2}}{A_{i\omega1}} = \frac{{n_{\omega_2}}^2 R^2}{{n_{\omega_1}}^2} = 6.25R^2 \; for \; n_{\omega_2} = 5 \; and \; n_{\omega_2} = 2 \tag{4.46}$$

$$\frac{B_{i\omega2}}{B_{i\omega1}} = \frac{n_{\omega_2} R}{n_{\omega_1}} = 2.5R \; for \; n_{\omega_2} = 5 \; and \; n_{\omega_2} = 2 \tag{4.47}$$

This gives 6 unknowns and 6 equations. Solving R involves a solving a cubic function, but only one of the roots makes physical sense. The value for R should be a positive value between 0 and 1, and R cannot equal $\frac{n_{\omega_1}}{n_{\omega_2}}$ because that would give an unidentified value for i_{ω_1,ω_2}. The first root for the cubic function gives a negative value of R and the second root gives $\frac{n_{\omega_1}}{n_{\omega_2}}$, therefore, only the third root for solving R should be used.

Alternatively, the empirically determined relationships can be used to calculate ${i_{\omega_1,\omega_2}}^2$. We suggest trying both to see which gives results that agree best with low frequency EFM results. The algebraic steps for solving the 6 equations is shown below. First equations 4.39 and 4.41 can be rearranged to give:

$$A_{i\omega1} = \frac{{\left({i_{\omega_1}}^*\right)_B}^2 - B_{i\omega1}\omega_{bB} - {i_{\omega_1,\omega_2}}^2}{{\omega_{bB}}^2} = \frac{\left({i_{\omega_1}}^*\right)^2 - B_{i\omega1}\omega_b - {i_{\omega_1,\omega_2}}^2}{{\omega_b}^2} \tag{4.48}$$

$$B_{i\omega1} = \frac{{\left({i_{\omega_1}}^*\right)_B}^2 - A_{i\omega1}{\omega_{bB}}^2 - {i_{\omega_1,\omega_2}}^2}{\omega_{bB}} = \frac{\left({i_{\omega_1}}^*\right)^2 - A_{i\omega1}{\omega_b}^2 - {i_{\omega_1,\omega_2}}^2}{\omega_b} \tag{4.49}$$

and by combining equation 4.48 or 4.49 (the halves rearranged from equation 4.41) with equation 4.39 we get:

$$\left(i_{\omega_1}{}^*\right)^2 = \frac{\left(i_{\omega_1}{}^*\right)_B{}^2 - B_{i\omega 1}\omega_{bB} - i_{\omega_1,\omega_2}{}^2}{\omega_{bB}{}^2}\omega_b{}^2 + B_{i\omega 1}\omega_b + i_{\omega_1,\omega_2}{}^2 \qquad (4.50)$$

$$\left(i_{\omega_1}{}^*\right)^2 = A_{i\omega 1}\omega_b{}^2 + \frac{\left(i_{\omega_1}{}^*\right)_B{}^2 - A_{i\omega 1}\omega_{bB}{}^2 - i_{\omega_1,\omega_2}{}^2}{\omega_{bB}}\omega_b + i_{\omega_1,\omega_2}{}^2 \qquad (4.51)$$

Placing all $B_{i\omega 1}$ terms from equation 4.50 on the left side yields:

$$B_{i\omega 1}\omega_b - B_{i\omega 1}\frac{\omega_b{}^2\omega_{bB}}{\omega_{bB}{}^2} = \left(i_{\omega_1}{}^*\right)^2 - \frac{\left(i_{\omega_1}{}^*\right)_B{}^2\omega_b{}^2}{\omega_{bB}{}^2} + \frac{\omega_b{}^2 i_{\omega_1,\omega_2}{}^2}{\omega_{bB}{}^2} - i_{\omega_1,\omega_2}{}^2 \qquad (4.52)$$

and an analogous derivation gives equation 4.53 by starting with equations 27 and 29:

$$B_{i\omega 2}\omega_b - B_{i\omega 2}\frac{\omega_b{}^2\omega_{bB}}{\omega_{bB}{}^2} = \left(i_{\omega_2}{}^*\right)^2 - \frac{\left(i_{\omega_2}{}^*\right)_B{}^2\omega_b{}^2}{\omega_{bB}{}^2} + \frac{\omega_b{}^2 i_{\omega_1,\omega_2}{}^2}{\omega_{bB}{}^2} - i_{\omega_1,\omega_2}{}^2 \qquad (4.53)$$

Similar to equations 4.52 and 4.53, equations 4.54 and 4.55 can be derived:

$$A_{i\omega 1}\omega_b{}^2 - A_{i\omega 1}\frac{\omega_b\omega_{bB}{}^2}{\omega_{bB}} = \left(i_{\omega_1}{}^*\right)^2 - \frac{\left(i_{\omega_1}{}^*\right)_B{}^2\omega_b}{\omega_{bB}} + \frac{\omega_b i_{\omega_1,\omega_2}{}^2}{\omega_{bB}} - i_{\omega_1,\omega_2}{}^2 \qquad (4.54)$$

$$A_{i\omega 2}\omega_b{}^2 - A_{i\omega 2}\frac{\omega_b\omega_{bB}{}^2}{\omega_{bB}} = \left(i_{\omega_2}{}^*\right)^2 - \frac{\left(i_{\omega_2}{}^*\right)_B{}^2\omega_b}{\omega_{bB}} + \frac{\omega_b i_{\omega_1,\omega_2}{}^2}{\omega_{bB}} - i_{\omega_1,\omega_2}{}^2 \qquad (4.55)$$

Dividing equation 4.53 by 4.52 and combining with equation 4.47 gives:

$$\frac{B_{i\omega 2}}{B_{i\omega 1}} = \frac{n_{\omega_2}R}{n_{\omega_1}} = \frac{\left(i_{\omega_2}{}^*\right)^2 - \frac{\left(i_{\omega_2}{}^*\right)_B{}^2\omega_b{}^2}{\omega_{bB}{}^2} + \frac{\omega_b{}^2 i_{\omega_1,\omega_2}{}^2}{\omega_{bB}{}^2} - i_{\omega_1,\omega_2}{}^2}{\left(i_{\omega_1}{}^*\right)^2 - \frac{\left(i_{\omega_1}{}^*\right)_B{}^2\omega_b{}^2}{\omega_{bB}{}^2} + \frac{\omega_b{}^2 i_{\omega_1,\omega_2}{}^2}{\omega_{bB}{}^2} - i_{\omega_1,\omega_2}{}^2} \qquad (4.56)$$

In a similar fashion, dividing equation 4.55 by 4.54 and combining with equation 4.48 gives:

$$\frac{A_{i\omega 2}}{A_{i\omega 1}} = \frac{n_{\omega_2}{}^2R^2}{n_{\omega_1}{}^2} = \frac{\left(i_{\omega_2}{}^*\right)^2 - \frac{\left(i_{\omega_2}{}^*\right)_B{}^2\omega_b}{\omega_{bB}} + \frac{\omega_b i_{\omega_1,\omega_2}{}^2}{\omega_{bB}} - i_{\omega_1,\omega_2}{}^2}{\left(i_{\omega_1}{}^*\right)^2 - \frac{\left(i_{\omega_1}{}^*\right)_B{}^2\omega_b}{\omega_{bB}} + \frac{\omega_b i_{\omega_1,\omega_2}{}^2}{\omega_{bB}} - i_{\omega_1,\omega_2}{}^2} \qquad (4.57)$$

Taking equation 4.56 and multiplying by the denominator of the right side and dividing by $\frac{n_{\omega_2}R}{n_{\omega_1}}$ results in:

$$\left(i_{\omega_1}{}^*\right)^2 - \frac{\left(i_{\omega_1}{}^*\right)_B{}^2\omega_b{}^2}{\omega_{bB}{}^2} + \frac{\omega_b{}^2 i_{\omega_1,\omega_2}{}^2}{\omega_{bB}{}^2} - i_{\omega_1,\omega_2}{}^2 = \frac{\left(i_{\omega_2}{}^*\right)^2 - \frac{\left(i_{\omega_2}{}^*\right)_B{}^2\omega_b{}^2}{\omega_{bB}{}^2} + \frac{\omega_b{}^2 i_{\omega_1,\omega_2}{}^2}{\omega_{bB}{}^2} - i_{\omega_1,\omega_2}{}^2}{\frac{n_{\omega_2}R}{n_{\omega_1}}} \tag{4.58}$$

And similarly, equation 4.57 can be rearranged:

$$\left(i_{\omega_1}{}^*\right)^2 - \frac{\left(i_{\omega_1}{}^*\right)_B{}^2\omega_b}{\omega_{bB}} + \frac{\omega_b i_{\omega_1,\omega_2}{}^2}{\omega_{bB}} - i_{\omega_1,\omega_2}{}^2 = \frac{\left(i_{\omega_2}{}^*\right)^2 - \frac{\left(i_{\omega_2}{}^*\right)_B{}^2\omega_b}{\omega_{bB}} + \frac{\omega_b i_{\omega_1,\omega_2}{}^2}{\omega_{bB}} - i_{\omega_1,\omega_2}{}^2}{\frac{n_{\omega_2}{}^2R^2}{n_{\omega_1}{}^2}} \tag{4.59}$$

Equations 4.58 and 4.59 can be solved for $i_{\omega_1,\omega_2}{}^2$ to give equations 4.60 and 4.61:

$$i_{\omega_1,\omega_2}{}^2 = \frac{\frac{\left(i_{\omega_2}{}^*\right)^2 - \frac{\left(i_{\omega_2}{}^*\right)_B{}^2\omega_b{}^2}{\omega_{bB}{}^2}}{\frac{n_{\omega_2}R}{n_{\omega_1}}} - \left(i_{\omega_1}{}^*\right)^2 + \frac{\left(i_{\omega_1}{}^*\right)_B{}^2\omega_b{}^2}{\omega_{bB}{}^2}}{\frac{\omega_b{}^2}{\omega_{bB}{}^2} - 1 - \frac{\frac{\omega_b{}^2}{\omega_{bB}{}^2} - 1}{\frac{n_{\omega_2}R}{n_{\omega_1}}}} \tag{4.60}$$

$$i_{\omega_1,\omega_2}{}^2 = \frac{\frac{\left(i_{\omega_2}{}^*\right)^2 - \frac{\left(i_{\omega_2}{}^*\right)_B{}^2\omega_b}{\omega_{bB}}}{\frac{n_{\omega_2}{}^2R^2}{n_{\omega_1}{}^2}} - \left(i_{\omega_1}{}^*\right)^2 - \frac{\left(i_{\omega_1}{}^*\right)_B{}^2\omega_b}{\omega_{bB}}}{\frac{\omega_b}{\omega_{bB}} - 1 - \frac{\frac{\omega_b}{\omega_{bB}} - 1}{\frac{n_{\omega_2}{}^2R^2}{n_{\omega_1}{}^2}}} \tag{4.61}$$

The final equations 4.60 and 4.61 allowed good estimations of i_{ω_1,ω_2} for calculating corrosion current when conducting fast acquisition EFM on early corrosion of a steel substrate in 5% w/v NaCl. The variable R can be estimated by taking multiple EFM spectra after the cell has stabilized and averaging the results of using equations 4.46 and 4.47, or it can be estimated using the two EFM spectra from fast acquisition by solving a cubic function. More accurate calculations would require a better approximation the transcendental equation resulting from equation 4.26:

$$(i_{\omega}{}^{*})^2 = {i_{\omega_1,\omega_2}}^2 + (U_o\omega^{\alpha}Q_o)^2 + 2i_{\omega_1,\omega_2}U_o\omega^{\alpha}Q_o\cos\left(\frac{\pi}{2}\alpha\right) \qquad (4.62)$$

4.3.4.3 Applicability of Using a Constant Phase Element for Correcting of Capacitive Charging

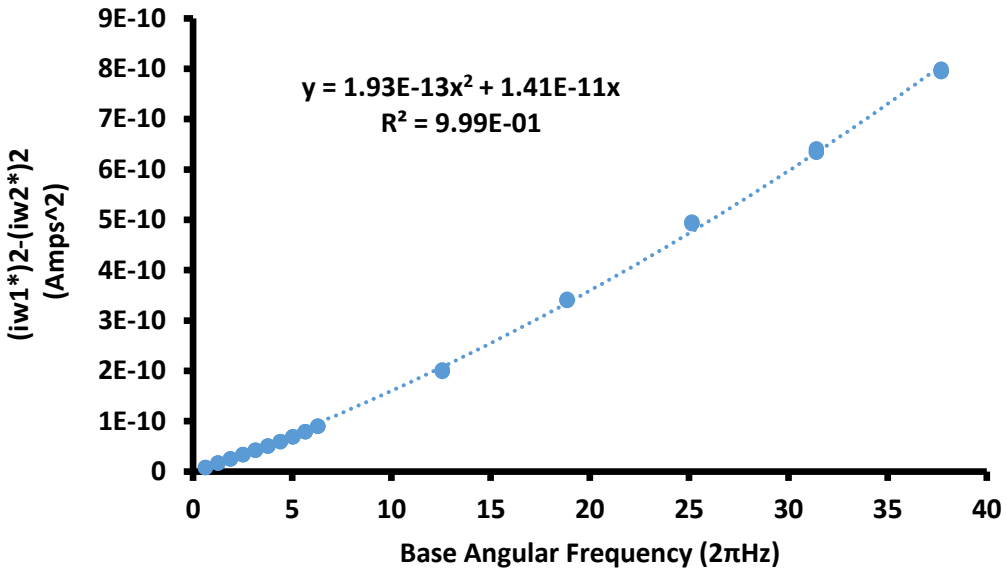

Figure 4.15 A plot of the squared difference in the primary modulation current peaks (SDMPCAPs) vs the applied base angular frequency for steel.

Note: All data was collected on a single acetone cleaned steel panel that has reached steady state corrosion by immersing for 24 hr in 5% v/w NaCl solution. Each base frequency was based upon 3 EFM spectra collected and all 3 points are shown. The excellent overlap in points demonstrates the accuracy and reproducibility of the capacitive charging event described by a quadratic relationship described in section 4.3.4.1.

The MPCAPs (labeled i_{w1} and i_{w2}) from the EFM spectra are squared and the absolute difference is plotted vs the base angular frequency (base frequency * 2π) to produce Figure 4.15. According to equation 4.31 derived above, the SDMPCAP should follow a quadratic relationship with base angular frequency that approaches zero. The excellent R^2 confirms a quadratic relationship as expected. Note that there were 3 EFM spectra collected at each base frequency, and all points are plotted in Figure 4.15. The high degree of reproducibility in the capacitive charging effect causes all 3 points at each frequency to overlap and appear like a single point on the graph.

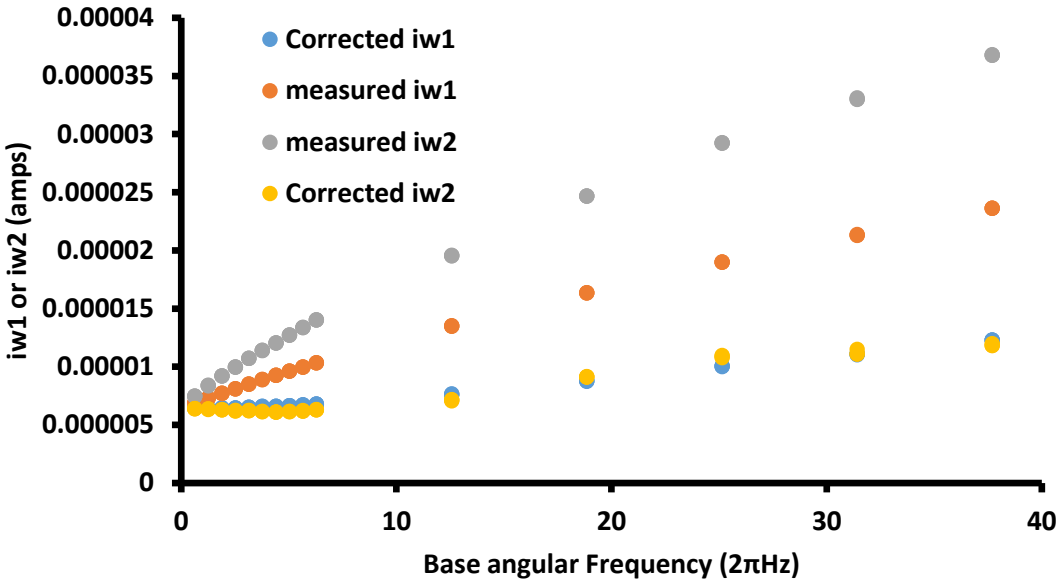

Figure 4.16 A plot of the MPCAPs and corrected MPCAPs vs the applied base angular frequency for steel.

Note: All data was collected from a single acetone cleaned steel panel that has reached steady state corrosion by immersing for 24 hr in 5% v/w NaCl solution. The capacitive charging was mostly removed by applying the general theory described in section 4.3.4.2.

By fitting the SDMPCAP vs base angular frequency we can extract the quadratic coefficients and use them to correct for the capacitive charging via equation 4.38 derived in section 4.2.4.2. The results are shown in Figure 4.16, a plot of the MPCAPs before and after correction. The frequency dependence in nearly gone, and both MPCAPs overlap, as expected after correction. The small dependence on frequency is due to the estimations used to derive equation 4.38 described above. Despite the estimations and the presence of a small frequency dependence on the MPCAPs, the resulting calculated corrosion currents lost their frequency dependence. The ability to mostly correct for the

capacitive charging using equation 4.38 help to validate how well equation 4.27 approximates the capacitive charging from the double layer.

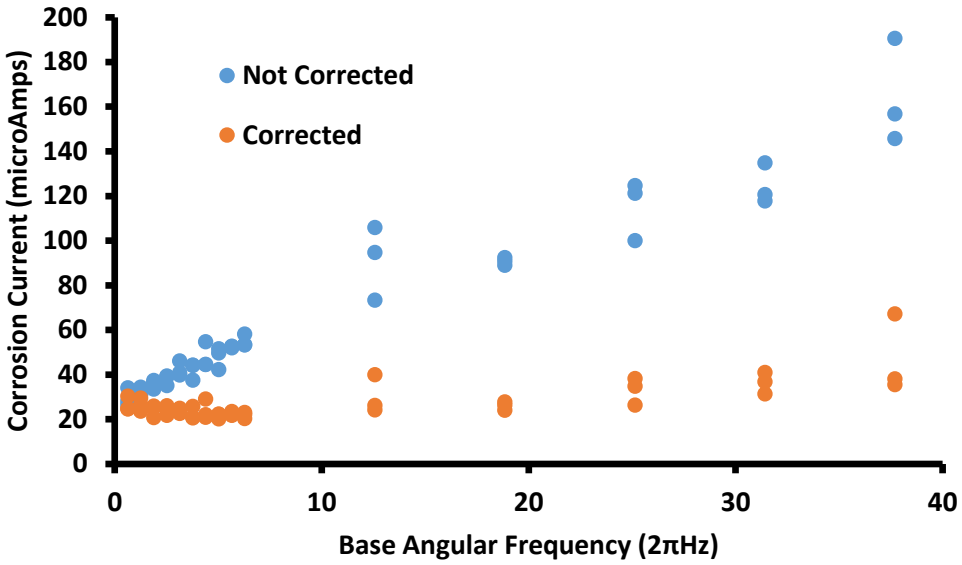

Figure 4.17 The calculated corrosion current before and after correcting for capacitive charging vs applied base angular frequency.

Note: The capacitive charging was corrected using a constant phase element as described in section 4.3.4.2. All data was collected from a single acetone cleaned steel panel that has reached steady state corrosion by immersing for 24 hr in 5% v/w NaCl solution. The removal of frequency dependence shows how well the correction works for calculating accurate corrosion currents at higher frequencies. All corrosion rates were calculated using the active corrosion equations.

The corrected theoretical Faradaic current i_{ω_1,ω_2} calculated using equation 4.38 were used to calculate the corrosion currents using the regular EFM equations previous derived by W. Bogaerts et al. in their papers.[115] We applied the equation for active corrosion for calculating the corrosion currents seen in Figure 4.17. Although corrosion of steel in NaCl solutions are usually diffusion controlled, our Tafel plots from previous experiments (not shown) support that under our conditions the corrosion of steel followed

a mixed kinetic control mechanism. To our knowledge, there does not exist a derived equation accurate for calculating corrosion currents for mixed kinetic controlled corrosion. Under mixed kinetic controlled corrosion, active corrosion dominates at low overpotentials and diffusion control dominates at high overpotentials, therefore, we used an equation for active corrosion because the applied voltage for EFM experiments are low. The equations for active corrosion have been used for studying steel corrosion in NaCl solutions before with good accuracy.[124] Using the Faradaic current from equation 4.38 for calculating the corrosion current, resulted in a loss of frequency dependence (Figure 4.17), suggesting that the slight frequency dependence in the Faradaic current from equation 4.38 was negligible during calculations for the corrosion currents unless very high frequencies were applied to the substrate (which we have not tested). If the same Faradaic currents were used in the equation for diffusion and passive controlled corrosion the frequency dependence would still be removed mathematically. The results reveal that empirically, correcting for capacitive charging by modeling the capacitive charging with a CPE as described in sections 4.3.4.1 and 4.3.4.2 was sufficient for developing a method for faster EFM acquisition. It should be noted that even though the frequency dependence on corrosion current is diminished, the error in the measurements increases, therefore, caution should be taken when trying to use ever increasing higher frequencies specific to determining corrosion currents. Faster acquisition EFM is best used for looking at trends in corrosion when the corrosion is not stable, steady state has not been established, and should be complimented with classical electrochemical techniques (normal EFM, EIS, Tafel analysis, etc.) when the corrosion is stable.

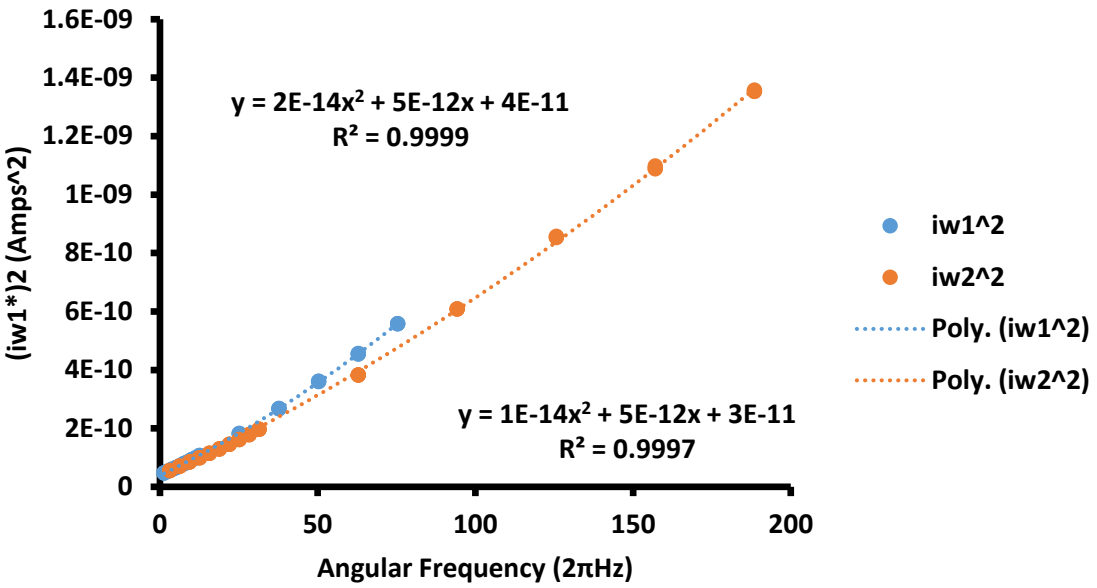

Figure 4.18 The squared MPCAPs vs the corresponding angular frequency (base angular frequency times frequency multiplier) for steel.

Note: All data was collected from a single acetone cleaned steel panel that has reached steady state corrosion by immersing for 24 hr in 5% v/w NaCl solution. The deviation demonstrates that modeling the capacitive charging with a simple CPE does not completely describe the effect. There is an apparent frequency dependence on the 2nd order coefficient.

Figure 4.18 was generated by plotting the squared MPCAP values from EFM spectra vs the angular frequency that corresponds with to the plotted MPCAPs. The deviations demonstrate a fault in the general theory described in section 4.3.4.1. The deviation may be the result of a change in the double layer caused by using a mixed frequency AC voltage. Due to there being a mixed frequency signal, the effect of charging and discharging at one frequency could alter how the second frequency charges and discharges the double layer. When assuming the constant Q_o does not change, equation 4.62 was used to calculate α for each MPCAP to get $\alpha = 0.684$ and $\alpha = 0.669$ for ${i_{\omega_1}}^*$

and $i_{\omega_2}{}^*$, respectively. Considering the effect is small (the αvalues were similar) , equation 4.62 is still a good model for the double layer charging effect on EFM results.

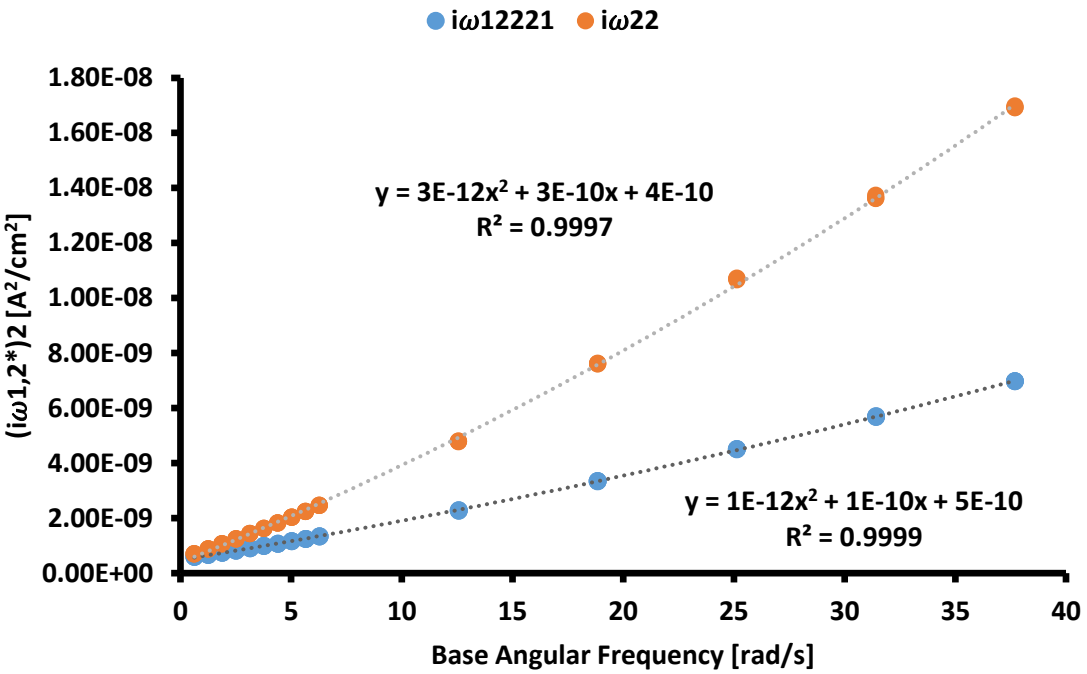

Figure 4.19 The squared MPCAPs vs the applied base angular frequency for steel.

Note: All data was collected from a single acetone cleaned steel panel that has reached steady state corrosion by immersing for 24 hr in 5% v/w NaCl solution. The currents follow an expected quadratic relationship and convert as they approach zero frequency.

To demonstrate how equations 4.29 and 4.30 work we plotted the squared MPCAPs vs base angular frequency (Figure 4.19). They share a similar y-intercept, which gives the squared Faradaic current for the corrosion process (see equations 4.29 and 4.30). The ratio of the quadratic coefficients were calculated to be $\frac{B_{i\omega 2}}{B_{i\omega 1}} = 2.46$ and $\frac{A_{i\omega 2}}{A_{i\omega 1}} = 2.84$. If the effect of variable r is low, then the results would follow equations 4.43 and 4.44, giving $\frac{B_{i\omega 2}}{B_{i\omega 1}} = 2.5$ and $\frac{A_{i\omega 2}}{A_{i\omega 1}} = 6.25$. The larger deviation for $\frac{A_{i\omega 2}}{A_{i\omega 1}}$ is expected because the

variable r would have to account for $\omega^{2\alpha}$ vs ω^2, as opposed to accounting for ω^{α} vs ω. Despite the deviation, solving for the Faradaic current using 4 points from base angular frequencies 2π and 4π (2 points from the ${i_{\omega_1}}^*$ curve and 2 points from the ${i_{\omega_2}}^*$) with equations 4.43 and 4.44 gave the values 4.28e-10 and 5.69e-10, respectively. Both are good approximations of the y-intercepts 4.87e-10 and 3.93e-10 in Figure 4.19. Alternatively, R can be solved for using the third root for equation 4.60 or 4.61, and then equations 4.46 and 4.47 can be used to calculate the squared Faradaic current (both equations 4.46 and 4.47 will give equivalent answers when R is known). Using the same 4 points as before we calculated $R = 0.87$ and got a squared Faradaic current value of 4.46e-10; falling right in between the intercepts from Figure 4.19. This demonstrates how well the equations derived in sections 4.3.4.1 and 4.3.4.2 approximate the Faradaic current, but when the corrosion rate is not at steady state, and the double layer changes between EFM spectra, how well these equations can be applied is still to be determined. These equations were tested further by applying it studying the early stages of steel corrosion in 5% w/v NaCl before steady state corrosion has been achieved.

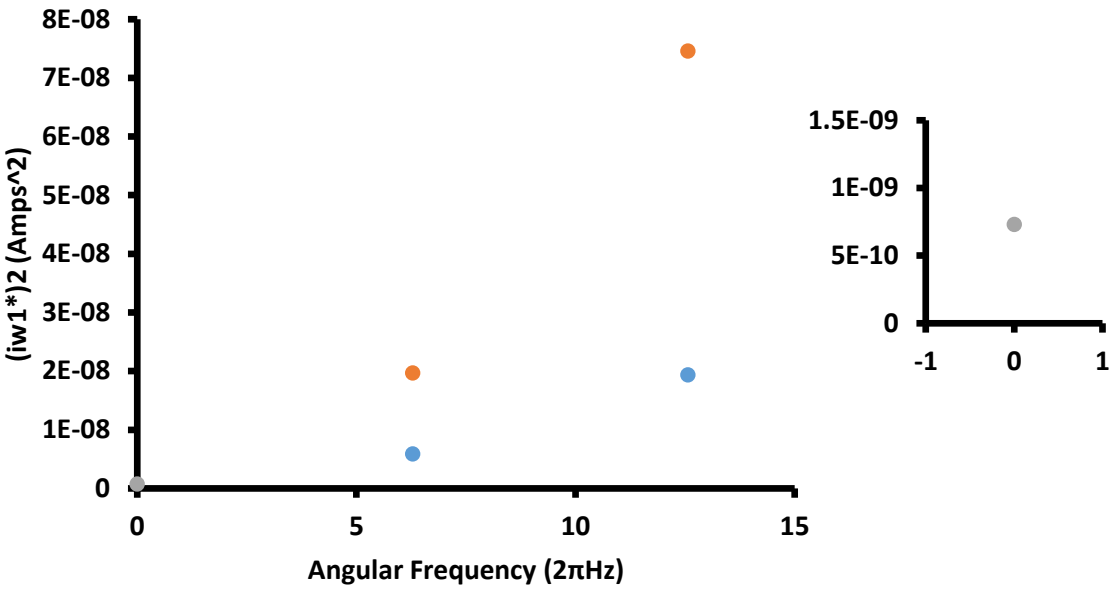

Figure 4.20 The MPCAPs from the last kinetic fast acquisition EFM spectra for steel.

Note: The data was collected from a single acetone cleaned steel panel that was immersed in 5% w/v NaCl solution vs the applied base angular frequency. The calculated corrected MPCAPs is plotted at base angular frequency 0 to demonstrate visually the method described in section 4.3.4.3. The zoomed in plot helps to show that the current for the corrected MPCAP is not zero.

Figure 4.20 is a visual demonstration of the method described in section 4.3.4.3. The example data is from the last corrosion data point from fast acquisition EFM (see below). Two EFM spectra at base frequencies 1 and 2 Hz (angular frequencies shown in Figure 4.20) are collected and each MPCAP produces a point. This gives four points that should follow equations from section 4.3.4.1 and 4.3.4.2. The result from using equations 4.50 and 4.51 with an R=0.79 calculated using a cubic solver is shown at zero base angular frequency. For this system the results from using equations 4.43 and 4.44 yielded 1.83e-8 and -3.31e-8, respectively, for the squared Faradaic current. A negative number is intuitively incorrect, and averaging the results still gives a negative number. It seems that for this system, when using these frequencies, the change in the double layer is large

enough that the variable r need to be better approximated using equations 4.46 and 4.47. Despite the improvement when using these equations, the results still overestimate the Faradaic current. This was tested by conducting a normal EFM experiment at low frequency for comparison.

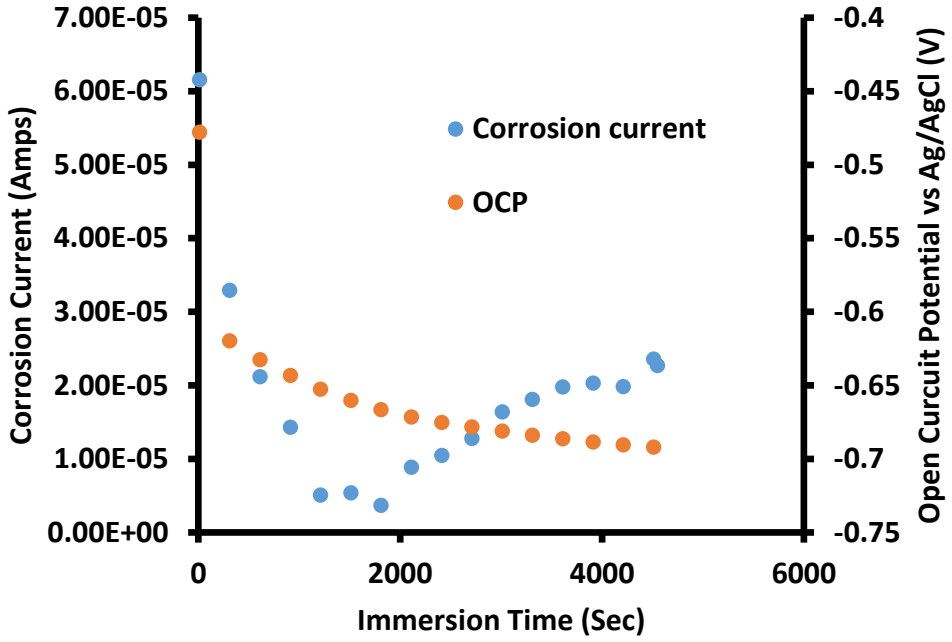

Figure 4.21 Kinetic corrosion current results from fast acquisition EFM for steel.

Note: The data was collected using base frequencies 1 and 2 Hz every 5 min for an acetone cleaned steel panel that was simply immersed in 5% w/v NaCl. The open circuit potential for the steel panel, which decreases as expected to a stable value is shown for comparison.

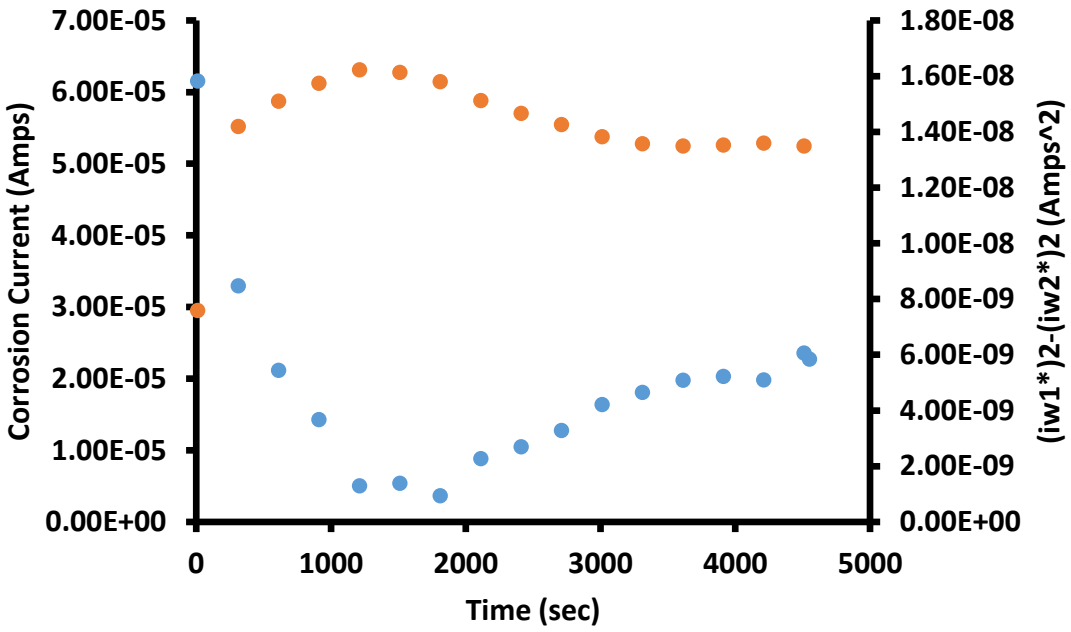

Figure 4.22 The results from fast acquisition EFM for steel along with a proxy for capacitance.

Note: The data was collected using base frequencies 1 and 2 Hz collected every 5 min for an acetone cleaned steel panel that was simply immersed in 5% w/v NaCl. The SDMPCAP is plotted as a proxy for capacitance.

Fast acquisition EFM was conducted by collecting 2 EFM spectra at base frequencies 1 and 2 Hz every 5 min for an acetone cleaned steel sample that was just immersed in 5% NaCl. The corrosion current was calculated using a corrected MPCAPs using the method described in section 4.3.4.2 (equations 4.50 and 4.51). Figure 4.22 shows the results from the experiment. It appears that the corrosion rate of steel during early stages of corrosion start high, due to high chemical potential from lack of iron ions in the water/electrolyte solution, and drops dramatically and yet rises again to establish a stable corrosion rate. The open circuit potential continually drops, as expected, during the experiment and starts to plateau around the time the corrosion rate begins to plateau. The

final point on Figure 4.22 was generated by standard lower frequency EFM (0.1Hz) for comparison, to show that accuracy of the fast acquisition method. The fast acquisition results still overestimate the corrosion current, but there is a vast improvement acquisition time. The SDMPCAPs was used as a proxy for capacitance, and it mirrors the corrosion rate. This suggests that the double layer plays an important role in early stages of steel corrosion in 5% NaCl. First metal dissolution alters the local ion strength and pH to cause an increase in double layer capacitance, and as corrosion produced ions diffuse away from the interface the local ionic strength and pH reaches a steady state and the double layer capacitance stabilizes. As a result, the corrosion rate begins to stabilize.

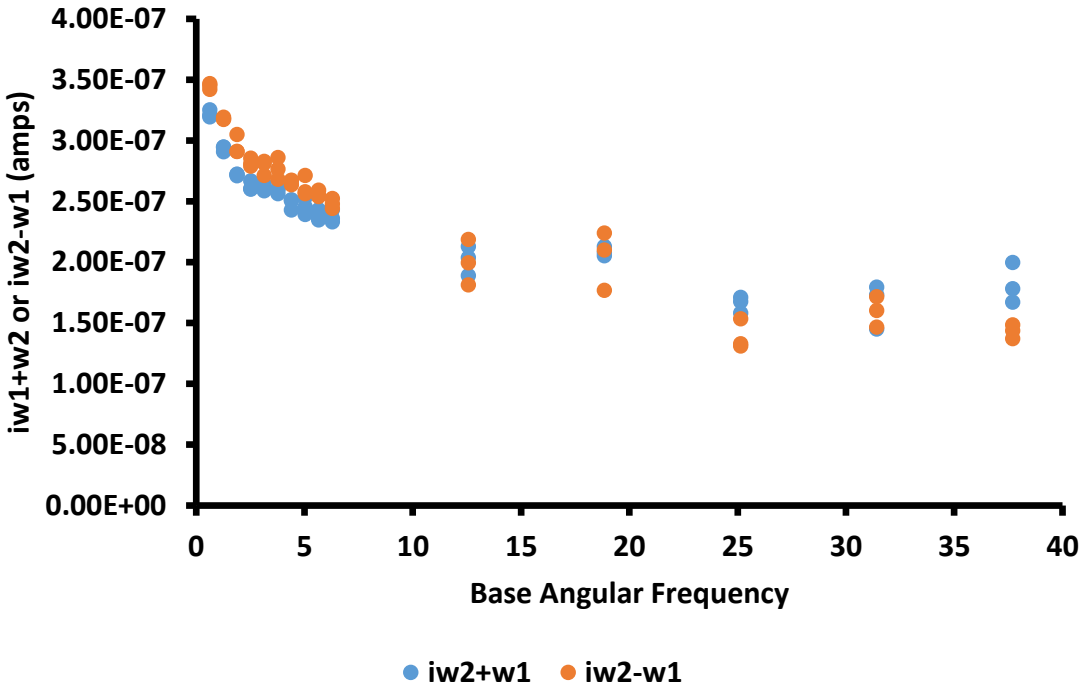

Figure 4.23 A plot of the intermodulation current peaks for frequencies 2w+w1 and 2w2-w1 vs the applied base angular frequency for steel.

Note: All data was collected from a single acetone cleaned steel panel that has reached steady state corrosion by immersing for 24 hr in 5% v/w NaCl solution. The frequency dependence shows that the general theory described in section 4.3.4.1 and 4.3.4.2 do not completely describe the capacitive charging event.

Unlike the results for the intermodulation current peaks at frequencies 2w+w1 and 2w2-w1, the intermodulation peaks for frequencies w1+w2 and w2-w1 do show frequency dependence (figure 4.23). This goes against the general theory that the capacitive charging event solely alters the MPCAPs for EFM.

One of the following was suggested to be true

1. The capacitive charging is non-linear and will give intermediated and harmonic speaks similar to how the Faradaic process of corrosion does.

2. The corrosion processes were altered by applied voltage frequency that is not described by classical Butler-Volmer equation
3. The phase shift in the CPE cases accidental overlap in this frequency after FFT of the data.

The causality factors and other intermodulation current peaks lack frequency dependence; therefore, we do not believe the corrosion processes were altered by the applied frequency. Instead this was an artifact from phase shifting or the capacitance requires a different model to accurately represent the corrosion process.

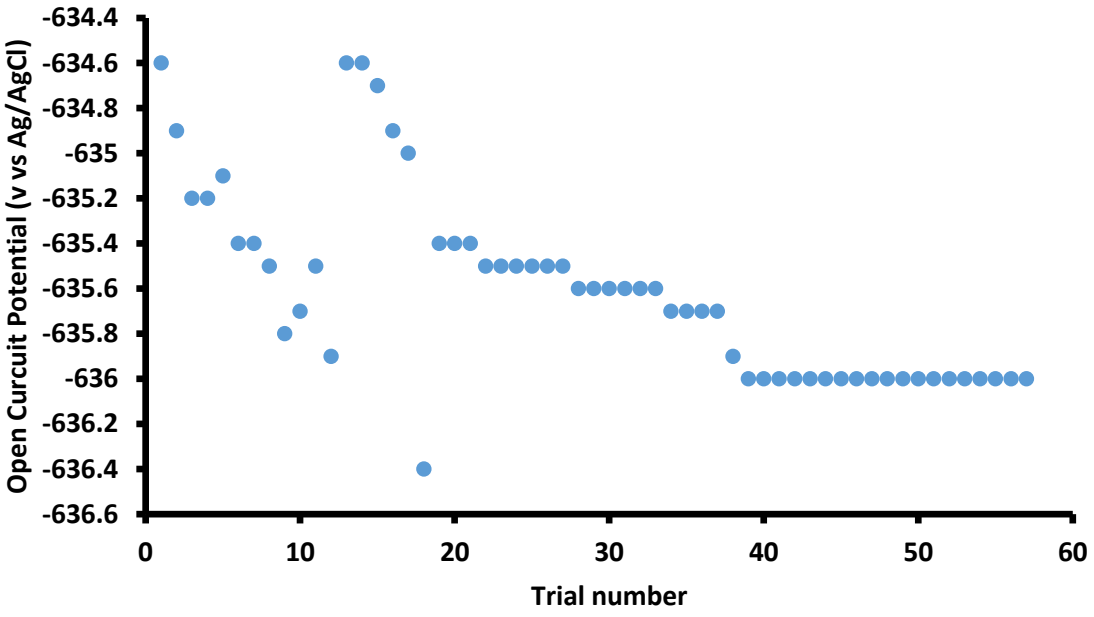

Figure 4.24 The OCP for each trial of EFM spectrum collection.

Note: All data was collected from a single acetone cleaned steel panel that has reached steady state corrosion by immersing for 24 hr in 5% v/w NaCl solution. The small change in OCP demonstrates that the corrosion is at a steady state during the entire experiment, so any changes are mostly due to changes in the capacitive charging effect.

The open circuit potential (OCP) of the steel after a duration considered commonly as stable, was measured for each trial, and the potential does not drift past 2 mVs in difference (Figure 4.24). The results demonstrate that the stability of the corrosion process is high within the timeframe and conditions of the test and that the corrosion rates should be constant between each EFM experiment. This means that any current differences measured from the EFM experiments are the results of change in frequency as opposed to change in corrosion rates.

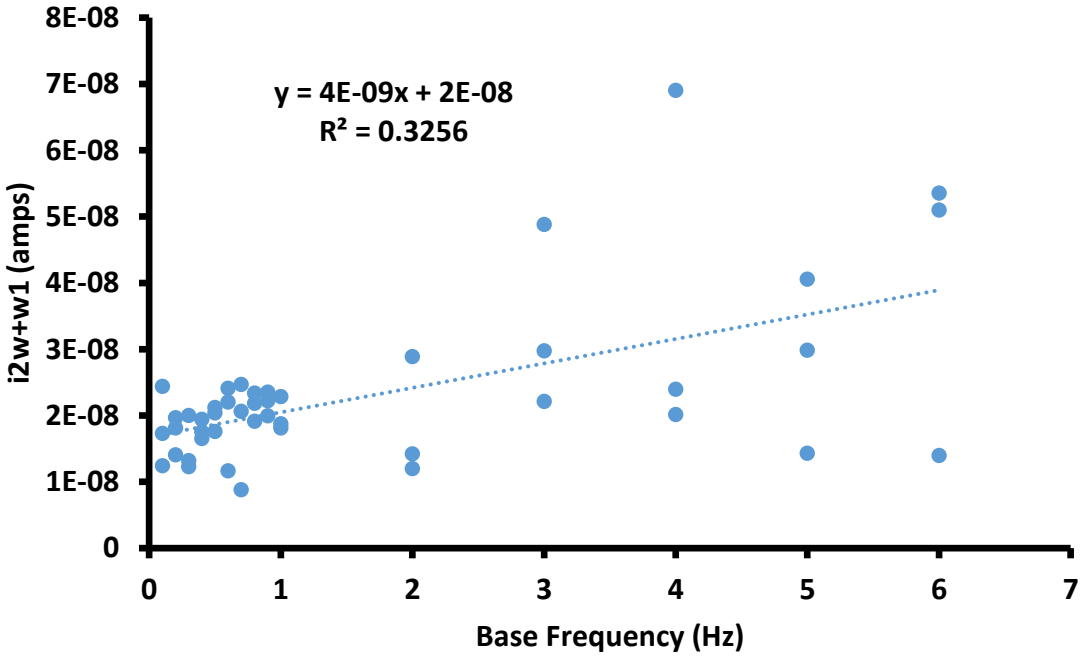

Figure 4.25 The relationship between intermodulation current peaks at frequencies 2w+w1 and 2w2-w1 vs the applied base angular frequency for steel.

Note: All data was collected from a single acetone cleaned steel panel that has reached steady state corrosion by immersing for 24 hr in 5% v/w NaCl solution. The poor frequency dependence shows supports the general theory shown in section 4.3.4.1 and 4.3.4.2.

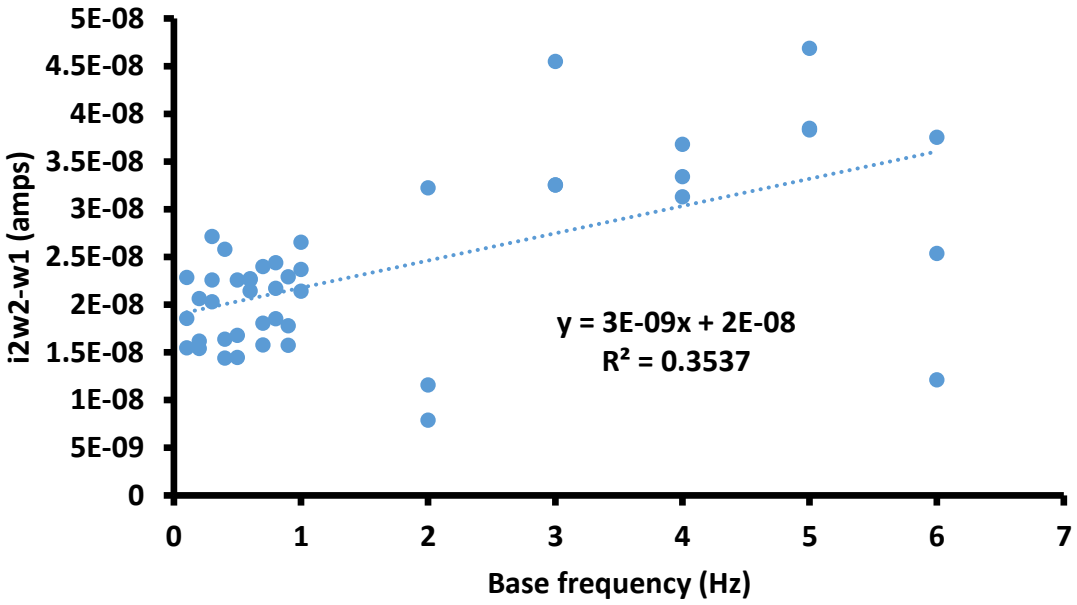

Figure 4.26 The relationship between intermodulation current peaks at frequencies 2w2-w1 vs the applied base angular frequency for steel.

Note: All data was collected from a single acetone cleaned steel panel that has reached steady state corrosion by immersing for 24 hr in 5% v/w NaCl solution. The poor frequency dependence shows supports the general theory shown in section 4.3.4.1 and 4.3.4.2.

The intermodulation current peaks for frequency 2w+w1 and 2w2-w1 exhibit very little frequency dependence (Figure 4.26). Because the capacitive charging should have a linear relationship with the applied voltage, the capacitive charging event should only alter the currents measured for the MPCAPs. The lack of frequency dependence on these intermodulation current peak support the general theory described in section 4.3.4.1.

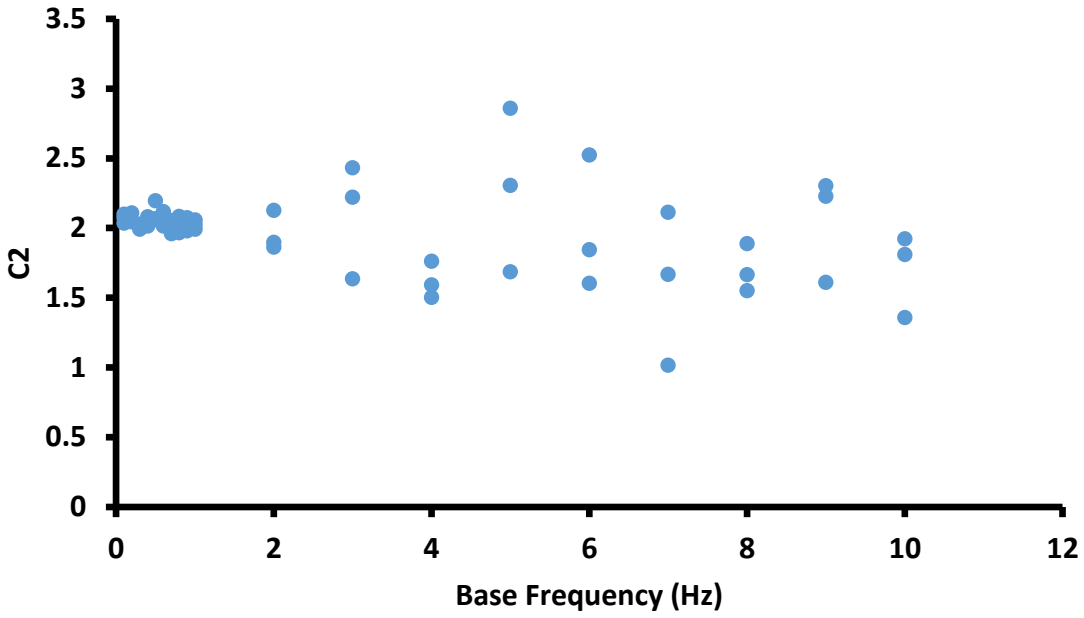

Figure 4.27 The causality factor C2 vs the applied base frequency for steel.

Note: All data was collected from a single acetone cleaned steel panel that has reached steady state corrosion by immersing for 24 hr in 5% v/w NaCl solution. The lack of frequency dependence suggests that the Butler Volmer equations for EFM still hold even at higher frequencies.

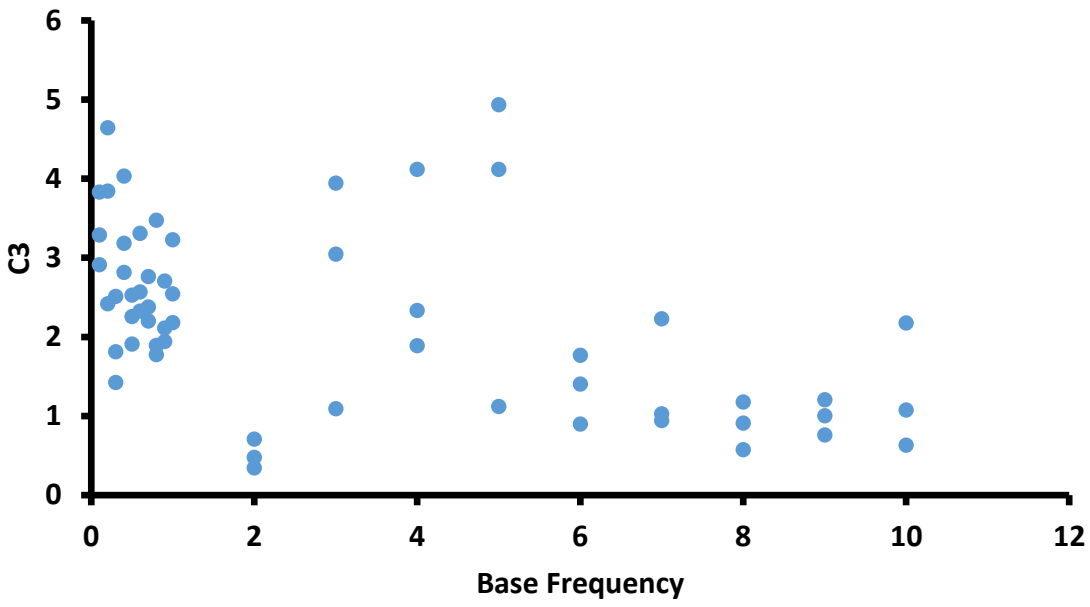

Figure 4.28 The causality factor C3 vs the applied base frequency for steel.

Note: All data was collected from a single acetone cleaned steel panel that has reached steady state corrosion by immersing for 24 hr in 5% v/w NaCl solution. The lack of frequency dependence suggests that the Butler Volmer equations for EFM still hold even at higher frequencies.

The causality factors C2 and C3 are both independent of the MPCAPs. Because the capacitive charging effect should solely alter the MPCAPs, the causality factors should still allow for a consistence of EFM theory confirmation and the quality of the data collected. Both causality factors remain at their expected values and are mostly independent of the base frequency. When applying frequencies greater than 1 Hz, the signal to noise for the EFM spectrum decreases and the scatter of the causality factors increases. The intermodulation peak used for calculating causality factor C3 has a particularly small current, and when signal to noise gets low enough the peak effectively disappears and gives the appearance that the experiment has collected poor data. This is

not necessarily true. When determining the optimal parameters for testing our corrosion cell by using low frequency EFM in conjunction with EIS and Tafel analysis, we found that the lower the voltage amplitude the less scattered the data appeared. Causality factor C2 maintained the expected value, but C3 would drop below the expected value of 3 at lower amplitude. By increasing the scan number, the signal to noise for the EFM spectrum would improve and the expected value for C3 would return to 3. For this reason, we believe the poor C3 values above base frequency of 5 Hz are likely caused by poor signal to noise for the EFM spectra collected at those frequencies. Despite C3 likely not showing the data is poor, we still recommend avoiding conclusions based on EFM data when C3 is not at the expected value.

4.4 Conclusions

The open circuit potential can be used to get a more qualitative understanding of the corrosion process. For steel the OCP will drop to between -600 and -750 mV vs Ag/AgCl, and a higher OCP suggests better barrier properties or anodic polarization of the substrate.

Tafel analysis is the basis for collecting corrosion kinetic data of metal substrates, but he technique is very destructive and limited when the corrosion cell has high resistance and capacitive properties. It is not recommended to use this technique for coated substrates, but the technique should still be understood for analysis of EFM data and should still be conducted on the bare substrate for calculation of corrosion rates using AC techniques.

Electrochemical impedance spectroscopy is the standard for analysis of non-conductive coated substrates besides visual inspection of accelerated corrosion. If

accurate determination of capacitance is important we recommend using an equation derived using a CPE. Generally, any equation that estimates capacitance is good enough for quantifying water uptake of films if the Bode plots show primarily capacitive behavior.

By modeling the capacitive charging of a corrosion cell using a constant phase element, we were able to show that the effect of capacitive charging can mostly be removed when collecting EFM spectra at higher frequencies. A method was developed to allow fast acquisition and the early stages of steel corrosion in 5% NaCl showed that corrosion rates start high, dip to lower rates, and then rise and plateau to a corrosion rate that stays constant over long periods of time. The shift in corrosion rates are likely due to changes in the double layer, because the capacitive charging of the substrate changes along with the corrosion rate changes. There is an additional apparent effect of frequency on EFM results that were unexplained with the general theory outlined, and further development of EFM theory and corrosion kinetics is required to better understand how AC voltages alter corrosion processes. We are in the process of evaluating coated substrates using EFM, both scribed and non-scribed.

CHAPTER V – Evaluation of Non-Conductive Films

The purpose of this chapter is to employ the methods described in chapter 4 to catalog the anti-corrosion properties of non-conductive films that we use to better study the anti-corrosive performance of the polythiophenes

5.1 Introduction

Studying corrosion of coated substrates adds another complication. The biggest is that most ways to measure corrosion kinetics require measuring current flow, and coatings primarily act as an electrically and ion transport property barriers that prevent current flow. Another complication is that corrosion rates are going to be directly related to coating failure rates, and there is much to be desired in this field of study as most researchers intentionally add failure points to decrease the time required for testing and characterization. In turn, we continue to ignore the benefit of defect free coatings in our corrosion studies as they don't fail over a convenient timeframe for study, however they do protect substrates better in almost all examples in the literature. In this chapter we will discuss the relationships between ion transport and general morphology of non-conductive films.

The open circuit potential can still be used to study corrosion of coated substrates, but there are some problems with using the technique. One problem is the way that potentiostats measure OCP. The voltage measurement process requires very small current flow, and the coating can act as a large capacitor. The result is that trickle current can flow from the instrument and charge the surface, causing the measured potential to shift continually over time. This potential can sometimes grow to plus or minus 20 volt w.r.t the reference electrode. Depending on the quality of the potentiostat and the

resistance of the film, you cannot reliably measure the OCP of the coated substrate. Other than that, OCP only really has the same downfall as OCP of non-coated substrates, and that is the analysis requires complimentary data to support your analysis and conclusions.

For coated substrates where the polymer film is primarily acting as a barrier it is common that the prevention of oxidizing species and the prevention of dissolution results in an OCP that is much higher than the OCP of the bare metal. This OCP will drop, much like with bare metals, and stabilize. Eventually, when the corrosion processes gains momentum the coating will have failure points and the OCP will drastically drop to a value much closer to that of the bare metal substrate. The time it takes for the OCP to drop can be used to evaluate a coatings corrosion performance (albeit possibly another oversimplification).

Electrochemical impedance spectroscopy (EIS) is commonly used for evaluation of coated substrates because the technique does not require much current flow through the film. There are several problems with using EIS to evaluate a protective polymer film, but the most common is the assumption that higher impedance means higher performance. For example, a sacrificial pigment based protective coating relies on the ability for the pigment to corrode in advance of the substrate and that inhibitor/pigment(s) will polarize the actual substrate to protect the substrate, and for that reason these films will have much lower impedance than clear polymer films, yet they may perform significantly better than a simple defect free clear-coat. Another assumption is a higher impedance means a lower corrosion rate, therefore, a higher performance. This may seem counterintuitive, but this line of logic is not necessarily true either. The reason is

that the performance of a protective coating is generally how long before you need to recoat the substrate, which means coating performance is more correlated with coating failure as opposed to corrosion rate. If a coating cannot adapt to the effect of corrosion or mechanical breach, then a coating may fail faster than another coating, while still having a higher impedance. As an example, consider two theoretical coatings, one with low impedance and one with high impedance. If both coatings get mechanically breached, it is possible that the coating with high impedance fails faster and the corrosion protection is much lower as a result, despite having a higher impedance. In this case the rate of impedance change from the high impedance coating would shift faster. In the end, it is best to understand what the coating might do under corrosion environment and how that might affect performance in the long run instead of just relying on the impedance of the film.

Another assumption is directly related to the Brasher-Kingsbury equation, used to calculate water volume fraction of the film using the capacitance from EIS data. The assumption of the Brasher-Kingsbury equation is that the mixing equation for the dielectric constant of the film is for a completely homogeneously mixed system.[110,114] If water uptake is not homogeneous, then the dielectric constant of the film would need to account for the shape of water rich regions. Spherical inclusions would give results similar, but not perfectly equivalent to, a perfectly homogeneously mixed system, but elongated inclusions like disks or rods would require different equations for the dielectric constant. The change per volume fraction of a high dielectric inclusion, like the water ingression into the film, would be higher the more elongated the shape of the inclusion. The result would be that the Brasher-Kingsbury equation would overestimate water

volume fraction in the film, and we demonstrate in this chapter that for some epoxy amine films the Brasher-Kingsbury equation overestimates the water volume fraction. Although the equation has a variable to account for swelling, we showed that swelling was insufficient for explaining the overestimation.

5.2 Materials and Methods

5.2.1 The Go9v10 series preparation

A polyetheramine crosslinker Jeffamine ED600 was used to control the hydrophilicity of a series of epoxy-amine films with variable crosslink-density and T_g designed to allow investigation of the effect T_g and crosslink-density has on water uptake, ion resistance, and water vapor transmission rates, and hygroscopic swelling. We found that ED600 content predicts water absorption, ion resistance, and water vapor transmission rates regardless of T_g and crosslink density of the material, and ED600 content also predicts hygroscopic swelling when considering testing near the wet T_g of the films, where testing near the wet T_g decreases hygroscopic swelling. We propose that the reason crosslink-density does not alter ion transport and water vapor transmission rates for these films is because of phase separation during cure that results in hydrophilic rich regions that are largely unaffected by bulk crosslink density and that ions and water molecules primarily transport through these regions. Heterogeneous water uptake is supported by the lack of correlation between film swelling and electrochemical impedance spectroscopy (EIS) overestimation of water. Our results suggest that using hydrophilic crosslinkers that phase separate from the bulk matrix like Jeffamine ED600 allows the preparation of epoxy-amine films with control over water uptake, ion resistance, and water vapor transmission rates separately from mechanical properties.

Potentially epoxy-amine films can be prepared with equivalent bulk crosslink-density and T_g but different hydrophilicity and ion resistance to better study the role hydrophilicity and ion resistance has on corrosion protecting coatings prepared with such polymers.

Table 5.1 Go9v10 compositions and mechanical properties.

Film Name	Epoxy Benzylamine Prereaction Equivalence	1,3-BAC:ED600 Equivalence Ratio	Dry T_g (°C)	Wet T_g (°C)	M_c (g/mol)
Alpha 1	49%	70:30	86.40	62.24	950.17
Alpha 2	27%	65:35	86.29	60.34	774.53
Alpha 3	9.0%	70:30	95.19	68.81	591.78
Beta 1	43%	50:50	72.35	49.79	950.61
Beta 2	23%	51:49	73.36	48.67	778.06
Beta 3	4.4%	50:50	71.90	45.62	596.82
Gamma 1	38%	30:70	60.51	38.74	960.24
Gamma 2	20%	35:65	60.17	36.94	786.61
Gamma 3	0.9%	67:33	54.87	31.86	603.36

EPON 825 and benzylamine were first mixed using Flak Tek @ 1800 RPM for 1 min and allowed to react with low agitation via tumbling for 1 hour prior to addition of Jeffamine ED600 and 1,3-BAC. After Jeffamine ED600 and 1,3-BAC were mixed using Flak Tek @ 1800 RPM for 1 min the formulations were once again allowed to react with low agitation via tumbling for 6, 8, and 12 hours for the alpha, beta, and gamma series, respectively. Films were prepared using 8 Mil wet draw downs on acetone washed QD

stele panels for bound substrates and t-butyl acetate cleaned polyester for free films. Thicknesses were measured using a positron thickness gauge. For NIR results the QD steel panels were polished to 600 grit prior to film preparation to reduce noise from scattering. Films were cured at ambient for 24 hours followed by 80°C for 4 hours. All films were stored with descant in sealed containers to dehydrate prior to testing.

5.2.2 Gravimetric Water Uptake

Free films were dehydrated using desiccant, massed, and then NIR spectra were taken to get the zero point. Afterwards the films were immersed in 5 wv% NaCl solution, making sure to push the films under the surface to break the tension and prevent the films from floating. At given time points the free films were removed from the solution, padded dry with a paper towel, NIR spectra were taken, and the masses were recorded. The films were replaced into the solution after each reading. The wt% water uptake was then determined via the following equation:

$$X_{wt} = \frac{(M_t - M_o) * 100\%}{M_t} \tag{5.1}$$

Water diffusion curves were generating using reduced time (τ) where:

$$\tau = \frac{\sqrt{time}}{thickness} \tag{5.2}$$

5.2.3 Near Infrared (NIR) Spectroscopy

NIR spectra were taken, and baselines were subtracted. The benzyl C-H stretch peak was normalized to a height of 1 and the area under the water peak was determined. This value was plotted vs wt%/(100-wt%) for each of the free films to allow quantification of water for substrate bound polymer films.

5.2.4 NIR Water Uptake for Bound Films

Substrate bound polymer films were dehydrated using desiccant, and then NIR spectra were taken to get the zero point. Afterwards a plastic cap with 2 small holes (one to inject solution and another for air to escape while injecting) was clamped over the testing area and 5 wv% NaCl solution was added using a syringe. At given time points the cap was removed and the film was dried using a paper towel, then NIR spectra were taken. The cap was replaced after each spectrum and filled with new solution. Water diffusion curves were generated using the same equation used for gravimetric experiments.

5.2.5 EIS Water Uptake for Bound Films

Substrate bound polymer films were dehydrated using desiccant, and then an EIS paint cell was clamped over the films to conduct two electrode EIS experiments. The working electrode was the coated substrate and the counter electrode was a graphite rod. A three-electrode setup was not used as the OCP was not required for water uptake experiments, a reference electrode can cause interference in high impedance experiments, and to best replicate the experiments conducted by C. Vosgien Lacombre et al.[125] so that they can be better compared to each other. The time between adding water to the cell and starting acquisition was recorded for better accuracy of the coating capacitance. EIS data was collected to get capacitance, and the capacitance was determined using the following equation:

$$C = \frac{-Z_{im}}{2\pi f\left({Z_{im}}^2 + {Z_{real}}^2\right)} \tag{5.3}$$

The capacitance was plotted vs reduced time, and the intercept for the linear regime was used to determine the initial dehydrated film capacitance. Water wt% was then calculated using the following equation:

$$wt\% = \frac{100 * \log\left(\frac{C(t)}{C(0)}\right)}{\log(80) * \rho_{polymer}} \quad (5.4)$$

Water diffusion curves were then generated in similar fashion to gravimetric and NIR results.

5.2.6 EIS for Resistance of Water Aged Samples

Substrate bound films were aged in 5 wv% NaCl for 10 days and EIS spectra were taken from 100 kHz to 10 mHz using the same two electrode setup for determining water uptake that C. Vosgien Lacombre et al used (for better comparison between data).[125] The real impedance value at low frequency was recorded as the film resistance. For films with high resistance, the data was fit to a simple Randles circuit to estimate film resistance.

5.2.7 Water Vapor Transmission

Permeability was measured using a TA Instruments VTI-SA vapor analyzer. Films were cut to fit the 10 mm permeability cup that was filled with a desiccant to absorb moisture as it passes thru the film. The method is similar to ASTM E2945 – 14 except the measurements of weight gain are conducted without removing the sample from the test chamber, smaller cup size reduces chances for film defects to influence data, and data is collected in a fraction of the time. When the system achieves to steady-state conditions, the cell weight will increase linearly with time and from the slope of this line (weight per unit time mg/min) and the diameter of the permeating film we can obtain the rate of

permeation in terms of weight per unit time per unit area. The data can be further normalized by dividing by the film thickness in get flow thru the film.[126]

$$Q = \frac{amount\ of\ permeant * film\ thickness}{area * time} \tag{5.5}$$

5.2.8 DMA swelling

A Q800 DMA equipped with relative humidity furnace was used to measure the change in length of films. The samples are run in a creep mode using a film clamp. Samples are conditioned are 35°C for 1 hour at 0% humidity and a constant force of 0.001 N. The length of the sample after conditioning is used as the initial length. Samples are then subjected to alternating periods of 95% and 0% relative humidity for 540 minutes at each humidity level. Length, displacement, and % stain signals are recorded.

5.2.9 DVS

Vapor absorption was conducted on a TA Instruments Q5000SA. The free-standing films were dried at 85°C and 0% humidity for an hour. Dried films were then equilibrated at 35°C and humidity was set to 95% for 300 minutes. Diffusion coefficient was calculated using the following equations:

$$\frac{M_t}{M_\infty} = \frac{4}{L} * \left(\frac{Dt}{\pi}\right)^n \tag{5.6}$$

$$D = \left(\frac{slope \times thickness}{4} \times \sqrt{\pi}\right)^2 \tag{5.7}$$

Where M_t and M_∞ are water uptake at time t and at saturation. L and D are thickness of coating and diffusion coefficient, respectively. The diffusion constant in the experiment applies only to adsorption of water into the film.

5.2.10 DMA

RHDMA was conducted using a TA Instruments Q800 DMA. Free standing films were conditioned at 25°C for an hour at the desired relative humidity (0 and 95%). Specimens were run at a strain of 0.1%, frequency of 1hz, and with a temperature sweep from 25°C to 120°C at a heating rate of 1°C per minute.

5.2.11 Unimodal and Bimodal Pigmented Film Preparation

The epoxy amine ratio for these two films were both at 1.05:1 and two different mixture procedures created either a unimodal or bimodal morphology within the films. The chemical composition for the films were identical, composed of EPON 825, benzyl amine, MPMD, and Jeffamine ED600. The coatings were designed to model after a MIL-SPEC 02Y040A epoxy amine coating Deft. The pigment loading was 3% reduced pigment volume concentration (RPVC) SrCrO4 and 27.5% RPVC TiO2. The base epoxy resin EPON 825 was mill ground to a Hegman 7 consistency and thinned to 71.8 wt% solids by addition of sec-butanol and 2-pentanone (0.73:1 blend).

(**Method 1**) For the Unimodal system the EPON 825 was first mixed with the benzylamine at a 2:1a stoichiometry for ca. 1 hour at room temperature. Then the MPMD and Jeffamine ED600 polyetheramine were mixed in and allowed to body for 1 more hour. (**Method 2**) For the Bimodal system all components were mixed together at once and allowed to body for 1 hour prior to application. Both films were cured at 60 °C/1 hour followed by 80 °C/1hour.

5.2.12 Open Circuit Potential

On a Princeton Applied Research VersaSTAT 4 using a 3 electrode cell with Pt counter electrode, a coated QD steel panel was the working electrode, and an Ag/AgCl

reference electrode was used. The electrolyte solution was the same used for Prohesion accelerated corrosion exposure (0.4% ammonium sulfate and 0.05% NaCl). Open circuit potential was then measured at 1 sec intervals.

5.2.13 Electrochemical Impedance Spectroscopy

Electrochemical impedance spectroscopy (EIS) was conducted using a three electrode cell using prohesion solution as the electrolyte and the coated steel substrate (masked working area of 6.45 cm2), a platinum mesh, and an Ag/AgCl electrode as the working electrode, counter electrode, and reference electrode, respectively. A Princeton Applied Research VersaSTAT 4 was used to apply 10 mV amplitude AC voltages vs the open circuit potential (OCP) and collect impedance data over a range of frequencies. To allow faster acquisition during water uptake, impedance data was collected from 100 kHz to 100 Hz. After longer immersion times the frequency range was increased (100 kHz to 100 mHz) to allow low frequency impedance data for coating resistance evaluation. The cell capacitance was estimated using the following equation:

$$C = \frac{-1}{2\pi f Z_{im}} \tag{5.8}$$

where C is capacitance, f is frequency, and Z_{im} is the imaginary portion of the impedance. We used the frequency 19952 Hz for capacitance evaluation because the frequency was large enough so that capacitance primarily dictated the impedance but still has low noise in the signal. The water content in the film can be estimated from the capacitance using the Brasher-Kingsbury equation:

$$\phi = \frac{\log\left(\frac{C}{C_o}\right)}{\log(\varepsilon_w)} \tag{5.9}$$

where ϕ is the water volume fraction, C_o is the initial capacitance, and ε_w is the dielectric constant of water (78.3).

5.2.14 Prohesion Accelerated Corrosion Exposure

Steel panels were acetone washed and wiped with a lint-free cloth for application of each coating system. Replicate samples were coated by drawdown at 6 wet mils and cured as described above. The resulting dry film thickness was 47.3 ± 4.5 μm as measured in several locations on each sample. The cured panels were edge-taped according to ASTM B117 using polyester adhesive film and placed in a Prohesion chamber (Q-Labs, City) for exposure using dilute Harrison's solution as specified (0.4% ammonium sulfate and 0.05% NaCl)(ASTM B117). The samples were evaluated for edge-independent iron oxidation appearance on the surface of coating at 48 and 120 hours of exposure.

5.3 Results and Discussion

5.3.1 Unimodal and Bimodal Films

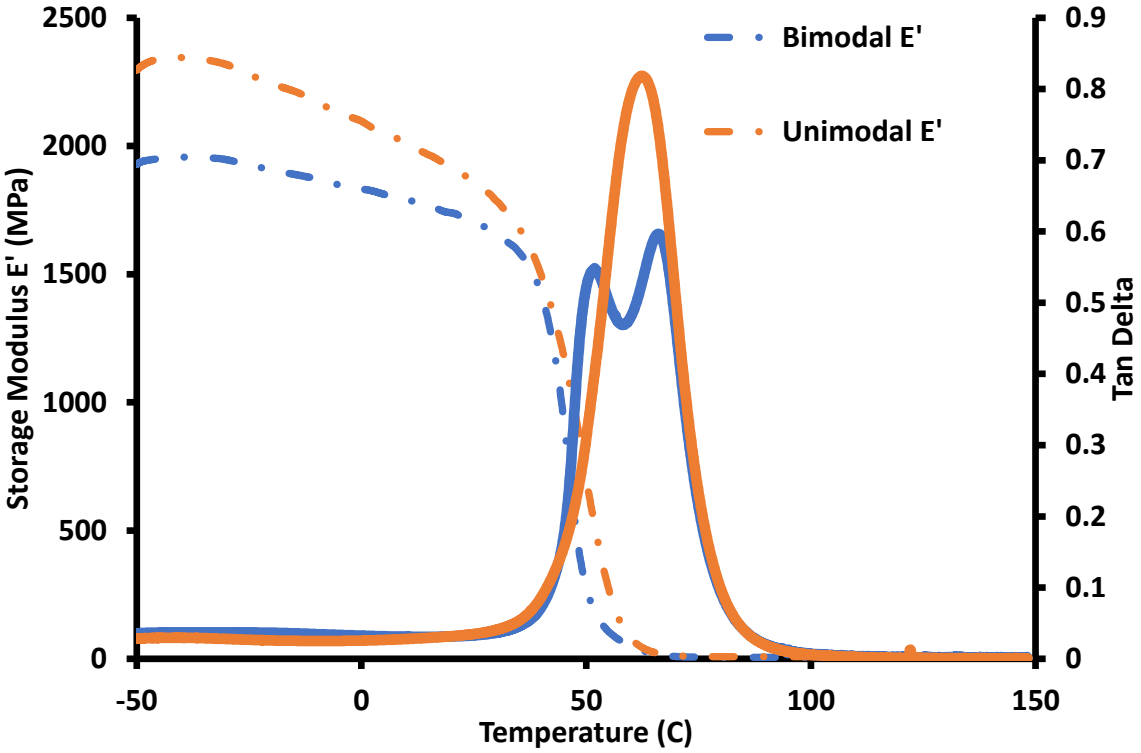

Figure 5.1 DMA results for the Unimodal and Bimodal free films.

Note: Unimodal films were prepared via method 1 and Bimodal films were prepared via method 2 found in section 5.2.11.

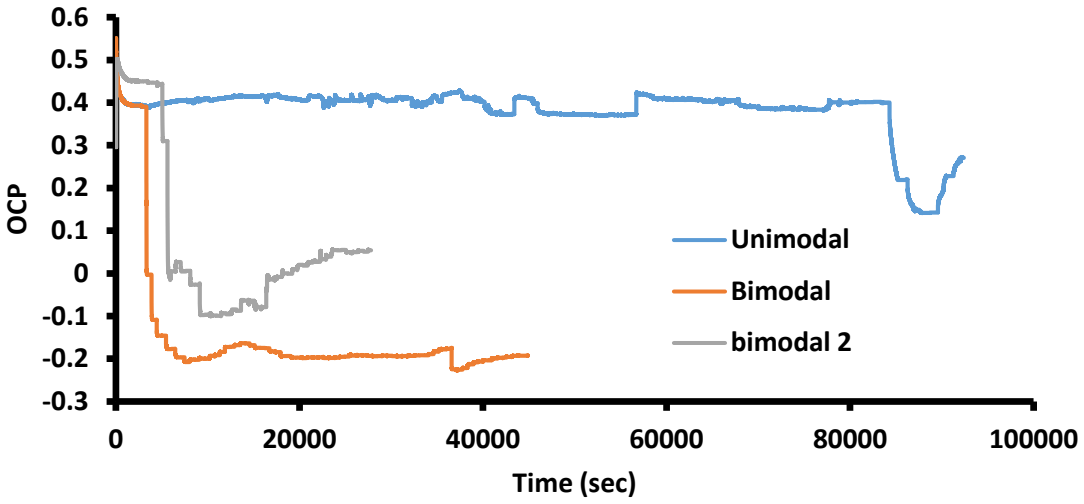

Figure 5.2 OCP for pigmented epoxy amine films.

Note: The epoxy amine films have equivalent composition, but they have wither unimodal or bimodal DMA mechanical properties. This is achieved via different mixing procedures.

Figure 5.2 shows the OCP for pigmented epoxy polymer films on steel that were prepared using two different techniques (methods 1 and 2 in section 5.2.11). One technique results in a bimodal DMA response, whereas the other results in a unimodal DMA response. The two polymer films are prepared using the same reagents but have different bodying times. The epoxy polymer film that had unimodal properties showed greater performance based on the OCP data. This data was complimented with other techniques like EIS and visual inspection after accelerated corrosion exposure, and the results show that the difference in the polymer films that resulted from different bodying procedures can affect performance of protective polymer films.

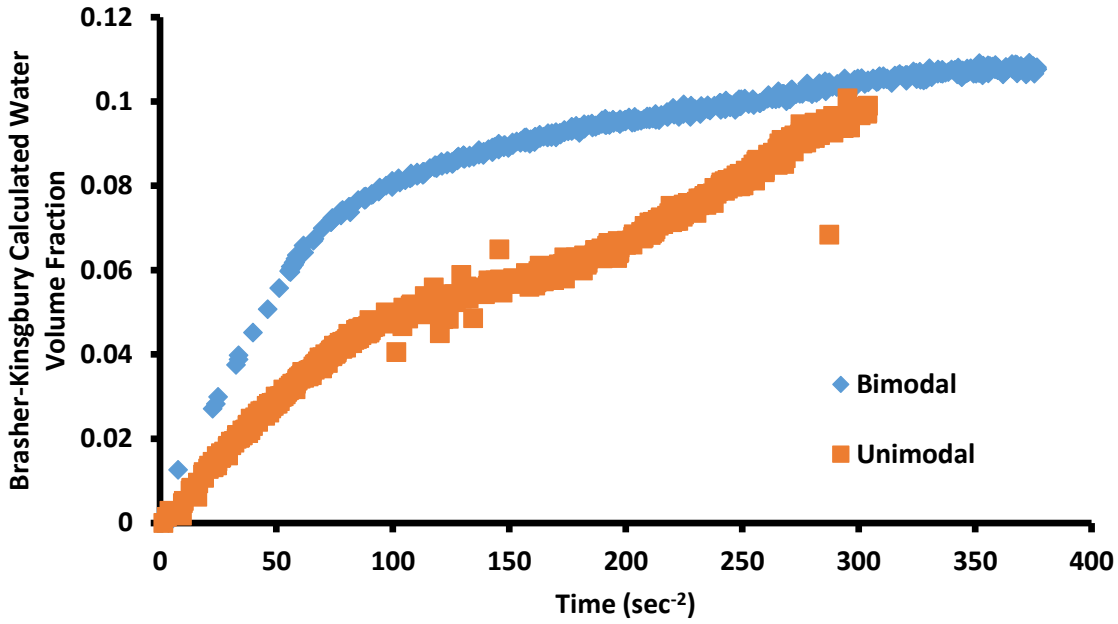

Figure 5.3 Brasher-Kingsbury calculated water volume fractions for the unimodal and bimodal Go9v9 beta 2 pigmented films vs sqrt of time to visualize Fickian regions.

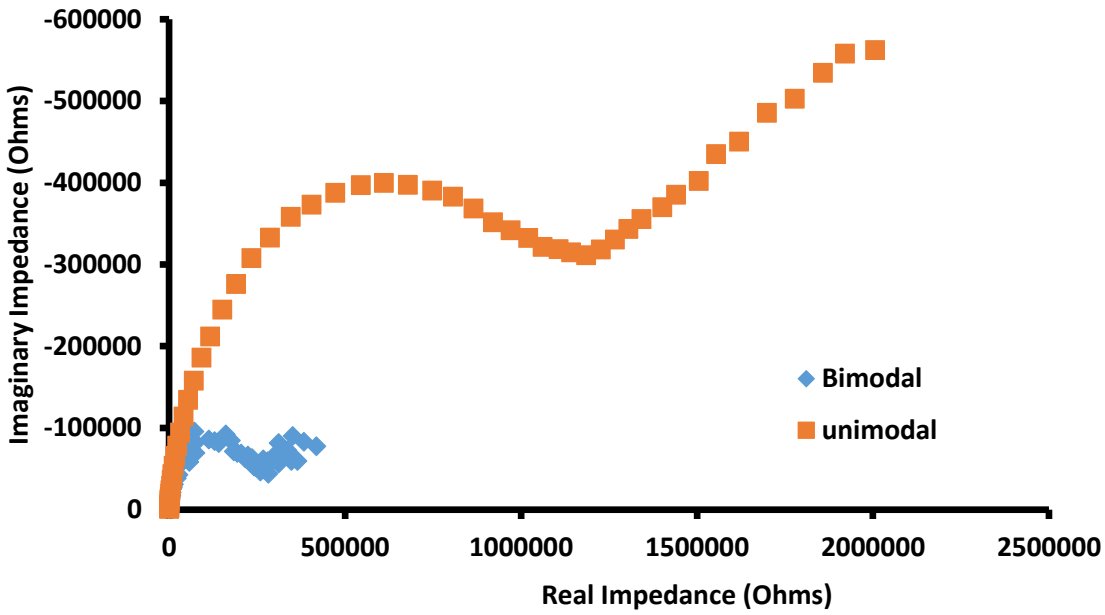

Figure 5.4 Nyquist plots for the unimodal and bimodal Go9v9 beta 2 pigmented films.

Note: The data was collected after 22 hours of immersion time in Prohesion solution (0.4% ammonium sulfate and 0.05% sodium chloride).

The EIS results for these films shows that the water uptake and ion resistance properties are different between the two. Brasher-Kingsbury determination of water volume uptake suggests that the bimodal system takes up water faster (Figure 5.3). Even though the Brasher-Kingsbury equation can overestimate water uptake for films (see future sections) it should be noted that the overestimation is generally a results of a combination of swelling and the morphology of the water rich region sin the film. If this is the case, and assuming the swelling behavior of these films are very similar, then the difference in calculated water volume fraction could also be affected by the morphology of the film, which we know is different between these films.

The apparent water uptake for the unimodal system is 2 stage, which if it is being altered by morphology would suggest that the water rich regions are relaxing towards a more elongated morphology (as opposed to a more uniform spherical morphology). If the results are showing difference in water volume uptake, then the unimodal system first take up water, then as the polymer system is allowed to relax, or hydroplasticized more water can enter the system. Either way there seems to be a relaxation in the unimodal system that alters the way water goes through the film that is not present in the bimodal system, and as a result more water can enter he film faster.

The Nyquist plots are after immersion in the Prohesion solution, and they demonstrate how the ion transport of the films are different. The smaller semi-circular shape of the bimodal system shows that the ion resistance of the film is lower than the unimodal film. When visually inspecting the films after testing with EIS there was a clear difference in the color of the films. The bimodal film had lost more of the yellow color. As a quick side experiment the concentration of inhibitor found in Prohesion solution after immersing the films were determined, and the concentration of inhibitor was higher for the solution used to immerse the bimodal films, suggesting that the bimodal film releases inhibitor faster when compared to the unimodal system. This compliments the EIS data that says the ion resistance for the bimodal system is lower than the unimodal system.

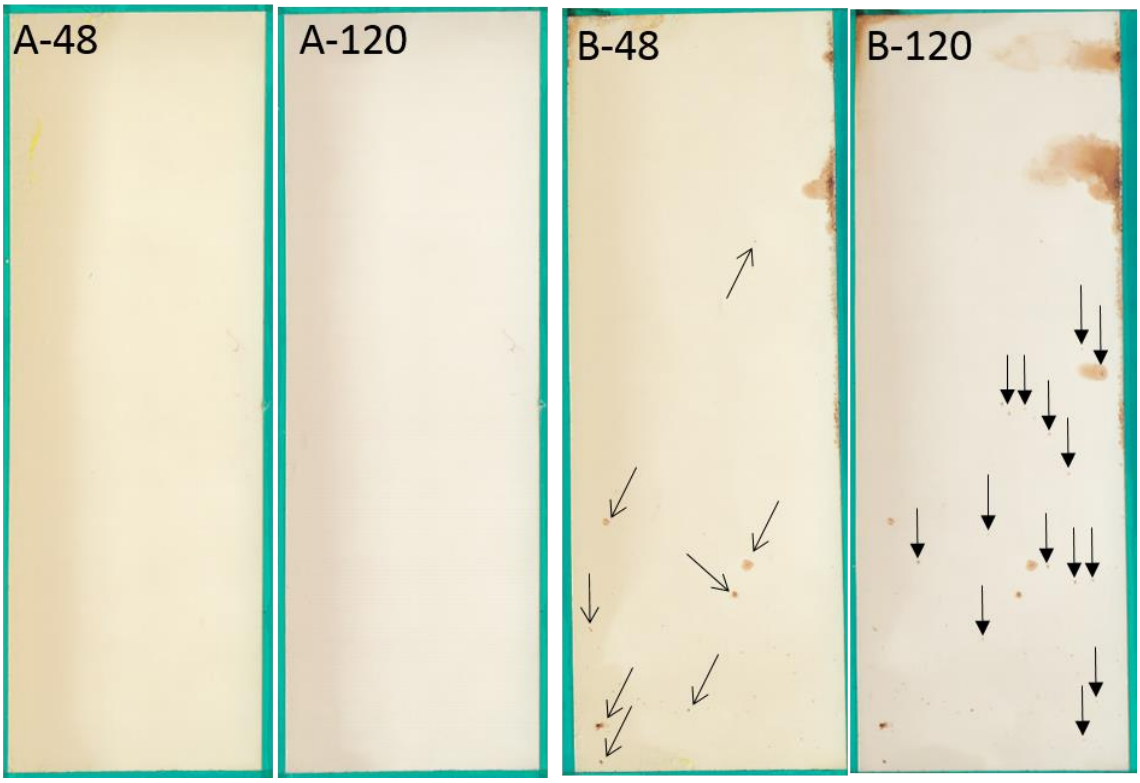

Figure 5.5 Pictures of the unimodal (A) and bimodal (B) Go9v9 beta 2 pigments films after 48 and 120 hours of exposure in a Prohesion chamber.

When challenging the films to the accelerated corrosion procedure called Prohesion, the unimodal system appeared to fair better than the bimodal system. As can be seen in Figure 5.5, the bimodal system showed rust spots. When combined with the EIS data and OCP data, it suggests that the unimodal system has better corrosion protection properties.

5.3.2 Go9v10 Water Uptake

5.3.2.1 Gravimetric Uptake

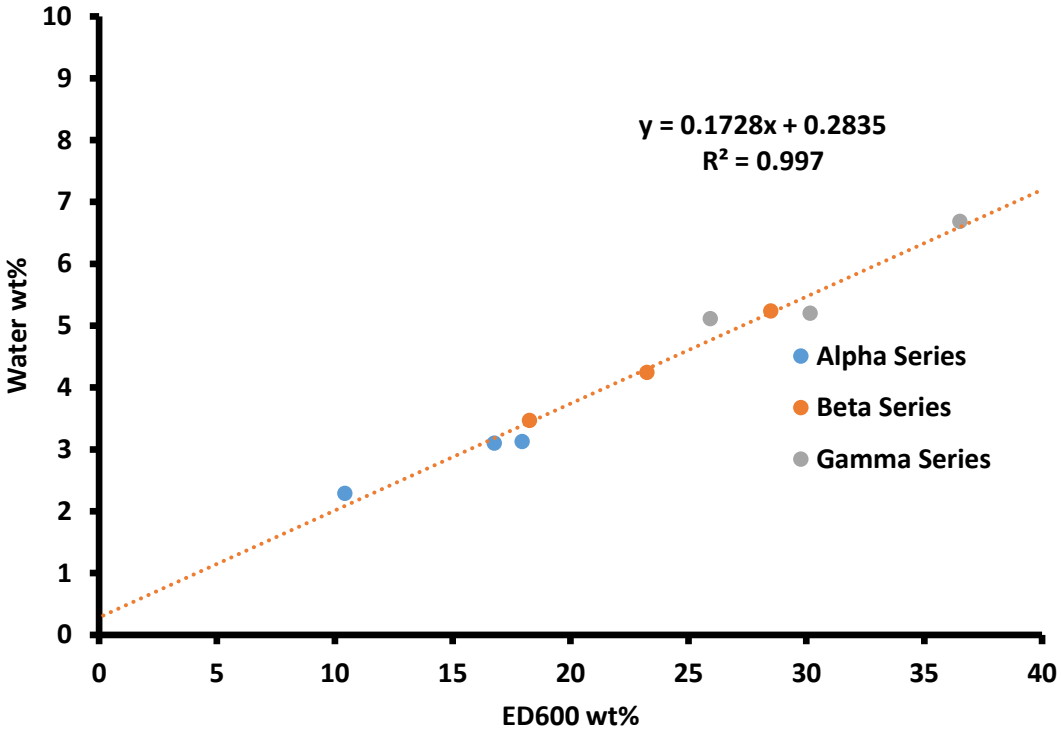

Figure 5.6 Gravimetric water uptake from free films immersed in 5% w/v NaCl.

Note: The epoxy amine free films were prepared as described in section 5.2.1.

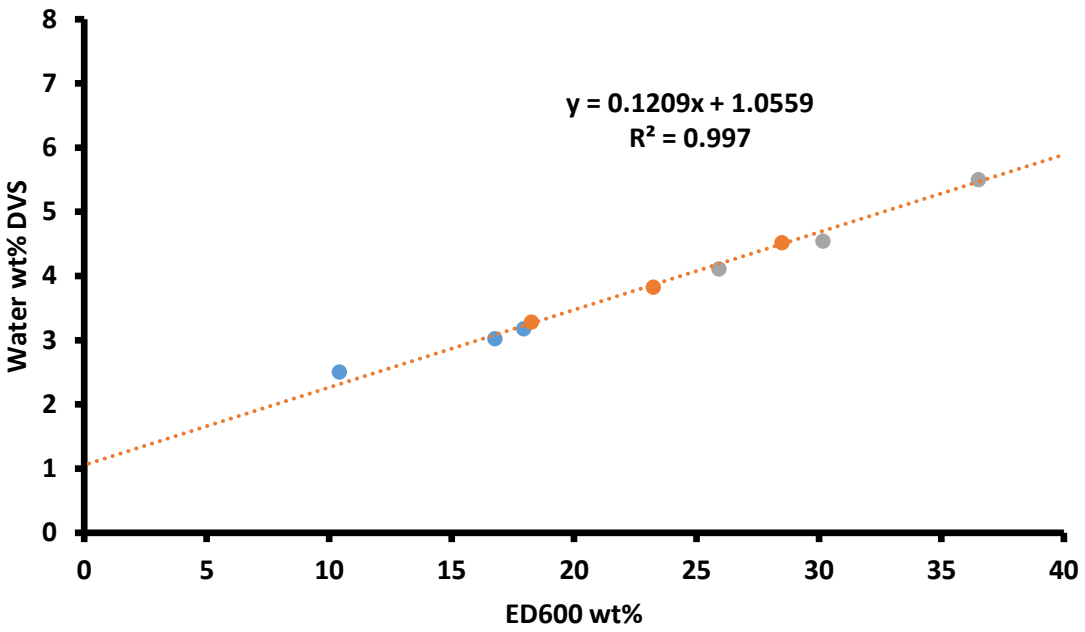

Figure 5.7 Gravimetric water uptake from free films using DVS.

Note: The epoxy amine free films were prepared as described in section 5.2.1.

Water uptake was primarily dictated by Jeffamine ED600 content within the films, with an increase in water content with Jeffamine ED600 (Figures 5.6 and 5.7). The effect of crosslink density on water uptake is minimal; the small change in hydrophilicity from secondary hydroxyl formation during cure is dwarfed by the effect of polyether content.

5.3.2.2 Near IR Water Uptake

Assuming the relationship between absorbance and concentration follow Beer's Law we should expect the following:

$$\frac{A_{5200}}{A_{4620}} = \frac{\varepsilon_{water}[water]}{\varepsilon_{benzyl}[benzyl]} \qquad (5.10)$$

Using the relationship between concentration of the normalized functionality that gives absorbance at 4620 cm^{-1} a calibration relationship can be derived:

$$[water] = \frac{m_{water}}{m_{film} MW_{water}} = \frac{\chi_{water}}{MW_{water}} \tag{5.11}$$

$$[benzyl] = \frac{m_{matrix}}{m_{film} EW_{benzyl}} = \frac{\chi_{matrix}}{EW_{benzyl}} \tag{5.12}$$

$$EW_{benzyl} = \frac{m_{matrix}}{\frac{8 * m_{EPON}}{MW_{EPON}} + \frac{5 * m_{BA}}{MW_{BA}}} \tag{5.13}$$

$$\frac{A_{5200}}{A_{4620}} = A_r = K \frac{\chi_{water}}{\chi_{matrix}} = K \chi_r \tag{5.14}$$

$$K = \frac{\varepsilon_{water} m_{film}}{\varepsilon_{benzyl} MW_{water} \left(\frac{8 * m_{epon}}{MW_{EPON}} + \frac{5 * m_{BA}}{MW_{BA}} \right)} \tag{5.15}$$

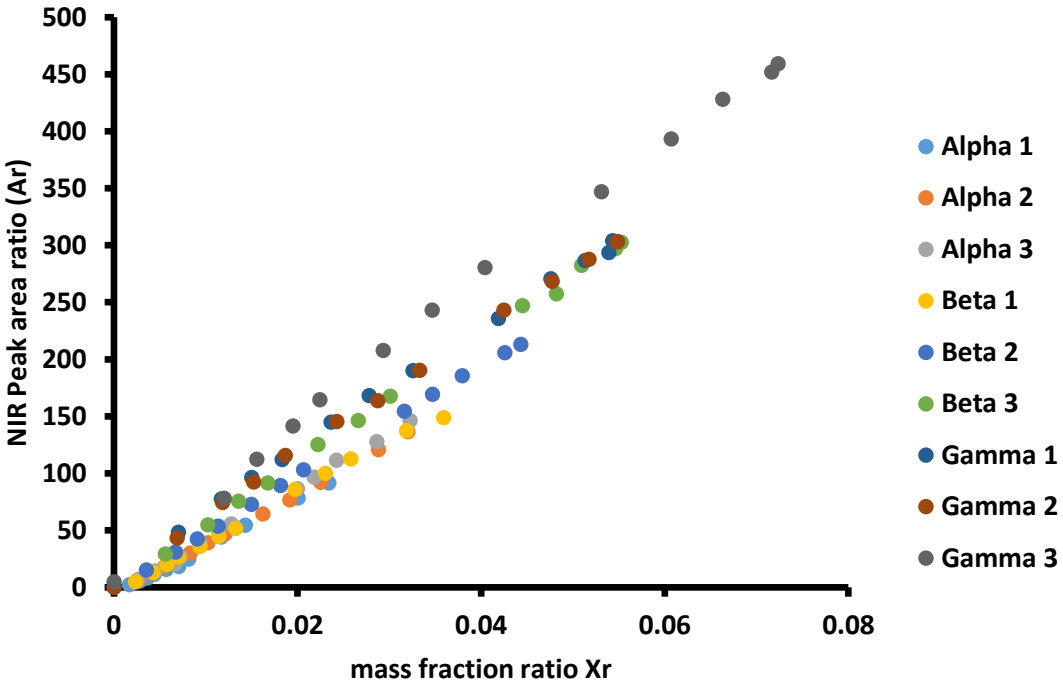

Figure 5.8 Plot of the area ratio vs mass fraction ratio for the Go9v10 free films immersed in 5% w/v NaCl.

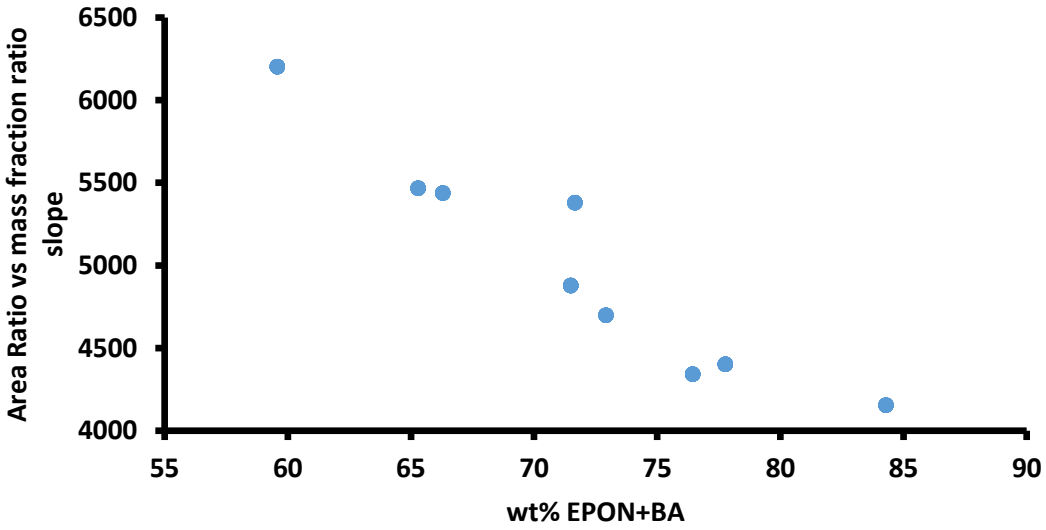

Figure 5.9 Relationship between the wt% of EPON and benzylamine in the Go9v10 films and the slope of the area ratio vs mass fraction ratio plots seen in Figure 5.8.

Based on the linearity of the plots produced for calibration (Figure 5.8), Beer's Law appears to hold true, and the slopes for the different films when plotting Ar vs χr increase with decreasing EPON 825 and benzylamine wt% in the formulation (Figure 5.9), as expected with the relationship derived above. When plotting Ar vs $\frac{EW_{benzyl}}{MW_{water}} * \chi_r$ the lines nearly fall on top of each other with the exception of the gamma series (Figure 5.10). It is unclear if this deviation is from error or caused from something else.

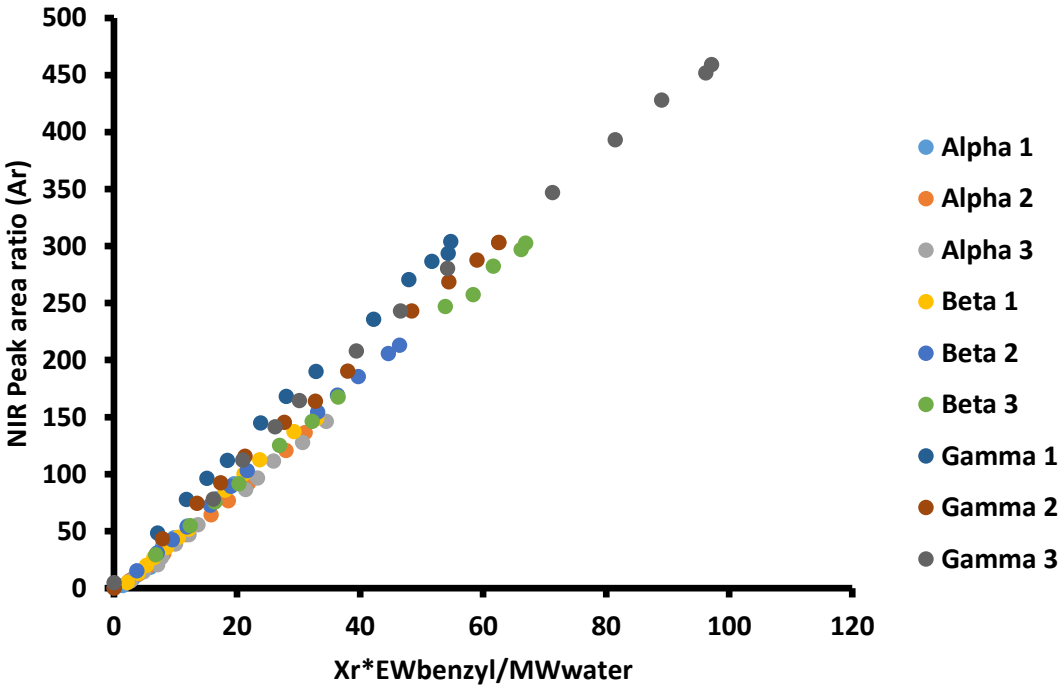

Figure 5.10 Plot of the area ratio vs the mass fraction ratio times $\frac{EW_{benzyl}}{MW_{water}}$ for the Go9v10 films immersed in 5% w/v NaCl.

5.3.2.3 Brasher-Kingsbury Evaluation

The Brasher-Kingsbury equation[114] was used to determine water vol fraction, and this volume fraction was used to estimate wt% :

$$water\ wt\% = \frac{100 * log\left(\frac{C(t)}{C(0)}\right)}{\log(80)\,\rho_{polymer}} \quad (5.16)$$

Densities of the polymers were found to be statistically the same at 1.16 g/ml using the Archimedes method. There are several assumptions associated with the Brasher-Kingsbury equation:[110]

- The dielectric constant of bound and unbound water is equal
- Water uptake into the film is homogenous and water inclusion shape does not affect the capacitance of the film
- The electrolyte composition of the solution does not affect the measured capacitance of the film
- There are no polar solvent that can leech out of the film to alter capacitance measurements
- The effect of swelling on capacitance is negligible

C. Vosgien Lacombre et al.[125] already studied the effect of swelling and how that can account for the deviation between gravimetric results and EIS results. To quantify how much EIS overestimates water wt%, the ratio between EIS and corrected gravimetric water wt% Fickian region slopes were recorded. These values are given in Figure 5.11.

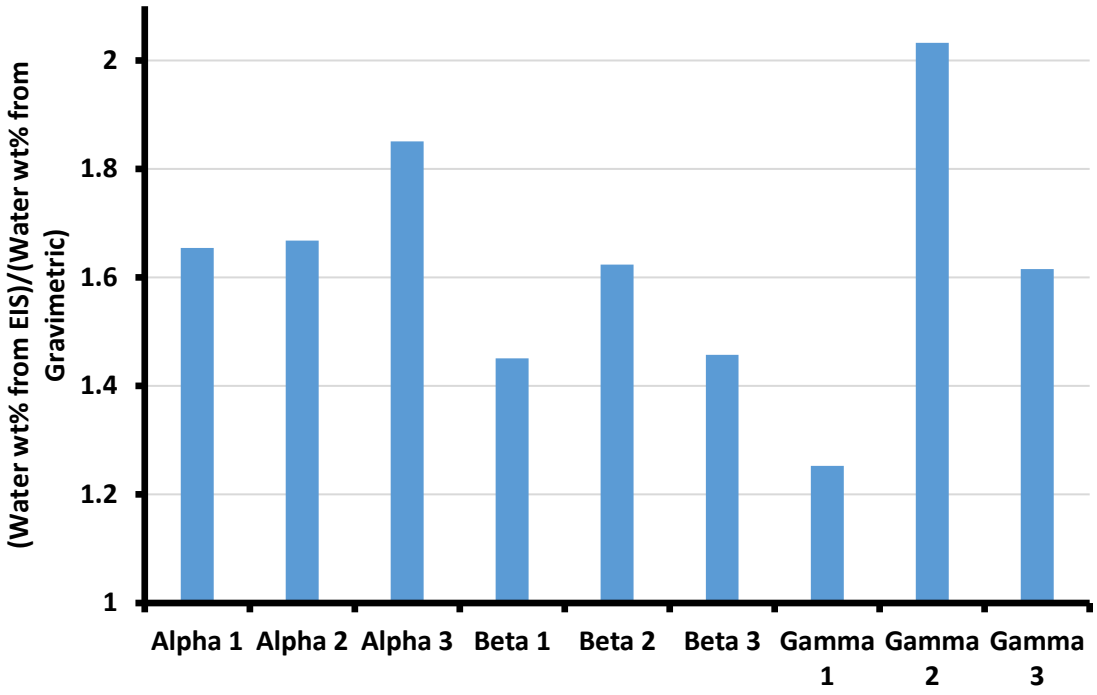

Figure 5.11 Overestimation of the Brasher-Kingsbury equation using EIS data for the Go9v10 series.

Assuming that swelling can fully account for these deviations, then overestimation of water content should follow:

$$\frac{\phi_{EIS}}{\phi_{Grav}} = \frac{log\left(\frac{C(t)}{C(0)}\right)}{log\left(\frac{C(t)d(0)}{C(0)d(t)}\right)} \tag{5.17}$$

$$\therefore \quad \frac{\phi_{Grav}}{\phi_{EIS}} = 1 + \left(\frac{log\left(\frac{d(0)}{d(t)}\right)}{log\left(\frac{C(t)}{C(0)}\right)}\right) \tag{5.18}$$

$$\therefore \quad log\left(\frac{C(t)}{C(0)}\right)\left(\frac{\phi_{Grav}}{\phi_{EIS}} - 1\right) = log\left(\frac{d(t)}{d(0)}\right) \tag{5.19}$$

$$\therefore \quad \frac{d(0)}{d(t)} = \left(\frac{C(t)}{C(0)}\right)^{\left(\frac{\phi_{Grav}}{\phi_{EIS}}-1\right)} \tag{5.20}$$

If we assume the following relationship is true:

$$\frac{d(0)}{d(t)} \propto \frac{l(0)}{l(t)} \tag{5.21}$$

Where d is the thickness and l is the length of the DMA bars used for RH_DMA swelling experiments, then a linear relationship between $\frac{l(0)}{l(t)}$ and $\left(\frac{C(t)}{C(0)}\right)^{\left(\frac{\phi_{Grav}}{\phi_{EIS}}-1\right)}$ is expected. Poor correlation suggests that at least one of the following assumptions cannot be true:

- The difference in proportionality constants for hygroscopic swelling between formulations are negligible
- $\frac{\phi_{EIS}}{\phi_{Grav}}$ is only affected by swelling of the polymer

There was a lack of correlation between $\frac{l(0)}{l(t)}$ and $\left(\frac{C(t)}{C(0)}\right)^{\left(\frac{\phi_{Grav}}{\phi_{EIS}}-1\right)}$ as seen in Figure 5.12, therefore, one of the above assumptions is false. To test which assumption is false requires direct measurement of thickness changes with swelling to see if proportionality constant differences are not negligible; the instrumentation we have prevent us from doing so. Future work to measure the differences between x, y, and z swelling of these films is required to better understand EIS overestimation.

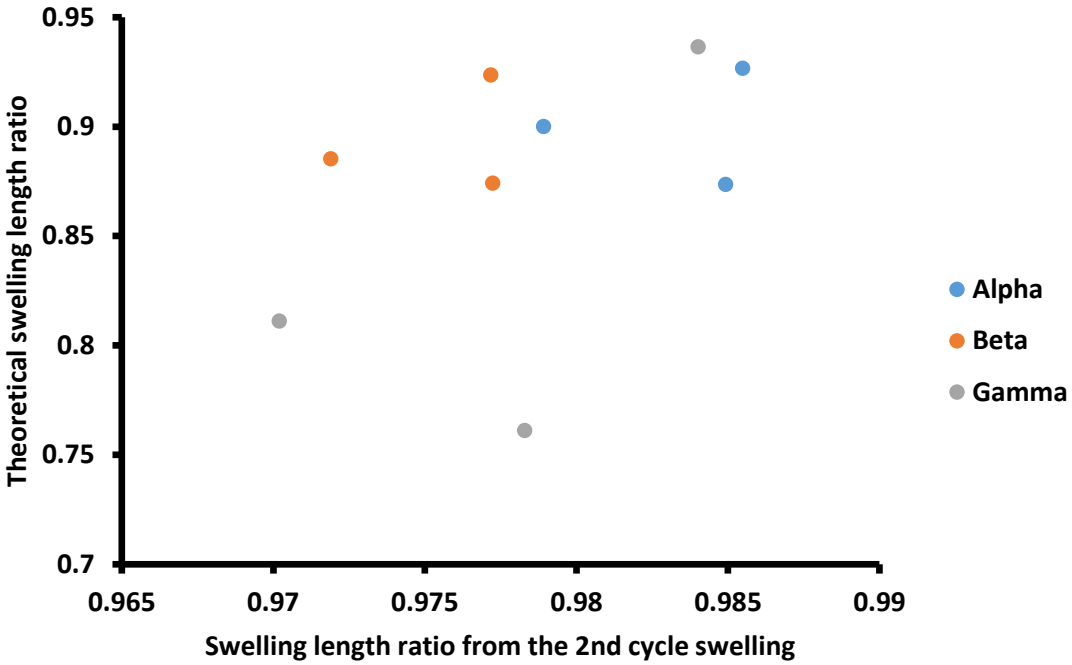

Figure 5.12 Plot of $\left(\frac{C(t)}{C(0)}\right)^{\left(\frac{\phi_{Grav}}{\phi_{EIS}}-1\right)}$ vs $\frac{l(0)}{l(t)}$ for the Go9v10 films.

Note: If swelling completely accounts for the overestimation of water volume fraction in the film, this should show a clear linear relationship. The poor correlation suggests that another variable should be introduced to account for the overestimation.

5.3.2.4 Film Resistance

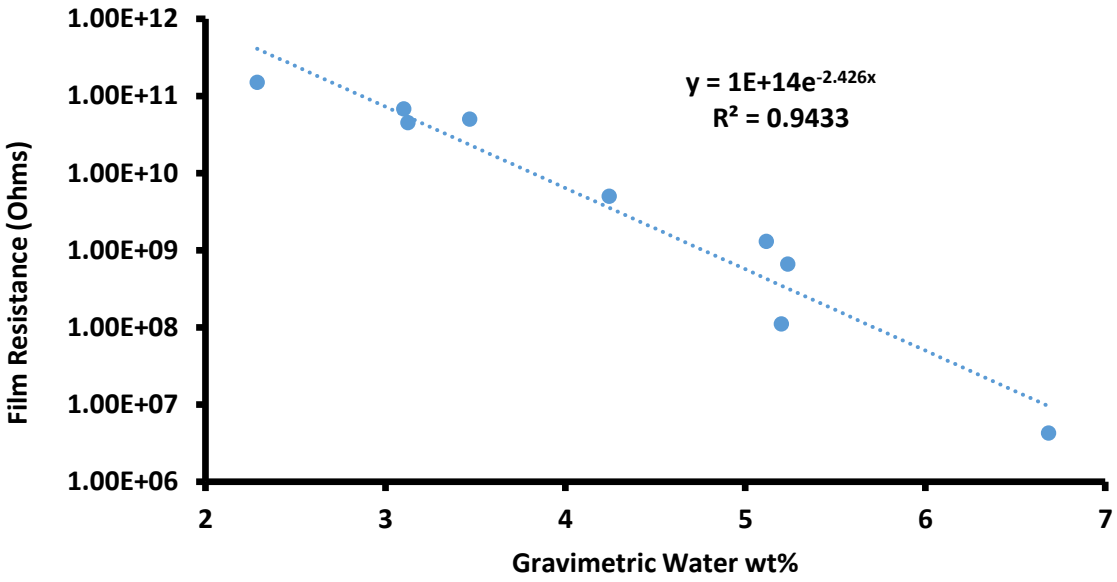

Figure 5.13 Relationship between film resistance after aging bound films in 5% w/v/ NaCl and the gravimetric uptake as saturation for that film.

The hydrophilicity of the films, quantified by water wt% at saturation and controlled by ED600 content, empirically had an exponential relationship with film resistance. Whether this is the result of some type of Arrhenius relationship with activation energy for ion transport being controlled by water content, or a percolation effect that appears exponential is unclear. Crosslink densities did not appear to influence film resistance; the film resistance of Gamma 1 and Beta 3 and well as Beta 1 and Alpha 3 have similar film resistance (Figure 5.13). Any apparent relationship between T_g and film resistance were likely coincidental, as T_g was partially controlled by ED600 content, which also controls water content.

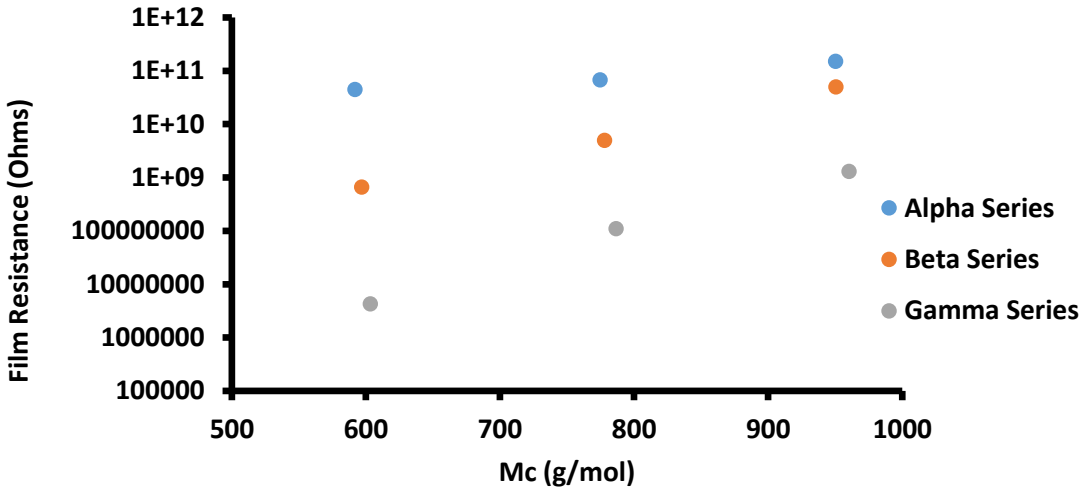

Figure 5.14 Relationship between bound film resistance and theoretical molecular weight between crosslinks.

Like ion resistance, water vapor transmission rates had an exponential relationship with water wt% at saturation, which may also be an Arrhenius like or percolation relationship like ion resistance. Considering that the ion resistance and water vapor transmission rate follow similar trends with water content, it is possible that water rich regions are forming in the films. Both ion and water molecules can then more easily transport through these water rich regions, which is why both follow exponential trends. Both an Arrhenius and percolation explanation for the trends support the possibility of water rich regions forming in the films. For an Arrhenius relationship to more water rich regions available the lower the activation energy for transport, and for percolation to occur at such low water content suggests more elongated regions to allow percolation to occur.

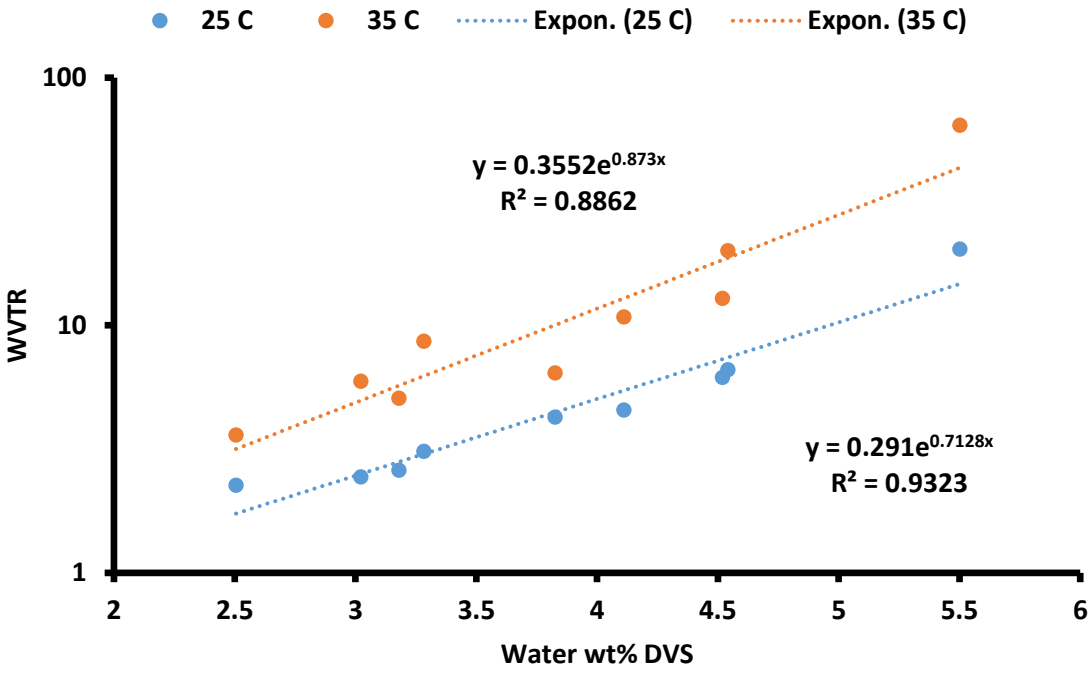

Figure 5.15 Relationship between DVS saturated water uptake and WVTR at 25 and 35 degrees Celsius.

To explain how water rich regions could be forming in the film, we propose that there was small scale phase separation between two portions of the crosslinked network; the more hydrophobic DGEBA chains crosslinked with 1,3-BAC, and the more hydrophilic ED600 crosslinks.

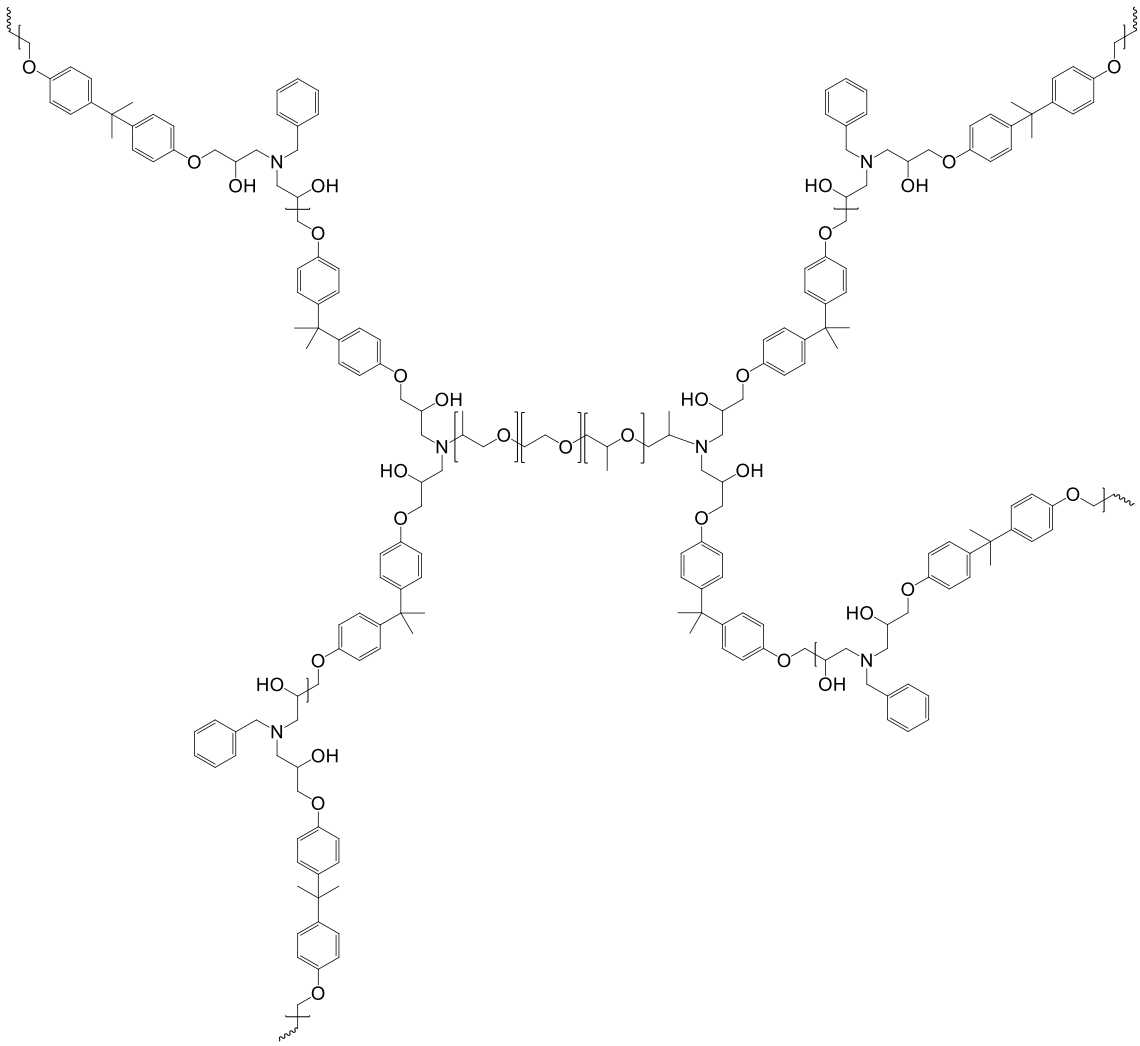

Scheme 5.1 Go9v10 more hydrophilic crosslink example.

Note: Exact stoichiometry is not shown in the above scheme. The scheme is meant to show one of many possible yet similar regions in the polymer matrix that would be more hydrophilic compared to other regions of the matrix.

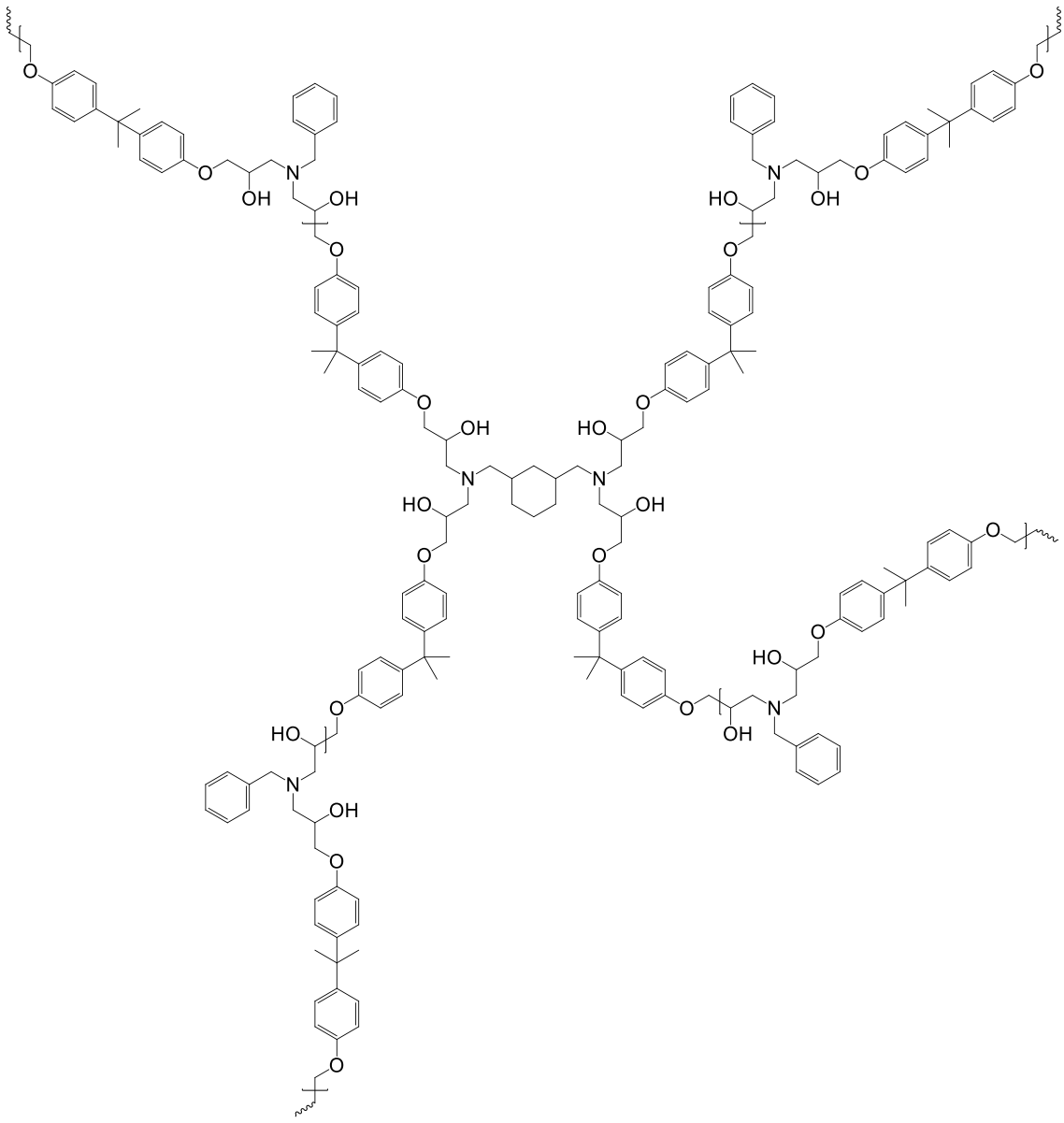

Scheme 5.2 Go9v10 more hydrophobic crosslink example.

Note: Exact stoichiometry is not shown in the above scheme. The scheme is meant to show one of many possible yet similar regions in the polymer matrix that would be more hydrophobic compared to other regions of the matrix.

The phase separation creates percolating hydrophilic paths that water will preferentially diffuse into. These channels dictate water vapor transmission, and act as low resistance pathways for ions. The crosslink density of the matrix mostly alters the mechanical

properties of the more hydrophobic portions of the matrix that act as walls for the hydrophilic channels. Increasing the crosslink density will not alter ion resistance and water vapor transmission rates because water molecules and ions primarily move through ED600 rich regions that are mostly unaltered by bulk matrix crosslink density.

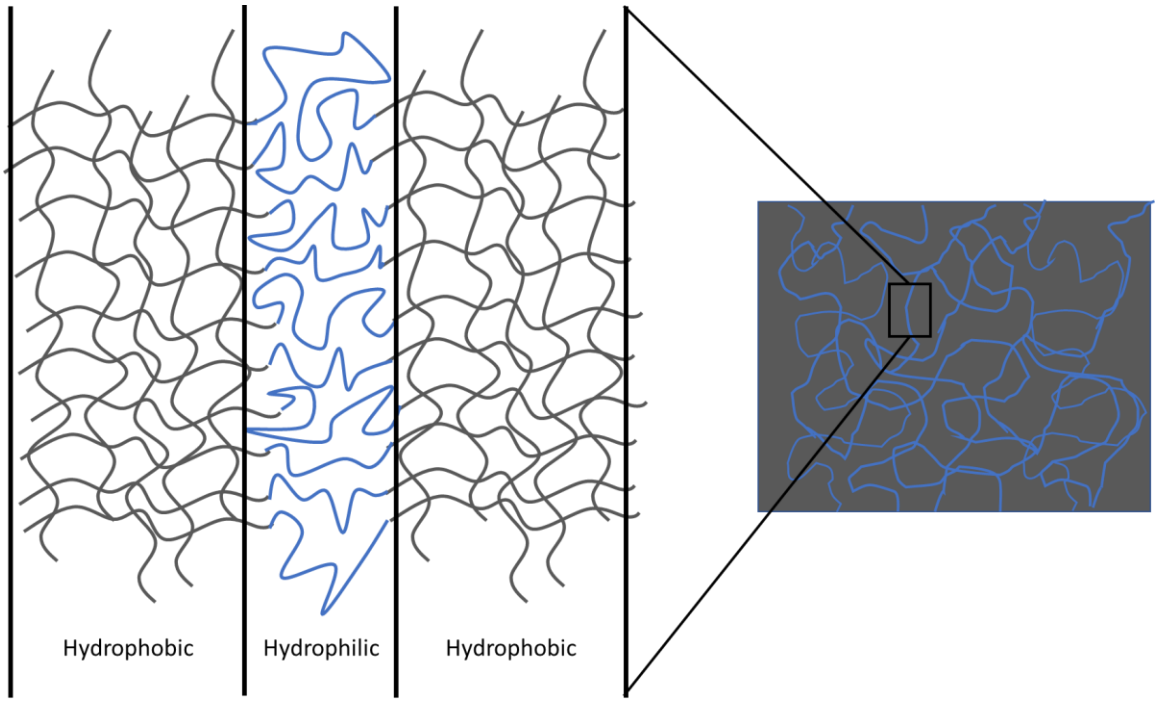

Figure 5.16 Diagram to help visual a possible morphology to explain results for the go9v10 series.

In an attempt to probe this morphology, we looked at relationships between swelling properties of the films and EIS overestimation of water fraction.

5.3.2.5 Hygroscopic Swelling

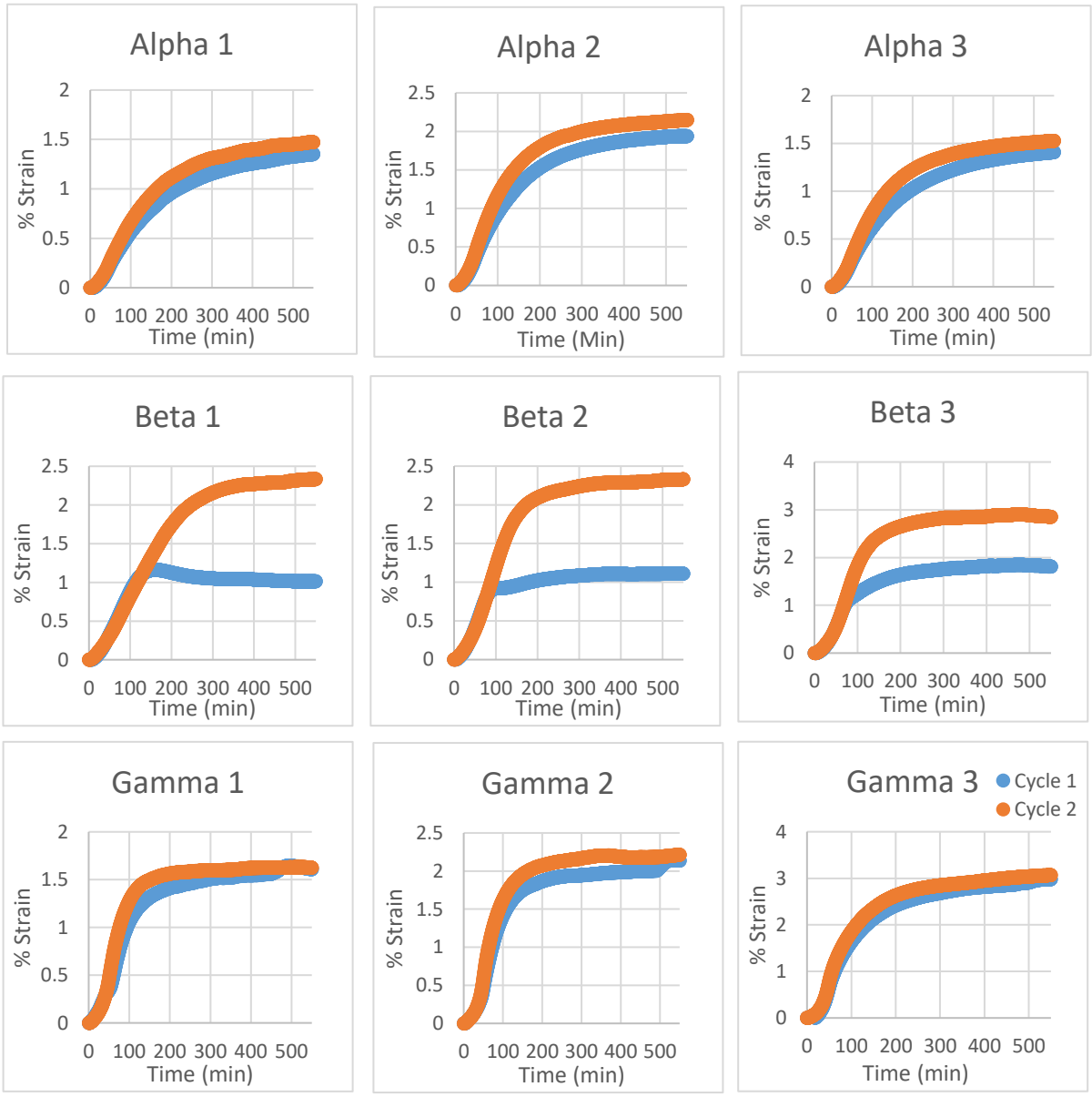

Figure 5.17 Hygroscopic swelling results for the go9v10 series.

For all films there was a difference between the first cycle and subsequent cycles for the RH-DMA swelling experiments (see Figures above). For the alpha and gamma series the strain is slightly larger on subsequent cycles, but for the beta series there is a large difference on subsequent cycles. The first cycle is removing an aging effect from the

films, and then cycles begin to fall on top of each other. It is not obvious why the beta series has such a large ageing effect, but we do know that Beta is the most likely to have conditionally specific shifts between glassy and rubbery physical states.

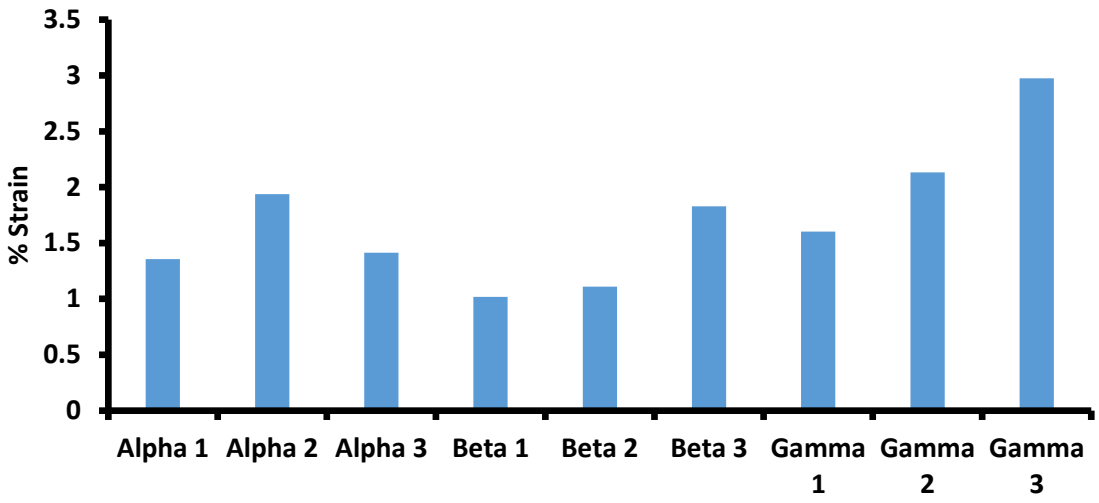

Figure 5.18 Max strain from swelling results on the first cycle for the Go9v10 series.

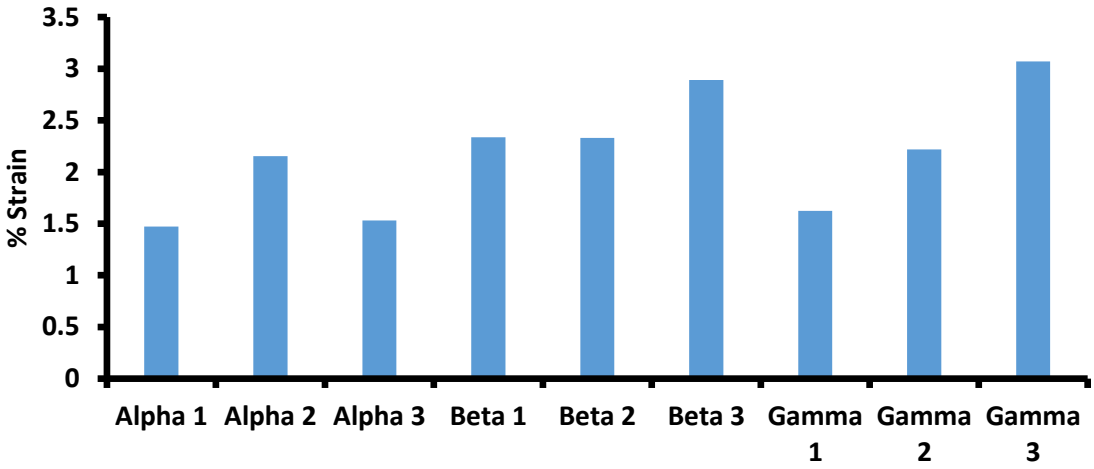

Figure 5.19 Max strain from the swelling results on the 2nd cycle for the go9v10 series.

Other than alpha 2, there seems to be a trend where swelling follows 1 < 2 < 3 within a series, which means that an increase in ED600 content increases swelling, but only within a series. Hydrophilicity, measured by water wt% at saturation, does not completely predict swelling for the films studied. This is because swelling also relates to the mechanical properties of the polymer matrix. When water enters a polymer matrix it first fills void space, and then displaces polymer chains which causes swelling.

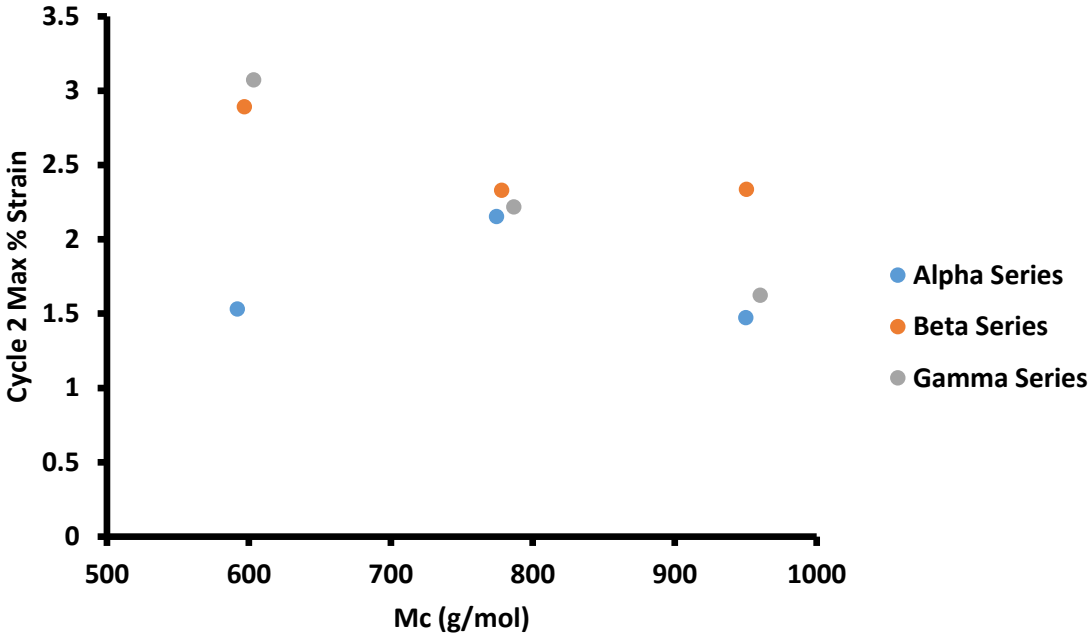

Figure 5.20 Relationship between max strain from the 2nd swelling cycle and the theoretical crosslink density of the go9v10 series.

When looking at the theoretical crosslink density of the films, it appears that the lower the M_c (higher crosslink density) the higher the swelling, which is counterintuitive because we would expect less mobility with a higher crosslink density. The reason for this apparent correlation is likely caused from the correlation between ED600 content and

M_c. For this reason, it appears that the swelling of the polymer films may not be affected by crosslink density.

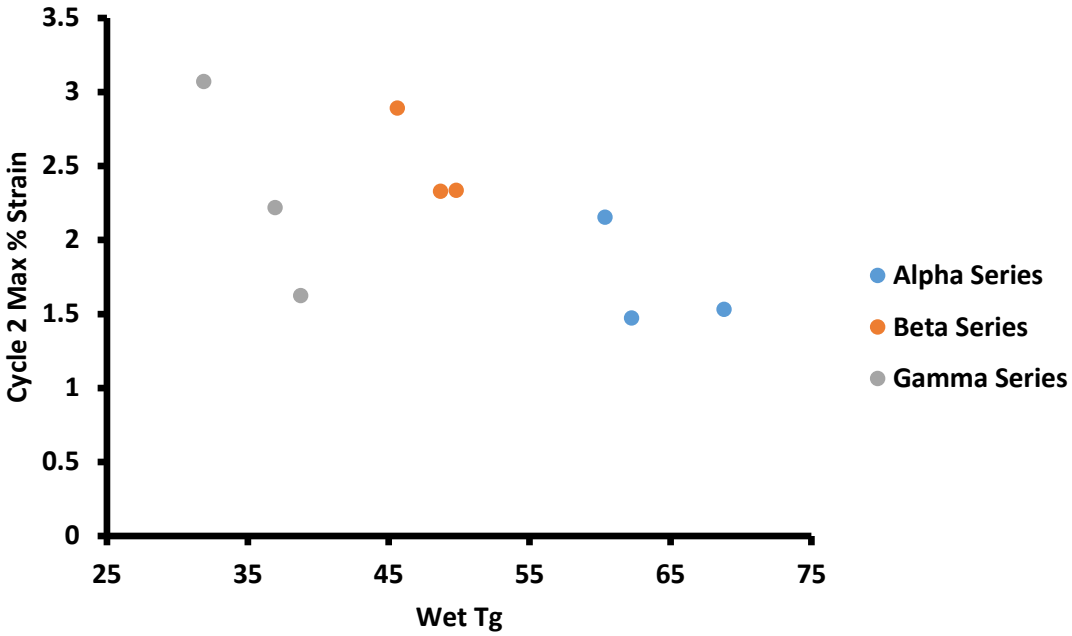

Figure 5.21 Relationship between the 2nd cycle swelling results and the wet T_g of the go9v10 series.

The swelling of the films occurs with water uptake, and the max swelling occurs after water saturation. For this reason, we looked at the wet T_g for correlating with swelling, as this is the T_g of the film when it has swelled. Within each series there is a correlation between the wet T_g and swelling, which is expected because a lower T_g means more chain mobility. Unfortunately, there is also a correlation between ED600 content and wet T_g of these films, so this too could be an accidental correlation.

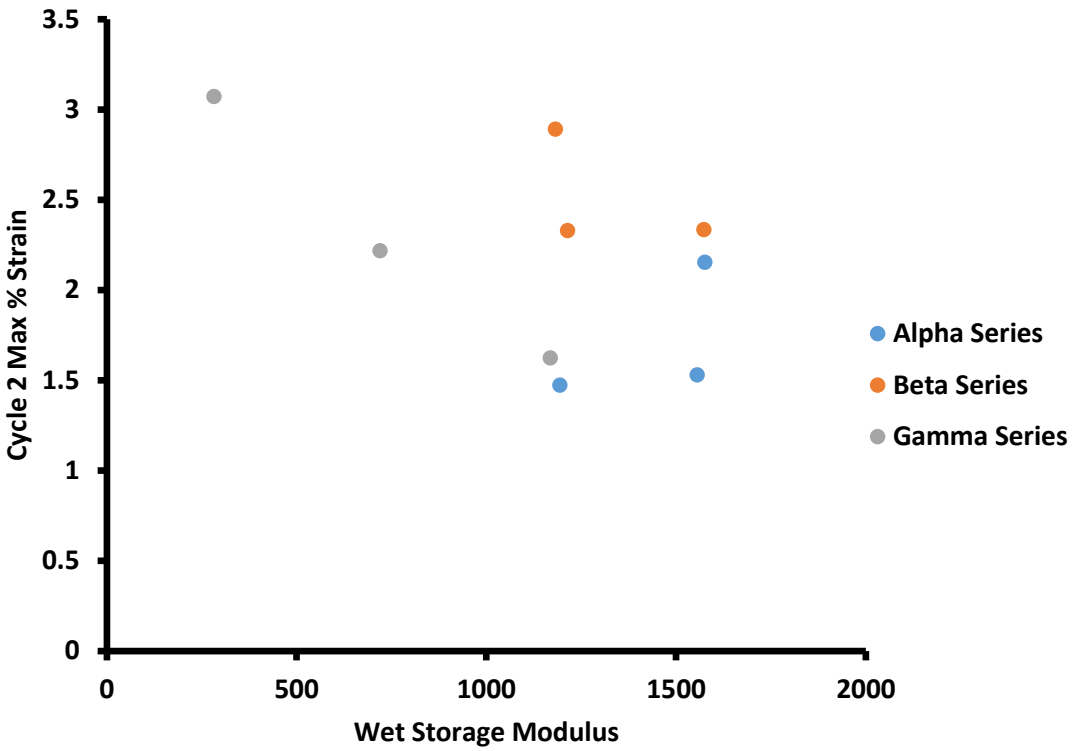

Figure 5.22 Relationship between the 2nd cycle swelling results and the wet storage modulus for the go9v10 series.

There was no correlation between wet storage modulus and swelling, except for the Gamma series, but once again any correlation could be accidental, and they are primarily controlled by ED600 content. For this reason, it appears that additional films should be studied to better understand what predicts swelling, but we hypothesize that the relationship between testing temperature and wet T_g is what is required. When looking at the relationship between ED600 content and swelling we found that there is a good correlation when separating Gamma from the rest. The testing temperature is near the wet T_g for the gamma series, so it may be the case that films tested near the T_g have a lower measured swelling.

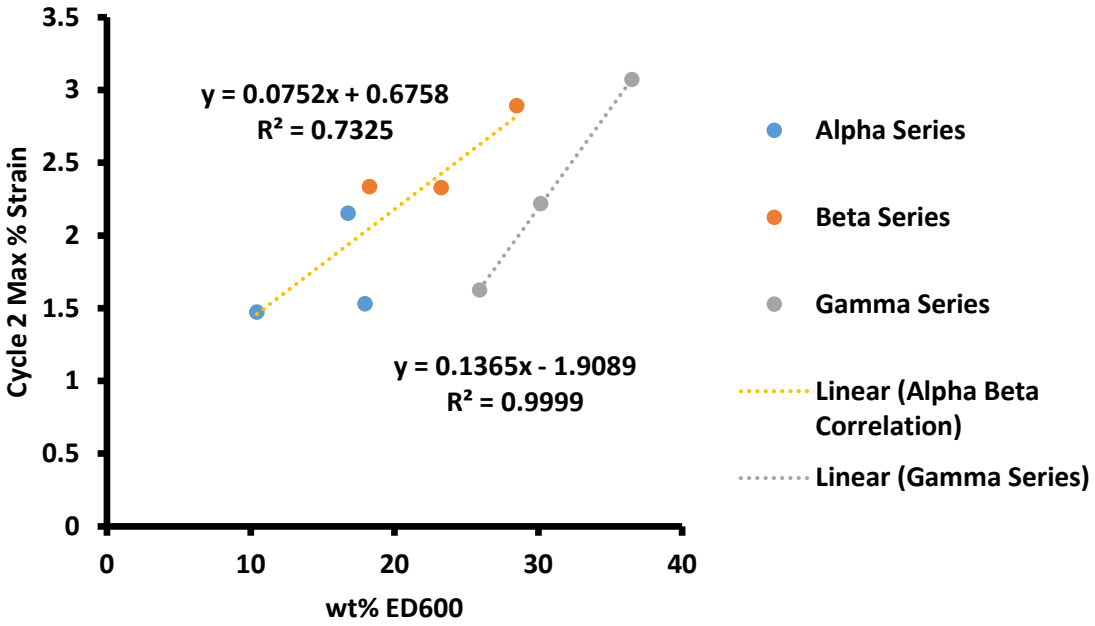

Figure 5.23 Relationship between the 2nd cycle swelling results and the ED600 content of the go9v10 films.

To test the relationship between swelling and measured properties, we conducted step linear regression. One variable we introduced was a Boolean variable "near T_g" where the testing is within 5°C of the wet T_g of the material it is given a value of 1, otherwise it is given a value of 0. The step regression found that only ED600 and "near T_g" predicted swelling of the films. The results suggest that when testing near the T_g of the film, swelling decreases. To test this, we could look at the swelling of the other series near their T_g, to see if this trend continues for the pother series. An explanation of this results is that water enters the water rich regions of the film, and these regions begin to swell. The larger the volume fraction of these hydrophilic regions the larger the swelling ratio of the film, which is an intuitive result. When the film is a glass (testing temperature not near wet T_g) film can only release the stress by moving hydrophobic regions away from the swelling hydrophilic regions to give bulk film swelling. When the

film is a rubber (testing temperature near wet T_g) the hydrophobic regions have enough mobility to relieve some of the stress from swelling by relaxing into free void space in the film, resulting in less bulk swelling of the film.

5.4 Conclusions

A series of epoxy-amine films were developed with controlled hydrophilicity, T_g, and Mc for evaluation of water uptake, water vapor transmission, and film ion resistance. Hydrophilicity of these films from bulk measurements were primarily dictated by polyether content controlled by Jeffamine ED600 wt% in the formulation. Evidence of heterogeneous water uptake was found from evaluating the lack of correlation between hygroscopic swelling measured using RH-DMA and Brasher-Kingsbury overestimation of water content from capacitance values quantified using EIS, but actual measurement of swelling in the z direction is required before a better conclusion can be drawn. Furthermore, ion resistance and water vapor transmission rates were mostly unaffected by film T_g and Mc, suggesting that water and ion transport through these films were through more hydrophilic pathways generated by phase separation between polyether segments and DGEBA segments during cure. Instead, film T_g and Mc altered hygroscopic swelling properties. Hygroscopic swelling of the films was best predicted using ED600 content and whether the film was test near the wet T_g or not. ED600 content gave the intuitive result of more swelling, and testing near the wet T_g of the film reduced measured swelling. This potentially allows development of a series of epoxy-amine films that have equivalent hydrophilicity, ion resistance, and water vapor transmission rates with different hygroscopic swelling parameters and different mechanical properties for evaluation of these properties on corrosion performance. Ion resistance and water vapor

transmission rates had exponential relationships with water content like an Arrhenius relationship. We expect that water and ion transport through epoxy-amine films without components that tend to phase separate would have tortuosity primarily controlled by crosslink density and free hole volume. From our experience regardless of hydrophilicity of the films, electrolytes will diffuse through the film in a relatively short timeframe, so the view that making a film more hydrophobic will improve performance of corrosion protection films is misplaced.

CHAPTER VI – Evaluation of Polythiophene Films

The purpose of this chapter is to evaluate the corrosion altering properties of polythiophenes using the copolymers synthesized in chapter 2, characterized in chapter 3, using the techniques outlined in chapter 4, and keeping in mind the data obtained in chapter 5 on non-conductive films for comparison.

6.1 Introduction

One of the proposed mechanisms for corrosion protection using conductive polymers is the anodic polarization of the substrate to induce a passive state that has a lower rate of corrosion compared to free dissolution of the metal. For anodic protection if the substrate is not polarized enough, then a passive state is never reached, and corrosion is accelerated, and if the polarization is too high the passive film breaks apart and the corrosion rate reaches disastrous rates. We hypothesize that there would be an optimal onset oxidation potential of the polythiophene for corrosion protection, where too high of a potential polarizes the substrate too much, and too low does not polarizes the substrate enough for induction of a passive state. Using a combination of EIS, OCP, and EFM we planned to determine if this hypothesis is correct.

6.2 Materials and Methods

All electrochemical experiments conducted in this section follow the same procedures previously described in this document, and the materials are those synthesized in house, as described in chapter 2.

6.2.1 Film Preparation

Preparation of consistent defect free polythiophene films is very important when trying to determine the anti-corrosive properties of the polymer because any barrier

properties of the film can be easily bypassed through defects. Spin coating was attempted at first due to the widespread use of the technique for polythiophenes,[127,128] and because it uses little material. The homopolymer P3HT gave even coverage of the substrate via spin coating, but the topology of the metal substrate made it easy for high parts of the metal to peak through the film, and the polymer to primarily pool in lower parts of the metal. Even with polishing the metal to a mirror finish using diamond paste would likely not alleviate the problem, as spin coating generally produces films on the nanometer scale in thickness and the polishing would produce micron scale roughness. Another coating technique was spray coating, and although we managed to produce uniform films, the amount of polythiophene used made this technique too expensive. Instead polythiophene films were prepared vi drop cast method for this project.

To give reproducible films we used a solvent mixture of chloroform and n-butanol. The chloroform would evaporate away and leave a poor solvent for the polythiophene behind. As this happens the polythiophene would begin to form a gel film. The butanol would then slowly evaporate away from the polymer and consistently leave a macroscopically referenced defect free film on the substrate that was around 5 um in thickness. The thickness could potentially be controlled by the volume of solution dropped on to the substrate as well as concentration. We would recommend not to lower or raise the concentration as that would require changing the solvent composition to get consistent films. The films first formed a gel from solubility decreases due to good solvent evaporation. This lessened edge and coffee ring effects. Even though there were edge effects, they were much smaller than if a single solvent were used, and the edges of

the substrate and film are masked during testing so only the center is used for collection of data.

Some of the copolymers did not make consistent films, but good films were produced for 6:1, 5:1, and 4:1 copolymers. It is unclear why some of the polythiophenes failed to produce films good enough to get reliable corrosion results.

6.3 Results and Discussion

6.3.1 Open Circuit Potential

Even though OCP measurements can be misleading, they still can help us in determining how the polythiophenes primarily alter corrosion. We hypothesized that due to the semi-conductive nature of the polythiophenes that they would not have large capacitive charging on the results, and that as the onset oxidation potential of the polymer decreased, so should the OCP of the coated substrate. What we found was that the OCP had a trend upwards as more 3,4-ethylenedioxythiophene was introduced into the polymer.

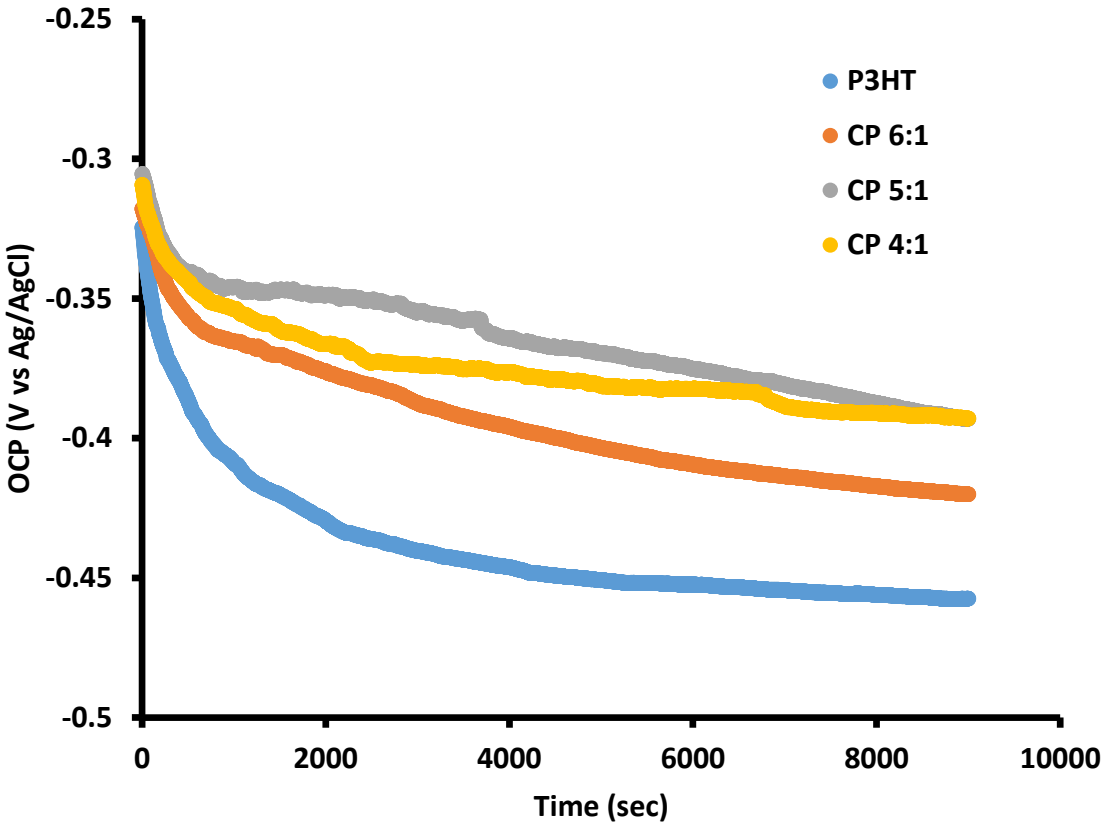

Figure 6.1 Average OCP for 3 samples of the polythiophenes.

Note: The CP ratio is the feed ratio between 3-hexylthiophene and 3,4-ethylenedioxythiophene used during synthesis.

With all of the films they started around the same potential and slowly decreased as to be expected. Unlike bare steel there was no two stage shift in the OCP. This likely indicates that the OCP is primarily shifting due to barrier properties of the films and decreasing the amount of oxygen that can reach the substrate. This would help to explain why the OCP trended away from what was expected. The lower reduction potential of the oxidation process for the polythiophenes suggests that the copolymers should have a smaller effect on polarizing the substrate, but if the polarization is primarily caused by concentration shifts due to barrier properties, then this effect could be masked. To better

understand what was happening we also measured corrosion kinetic data from EFM and film impedance data using EIS.

6.3.2 Electrochemical Frequency Modulation

For all films it did not appear that capacitive charging was having a significant effect on the results, but it should be kept in mind that capacitive charging would trend with impedance and would also cause overestimations in the corrosion rates.

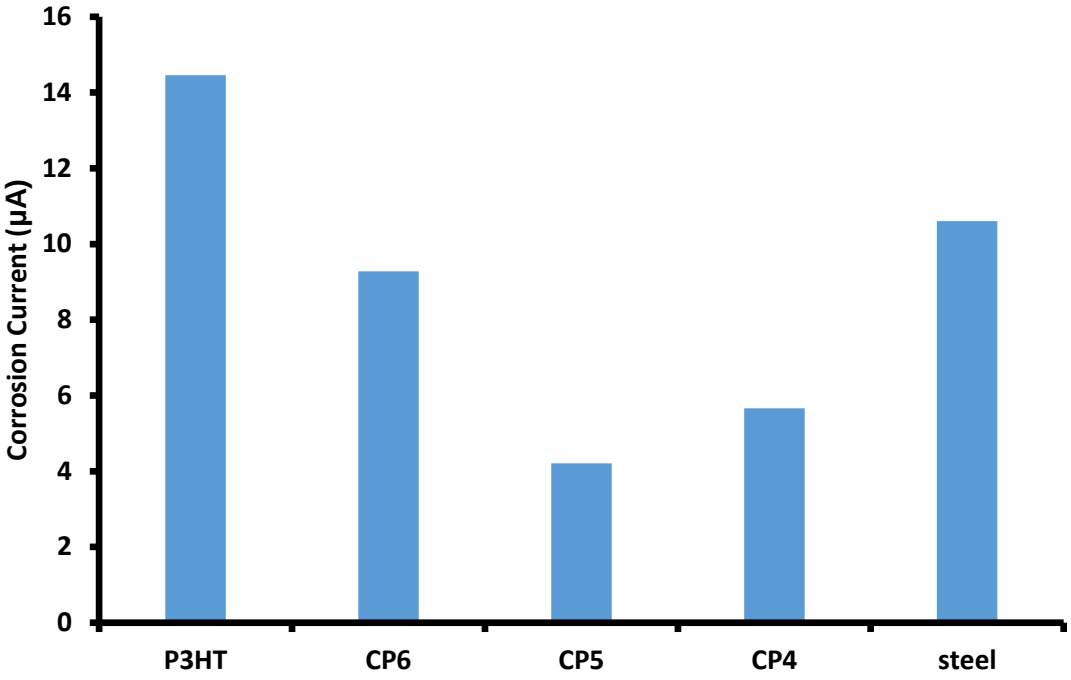

Figure 6.2 Corrosion current calculated using EFM for the different polythiophenes and bare steel for comparison.

When comparing the corrosion rates calculated using EFM there was an unusual trend. The corrosion rate decreased with increasing 3,4-ethylenedioxythiophene up until the ratio 4:1. The homopolymer P3HT resulted in a perceived and possibly real higher corrosion current than bare steel. This could be attributed to capacitive charging effecting the measured results. When only comparing the coated substrates the OCP

results trended with the calculated corrosion rates, which helps to support the idea that OCP can be used to give an idea on the performance of the films. For all the films there was also a relationship with the Tafel slopes, namely that the slopes increased as the corrosion current increased. Combined with the OCP data it appears that the onset oxidation potential of the polythiophenes does not have a large effect on the corrosion altering properties of the polythiophene films, but instead that the film barrier properties are dominant. To further test this we would have to measure the impedance of these films and see if the trend continues.

6.3.3 Electrochemical Impedance Spectroscopy

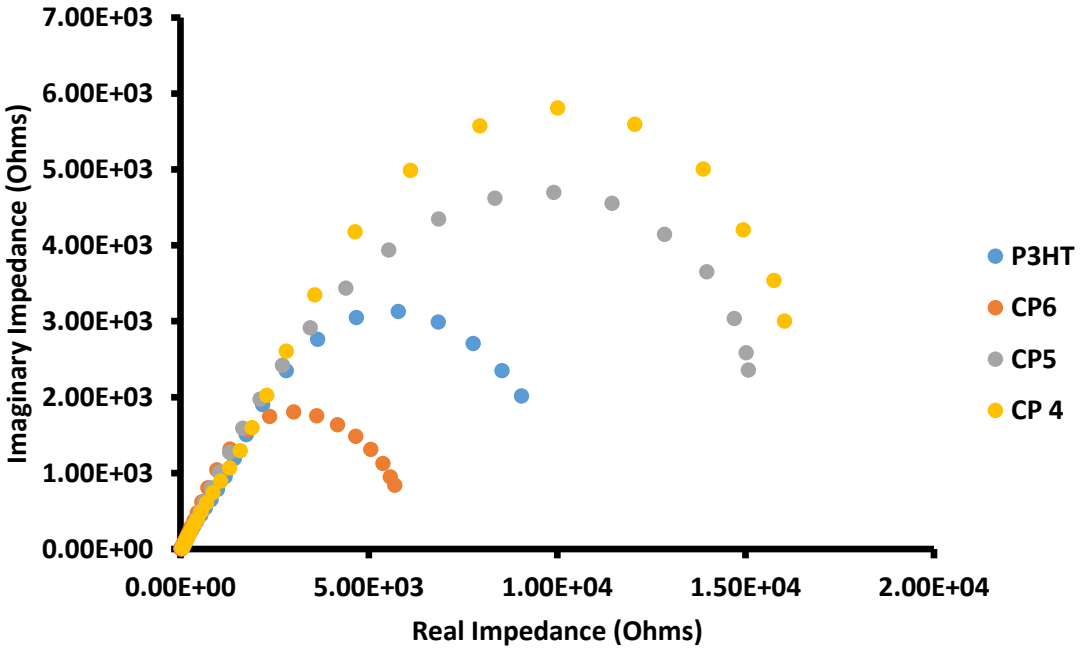

Figure 6.3 Nyquist plots of the different polythiophenes.

Note: The cumber corresponds to how many 3-hexylthiophene type monomers were used per 3,4-ethylenedioxythiophene in the feed during synthesis.

The trend previously seen in both the OCP and the EFM results seems to have changed. For the copolymers there was a trend where the increase in the 3,4-ethylenedioxythiophene content results in an increase in the impedance of the film. This could be attributed to lower solubility of the 3,4-ethylenedioxythiophene units. The lower solubility would change the film formation of the polymers during the drop casting. The copolymers would begin to precipitate earlier than the homopolymer, and they would precipitate sooner the more 3,4-ethylenedioxythiophene units in the backbone of the polythiophene. This would result in the gel forming sooner not allowing flow for defects that drop casting usually produces to form. Alternatively, the introduction of the 3,4-ethylenedioxythiophene unit could be decreasing the crystallization of the polymer, therefore, there would be more amorphous regions in the film that can relax for a more even film formation and better barrier properties. Finally, it could also be the solubility loss from introducing 3,4-ethylenedioxythiophene decreases the hydration level of the films, therefore having less water to allow ion transport through the film.

The P3HT homopolymer had an intermediate impedance compared to the copolymers. The homopolymer is known to form nanowires during slow precipitation, so it is possible that the nanowire morphology of the P3HT has an increased impedance compared to the copolymers. Based on the OCP and EFM data we originally thought that the performance was primarily due to barrier properties, which would trend with impedance, but now it seems that there could be a mixed effect.

6.3.4 Comparing Impedance with Kinetic Data

Although it makes sense that the higher impedance copolymers have lower corrosion currents, it is counterintuitive for P3HT to have the highest corrosion currents,

yet have an intermediate impedance response form EIS. To try and better understand what the data means we looked at the effect of impedance on OCP and EFM results for all the polymers to see if more trends appeared

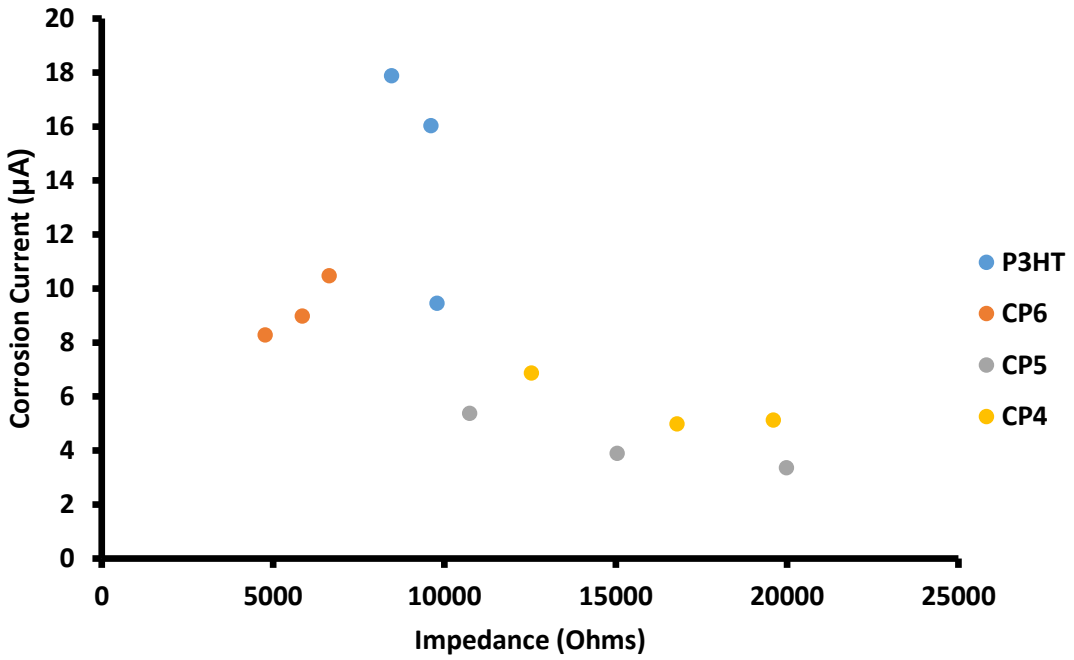

Figure 6.4 Relationship between film impedance and corrosion current from EFM for the different samples grouped by polythiophene type.

The observed overall trend of higher impedances leading to lower corrosion rates were expected. However, this trend does not hold true within each series. For example, the copolymer 6:1 has an increase in corrosion current and an increasing impedance. The polarization effects of the copolymer could have a larger effect than expected. As the impedance increased for this polymer, the corrosion altering properties maximized. It is possible the polarization was insufficient to induce passivation, thus corrosion rate accelerated.

Corrosion rates of copolymer 4:1 were consistently higher than copolymer 5:1 despite impedance shifts. Increasing 3,4-ethylenedioxythiophene content decreases polarization. The impedance has little effect on corrosion rates for these copolymers, as seen by the low slope. Therefore, polarization dominates the corrosion altering. Data suggests an optimal polarization for corrosion performance exists when using polythiophenes.

6.4 Conclusions

We originally hypothesized that a lower onset oxidation potential would decrease corrosion performance due to the lower level of polarization with the substrate, and that barrier properties of the films would play a significant role in the overall performance of the films. When looking at the OCP of the films and the EFM results it first appeared that the barrier properties of the films were dominating the corrosion altering properties of the polythiophene films, and that polarization of the substrate was masked by concentration polarization. When comparing with the EIS data it appeared that there is indeed a competing effect between barrier properties of the film and the polarizing effects of the polythiophene.

For the homopolymer P3HT it seems that the nanowire formation properties are detrimental to performance, despite the increase in barrier properties, likely due to poor passivation of the substrate. Lowering the onset oxidation potential of the polymer by introduction of 3,4-ethylendioxythiophene units into the backbone improved corrosion altering properties of the films up to when a 4:1 ratio was achieved. This suggests that polythiophenes do not polarize steel enough to completely passivate the substrate, and the

lowering the onset oxidation potential could improve performance, but to get the best performance a larger polarization is needed to induce passivation.

With more 3,4-ethylenedioxythiophene the impedance of the polymers increased, and the corrosion rates decreased accordingly, but there seemed to also be an optimal onset oxidation potential for the copolymers used. Too low of n onset oxidation potential having a detrimental effect on performance is likely due to poor passivation of the substrate.

Overall it seems that decreasing the onset oxidation potential of polythiophenes can improve performance even though theses do not appear to polarize significantly, and the CPs likely do not polarize to allow complete passive behavior of steel substrates. Instead it seems that barrier properties synergize with the polarization properties, allowing steel to passivate when it normally would not.

CHAPTER VII – Conclusions and Outlook

This chapter gives the final conclusions and outlook of the project. It also describes what needs to be accomplished and what kind of experiments could be conducted to continue work on this project.

7.1 Overall Findings

By studying polythiophene copolymers with controllable differences in solubility parameters and onset oxidation potentials we were able to improve understanding on how conductive polymers in general alter corrosion performance. The GRIM polymerization route is quasi living for copolymerizing 2,5-dibromo-3-hexylthiophene and 2,5-dibromo-3,4-ethylenedioxythiophene when the metathesis step is completed, but one pot synthesis does not give desired results. Additionally, side reactions from acid catalyzed homopolymerization of EDOT based units can give insoluble products both when synthesizing the monomers and when quenching copolymers. The side reaction can be avoided during quenching of the polymer by using allyl magnesium bromide and the homopolymerization can be avoided when using DMF and excess thiophene.

Despite differences in the apparent nucleophilicity of the comonomers, there is an apparent reactivity ratio close to 1 and feed does control composition of the copolymers. Although composition can be controlled the solubility limitation of the EDOT units means that no fewer than two 3HT units can be with 1 EDOT unit before losing control of the polymerization.

Standard techniques for studying corrosion kinetics of bare substrates can be misleading when applied to coated substrates. By combining results from all techniques, conclusions can still be drawn, and some technique require additional calculations to give

accurate results. Results from OCP should always fall and climbing of the OCP suggests that the polymer film is highly capacitive. If this is the case, then EIS test should be performed close to the OCP of the bare substrate as EIS results are dependent on the potential used. For EIS the Brasher-Kingsbury equation will overestimate the amount of water found in films. The swelling of films should be considered, and if the swelling does not account for all deviation any additional deviation is the result of heterogeneous water uptake that has elongated morphology within the film.

Capacitive charging from EFM can cause overestimation of Corrosion kinetics, but the capacitive charging can be subtracted. The best way to model the capacitive charging was with a constant phase element, and a method for fast EFM was developed for monitoring early stages of corrosion.

When using a hydrophilic crosslinker in epoxy amine topcoats the phase separation does not create heterogeneous relaxation that would be seen in DMA, but there is still phase separation. Some regions are more hydrophilic, and these regions alter the way the film swells and takes in water. Films produced in this manner have an elongated hydrophilic structure that results in a strong correlation between water uptake and ion resistance, and EIS results will overestimate water uptake. Additionally, these films will swell less when the application temperature approaches wet T_g.

Polythiophene films alter corrosion through a combination of ion barrier properties and anodic polarization to induce passivity. Passive films for steel are weak, and the anodic polarization from polythiophenes is not strong enough to create a strongly passive steel substrate, but polythiophenes would work better on metals like aluminum that have more stable passivation behavior. Due to poor passivation lowering the onset

oxidation potential of polythiophenes generally decreases corrosion kinetics up to appoint when the polythiophene is essentially not polarizing enough to cause any passivation at all, which then leads to the polythiophene increasing corrosion rates compared to bare steel. The homopolymer P3HT appears to increase corrosion kinetics based on EFM results, but this is likely an artifact of capacitive charging. The nanowire morphology of P3HT is likely the reason P3HT acts so differently from the copolymers, suggesting that crystallization is detrimental to corrosion performance.

7.2 New Questions

We managed to synthesize the monomers and control both molecular weight and composition during this project, but there are still unanswered questions in relation to the synthesis. Although homopolymerization was decreased by changing the conditions for synthesis of 2,5-dibromo-3,4-ethylenedioxythiophene, the actual cause and optimized conditions were not found. The minimum ratio of 3-hexylthiophene per 3,4-ethylenedioxythiophene is 2:1for controlled copolymerization, but how would this change if blocky architectures were synthesized? Quasi-living conditions were observed with a slow decrease in rate that could be explained by first order chain termination, but what are the expected changes in kinetics assuming chain walking? The concentration of active chains should decrease over time according to the chain walking mechanism, which would also cause the pseudo first order data to depress. It is still unclear why polymerization is more likely to work when the comonomers are metathesized separately as opposed to in one pot. It may be due to differences in the higher stability of 3,4-ethylenedioxythiophene for metathesis and there is a small portion that gets metathesized twice, or it may be related to the active Grignard species during polymerization. It may

be possible that the Grignard dimer of the comonomers is much less reactive than dimers of the monomers individually (see Figure for explanation). The Schlenk equilibrium described the equilibrium between dimers and monomer version of Grignard reagents.

Scheme 7.1 Schlenk equilibrium and hypothesized less reactive thiophene dimer

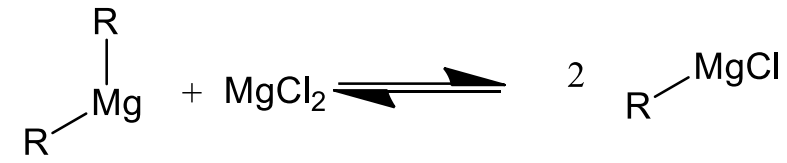

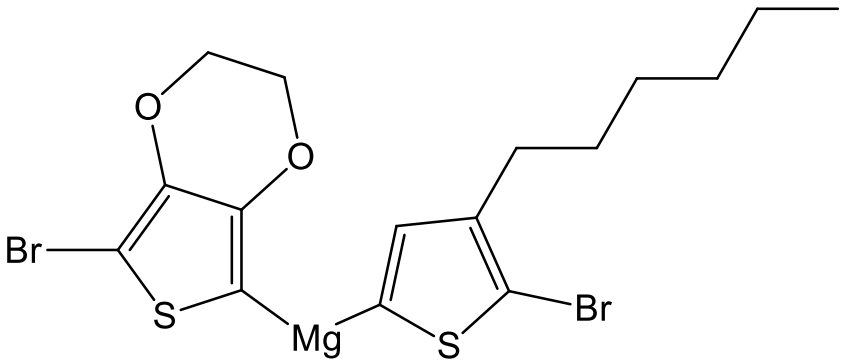

less reactive?

Most of the properties observed for the resulting polythiophenes can be easily explained, but the optical bandgap and fluorescent properties lead to some new questions. Is the effective conjugation length of the copolymers smaller, and can this explain the small shifts in optical bandgap for the films? Why are there two primary peaks for the fluorescence of P3HT as a film and is it related to the morphology? Also, there are multiple properties not measured during this project that could prove insightful. What are the crystallinity and crystal structures of the polythiophene films studied? What would

be the expected residual solvent content of these films? What are the water transport properties of the polythiophenes? How do all these properties change when the polymer is doped?

The electrochemical techniques have mostly been optimized for the relevant study, but there are a few avenues for unique techniques that were not looked into. Would it be possible to change the cell during EIS to separate the effect of barrier properties and actual corrosion kinetic data? Can EFM give corrosion kinetic data through films if a series of frequencies are used to account for the large capacitive properties of the films? Can cyclic voltammetry conditions be altered to give reliable Tafel data without capacitive distortions?

The EIS study on the Go9 series helped to better understand how morphology could alter EIS results and why, but there are a lot of unanswered questions. What are the actual z direction swelling properties for these films? If we raise the temperature can we see the same decrease in swelling for the other films when tested near the wet T_g? Can we get a microscopy or scattering technique to confirm the morphology suggested from DMA and EIS deviations, and would those morphologies match what was suggested? How would the morphology of the films alter the ion transport properties measured via EIS? Can mid-IR data be used to help elucidate the way water and ion transports through these films?

Although conclusions were drawn on the corrosion altering performance of the polythiophenes studied here, there are many unanswered questions. The most obvious questions would be: how does film morphology alter the results, and can they be

controlled? What effect would doping have on the corrosion performance? How would using a top coat alter the corrosion performance of these films?

7.3 Concluding Remarks

The data found within this document helps to improve our understanding of how polythiophenes alter corrosion of steel, how to best evaluate semi-conductive polymer films for corrosion altering properties, and how to study non-conductive polymer films using traditional electrochemical techniques. We show how multiple traditional methods can give misleading information, and how to interpret the data to avoid being misled. The data herein consistently support that polythiophenes alter the corrosion of steel by a combination of ion barrier properties and a passive state inducing polarization of the substrate, and that there exists an optimal onset oxidation potential of the polythiophene for the best performance. This potential can be controlled via copolymerization of two different monomers, and this technique can likely be applied to other conductive polymers for corrosion protection applications.

APPENDIX A – Solvent Mixtures Index

Table A.1 Solvent Mixture Index foe HSP Section

Solvent index	P3HT stock injection (uL)	bromobenzene (mL)	Acetone (mL)	Cyclohexane (mL)	oleic acid (mL)	Methanol (mL)	Target concentration mg/mL	volume fraction of bromobenzene
1	500	4.5	0	0	0	0	0.125	1
2	500	0	0	0	0	4.5	0.125	0.1
3	400	4.6	0	0	0	0	0.1	1
4	400	4.1	0	0.5	0	0	0.1	0.9
5	400	3.6	0	1	0	0	0.1	0.8
6	400	3.1	0	1.5	0	0	0.1	0.7
7	400	2.6	0	2	0	0	0.1	0.6
8	400	2.1	0	2.5	0	0	0.1	0.5
9	400	1.6	0	3	0	0	0.1	0.4
10	400	1.1	0	3.5	0	0	0.1	0.3
11	400	0.6	0	4	0	0	0.1	0.2
12	400	0.1	0	4.5	0	0	0.1	0.1
13	400	4.35	0.25	0	0	0	0.1	0.95

Table Continued

Solvent index	P3HT stock injection (uL)	bromobenzene (mL)	Acetone (mL)	Cyclohexane (mL)	oleic acid (mL)	Methanol (mL)	Target concentration mg/mL	volume fraction of bromobenzene
14	400	4.1	0.5	0	0	0	0.1	0.9
15	400	3.85	0.75	0	0	0	0.1	0.85
16	400	3.6	1	0	0	0	0.1	0.8
17	400	3.35	1.25	0	0	0	0.1	0.75
18	400	3.1	1.5	0	0	0	0.1	0.7
19	400	2.85	1.75	0	0	0	0.1	0.65
20	400	2.6	2	0	0	0	0.1	0.6
21	400	2.35	2.25	0	0	0	0.1	0.55
22	400	2.1	2.5	0	0	0	0.1	0.5
23	400	1.6	3	0	0	0	0.1	0.4
24	400	1.1	3.5	0	0	0	0.1	0.3
25	400	0.6	4	0	0	0	0.1	0.2
26	400	0.1	4.5	0	0	0	0.1	0.1
27	400	4.35	0	0	0.25	0	0.1	0.95

Table Continued

Solvent index	P3HT stock injection (uL)	bromobenzene (mL)	Acetone (mL)	Cyclohexane (mL)	oleic acid (mL)	Methanol (mL)	Target concentration mg/mL	volume fraction of bromobenzene
28	400	4.1	0	0	0.5	0	0.1	0.9
29	400	3.85	0	0	0.75	0	0.1	0.85
30	400	3.6	0	0	1	0	0.1	0.8
31	400	3.35	0	0	1.25	0	0.1	0.75
32	400	3.1	0	0	1.5	0	0.1	0.7
33	400	2.85	0	0	1.75	0	0.1	0.65
34	400	2.6	0	0	2	0	0.1	0.6
35	400	2.35	0	0	2.25	0	0.1	0.55
36	400	2.1	0	0	2.5	0	0.1	0.5
37	400	1.6	0	0	3	0	0.1	0.4
38	400	1.1	0	0	3.5	0	0.1	0.3
39	400	0.6	0	0	4	0	0.1	0.2
40	400	0.1	0	0	4.5	0	0.1	0.1

APPENDIX B – Relevant Chemical Structures

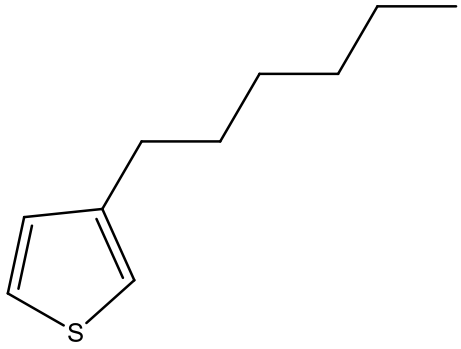

Scheme B.1 3-hexylthiophene

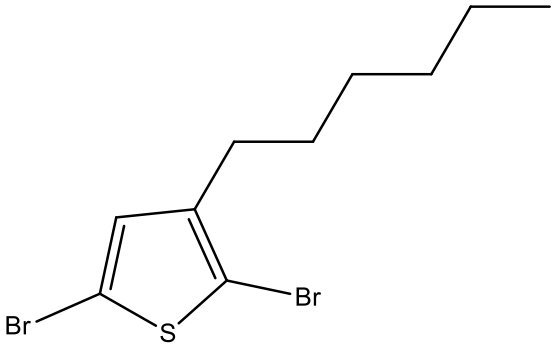

Scheme B.2 2,5-dibromo-3-hexylthiophene

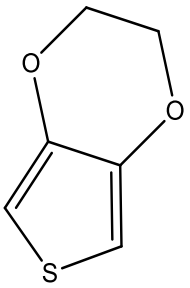

Scheme B.3 3,4-ethylenedioxythiophene

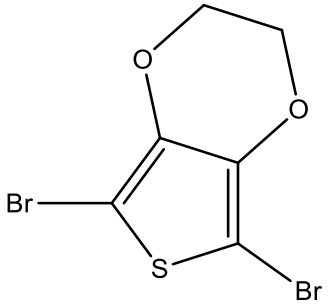

Scheme B.4 2,5-dibromo-3,4-ethylenedoxythiophene

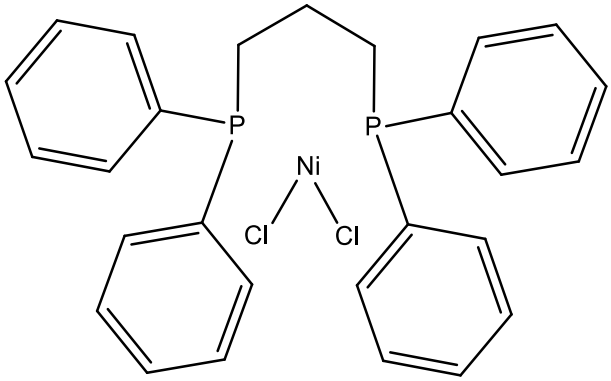

Scheme B.5 [1,3-Bis(diphenylphosphino)propane]dichloronickel(II)

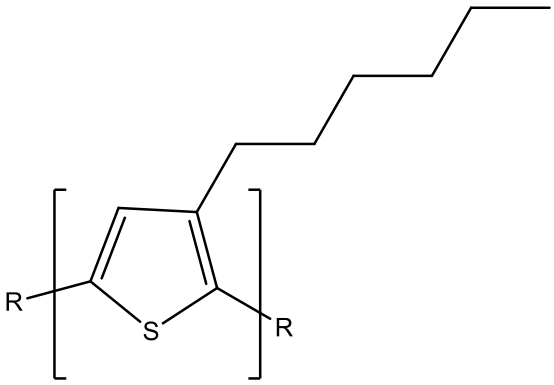

Scheme B.6 Poly(3-hexylthiophene)

P3HT is terminated with either Br, H, or an allyl group.

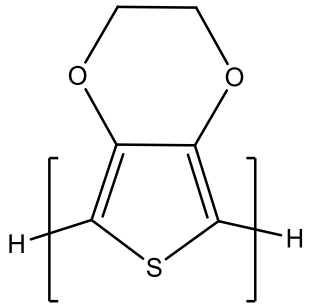

Scheme B.7 Poly(3,4-ethylenedioxythiophene)

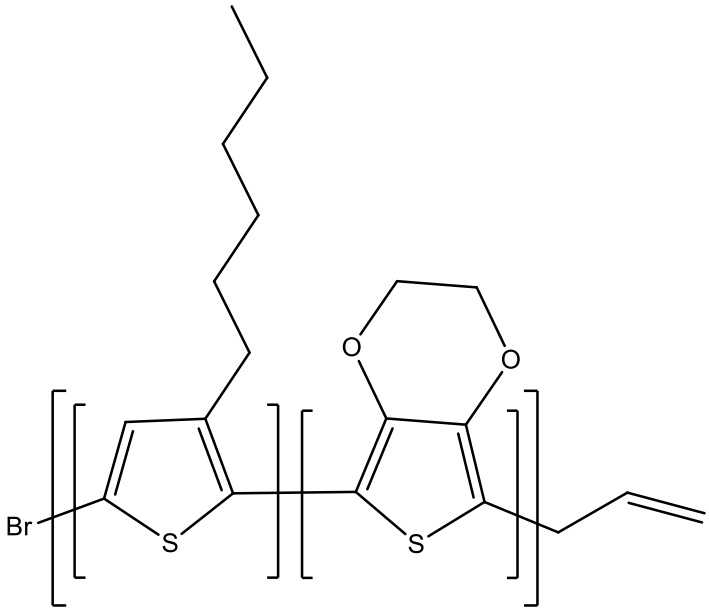

Scheme B.8 Poly(3-hexlythiophene-co-3,4-ethylenedioxythiophene)

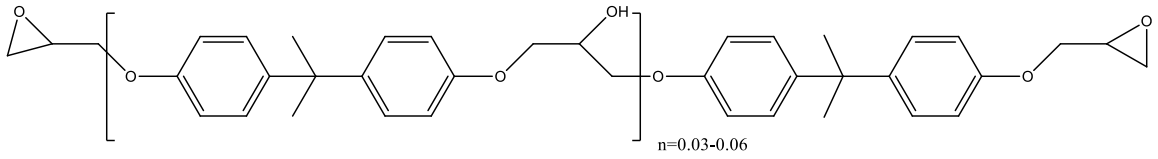

Scheme B.9 EPON 825

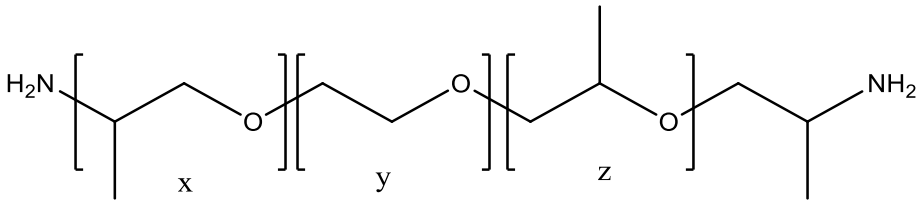

y~9, (x+z)~3.6

Scheme B.10 Jeffamine ED600

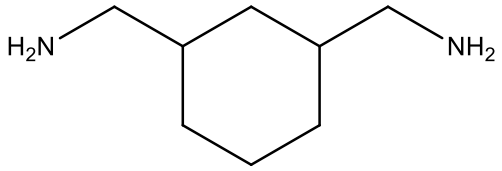

Scheme B.11 1,3-Bis(aminomethyl)cyclohexane

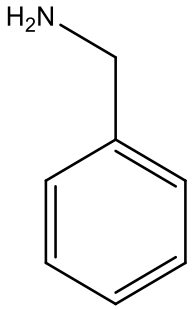

Scheme B.12 Benzylamine

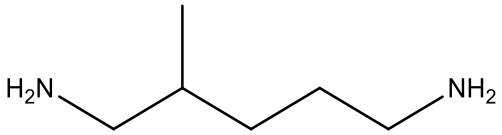

Scheme B.13 2-methylpentane-1,5-diamine

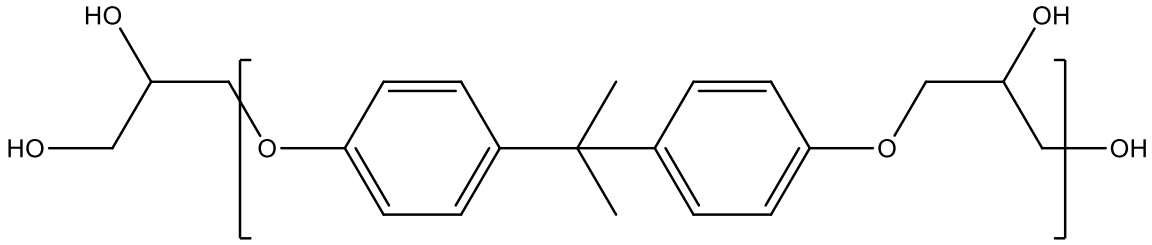

Mn=13,000 Mw=52,000

Scheme B.14 PKHH phenoxy resin

REFERENCES

(1) Koch, G. H.; Brongers, M. P.; Thompson, N. G.; Virmani, Y. P.; Payer, J. *Houston: NACE International* **2002**.

(2) Jackson, J.; Vol. 2019.

(3) Unceta, N.; Séby, F.; Malherbe, J.; Donard, O. *Anal Bioanal Chem* **2010**, *397*, 1097.

(4) Twite, R.; Bierwagen, G. P. *Progress in Organic Coatings* **1998**, *33*, 91.

(5) Coakley, K. M.; McGehee, M. D. *Chemistry of materials* **2004**, *16*, 4533.

(6) Grimsdale, A. C.; Leok Chan, K.; Martin, R. E.; Jokisz, P. G.; Holmes, A. B. *Chemical reviews* **2009**, *109*, 897.

(7) Horowitz, G. *Advanced materials* **1998**, *10*, 365.

(8) Jaiswal, M.; Menon, R. *Polymer international* **2006**, *55*, 1371.

(9) Bosch, R.; Hubrecht, J.; Bogaerts, W.; Syrett, B. *Corrosion* **2001**, *57*, 60.

(10) Zou, Y.; Sang, G.; Zhou, E.; Li, Y. *Macromolecular Chemistry and Physics* **2008**, *209*, 431.

(11) Kozycz, L. M.; Gao, D.; Seferos, D. S. *Macromolecules* **2013**, *46*, 613.

(12) Iovu, M. C.; Sheina, E. E.; Gil, R. R.; McCullough, R. D. *Macromolecules* **2005**, *38*, 8649.

(13) Loewe, R. S.; Khersonsky, S. M.; McCullough, R. D. *Advanced materials* **1999**, *11*, 250.

(14) Beryozkina, T.; Senkovskyy, V.; Kaul, E.; Kiriy, A. *Macromolecules* **2008**, *41*, 7817.

(15) Miozzo, L.; Battaglini, N.; Braga, D.; Kergoat, L.; Suspène, C.; Yassar, A. *Journal of Polymer Science Part A: Polymer Chemistry* **2012**, *50*, 534.

(16) Yang, Y. L.; Lee, Y. H.; Lee, Y. P.; Chiang, C. J.; Shen, C.; Wu, C. C.; Ohta, Y.; Yokozawa, T.; Dai, C. A. *Polymer international* **2014**, *63*, 2068.

(17) Govaerts, S.; Verstappen, P.; Penxten, H.; Defour, M.; Van Mele, B.; Lutsen, L.; Vanderzande, D.; Maes, W. *Macromolecules* **2016**, *49*, 6411.

(18) Stern, M.; Geary, A. L. *Journal of The Electrochemical Society* **1957**, *104*, 56.

(19) Mansfeld, F. *Electrochimica Acta* **1990**, *35*, 1533.

(20) Wint, N.; Bennett, A.; Williams, G.; McMurray, H. *Journal of The Electrochemical Society* **2018**, *165*, C890.

(21) Deshpande, P. P.; Jadhav, N. G.; Gelling, V. J.; Sazou, D. *Journal of Coatings Technology and Research* **2014**, *11*, 473.

(22) Schweitzer, P. A. *Corrosion Engineering Handbook, -3 Volume Set*; CRC Press, 1996.

(23) Marcus, R. A. *Canadian Journal of Chemistry* **1959**, *37*, 155.

(24) Marcus, R. A. *Reviews of Modern Physics* **1993**, *65*, 599.

(25) Tender, L.; Carter, M. T.; Murray, R. W. *Analytical Chemistry* **1994**, *66*, 3173.

(26) Laborda, E.; Suwatchara, D.; Rees, N. V.; Henstridge, M. C.; Molina, A.; Compton, R. G. *Electrochimica Acta* **2013**, *110*, 772.

(27) Silverstein, T. P. *Journal of Chemical Education* **2012**, *89*, 1159.

(28) Erdey-Gruz, T. *Kinetics of electrode processes.[Translated by L. Simandi. Translation rev. by DA Durham]*, 1972.
(29) Mirkin, M. V. In *Handbook of Electrochemistry*; Elsevier: 2007, p 639.
(30) Petrocelli, J. *Journal of The Electrochemical Society* **1950**, *97*, 10.
(31) Kolthoff, I.; Miller, C. *Journal of the American Chemical Society* **1940**, *62*, 2171.
(32) Butler, J.; Hugh, W.; Hey, D. *Transactions of the Faraday Society* **1926**, *22*, 24.
(33) Prasai, D.; Tuberquia, J. C.; Harl, R. R.; Jennings, G. K.; Bolotin, K. I. *ACS Nano* **2012**, *6*, 1102.
(34) Prasai, D.; Tuberquia, J. C.; Harl, R. R.; Jennings, G. K.; Rogers, B. R.; Bolotin, K. I. *ACS Nano* **2012**, *6*, 4540.
(35) Mabbott, G. A. *Journal of Chemical Education* **1983**, *60*, 697.
(36) King, A.; Scully, J. *Corrosion* **2011**, *67*, 055004.
(37) Kamaraj, K.; Karpakam, V.; Azim, S. S.; Sathiyanarayanan, S. *Synthetic Metals* **2012**, *162*, 536.
(38) Tafel, J. *Zeitschrift für physikalische Chemie* **1905**, *50*, 641.
(39) Fang, Y.-H.; Liu, Z.-P. *ACS Catalysis* **2014**, *4*, 4364.
(40) Edison, T. N. J. I.; Atchudan, R.; Pugazhendhi, A.; Lee, Y. R.; Sethuraman, M. G. *Journal of Molecular Liquids* **2018**, *264*, 483.
(41) Lorenz, W.; Mansfeld, F. *Corrosion Science* **1981**, *21*, 647.
(42) Zhang, J.-T.; Hu, J.-M.; Zhang, J.-Q.; Cao, C.-N. *Progress in Organic Coatings* **2004**, *51*, 145.
(43) Hinderliter, B.; Croll, S.; Tallman, D.; Su, Q.; Bierwagen, G. *Electrochimica Acta* **2006**, *51*, 4505.
(44) Reiss, H. *The Journal of Physical Chemistry* **1985**, *89*, 3783.
(45) Fermi, E. *Rendiconti Lincei* **1926**, *145*.
(46) Gerischer, H. *Applied Physics Letters* **1984**, *45*, 913.
(47) Gerischer, H.; Ekardt, W. *Applied Physics Letters* **1983**, *43*, 393.
(48) Reiss, H. *Journal of The Electrochemical Society* **1988**, *135*, 247C.
(49) Trasatti, S. *Pure and Applied Chemistry* **1986**, *58*, 955.
(50) Trasatti, S. *Electrochimica Acta* **1990**, *35*, 269.
(51) Hansen, W. N.; Hansen, G. J. *Surface science* **2001**, *481*, 172.
(52) Pludek, V. R. *Design and corrosion control*; Macmillan, 1977.
(53) Cicek, V.; Al-Numan, B. *Corrosion chemistry*; John Wiley & Sons, 2011.
(54) Reut, J.; Öpik, A.; Idla, K. *Synthetic Metals* **1999**, *102*, 1392.
(55) Zhong, L.; Xiao, S.; Hu, J.; Zhu, H.; Gan, F. *Corrosion Science* **2006**, *48*, 3960.
(56) Tallman, D. E.; Spinks, G.; Dominis, A.; Wallace, G. G. *Journal of Solid State Electrochemistry* **2002**, *6*, 73.
(57) Spinks, G. M.; Dominis, A. J.; Wallace, G. G.; Tallman, D. E. *Journal of Solid State Electrochemistry* **2002**, *6*, 85.
(58) Gelling, V. J.; Wiest, M. M.; Tallman, D. E.; Bierwagen, G. P.; Wallace, G. G. *Progress in Organic Coatings* **2001**, *43*, 149.
(59) Ohtsuka, T. *International Journal of Corrosion* **2012**, *2012*.

(60) de Leon, A. C. C.; Pernites, R. B.; Advincula, R. C. *ACS Appl Mater Interfaces* **2012**, *4*, 3169.
(61) Li, Y.; Zhang, H.; Wang, X.; Li, J.; Wang, F. *Synthetic Metals* **2011**, *161*, 2312.
(62) Rohwerder, M.; Michalik, A. *Electrochimica Acta* **2007**, *53*, 1300.
(63) Yu, W.; Yao, T.; Li, X.; Wang, T.; Gao, H.; Zhang, J.; Yang, B. *Journal of Applied Polymer Science* **2011**, *119*, 1052.
(64) Rammelt, U.; Nguyen, P.; Plieth, W. *Electrochimica Acta* **2003**, *48*, 1257.
(65) Glass, G.; Chadwick, J. *Corrosion Science* **1994**, *36*, 2193.
(66) De Leeuw, D.; Simenon, M.; Brown, A.; Einerhand, R. *Synthetic Metals* **1997**, *87*, 53.
(67) Yan, M.; Tallman, D.; Rasmussen, S.; Bierwagen, G. *Journal of The Electrochemical Society* **2009**, *156*, C360.
(68) Meroufel, A.; Deslouis, C.; Touzain, S. *Electrochimica Acta* **2008**, *53*, 2331.
(69) Johansen, H. D.; Brett, C. M.; Motheo, A. J. *Corrosion Science* **2012**, *63*, 342.
(70) Paliwoda-Porebska, G.; Stratmann, M.; Rohwerder, M.; Potje-Kamloth, K.; Lu, Y.; Pich, A. Z.; Adler, H.-J. *Corrosion Science* **2005**, *47*, 3216.
(71) Al-Ibrahim, M.; Roth, H.-K.; Zhokhavets, U.; Gobsch, G.; Sensfuss, S. *Solar Energy Materials and Solar Cells* **2005**, *85*, 13.
(72) Feng, Z.; Mo, D.; Wang, Z.; Zhen, S.; Xu, J.; Lu, B.; Ming, S.; Lin, K.; Xiong, J. *Electrochimica Acta* **2015**, *160*, 160.
(73) Jönsson, S.; Birgerson, J.; Crispin, X.; Greczynski, G.; Osikowicz, W.; Van Der Gon, A. D.; Salaneck, W. R.; Fahlman, M. *Synthetic Metals* **2003**, *139*, 1.
(74) McFarlane, S. L.; Deore, B. A.; Svenda, N.; Freund, M. S. *Macromolecules* **2010**, *43*, 10241.
(75) Wang, T.; Qi, Y.; Xu, J.; Hu, X.; Chen, P. *Applied Surface Science* **2005**, *250*, 188.
(76) Ramírez-Gómez, M. A.; Guzmán-Rabadán, K. K.; Gonzalez-Juarez, E.; Güizado-Rodríguez, M.; Ramos-Ortiz, G.; Alba-Rosales, J. E.; Panzo-Medrano, H.; Barba, V.; Rodriguez, M.; Maldonado, J. L. *International Journal of Polymer Science* **2017**, *2017*.
(77) Bhardwaj, D.; Gupta, S.; Yadav, P.; Bhargav, R.; Patra, A. *ChemistrySelect* **2017**, *2*, 9557.
(78) Achord, B. C.; Rawlins, J. W. *Macromolecules* **2009**, *42*, 8634.
(79) Wu, S.; Huang, L.; Tian, H.; Geng, Y.; Wang, F. *Macromolecules* **2011**, *44*, 7558.
(80) Verswyvel, M.; Verstappen, P.; De Cremer, L.; Verbiest, T.; Koeckelberghs, G. *Journal of Polymer Science Part A: Polymer Chemistry* **2011**, *49*, 5339.
(81) Britze, A.; Möllmann, V.; Grundmeier, G.; Luftmann, H.; Kuckling, D. *Macromolecular Chemistry and Physics* **2011**, *212*, 679.
(82) Zhu, Y.; Wolf, M. O. *Journal of the American Chemical Society* **2000**, *122*, 10121.

(83) Lee, E.; Hammer, B.; Kim, J.-K.; Page, Z.; Emrick, T.; Hayward, R. C. *Journal of the American Chemical Society* **2011**, *133*, 10390.
(84) Meng, H.; Perepichka, D. F.; Wudl, F. *Angewandte Chemie International Edition* **2003**, *42*, 658.
(85) Meng, H.; Perepichka, D. F.; Bendikov, M.; Wudl, F.; Pan, G. Z.; Yu, W.; Dong, W.; Brown, S. *Journal of the American Chemical Society* **2003**, *125*, 15151.
(86) Yin, Y.; Li, Z.; Jin, J.; Tusy, C.; Xia, J. *Synthetic Metals* **2013**, *175*, 97.
(87) Hou, J.; Park, M.-H.; Zhang, S.; Yao, Y.; Chen, L.-M.; Li, J.-H.; Yang, Y. *Macromolecules* **2008**, *41*, 6012.
(88) Nie, G.; Qu, L.; Xu, J.; Zhang, S. *Electrochimica Acta* **2008**, *53*, 8351.
(89) Achord, B. C. **2011**.
(90) Stefan, M. C.; Javier, A. E.; Osaka, I.; McCullough, R. D. *Macromolecules* **2008**, *42*, 30.
(91) Brodmann, T.; Koos, P.; Metzger, A.; Knochel, P.; Ley, S. V. *Organic Process Research & Development* **2011**, *16*, 1102.
(92) am Ende, D. J.; Clifford, P. J.; DeAntonis, D. M.; SantaMaria, C.; Brenek, S. J. *Organic Process Research & Development* **1999**, *3*, 319.
(93) Tkachov, R.; Senkovskyy, V.; Komber, H.; Sommer, J.-U.; Kiriy, A. *Journal of the American Chemical Society* **2010**, *132*, 7803.
(94) Miyakoshi, R.; Yokoyama, A.; Yokozawa, T. *Macromolecular rapid communications* **2004**, *25*, 1663.
(95) Costa, J. C.; Taveira, R. J.; Lima, C. F.; Mendes, A.; Santos, L. M. *Optical Materials* **2016**, *58*, 51.
(96) Spoltore, D.; Oosterbaan, W. D.; Khelifi, S.; Clifford, J. N.; Viterisi, A.; Palomares, E.; Burgelman, M.; Lutsen, L.; Vanderzande, D.; Manca, J. *Advanced Energy Materials* **2013**, *3*, 466.
(97) Cardona, C. M.; Li, W.; Kaifer, A. E.; Stockdale, D.; Bazan, G. C. *Advanced materials* **2011**, *23*, 2367.
(98) Machui, F.; Langner, S.; Zhu, X.; Abbott, S.; Brabec, C. J. *Solar Energy Materials and Solar Cells* **2012**, *100*, 138.
(99) Yuan, Y.; Shu, J.; Liu, P.; Zhang, Y.; Duan, Y.; Zhang, J. *The Journal of Physical Chemistry B* **2015**, *119*, 8446.
(100) Zoski, C. G. *Handbook of electrochemistry*; Elsevier, 2006.
(101) Goidanich, S.; Lazzari, L.; Ormellese, M. *Corrosion Science* **2010**, *52*, 916.
(102) Cassoux, P.; Dartiguepeyron, R.; Fabre, P.-L.; De Montauzon, D. *Electrochimica Acta* **1985**, *30*, 1485.
(103) Van Dyke, L. S.; Martin, C. R. *Langmuir* **1990**, *6*, 1118.
(104) Vakili, H.; Ramezanzadeh, B.; Amini, R. *Corrosion Science* **2015**, *94*, 466.
(105) McCafferty, E. *Corrosion Science* **2005**, *47*, 3202.
(106) Badea, G.; Caraban, A.; Sebesan, M.; Dzitac, S.; Cret, P.; Setel, A. *Journal of sustenable energy* **2010**, *1*.
(107) Noor, E. A.; Al-Moubaraki, A. H. *Int. J. Electrochem. Sci* **2008**, *3*, 806.

(108) Zhang, X.; Jiang, Z. H.; Yao, Z. P.; Song, Y.; Wu, Z. D. *Corrosion Science* **2009**, *51*, 581.
(109) Vlasak, R.; Klueppel, I.; Grundmeier, G. *Electrochimica Acta* **2007**, *52*, 8075.
(110) Castela, A.; Simoes, A. *Corrosion Science* **2003**, *45*, 1631.
(111) Philippe, L.; Lyon, S.; Sammon, C.; Yarwood, J. *Corrosion Science* **2008**, *50*, 887.
(112) Hirschorn, B.; Orazem, M. E.; Tribollet, B.; Vivier, V.; Frateur, I.; Musiani, M. *Electrochimica Acta* **2010**, *55*, 6218.
(113) Owen, B. B.; Miller, R. C.; Milner, C. E.; Cogan, H. L. *The Journal of Physical Chemistry* **1961**, *65*, 2065.
(114) Brasher, D.; Kingsbury, A. *Journal of Applied Chemistry* **1954**, *4*, 62.
(115) Bosch, R.-W.; Bogaerts, W. *Corrosion* **1996**, *52*, 204.
(116) Devay, J.; Meszaros, L. *Acta Chim. Aead. Sei. Hutu* **1979**, *100*, 183.
(117) Devay, J.; Meszaros, L. *ACTA CHIMICA ACADEMIAE SCIENTARIUM HUNGARICAE* **1980**, *104*, 311.
(118) Meszaros, L.; Devay, J. *Acta Chim. Acad. Sci. Hung.* **1980**, *105*, 1.
(119) Meszaros, L.; Devay, J. *Acta Chim. Acad. Sci. Hung.* **1982**, *109*, 241.
(120) Khaled, K. *Journal of Applied Electrochemistry* **2009**, *39*, 429.
(121) Obot, I.; Onyeachu, I. B. *Journal of Molecular Liquids* **2018**, *249*, 83.
(122) Kuş, E.; Mansfeld, F. *Corrosion Science* **2006**, *48*, 965.
(123) Abdel-Rehim, S.; Khaled, K.; Abd-Elshafi, N. *Electrochimica Acta* **2006**, *51*, 3269.
(124) Han, L.; Song, S. *Corrosion Science* **2008**, *50*, 1551.
(125) Lacombre, C. V.; Bouvet, G.; Trinh, D.; Mallarino, S.; Touzain, S. *Electrochimica Acta* **2017**, *231*, 162.
(126) Thomas, N. L. **1991**.
(127) Chang, J.-F.; Sun, B.; Breiby, D. W.; Nielsen, M. M.; Sölling, T. I.; Giles, M.; McCulloch, I.; Sirringhaus, H. *Chemistry of materials* **2004**, *16*, 4772.
(128) Janssen, G.; Aguirre, A.; Goovaerts, E.; Vanlaeke, P.; Poortmans, J.; Manca, J. *The European Physical Journal-Applied Physics* **2007**, *37*, 287.